The evolution of galaxies in the context of the cosmic web

Mădălina Nicoleta Tudorache
Christ Church
University of Oxford

A thesis submitted for the degree of
Doctor of Philosophy
Trinity 2024

DECLARATION

I declare that no part of this thesis has been accepted, or is currently being submitted, for any degree or diploma or certificate or any other qualification in this University or elsewhere.

The chapters of this thesis are based on either already published works, works under review or projects due to be submitted. Chapter 3 is based on Tudorache et al. (2022). This chapter is based on a project I led and performed the data analysis within the MIGHTEE-HI collaboration. For this project, data reduction was done by Ian Heywood and Anastasia Ponomareva. Matt Jarvis, Ian Heywood, Anastasia Ponomareva, Natasha Maddox and Imogen Whittam provided scientific, as well as technical advice. Other co-authors on this project provided technical advice. Chapter 5 is based on Tudorache et al. (2024a), which will be submitted to Monthly Notices of the Royal Astronomical Society. For this work, I am the lead author and I have performed the data analysis using the catalogues in Hatfield et al. (2022), with additional photometry provided by Rohan Varadaraj and Natalia Stylianou. Chapter 4 is a current project based on MIGHTEE-HI data approaching completion, using the same data provided by the MIGHTEE-HI collaboration in Chapter 3. It is a follow-up project from Chapter 3, in which I am also the lead author. Finally, Chapter 6 is based on Tudorache et al. (2024b), which will be submitted as soon as the data reduction and the analysis is completed. For this chapter, data reduction has been done by Ian Heywood and Anastasia Ponomareva and some of the figures provided are created by them. Scientific advice was provided by Matt Jarvis, Ian Heywood, Anastasia Ponomareva and Lyla Jung.

The work contained in this thesis was supported by the Hintze Centre for Extragalactic Astrophysics and Christ Church College, Oxford.

Madalina Tudorache — September 11, 2024

Acknowledgements

I've already warned a few people that this section is going to be longer than my actual thesis, as I feel this PhD could have not been possible without the help and support of a lot of my friends and co-workers that I've met along the way. A blanket thank you to everyone that crossed my path and helped me reach this point.

First and foremost, I want to thank Matt and Ian for giving me the chance to embark on this journey. Before I started all of this, I got told *"Matt is the kind of person who you can go for a pint with after work"*, which really turned out to be true. Thank you for your support in both academic and personal matters. Thanks to Ian for sharing his love for radio astronomy with me. Thanks both for taking a leap of faith with me in a subject that none of us was truly familiar with and trusting that I can achieve something in the field - even when I didn't trust myself that I could.

I'd also like to thank my entire research group for providing me with a great environment to not only do good science, but also develop as a person. Thank you to Imogen, Nathan, Aprajita, Nijin, Tariq, Catherine and Lyla for making my work life a lot more brighter. To Rohan, thanks for listening to my rants about LEPHARE and BAGPIPES. To Natalia, my sister in suffering, both in SED fitting and commuting by train (*"We are sorry to announce that this Great Western Railway service to Oxford has been cancelled..."*), thanks for providing all the moral support I needed quite a lot of times. To Andreea, even though our time knowing each other was pretty short, you've always provided me with snacks and a feeling of being close to home. To Anastasia - I don't even know where to begin. If there is someone without whom this PhD truly wouldn't have been possible, it's you. From our lockdown brunches in London to crying in Maidenhead, both your moral and academic support were the things that really kept me going. *Может нас выгнали из восточной Европы, но восточную Европу не выгнят из нас.*

Thanks to Ashling for de-facto running the whole department and for making sure I had access to anything I needed. Thanks to Jonathan for running GLAMDRING (despite all my complaints about the cluster) and for being so quick to solve all my computing issues. Thank you to the Dalitz people, Phil and Fergus, for letting me steal their palmeritas and letting me rant about anything from my work to my broken shower. James, I wasn't sure if I should list you under Dalitz people, Tower people or flatmates - but either way - thank you for the industrial quantities

of cat memes and letting me know whenever palmeritas were available in your office - and thank you so much for being my friend.

Thank you to the Tower - both the building and the people. I don't think I will ever find an office like this - I will truly cherish the years we've spent together despite the lack of natural light, the fly infestation and the possibility of the roof collapsing on top of us at any given moment. To Alex, whose love for radio astronomy, flags and geography taught me invaluable things. Shout-out to my favourite overseas territories that I've learnt for you - Akrotiri and Dhekelia, Wallis and Futuna, Tokelau, Aruba - we'd be here all day if I list all of them. I hope we'll get to do more quizzes even if we won't be in the same office/city/country anymore. *Tack!* To Casey, the author of all the quotes from my chapters - you truly are the weirdest person I've ever met, in the best way possible. This PhD would have been a lot more boring (but maybe more productive) if you weren't here, so I am really glad we got to share the last three years in the same office. Thanks for protecting the DWB from the demons during the night shift so we could all come in the morning and work as normal. *Go raibh maith agat!* To Curro, I'm glad someone else in the office understood the struggle of trying to understand galaxy evolution intertwined with cosmology. Thanks for sitting with me through all my complains about star formation, for organising the NAM session with us (and the associated problems) and for making sure we had a great social life in the office outside of the office. *¡Gracias!* To Eric, a fellow gas in galaxies observations person, thanks for also joining us in the mess the NAM session brought us, for listening to me talk about my Japanese classes - sorry we warped your perception of what a Western person is meant to be. 谢谢。 To Jaime, the first person I made friends in Oxford outside my house (not counting our prior meeting in Cambridge), thanks for making 1st year a lot more easier to get through - I can't convey how much the trips to Najar's really helped me during the lockdowns. Thank you for being my officemate, my flatmate, one of my best friends - these years have truly been a blast. *¡Gracias!*

I also want thank my flatmates, both current and past. To Dani, Daniel, Richard and Suzi - thanks for making my lockdown year a lot more bearable, despite the college's attempts to make it miserable. Sitting in the kitchen with biscuits, Phife Dawg the cat (that we did not kidnap) and Boris the cat truly made a difference to me. Thanks to Will and his coffee grinder, that made sure I was well caffeinated for work. Thanks to Loren for all the hugs and the times she's listened to me cry about my work. Fabian, I've never been more honoured to share a brain cell with someone. Thank you for making sure I was well-fed, somewhat mentally stable, overexposed to Balkan culture and just having a great time by just sitting in the living room for weeks in a row.

To all my friends outside of Oxford - Shriya, Calvin, Nathan and Teia, thanks for sticking with me for all these years and understanding my plight. To Olivia, whose evening podcasts always made sure I had to finish work in time so I can listen to them.

For Matthew, thanks for tagging along this rollercoaster of a journey. Your love made this all possible and I can't imagine doing any of this without you. Thanks for believing in me (and forcing me to believe in myself) and for supporting me throughout all circumstances.

Pentru mama si tata, care acum opt ani m-au pus pe un avion spre Marea Britanie și și-au pus toate speranțele în mine. Nu aș fi reușit să ajung aici fără suportul vostru. Sper că v-am făcut mândri.

Abstract

Traditionally, studies of the cosmic web in observations are done using optical/near-infrared data. However, there is a plethora of information hidden in the other wavelengths - especially in radio. In this thesis, I discuss how observations of neutral hydrogen (HI) can be used to understand the flow of gas in the intergalactic medium and how it links to the filaments of the cosmic web. Specifically, I investigate how the filaments of the cosmic web have an effect on the spin of the filaments and the physical processes that could be involved. Additionally, I explore how star formation histories (SFHs) derived from photometric bands and spectroscopy can be used to elucidate the relationship between neutral gas fraction and spin-filament alignment. Furthermore, I investigate the utilisation of SFH-derived parameters within an HI-selected sample to establish correlations between star formation, stellar mass, and HI mass. Moreover, I delve into the use of photometric redshifts, despite their inherent uncertainties, to probe the cosmic web at higher redshifts and draw insights into their impact on galaxy properties. Lastly, I discuss preliminary findings regarding an elongated HI structure comprising 14 dwarf galaxies discovered in the local Universe, which appears to trace the cosmic web, and its implications for models of galaxy evolution.

Contents

List of Abbreviations

ΛCDM . . . . **Λ** **C**old **D**ark **M**atter.

AGN . . . . . **A**ctive **G**alactic **N**uclei.

CGM . . . . . **C**ircum**g**alactic **M**edium.

CMB . . . . . **C**osmic **M**icrowave **B**ackground.

DTFE . . . . . **D**elaunay **T**essellation **F**ield **E**stimator.

FIR . . . . . **F**ar **I**nfra**r**ed.

FLRW . . . . . **F**riedmann-**L**emaître-**R**obertson-**W**alker.

i . . . . . **I**nclination.

IGM . . . . . **I**nter**g**alactic **M**edium.

IMF . . . . . **I**nitial **M**ass **F**unction.

IR . . . . . **I**nfra**r**ed.

HI . . . . . Neutral Hydrogen.

MIR . . . . . **M**id **I**nfra**r**ed.

MIGHTEE . . The **M**eerKAT **I**nternational **G**iga**H**ertz **T**iered **E**xtragalactic **E**xploration.

NFW . . . . . **N**avarro-**F**renk-**W**hite.

NIR . . . . . **N**ear **I**nfra**r**ed.

PA . . . . . **P**osition **A**ngle.

SED . . . . . **S**pectral **E**nergy **D**ensity.

SFH . . . . . **S**tar **F**ormation **H**istory.

SFR . . . . . **S**tar **F**ormation **R**ate.

SFRD . . . . . **S**tar **F**ormation **R**ate **D**ensity.

SMBH . . . . . **S**uper**m**assive **B**lack **H**ole.

SN . . . . . **S**uper**n**ova.

SPS . . . . . **S**tellar **P**opulation **S**ynthesis.

sSFR . . . . . **S**pecific **S**tar **F**ormation **R**ate.

TTT . . . . . **T**idal **T**orque **T**heory.

UV . . . . . **U**ltra**v**iolet.

You know how people look at constellations on romantic dates, I will take my date out and point at the sky and say: In that strip of the sky the m-bias is $5 \cdot 10^{-6}$.

Casey Cragg

1 Introduction

Contents

Galaxy evolution stands at the forefront of contemporary astrophysics, employing a multifaceted approach blending observational data, theoretical modelling, and computational simulations to elucidate to evolution of cosmic structures across cosmic epochs. In this context, studies of large-scale structures constitute a cornerstone of modern astrophysics, probing the cosmic web's intricate architecture

and the influence it exerts on galaxy formation and evolution. In this chapter, I will explore the interlink between cosmology and galaxy evolution, and lay the base necessary for understanding the effects on large-scale structures on galaxy properties.

1.1 Cosmology

The study of galaxy evolution is intimately connected to cosmology, as both fields seek to understand the fundamental nature and evolution of the Universe and its constituent structures. Understanding the evolution of the Universe has been a significant focus in modern cosmology. Various efforts have been made to comprehend the evolution of the Universe: de Sitter, Lemaître, Friedmann and others attempted to solve Einstein's equations (Einstein, 1917) in order to elucidate the expansion and development of the Universe. As such, we will also start from the Einstein Field Equations (Einstein, 1915):

$$G_{\mu\nu} - \Lambda g_{\mu\nu} = \kappa T_{\mu\nu} \tag{1.1}$$

where $G_{\mu\nu}$ is the Einstein tensor (which is a function of the Ricci curvature tensor $R_{\mu\nu}$ and the scalar curvature R, such that $G_{\mu\nu} = R_{\mu\nu} - \frac{1}{2}Rg_{\mu\nu}$), $g_{\mu\nu}$ is the metric tensor, $T_{\mu\nu}$ is the stress–energy tensor, Λ is the cosmological constant and κ is the Einstein gravitational constant $\left(\text{given by } {}^{8\pi G}/_{c^4}\right)$. $G_{\mu\nu}$ provides information about curvature, $T_{\mu\nu}$ incorporates information about matter (for an ideal fluid case it is a function of energy density ρ and pressure P and is dependent on the choice of metric), whilst Λ is the cosmological constant.

In order to describe the geometry of the problem, we require a metric. We define:

$$ds^2 = -dt^2 + a(t)^2 \left(\frac{dr^2}{1 - kr^2} + r^2(d\theta^2 + \sin^2\theta d\phi^2) \right) \tag{1.2}$$

where ds^2 is the spacetime interval (s represents the proper time), t is the time coordinate, $a(t)$ is the scale factor, r is the radial coordinate, k is the curvature constant, θ is the polar angle, and ϕ is the azimuthal angle. This is known as the Friedmann-Lemaître-Robertson-Walker (FLRW) metric (Robertson, 1935), which describes a homogeneous and isotropic Universe on the largest scales. The definition

of k gives us different possible universes in terms of their spatial curvature: for $k = -1$ we have an open Universe, for $k = 1$ we have a closed Universe, whilst for $k = 0$ we have a flat Universe.

By substituting the FLRW metric (Eq. 1.2) into the Einstein Field Equations (Eq. 1.1), we obtain the Friedmann Equations, which are given by:

$$H^2 = \left(\frac{\dot{a}}{a}\right)^2 = \frac{8\pi G}{3}\rho - \frac{kc^2}{a^2} + \frac{\Lambda c^2}{3} \tag{1.3}$$

and

$$\frac{\ddot{a}}{a} = -\frac{4\pi G}{3}(\frac{\rho}{c^2} + 3P) + \frac{\Lambda c^2}{3} \tag{1.4}$$

where the dot represents the time derivative, H is the Hubble parameter (also known as the expansion rate) and G is the gravitational constant.

Often, accompanying these equations we have the conservation equation for the energy density ρ:

$$\dot{\rho} + 3(\rho + \frac{P}{c^2})\frac{\dot{a}}{a} = 0. \tag{1.5}$$

By assuming the equation of state $P = w\rho$, where w is a constant, we can solve Eq. 1.5 for ρ, such that $\rho \propto a^{-3(1+w)}$. For $w = 0$ (which implies $P = 0$), we will have $\rho \propto a^{-3}$. This represents a matter dominated Universe. For $w = -1/3$, we will have $\rho \propto a^{-4}$, corresponding to a radiation dominated Universe. Finally, for $w = -1$ (which implies $P = -\rho$), we have $\rho =$ constant. This is a very interesting case, where we have negative pressure, which corresponds to a non-zero cosmological constant Λ.

The first Friedmann equation (Eq. 1.3), can be rearranged, such that:

$$1 = \frac{8\pi G}{3H^2}(\rho_M + \rho_R) - \frac{kc^2}{H^2a^2} + \frac{\Lambda c^2}{3H^2}, \tag{1.6}$$

where ρ has been split in two components, matter ρ_M and radiation ρ_R.

By defining the critical density (corresponding to a flat Universe) as:

$$\rho_c = \frac{3H^2}{8\pi G}, \tag{1.7}$$

we can then re-write Eq. 1.3 in terms of fractional densities, such that:

$$\Omega_M + \Omega_R + \Omega_k + \Omega_\Lambda = 1, \tag{1.8}$$

where Ω_M represents matter (both baryonic and dark matter) and is given by $\Omega_M = {}^{\rho_M}/_{\rho_c}$, Ω_R represents radiation and is given by $\Omega_R = {}^{\rho_R}/_{\rho_c}$, $\Omega_k = {}^{-kc^2}/_{H^2a^2}$ represents curvature and $\Omega_\Lambda = {}^{\Lambda c^2}/_{3H^2}$ represents dark energy.

In a radiation dominated Universe, the scale factor can be linked to time such that $a(t) \propto t^{1/2}$. Similarly, in a matter-dominated Universe, we have $a(t) \propto t^{2/3}$, and in a dark energy dominated Universe we have $a(t) \propto e^{\sqrt{\Lambda/3}t}$. Given the dependency of ρ on the scale factor a and the scale factor's dependency on time t, we can describe the Universe as radiation-dominated in its very early stages and origins; matter-dominated in later phases; and dark energy-dominated portraying its state in the current stage. The model with this requirement, together with the non-zero cosmological constant, is known as the ΛCDM (cold dark matter with a cosmological constant) model of the Universe.

Before we continue discussing the ΛCDM model and its parameters, another useful quantity to define is the redshift, z. The name *red*shift comes from the fact that, as the Universe expands, photons emitted at one wavelength will be stretched as space expands on their journey to an observer, hence will be shifted towards redder colours. As such, the definition of redshift can be written down:

$$z = \frac{\lambda_{\text{observed}} - \lambda_{\text{emitted}}}{\lambda_{\text{emitted}}}, \tag{1.9}$$

as a function of the wavelength of the light emitted and observed. Since $\lambda_{\text{observed}} = \lambda_{\text{emitted}} \frac{a(t=0)}{a(t)}$, redshift can then also be related to the scale factor such that:

$$1 + z = \frac{a(t=0)}{a(t)}, \tag{1.10}$$

where $a(t=0) = 1$ is the current scale factor. Hence, our current redshift is $z = 0$, whilst the redshift approaching the Big Bang would be $z \to \infty$.

Even without the formalism above, the idea of an expanding Universe was noted by Edwin Hubble (Hubble, 1929). He observed that the velocities of galaxies that

were further from the Earth were moving away faster than those closer to the Earth. He characterised the relation between the measured recessional velocity v a galaxy and the distance to a galaxy d as $v = H_0 d$, where H_0 is Hubble's constant. For the local Universe, it can be approximately related to redshift, such that:

$$z \approx \frac{H_0}{c} d. \tag{1.11}$$

It must be noted that this relationship breaks at higher redshift, as the Hubble parameter H depends on the scale factor a, as seen in Eq. 1.3.

Whilst Hubble's measurement of H_0 was ~ 500 kms^{-1}Mpc^{-1}, today we have access to a plethora of information which can constrain it better. Measuring H_0, as well as the other ΛCDM parameters can be achieved through several cosmological probes. One of them is via measuring the power spectrum of the Cosmic Microwave Background (CMB), which is a black-body radiation left over from the Big Bang with a present-day temperature of 2.73 K. First detected by Penzias and Wilson (1965), the CMB and its anisotropies (tiny temperature fluctuations) have given us very important constraints to our cosmological models (e.g. Spergel et al., 2003; Planck Collaboration et al., 2020). Other techniques used in parameter constraints are via distance measurements using Type Ia Supernovae (Riess et al., 1998) or via galaxy weak lensing (Hoekstra et al., 2002). Locally, we can use Cepheid variable stars (which are a type of pulsating star that varies in brightness predictably over time) to infer distances (Riess et al., 2016). In regards to H_0, by using supernova distance ladder measurements, Cepheid variables, or using the CMB power spectrum, we can constrain H_0 with much more accuracy, which gives $H_0 \approx 70$ kms^{-1}Mpc^{-1}. However, this has led to a 5σ discrepancy in the value of H_0 from the type Ia and CMB methods (Riess et al., 2022; Planck Collaboration et al., 2020).

Before moving onto the next section, we need to define distances in the context of ΛCDM cosmology. Eq. 1.2 can be rewritten in terms of the comoving radial distance, χ, which, in the absence of curvature, is equivalent to $\chi \equiv r$ in said equation. Then, the comoving distance χ in a flat Universe can be defined as:

$$\chi = \frac{c}{H_0} \int_0^z \frac{dz'}{\sqrt{\Omega_r (1+z')^4 + \Omega_m (1+z')^3 + \Omega_k (1+z')^2 + \Omega_\Lambda}}. \tag{1.12}$$

However, in astronomy, we often measure proxies of this distance. The angular diameter distance d_A represents how big an object would appear in the sky given its actual size and distance from the observer. It is related to the comoving distance χ by:

$$d_A = \frac{\chi}{1+z}. \tag{1.13}$$

The luminosity distance d_L is another important cosmological concept that relates to how bright an object appears from Earth, given its intrinsic luminosity and its distance from the observer. It is defined such that:

$$F = \frac{L}{4\pi d_L^2}, \tag{1.14}$$

where F is the flux measured by the observer, and L is the source luminosity. In relation to the comoving distance χ, it can be written as:

$$d_L = \chi(1+z). \tag{1.15}$$

In the context of this work, I will assume a standard cosmology of a flat ($\Omega_k(z=0)=0$), radiation-less Universe ($\Omega_R(z=0)\approx 0$), where the contribution of matter to the total energy density is $\Omega_M(z=0)=0.3$ and the density of the dark energy is $\Omega_\Lambda = 0.7$. I will use a value for H_0 of 70 $\mathrm{kms}^{-1}\mathrm{Mpc}^{-1}$.

1.1.1 The nature of Dark Matter

When we defined Ω_M in the section above, we mentioned matter as both baryonic and dark matter. Baryonic matter refers to any form of visible matter such as gas, planets, stars and galaxies and it only makes up $\sim 20\%$ of the total matter budget. The rest is made up of dark matter - a mysterious form of matter that does not interact with light or any other electromagnetic radiation, making it invisible to telescopes and detectors (Bertone and Hooper, 2018). However, its existence can be inferred through its gravitational effects on visible matter and the large-scale structure of the Universe. We have been able to study the effects of dark matter by observing galaxy dynamics. The existence of dark matter was

initially deduced from the analysis of the velocity dispersion of the Coma cluster by Zwicky (Zwicky, 1937). The estimated mass derived from the cluster's behaviour far exceeded that calculated based on the observed light emitted by galaxies within it. Through observations of galaxy rotation curves (e.g. see the work of Rubin and Ford, 1970 for an early example of a measurement of Andromeda's rotation curve) and gravitational lensing (e.g. Bartelmann and Schneider, 2001; Treu and Koopmans, 2004; Clowe et al., 2006; Massey et al., 2010), it has become clear that there is more mass in galaxies than can be accounted for by visible matter alone.

Dark matter candidates can be broken down into 'hot' (HDM), 'warm' (WDM), and 'cold' dark matter (CDM) in terms of their velocity. HDM refers to particles that were highly energetic at the time of decoupling from radiation and are still moving at high speeds (Hannestad et al., 2010). WDM refers to particles that have intermediate energies at the time of decoupling and move at slower speeds compared to hot dark matter (Viel et al., 2005). CDM, on the other hand, refers to particles that were non-relativistic at the time of decoupling and move at relatively slow speeds. The most widely accepted and supported candidate for dark matter is the CDM model. Notably, CDM solves the observed flat rotation curves of galaxies, a phenomenon inconsistent with the predictions of alternative models such as HDM (Kravtsov et al., 1998; Del Popolo, 2014). The hierarchical formation of structures, from the large-scale cosmic web and its components (Frenk and White, 2012) down to dwarf galaxies (with some exceptions, see Bullock and Boylan-Kolchin, 2017, for a discussion on the problems of CDM on small scales), is naturally explained by CDM, in accordance with both theoretical predictions and observational data. Additionally, CDM is consistent with the patterns observed in the CMB (Bond and Efstathiou, 1987; de Bernardis et al., 2000).

There are several candidates for cold dark matter: primordial black holes, weakly interacting massive particles (WIMPS), axions, and sterile neutrinos, however we have not been able to confirm any of them. For a recent review on dark matter models and the developments in their detection, see Arbey and Mahmoudi (2021). Within CDM, we also have more exotic sub-categories such as 'self-interacting' dark

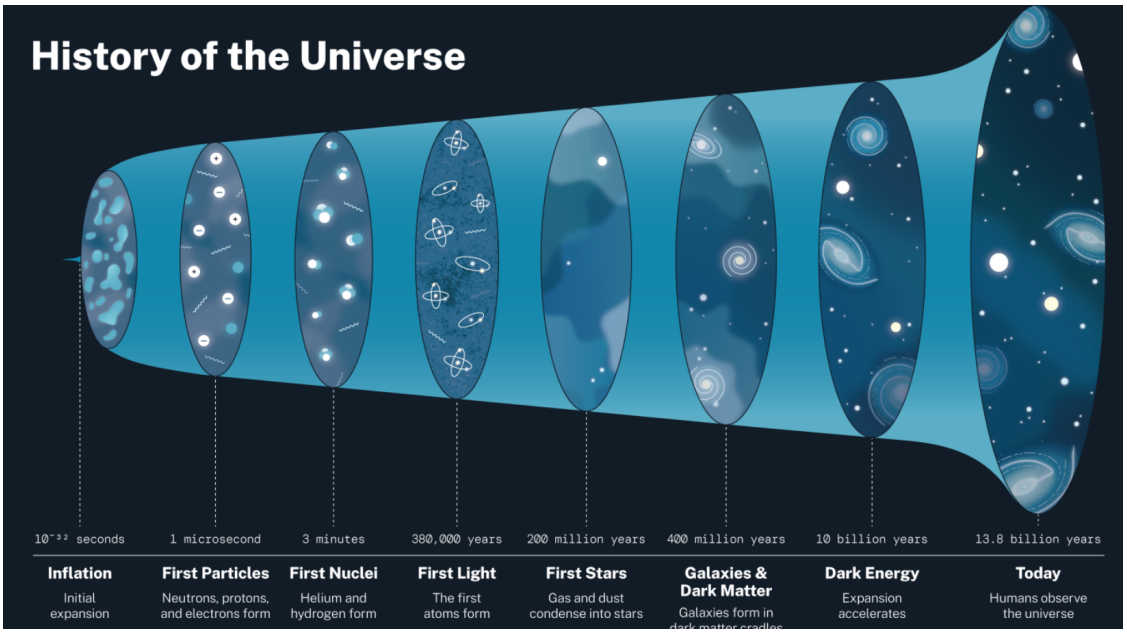

Figure 1.1: A cartoon representation from NASA of the timeline of the Universe.

matter (SIDM; Spergel and Steinhardt, 2000) or 'fuzzy dark matter' (FDM; Hu et al., 2000). SIDM refers to particles that interact with each other through forces other than gravity (Tulin and Yu, 2018), whilst FDM is a modified form of CDM which is DM candidate with a wave-like behaviour (Zhang et al., 2018).

1.1.2 Chronology of the Universe

Atoms started forming during **recombination** at a redshift of $z = 1100$, which represents the change between the radiation-dominated era to the matter-dominated era, as matter and radiation decouple. The epoch following recombination was known as the **Dark Ages** ($25 \lesssim z \lesssim 1000$), in which no structures that produced light existed (Miralda-Escudé, 2003). This was followed by the formation of the first stars and galaxies, which is known as the **Cosmic Dawn**. Following this era, the first luminous sources ionised the neutral hydrogen found in the intergalactic medium (IGM), which is known as the **Epoch of Reionisation** (Gunn and Peterson, 1965). After the reionisation of the Universe, galaxies continued to evolve through various processes including star formation, growth of black holes, mergers with other galaxies, and interactions with the surrounding environment. The peak of the cosmic star formation rate, known as the **Cosmic Noon**, is reached at a redshift of

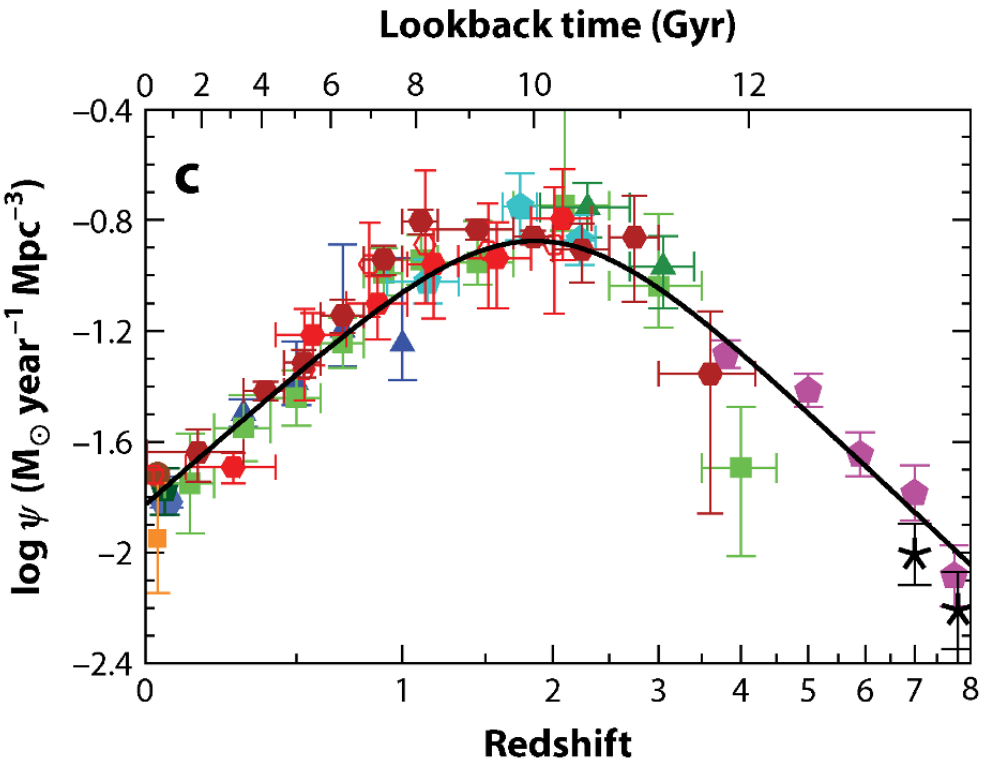

Figure 1.2: The cosmic star formation ψ as a function of redshift. The points represent the cosmic star formation rate density (SFRD) from far-UV and IR data, whilst the solid line plots the best-fit SFRD. Reproduced from Madau and Dickinson (2014).

$z \approx 2$ (Shapley, 2011; Madau and Dickinson, 2014; Conselice, 2014), as illustrated in Figure 1.2. During this period, galaxies were forming stars at a very rapid rate, fuelled by the abundant supply of gas and matter in the Universe (Tumlinson et al., 2017). However, as the Universe continued to expand and age, the rate of star formation gradually declined, due to several processes, which I will discuss in more details in Section 1.2. In the present epoch, the rate of star formation has dropped to a tenth of its peak value, and most galaxies have transitioned to a quiescent state, with only a small fraction of their remaining gas being converted into stars. As the Universe gets older and older, it will continue to expand. Galaxies, unable to produce stars at a sufficient rate, will eventually fade into stellar remnants, leaving behind only objects such as black holes, white dwarfs and neutron stars.

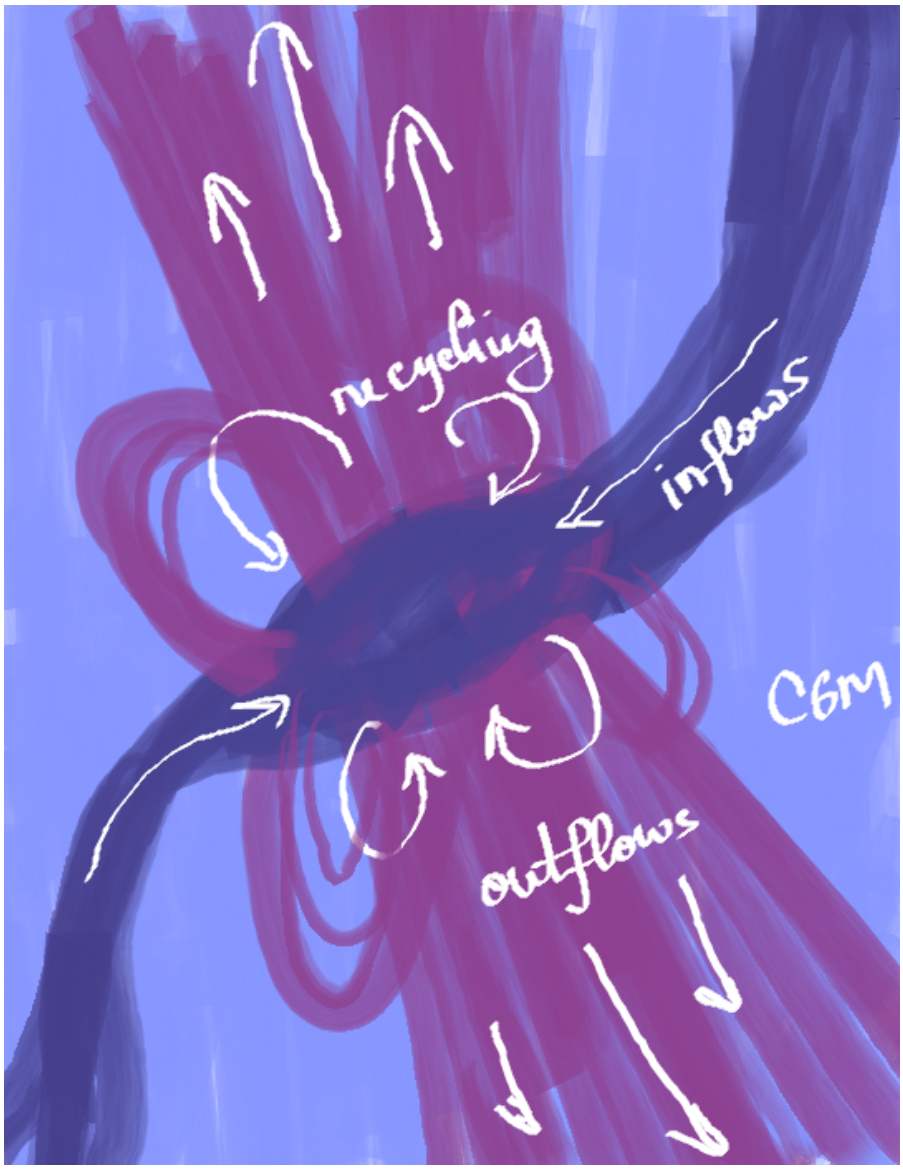

Figure 1.3: A schematic diagram of the inflows and the outflows of a galaxy, as presented in Tumlinson et al. (2017). The galaxy is fed by filamentary accretion (purple) from the IGM. Outflows emerge from the disk, while gas that was previously ejected is recycling (fuchsia). The "diffuse gas" halo (light purple) includes gas that is likely contributed by all these sources and mixed together over time.

1.2 The life-cycle of a galaxy

The life cycle of a galaxy, known as the baryon cycle, spans billions of years and is shaped by various processes such as gravity, accretion, star formation, and interactions with other galaxies. In this section, I discuss the main stages in the life of a galaxy, from formation to cessation of star formation.

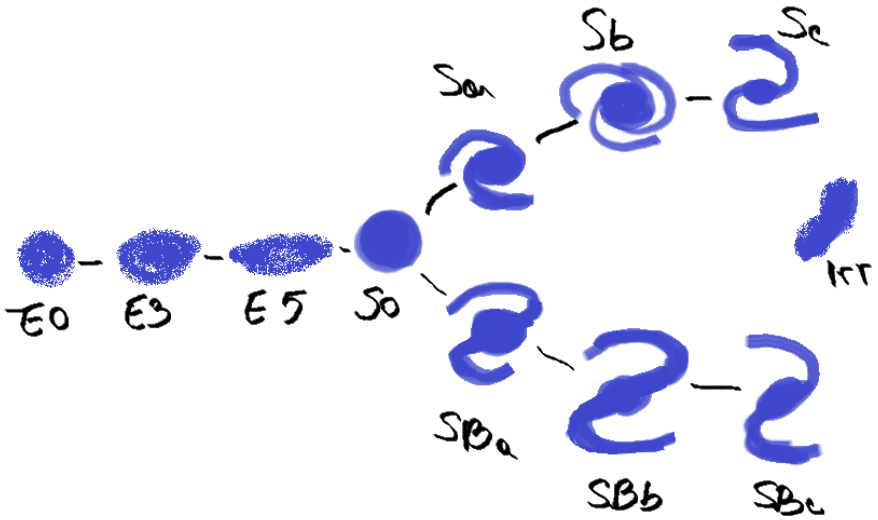

Figure 1.4: A cartoon representation of the Hubble tuning fork. On the left side, there are three types of elliptical galaxies (E0, E3 and E5), at the centre there are lenticular galaxies (S0), whilst on the right side lie the two types of spiral - barred (SBa, SBb, SBc) and unbarred (Sa, Sb, Sc). Also to the right are irregular galaxies (Irr), which fall outside of the fork.

1.2.1 Forming a galaxy

An important contribution that Edwin Hubble made was the classification scheme for galaxies, known as Hubble sequence (or the Hubble tuning fork diagram), which separates galaxies into two types: disk galaxies and elliptical galaxies (Hubble, 1926). Elliptical galaxies exhibit smooth and featureless profiles, while spiral galaxies showcase central bulges surrounded by spiral arms. In reality, galaxies are a lot more diverse - there are more types of elliptical galaxies, spiral galaxies can be split in barred (S) and unbarred (SB), and lenticular (S0) and irregular (Irr) galaxies also exist. Elliptical galaxies are classified on a scale from E0 (nearly spherical) to E7 (elongated). The spirals are further split within unbarred (Sa, Sb, Sc) or barred (SBa, SBb, SBc). Lenticular galaxies share characteristics of both elliptical and spiral galaxies but lack distinct spiral arms. Lastly, irregular galaxies, with their irregular shapes, represent a separate category (see Figure 1.4 for a schematic representation of the tuning fork).

The mechanisms via which galaxies formed were not well understood at the time and it took decades to grasp the many potential processes involved. The

first numerical simulations (e.g. Larson, 1976) which attempted to explain galaxy formation via collapse of gas clouds initially faced challenges in reproducing the observed properties of elliptical galaxies. Toomre and Toomre (1972) proposed that interactions and mergers between disk galaxies could explain the formation of elliptical galaxies, providing some solution to the discrepancy. However, this model was still incomplete, as it still did not accurately predict properties of some observed bright elliptical galaxies. Because of this, as well as the shape of the galaxy rotation curves, it became apparent that the effects of dark matter needed to be included in the formation of galaxies.

Thus, in order to understand how galaxies formed, we first need to understand the formation of dark matter haloes. Dark matter haloes are generated by random quantum fluctuations in the early Universe, and they serve as the building blocks for galaxy formation. White and Rees (1978) proposed the hierarchical growth model: as small dark matter haloes merge, baryonic matter is drawn towards the centre of these haloes due to gravity and it cools down through radiating light, which speeds up the process. The cooling of baryonic matter allows it to compress under the force of gravity, leading to the formation of proto-galaxies. These proto-galaxies consist mainly of clouds of hydrogen and helium gas that cool through thermal radiation and undergo compression due to gravity. However, this hierarchical model predicted a much higher number of faint galaxies than observed. Fall and Efstathiou (1980) proposed a model within the CDM formalism for disk formation within dark matter haloes, incorporating expected angular momentum from tidal torques, which explained various observed properties of disk galaxies. Further investigations followed into galaxy formation (e.g. Efstathiou and Silk, 1983; Blumenthal et al., 1984), leading to more sophisticated numerical simulations and a deeper understanding of the role of dark matter in shaping the formation of galaxies, particularly through semi-analytical models (SAMs) and hydrodynamical simulations. The semi-analytical approach, pioneered by White and Frenk (1991), utilises knowledge about CDM halo structure and assembly history to model the gravitational potential wells where galaxies form and evolve, incorporating relevant

physical processes in a semi-analytical manner. On the other hand, the first three-dimensional hydrodynamical simulations of galaxy formation involving dark matter (Katz and Gunn, 1991; Katz, 1992) were focusing on the collapse of a rotating sphere. Navarro and Benz (1991) conducted the first simulation of galaxy formation via hierarchical clustering from cosmological initial conditions, followed by Navarro and White (1994) who performed the first simulation of galaxy formation from CDM initial conditions, which were a subset of initial conditions. From these simulations, we can infer how dark matter haloes evolve non-linearly via gravitational instability. Initially, density inhomogeneities grow linearly until reaching a critical density threshold and collapse under their own gravity. Then, the kinetic energy of particles within the halo reaches a balance with the gravitational potential energy, resulting in a stable, self-gravitating system (the halo becomes virialised). These haloes continuously accumulate mass, either by drawing in material from their vicinity or by merging with other haloes. Following mergers, some haloes persist as bound structures, resulting in a population of sub-haloes. Over time, small-scale irregularities develop into individual small haloes, which subsequently coalesce to form a larger, ellipsoidal-shaped virialised dark matter halo. This larger halo exhibits substructure in the form of dark matter sub-haloes. These sub-haloes will represent the hosts for the proto-galaxies that will form.

An important result from N-body numerical simulations of hierarchical structure formation in the universe, particularly in the context of cold dark matter (CDM) cosmologies is the halo density profile. One of the most commonly used profile is the Navarro-Frenk-White (NFW) profile (Navarro et al., 1996b). The NFW profile emerged as a robust description of the typical density distribution of dark matter haloes in the universe, by repeatedly simulating a large number of haloes in different conditions. The NFW profile of the density of dark matter ρ in a halo as a function of the distance from the centre r is then given by:

$$\rho(r) = \frac{\rho_0}{\frac{r}{r_s}\left(1+\frac{r}{r_s}\right)^2} \tag{1.16}$$

where ρ_0 is the characteristic density of the halo and R_s is the scale radius of the halo (the radius at which the logarithmic slope of the density profile is -2). The profile exhibits a steep rise towards the centre and a power-law decline in the outer regions, making it suitable for describing the density distribution of dark matter haloes in a wide range of mass scales. Whilst successful at large scales, the NFW profile has been found to have some limitations when applied to smaller scales. These limitations include discrepancies between the predicted and observed profiles of low surface brightness galaxies and late-time dwarfs, known as the cusp-core problem (Navarro et al., 1996a). This discrepancy suggests that there may be additional physical processes at play in shaping the density profiles of these systems. One obvious explanation for the cusp-core problem is the presence of baryonic matter, such as gas and stars, which can affect the distribution of dark matter through processes like dynamical friction, gravitational interactions, and feedback effects. Other possible explanations could be provided by a different model of dark matter, such as self-interacting dark matter, fuzzy dark matter or warm dark matter, which can lead to a smoother and more core-like density profile (see Section 1.1.1). There are alternative profiles that can be used, such as the Einasto profile (Einasto, 1965), the Burkert profile (Burkert, 1995) or the Moore profle (Moore et al., 1998a). A comparison between the four profiles named here can be seen in Figure 1.5. However, irrespective on the parametrisation, most profiles agree on average with simulations.

1.2.2 Fuelling the evolution of a galaxy

The evolution of a galaxy is often described through its star formation. However, the process of star formation is still not fully understood. We have yet to accurately predict the mass fraction and time scale for a self-gravitating cloud to transform into stars (McKee and Ostriker, 2007). Furthermore, the mass distribution with which stars are formed, known as the initial mass function (IMF; Chabrier, 2003), remains a poorly understood aspect of galaxy evolution. Here, I will only introduce processes that induce/maintain star formation, with a brief discussion about IMFs in Section 1.3.2.

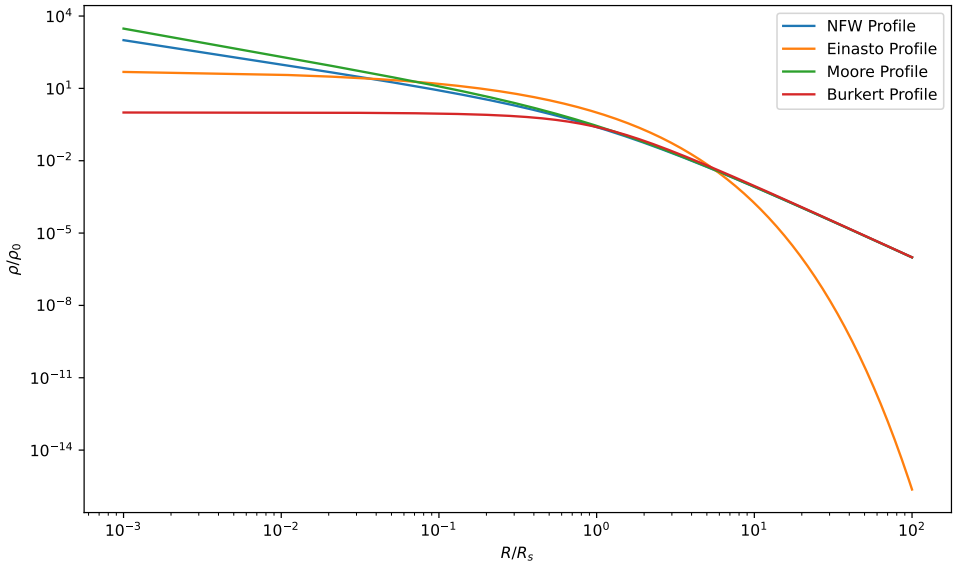

Figure 1.5: A comparison between different dark matter density profiles (NFW, Einasto, Moore and Burkert), normalised to the same mass

.

It is widely agreed that there is a bimodality in the population of galaxies: there are blue, younger, star-forming galaxies and red, quenched galaxies (Kennicutt, 1998; McKee and Ostriker, 2007; Kennicutt and Evans, 2012). This can be further split into categories such as 'star-bursting' galaxies, 'star forming main sequence' galaxies (falling under the star-forming umbrella) and 'green valley' galaxies, and 'passive' galaxies (falling under the 'quenched' umbrella) based on their level of star formation activity, as can be seen in Figure 1.6. In this section, I will focus on the blue galaxies, whilst in Section 1.2.3, I will focus on the pathways from which galaxies become red. The star formation of a galaxy is closely tied to its total stellar mass. Galaxies with larger stellar masses tend to have higher star formation rates compared to galaxies with lower stellar masses. This correlation between stellar mass and star formation rate is known as the star forming main sequence (SFR$-M_*$ relation; Noeske et al., 2007; Whitaker et al., 2012; Johnston et al., 2015; Popesso et al., 2019a; Popesso et al., 2019b; Leslie et al., 2020; Fraser-McKelvie et al., 2021).

The main processes that drive star formation in a galaxy are the availability of dense molecular gas (which needs to be converted from cold, neutral gas) and

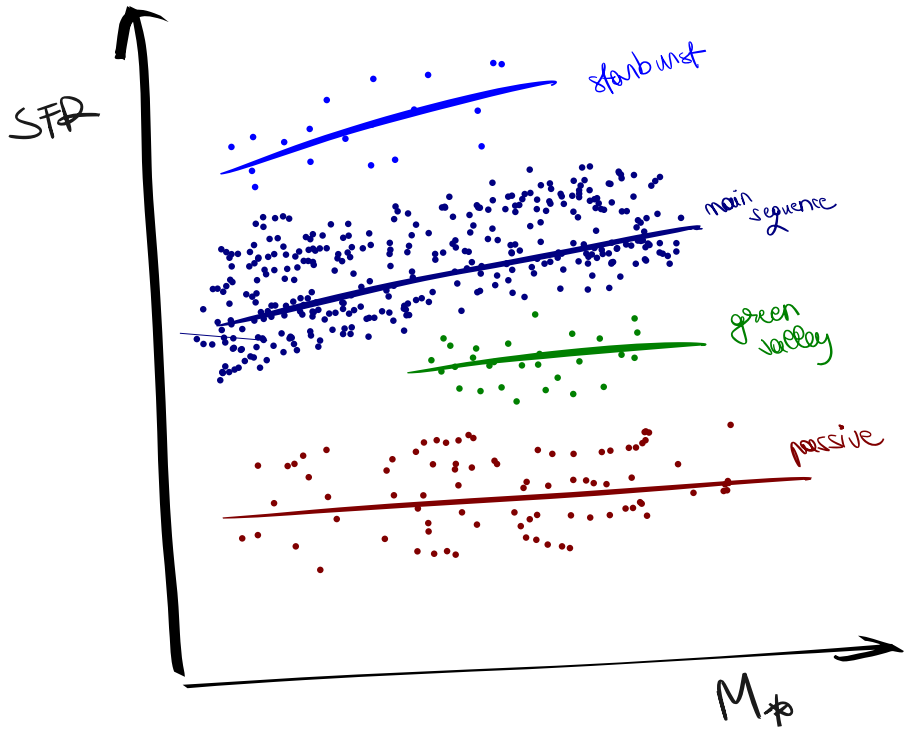

Figure 1.6: A cartoon representation of the stellar mass-star formation rate diagram, showing each category of galaxies that lie along it.

the ability of a galaxy to form molecular clouds (Wong and Blitz, 2002). Theory predicts that all star formation takes place in dense molecular clouds (McKee and Ostriker, 2007; Kennicutt and Evans, 2012). Furthermore, starbursts in galaxies are associated with large amounts of molecular gas confined to small volumes (Scoville et al., 1989; Wilson et al., 2008; Saintonge et al., 2012). In order to obtain molecular gas, a galaxy can acquire it through various sources. One important source of molecular gas is via conversion from atomic gas, which can be accreted from large-scale structures (see Section 1.5.2 for how the cosmic web supplies gas onto galaxies, as well as discussions in Chapters 3-6) or from the ISM (Krumholz et al., 2009; Krumholz et al., 2011). Other sources of molecular gas originate from satellite galaxies or interacting galaxies (e.g. Barton et al., 2000; Ann et al., 2008; Kauffmann et al., 2010; Grootes et al., 2017), and recycling of gas from stellar mass loss through stellar winds and supernova explosions (e.g. Dekel and Silk, 1986; Kauffmann et al., 2003; Bertone et al., 2007).

Another key process that can also drive star formation is the occurrence of

merger events (Barnes and Hernquist, 1991; Lacey and Cole, 1993). These merger events involve the collision and subsequent merging of two or more galaxies. During a merger event, the gravitational forces between the galaxies cause them to interact and merge together. This interaction can have profound effects on the structure and composition of the galaxies involved. As the galaxies merge, their gas and stars become mixed together, leading to the formation of new structures and configurations as they create regions of increased density and pressure. These conditions provide the ideal environment for the formation of new stars (Kauffmann et al., 1993; Somerville et al., 2001).

There are two types of mergers: major mergers and minor mergers (Tremaine, 1981). Major mergers involve the collision and merging of two similarly sized galaxies. During major mergers, the combined gravitational forces of the galaxies can cause significant disturbances in their structures, leading to the formation of tidal tails, bridges, and other morphological features (Toomre, 1977; Negroponte and White, 1983; Conselice et al., 2003; Cox et al., 2006; Wang et al., 2012). Minor mergers, on the other hand, involve the interaction and merging of a smaller galaxy with a larger one (with stellar mass ratios of 3:1 or higher). During minor mergers, the smaller galaxy is typically disrupted and absorbed into the larger galaxy, contributing its gas and stars to the overall mass of the system and potentially fuelling new episodes of star formation (Quinn et al., 1993; Walker et al., 1996; Bournaud et al., 2005; Qu et al., 2011). On average, there are a lot more minor mergers occurring than major mergers (Lotz et al., 2011). Mergers can also be classified as either dry or wet mergers depending on the presence of gas in the interacting galaxies. Dry mergers occur when two gas-poor galaxies merge, resulting in no change in the overall star formation rate (Bell et al., 2006; Khochfar and Silk, 2009; Liu et al., 2009). On the other hand, wet mergers involve gas-rich galaxies merging, leading to spikes in star formation rates during the merging process (Lin et al., 2010; Chou et al., 2013). However, some gas-rich mergers might not always lead to an increase in stellar mass as well. In these cases, the gas fraction (or the HI-to-stellar mass ratio, as we discuss in the following chapters) increases after the merger. For example, at low redshift,

gas-rich galaxy mergers can exert a minimal impact on the galaxies' SFR (Li et al., 2023) or fail to trigger starbursts due to short timescales (Di Matteo et al., 2008; Cortijo-Ferrero et al., 2017) or a clumpy, turbulent interstellar medium (Perret et al., 2014). On the former, short merger timescales can impede starbursts as the rapid interactions may not allow sufficient time for the gas to cool and collapse into new stars. On the latter, a clumpy, turbulent ISM can distribute gas inefficiently, preventing the dense concentrations required for starburst activity (Teyssier et al., 2010; Renaud et al., 2014). Another factor is the geometry of the merging galaxies; if the galaxies collide in such a way that the gas does not compress significantly, star formation rates will remain low (Bergvall et al., 2003; Di Matteo et al., 2007; Di Matteo et al., 2008; Sparre and Springel, 2016). Furthermore, feedback mechanisms from AGN can heat the gas, expelling it from the galaxy and quenching potential star formation (Emonts et al., 2006). Environmental factors, such as the presence of a hot ICM, can also strip gas from galaxies during mergers, reducing the fuel available for starbursts (Pearson et al., 2019).

1.2.3 Galaxy quenching

The processes involved in how galaxies stop forming stars are a complex matter and there have been a lot of efforts into understanding what quenches galaxies and how they move from the blue cloud to the red sequence. From feedback processes (reciprocal interaction between a galaxy and its surrounding environment, where energy is re-released by certain astrophysical phenomena such as supernovae and AGN into the environment) to mergers and environmental processes, there are a lot of effects that need to be taken into account to understand how galaxies depart from the star-forming main sequence, which characterises the SFR-M_* relation. Given the focus of this thesis, I will discuss the environmental quenching in Section 1.5 as part of the effects of the large-scale structure on the galaxies. As such, here I will focus on the feedback effects (from both active galactic nuclei and supernovae) and how they stop the formation of stars in galaxies.

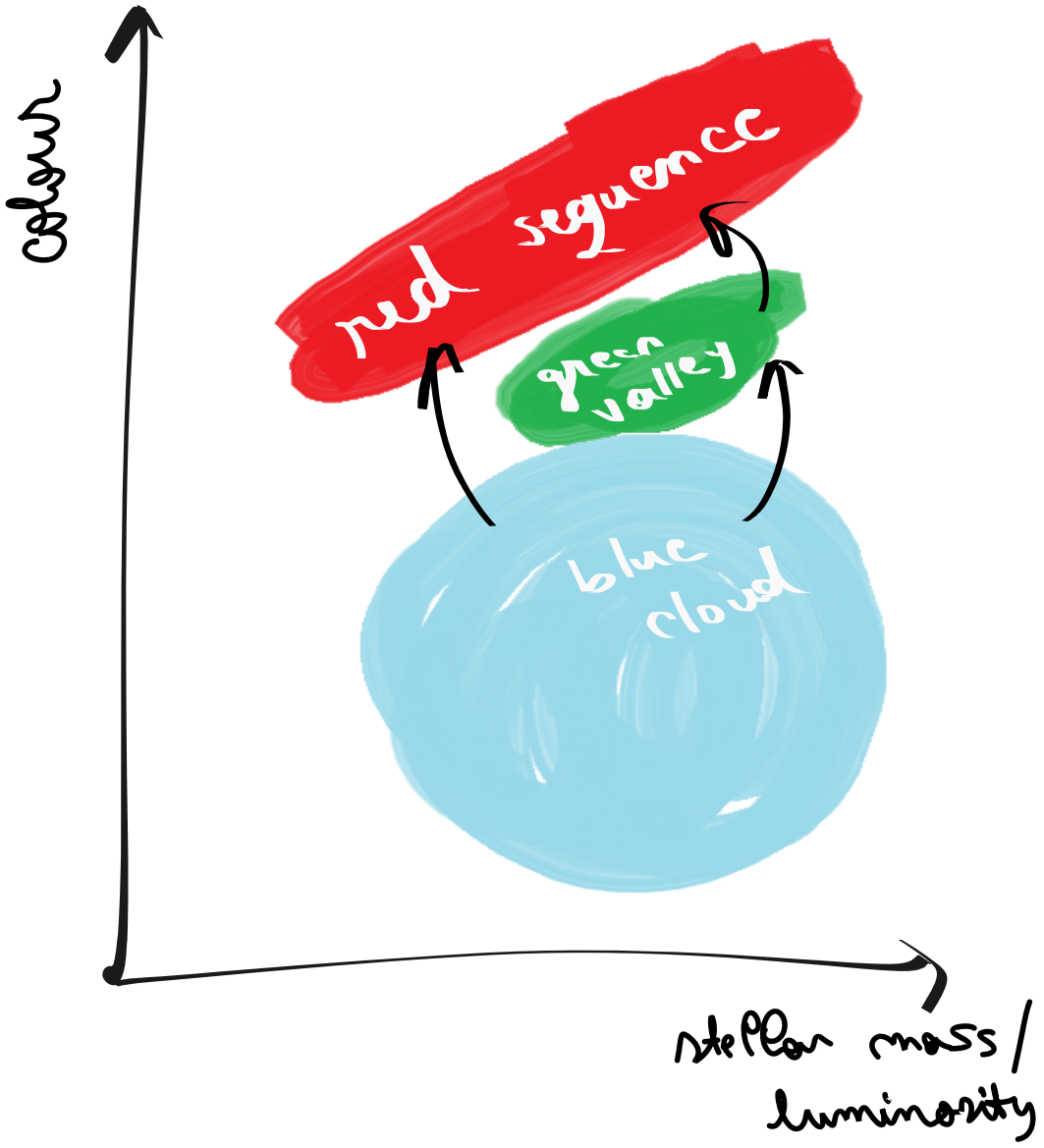

Figure 1.7: A cartoon diagram of the colour of a galaxy as a function of luminosity (stellar mass). Galaxies move from the blue cloud into the red sequence (sometimes via 'the green valley') as their star formation is suppressed.

Supernova feedback

Supernova (SN) feedback is a crucial mechanism in galaxy quenching that can hinder the formation of stars. A supernova is a powerful and catastrophic explosion that occurs at the end of a massive star's (with a mass greater than $8M_{\odot}$) life. During a supernova, the star releases an immense amount of energy and ejects its outer layers into the interstellar medium (Janka, 2012). This feedback process can have a significant impact on the surrounding gas and can suppress further star formation in several ways. First, the energy from supernovae can heat up and disperse the cold gas in the interstellar medium (ISM), preventing it from collapsing under its own gravity and forming new stars (Hopkins et al., 2014). Second, the ejected material from SNe carries heavy elements and metals, which can enrich the surrounding gas. This enrichment introduces feedback through radiative cooling by metals (as cooling time is decreased), driving gas outflows (Dekel and Silk, 1986). Third, SN explosions can generate powerful shock waves that compress the surrounding gas, triggering the formation of dense regions and molecular clouds (Saintonge and Catinella, 2022). These dense regions can potentially lead to star formation, but the energy and turbulence generated by the supernova explosions can disrupt the gravitational collapse of these clouds and prevent the formation of new stars (Silk and Mamon, 2012).

The galaxies affected by SN feedback tend to have lower stellar masses. This is due to the fact that SN feedback is most effective in low-mass galaxies, where the gravitational potential well is shallow and the expelled gas can easily escape from the galaxy (Dekel and Silk, 1986). In the case of higher mass galaxies, the gravitational potential well is deeper, making it more difficult for the expelled gas to escape. Instead, the expelled gas can recycle back into the galaxy and undergo further cooling and star formation (Kim and Ostriker, 2015).

AGN feedback

Another important mechanism in galaxy quenching is the active galactic nuclei (AGN) feedback, which encapsulates the impact of a supermassive black hole

(SMBH) on the surrounding gas and stars in a galaxy (e.g. Rees, 1984; Kormendy and Richstone, 1995; Magorrian et al., 1998; Fabian, 1999; Kormendy and Ho, 2013; Hardcastle and Croston, 2020). AGN are powered by the accretion of matter onto a SMBH at the centre of a galaxy. As material falls onto the black hole, it forms an accretion disk where gravitational potential energy is converted into thermal energy and emitted as light. This process can generate tremendous amounts of energy and radiation, which can have a profound effect on the surrounding gas and stars in the galaxy (see Heckman and Best, 2014; Blandford et al., 2019 for reviews on AGN types and AGN jet accretion).

AGN feedback can operate through multiple channels, including radiative and kinetic mechanisms (Begelman, 2004; Bower et al., 2006; Croton et al., 2006; Somerville et al., 2008). The radiative mechanisms involve the emission of intense radiation by the AGN, which can heat up and ionise the surrounding gas. This can prevent the gas from cooling and condensing to form stars (McNamara and Nulsen, 2007). In addition to radiative mechanisms, AGN feedback can also operate through kinetic mechanisms. These mechanisms involve the ejection of high-velocity jets and outflows from the AGN, which can blow away or shock the surrounding gas, disrupting its gravitational collapse and inhibiting star formation (King, 2005; Fabian, 2012). These include processes such as the release of high-energy particles, magnetic fields, and cosmic rays, which can influence the gas dynamics and regulate star formation in the galaxy (Di Matteo et al., 2005; Croton et al., 2006).

The combination of SN and AGN feedback plays a crucial role in regulating the star formation and gas content of galaxies, ultimately leading to galaxy quenching. This is notable in the effects on the luminosity function, which is a measure of the distribution of galaxies based on their intrinsic luminosities (Binggeli et al., 1988; Binney, 2004). The theoretical prediction of the luminosity function suggests a larger number of galaxies at different luminosities, as indicated by the red line in Figure 1.8. However, observations show a deficit of low-luminosity/mass systems and high-luminosity/mass systems compared to the theoretical prediction, as indicated by the blue line in Figure 1.8. This deficit in the observed luminosity function can

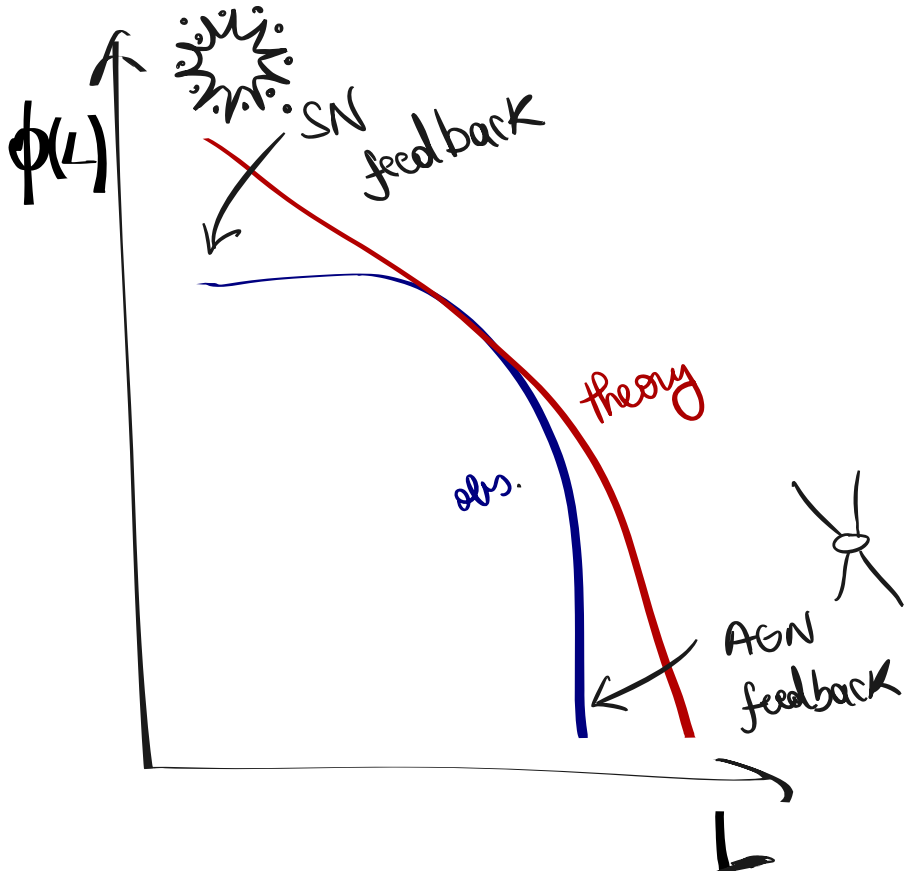

Figure 1.8: A cartoon graphic showing the difference between the luminosity function as predicted by simulations based on ΛCDM and assuming a direct mapping from halo mass to stellar mass (red) and the observed one (blue). The mismatch between the two can be corrected by adding supernova feedback and AGN feedback into the luminosity function predicted by simulations.

be attributed to the combined effects of supernova and AGN feedback (Benson et al., 2003; Silk and Mamon, 2012). SN feedback primarily affects the low-luminosity/mass systems, leading to a deficit of such galaxies due to the energy introduced by the feedback (Hopkins et al., 2012). On the other hand, AGN feedback primarily affects the high-luminosity/mass systems, leading to a deficit of these galaxies as well (Morganti, 2017). Therefore, the combined effect of SN and AGN feedback results in a distribution of galaxy luminosities, with a deficit of both low-luminosity and high-luminosity galaxies.

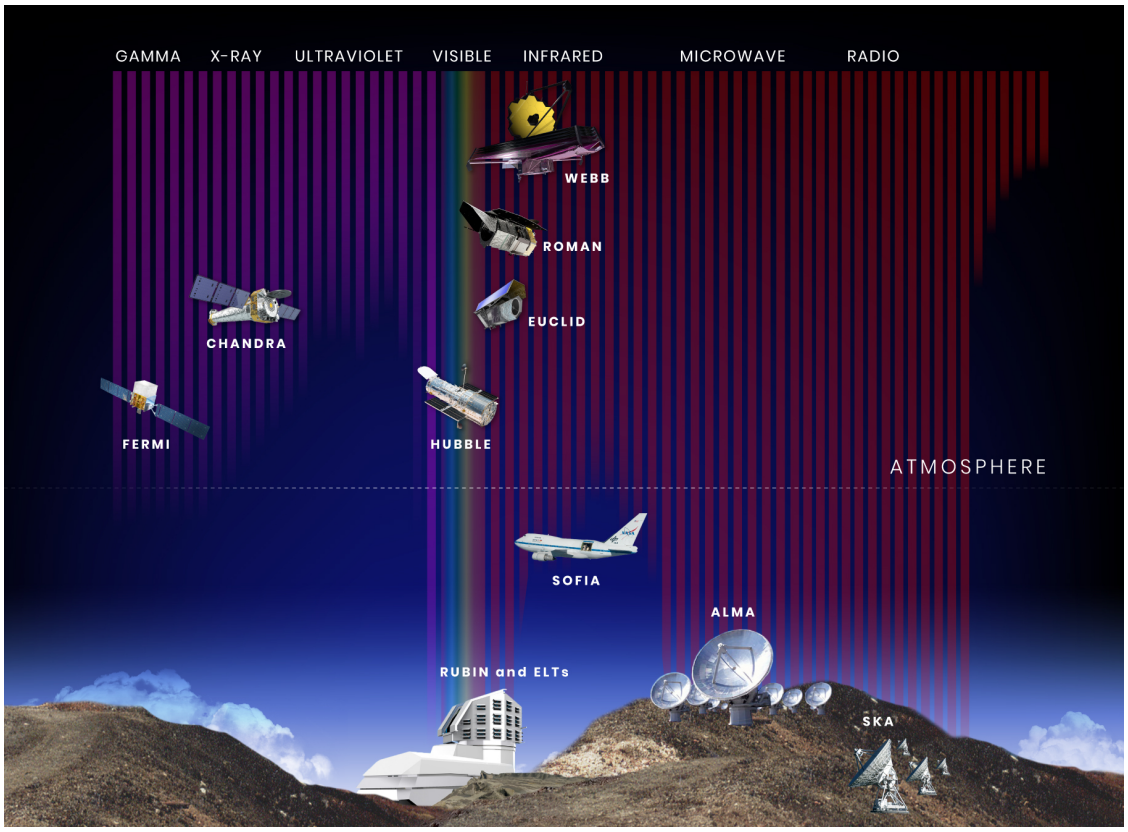

Figure 1.9: A cartoon representation from STSci on behalf of NASA, of the wavelength sensitivity of a number of current and future space- and ground-based observatories, along with their position relative to the ground and to Earth's atmosphere.

1.3 Tracing the evolution of a galaxy through its spectrum

The electromagnetic spectrum encompasses all forms of electromagnetic radiation. It allows us to probe a wide range of astrophysical phenomena, from gamma rays with extremely short wavelengths to radio waves with long wavelengths. Up until the 1950s, most observational astronomy was done at optical wavelengths, due to either the opacity of Earth's atmosphere to other wavelengths or lack of appropriate technology. These days, however, we have access to the full electromagnetic spectrum, both from ground-based observations, as well as observations from space, as can be seen in Figure 1.9.

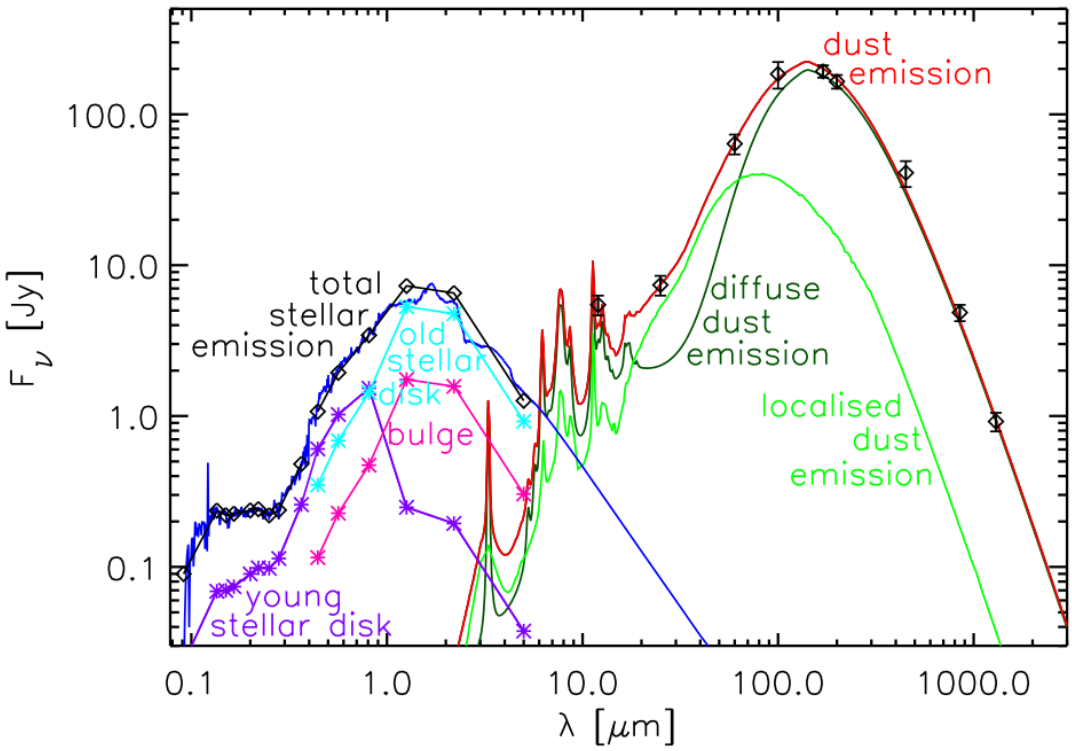

Figure 1.10: Example of a best fit model SED of NGC891, encompassing radiation from infrared to UV, reproduced from Popescu et al. (2011).

1.3.1 The Spectral Energy Distribution

By observing galaxies across different wavelengths of the electromagnetic spectrum, we can measure their spectral energy distribution (SED) and gain a more comprehensive understanding of their properties, dynamics, and evolutionary processes. The SED is comprised of the light from all the stars, gas, and dust within the galaxy, including any AGN. An example of a galaxy spectrum can be seen in Figure 1.10.

This multi-wavelength approach is essential for unravelling the complex processes and mechanisms driving galaxy evolution over cosmic time. Here, I present a very quick overview for each wavelength shown in Figure 1.9, along with some of the processes they can provide insights into.

Radio

There are two ways from which we gain insights into galaxy processes and properties from radio observations: via spectral line observations or via radio continuum

observations. In terms of spectral line observations, we can trace the cold gas content of galaxies, particularly neutral hydrogen (HI), as well as molecular gas (such as carbon monoxide - CO) which is crucial for star formation (Braine and Combes, 1992; Combes et al., 2007; Spilker et al., 2018). Radio telescopes can map the spatial distribution of HI gas in galaxies, revealing structures such as spiral arms, bars, and galactic outflows (Haynes et al., 1984). Similarly for CO, radio observations can provide valuable information about the gas dynamics and kinematics within galaxies. In terms of radio continuum, radio emission from synchrotron radiation can trace the presence of magnetic fields and cosmic rays in galaxies (Huege, 2016). Also from radio synchrotron emission, we can study the formation and evolution of SN remnants, which can then be used to trace star formation (see Condon, 1992 for a review). Radio data can also be used to explore the supermassive black holes at the centre of the galaxy. By looking at the bright jet emissions from these supermassive black holes (the AGN), we can map extended structures like jets and lobes, shedding light on their orientation, dynamics and kinematics. Monitoring AGN over time reveals significant variability, providing insights into accretion processes, jet launching mechanisms, and host galaxy interactions (see review by Heckman and Best, 2014).

Infrared

Infrared observations provide vital information for studying the dusty environments of galaxies, where stars form and evolve. Dust absorbs and re-emits light from the stars, making it challenging to observe certain regions in optical/UV (see Draine, 2003 for a review). However, infrared radiation can penetrate through dust clouds, allowing us to trace different regions of galaxies, depending on the wavelength. There are three types of infrared radiation that one must consider: near infrared radiation (NIR), mid infrared radiation (MIR) and far infrared radiation (FIR). NIR is often coupled with optical observations and can provide valuable information about the stellar populations and 3D structure of galaxies. NIR observations also trace the older stellar populations, including the bulges and haloes of galaxies,

which are dominated by older stars (Draine and Li, 2007; da Cunha et al., 2008). MIR, which is emitted by warm dust grains and organic molecules, can provide insights into the ISM and star-forming regions within galaxies (Soifer et al., 2000; Soifer et al., 2001). Furthermore, the dusty torus of AGN also emits in MIR - this has a characteristic power-law emission, which helps in selecting AGN from star-forming galaxies (Sajina et al., 2022). Meanwhile, FIR, which is emitted by cooler dust grains, can provide insights into the cold, molecular gas reservoirs from which stars form (Cortese et al., 2012; Smith et al., 2012a).

Visible

Visible light observations provide detailed information about the distribution of stars within galaxies. With it, we can also study the structures of spiral arms (Elmegreen and Elmegreen, 1987), the shapes of elliptical galaxies (Emsellem et al., 2004; Kormendy and Bender, 2012), and the presence of tidal interactions between galaxies (Veilleux et al., 2002; Tal et al., 2009). Furthermore, by analysing the colours and spectra of stars, we can determine their ages, metallicities, and evolutionary stages. Optical observations also allow us to study the emission lines present in the spectra of galaxies (see Kewley et al., 2019 for a review on emission lines and their role in unveilling galaxy evolution). Moreover, optical observations can also provide information about the velocity and structure of the ionised gas within a galaxy, allowing us to study gas outflows (Rodríguez-Baras et al., 2014), as well as the presence of star-forming regions or AGN (Baldwin et al., 1981; Kewley et al., 2006). Also in the context of AGN, visible light can reveal the presence of broad emission lines, indicating the presence of a SMBH accreting matter and emitting radiation (Barth et al., 1999; Constantin et al., 2015).

Ultraviolet

Ultraviolet radiation is useful for studying the youngest and hottest stars in galaxies. Massive, young stars emit copious amounts of ultraviolet radiation, which ionises surrounding gas and drives powerful stellar winds (Bruzual and Charlot, 2003). Therefore, UV observations can trace recent star formation activity, identify massive

star clusters, and probe the effects of feedback processes on the interstellar medium (Boselli et al., 2005). In the context of AGN, UV observations can also help in studying the accretion processes and jet launching mechanisms. This is done via the detection of UV emission from the accretion disk and the study of UV absorption lines in the spectra of AGN (Murray and Chiang, 1995; Laor and Brandt, 2002).

X-rays

X-ray observations are valuable for probing the high-energy processes associated with black holes and AGN, SN remnants, and intracluster gas within galaxy clusters (see Barcons et al., 2001 for a review, as well as Section 1.4.2 for a brief discussion about X-rays in clusters). In terms of AGN, they emit X-rays due to the accretion of matter onto the supermassive black holes. Therefore, by studying the spectral characteristics and variability of these emissions, we can gain insights into the interplay between accretion disks, coronae, and the surrounding environments, shedding light on the mechanisms governing AGN activity and jet formation (see Fabian, 2012 for a review on X-rays in AGN). Additionally, X-ray observations can detect the remnants of SN explosions and study the interactions between SN shocks and the interstellar medium, which shows complex dynamics of shock propagation and particle acceleration (Brinkmann, 1989; Vink, 2020). By examining the effects of the SNe explosions in a galaxy and its surrounding gas we can also gain insights into the feedback processes (as seen in Section 1.2.3) that regulate star formation and the redistribution of matter in galaxies.

Gamma-rays

Gamma-ray observations probe the most energetic processes in galaxies, including SN explosions, black hole accretion, and particle acceleration in AGN. Gamma-rays are produced by high-energy particles interacting with matter or magnetic fields, providing insights into the sources of cosmic rays and the mechanisms driving galaxy evolution (see Acero et al., 2009 for an example of a detection of gamma-rays from a starburst galaxy). Gamma-ray telescopes can detect gamma-ray bursts (GRBs),

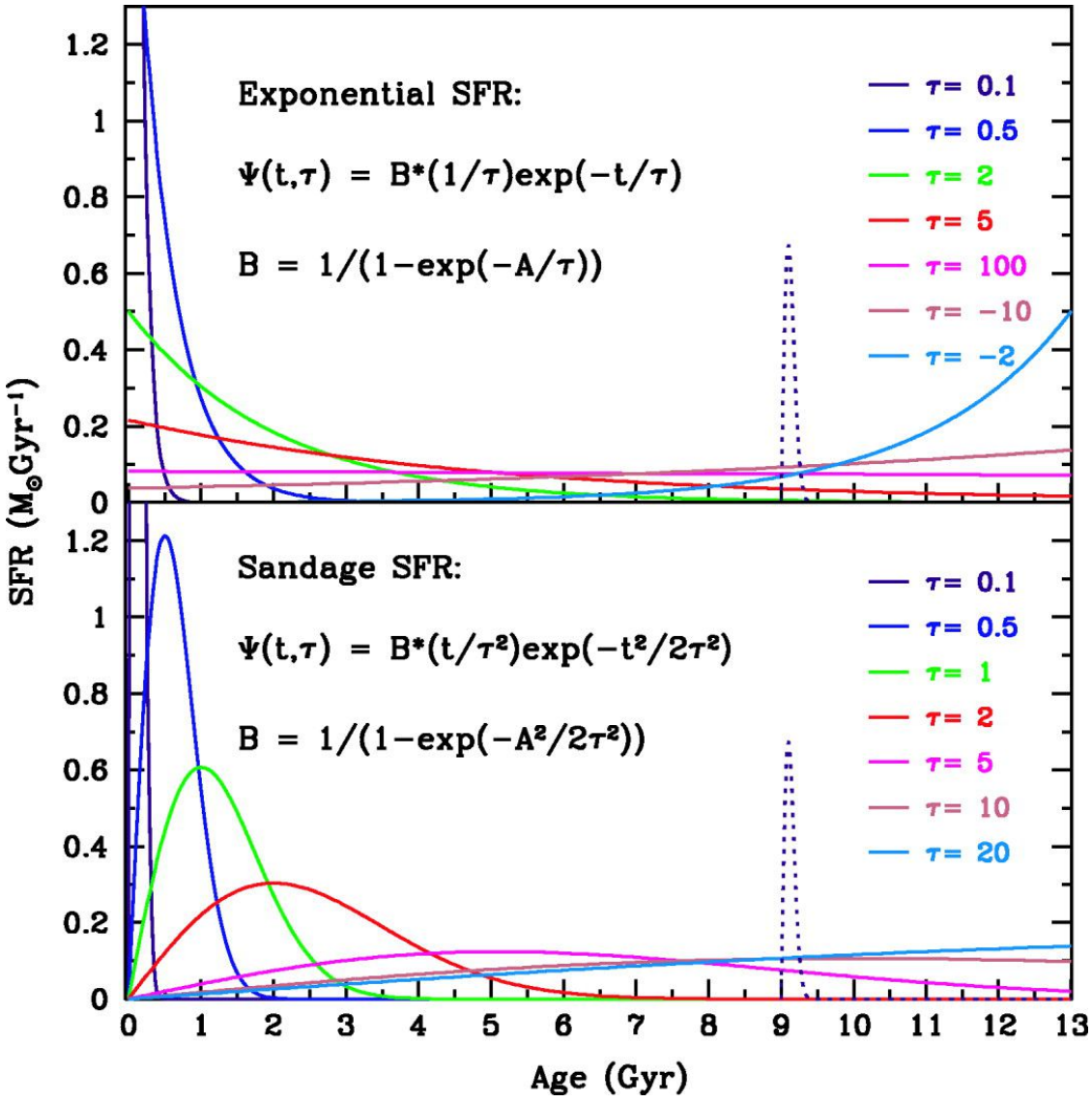

Figure 1.11: Time evolution of two SFH models for different time scales τ: exponential (upper panel) and a custom SFH model described by delayed rise in the SFR, followed by an exponential decline (Sandage, 1986, lower panel). The dotted line shows a possible star burst. Reproduced from MacArthur et al. (2004).

the most energetic explosions in the universe, which can prove to be a tracer of extreme star formation systems (see Berger, 2014 for a review).

1.3.2 Star formation histories from spectra

The star formation history (SFH) encodes the temporal narrative of a galaxy's star formation activity. Inferring SFHs involves deciphering the distribution of stellar ages, shedding light on the intensity and duration of past star-forming epochs. As

such, the SFHs of quenched galaxies can give us insights into the mechanisms which caused the stopping of star-formation and the galaxy's conditions (e.g. Schreiber et al., 2018). Similarly, the SFHs of star-forming galaxies can give us information about the assembly of the stellar mass in the galaxy (e.g. Leitner, 2012). Various observational methods contribute to this endeavour, including the analysis of resolved stellar populations in nearby galaxies (Cignoni et al., 2009; Tosi, 2009; Pessa et al., 2023) and the examination of SEDs in more distant, unresolved systems (Sorba and Sawicki, 2018). The study of stellar populations through colour-magnitude diagrams, spectroscopy, and sophisticated modelling techniques can contribute to disentangling the complex interplay of factors influencing star formation, such as gas availability, environmental conditions, and feedback processes (Ocvirk et al., 2006; Dye, 2008; Leja et al., 2017; Leja et al., 2019; Tacchella et al., 2022).

Using the SFH, together with stellar spectra, the initial mass function (IMF) and dust extinction, a stellar population synthesis (SPS) model can be built. However, the inverse (using the SPS to infer SFHs) can be a highly degenerate problem (Conselice, 2003). One major issue is the degeneracy between age, extinction, and metallicity, which all affect the integrated colours of a galaxy. This degeneracy means that the derived values of these parameters tend to be highly covariant, as different combinations of these properties can produce similar colours and magnitudes in a galaxy's spectrum. This makes it difficult to uniquely determine the SFH of a galaxy based solely on observed properties. Whilst there is a reasonable understanding of stellar evolution (see Gallart et al., 2005 for a review), the choice of the IMF and understanding the effect of dust on the observed spectrum also pose significant challenges in recovering the SFH of a galaxy using SPS models. When it comes to the IMF, there is still ongoing debate and uncertainty about its precise form and universality. Several forms have been proposed, including the Salpeter IMF (Salpeter, 1955), the Chabrier IMF (Chabrier, 2003), and the Kroupa IMF (Kroupa, 2001), each with different assumptions about the distribution of stellar masses and the ratio of high-mass to low-mass stars. These different IMFs can have significant implications for the interpretation of mass-to-light ratios and the overall

stellar content of galaxies (see the Bastian et al., 2010 review for a more in-depth discussion). The effect of the dust can be another complicating factor in SPS models. As mentioned in Section 1.3.1, dust attenuates the light from stars before it emerges from the galaxy, leading to dimming and reddening of the observed spectrum. This dust extinction can introduce uncertainties in the derived parameters, such as age and metallicity, as the observed colours may be affected by both dust attenuation and intrinsic properties of the galaxy (see the Draine, 2003 review). This results in uncertainties in estimating galaxy masses and underestimating the age of the galaxy or the potential contribution of older stars to the mass. Another issue is the usage of smoothly-varying SFRs in simulations in order to build models, while real galaxies may have complex and non-monotonic SFHs, including fluctuations and bursts (Leja et al., 2019; Iyer et al., 2019). This problem can be slightly mediated by modelling SFHs with more complex forms (i.e. see bottom panel of Figure 1.11 for an example) or by using non-parametric SFHs. These challenges highlight the need for careful interpretation and analysis when using SPS models to infer the SFHs of galaxies.

1.4 The Cosmic Web

The Universe is described by a network-like distribution of galaxies, gas and dark matter on megaparsec scales. This distribution is known as the cosmic web (Bond et al., 1996) and it is formed of clusters, walls, voids and filaments. Zel'dovich's model of the evolution of the non-linear growth of primordial density perturbations (Zel'dovich, 1970) predicts the formation of such a structure. In the context of Zel'dovich's model, the evolution of primordial density perturbations leads to the formation of overdense regions, where gravitational collapse initiates the condensation of matter into filaments and haloes, and underdense regions, where matter flows away, creating voids. As these regions evolve, overdensities grow via gravitational instability, causing matter to flow along the filamentary structures, while underdense regions expand, delineating the voids. The resulting cosmic web emerges as a consequence of the non-linear evolution of these density perturbations,

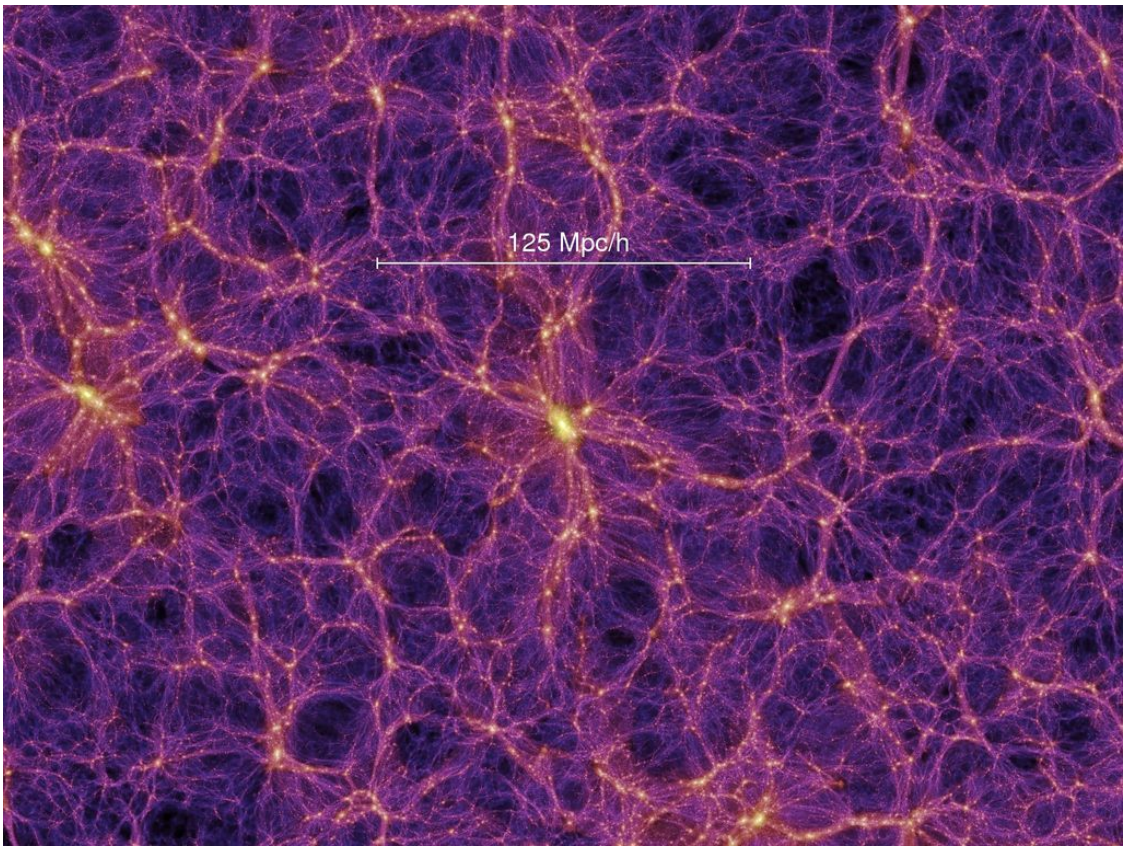

Figure 1.12: An example of the cosmic web as seen from the dark matter distribution computed in the Millennium Simulation (Springel et al., 2005).

where filaments intersect within nodes, which host clusters of galaxies, while voids occupy the regions in between.

The detection of the cosmic web and its components is achieved through various observational and theoretical methods. One of the key observational methods for detecting the cosmic web is through galaxy redshift surveys. Davis et al. (1982) and de Lapparent et al. (1986) present the earliest evidence of tracing the cosmic web, finding a web-like distribution of galaxies. More recent galaxy surveys such as the Sloan Digital Sky Survey (SDSS; York et al., 2000), 2dF Galaxy Redshift Survey (2dFGRS; Colless et al., 2001) and 2MASS Redshift Survey (2MRS; Huchra et al., 2012) have traced it over larger scales to greater fidelity. The first N-body simulations (Centrella and Melott, 1983; Klypin and Shandarin, 1983) and more modern hydrodynamical simulations (Springel et al., 2005; Schaye et al., 2015) as well as Bayesian reconstructions of the dark matter distribution in the Local

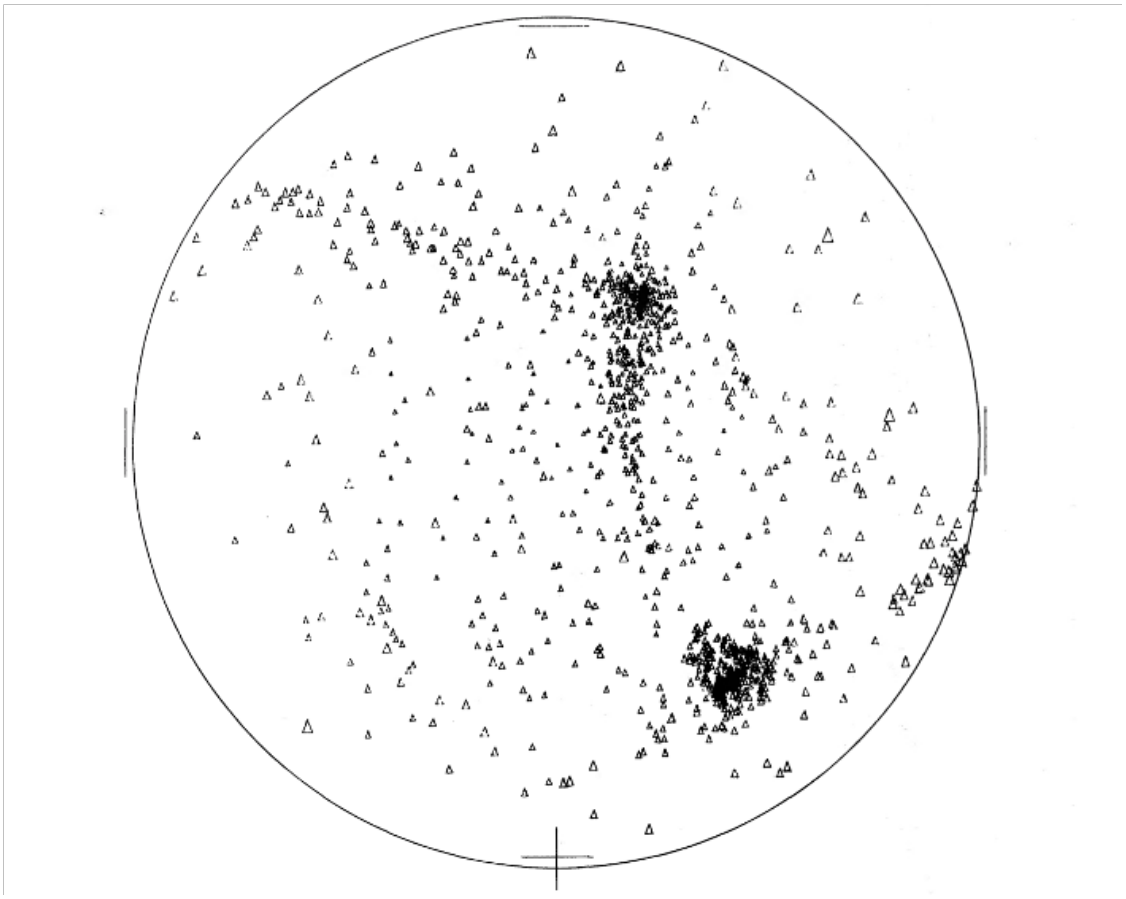

Figure 1.13: A distribution of simulated dark matter haloes as presented in Klypin and Shandarin (1983). This was one of the first times the Zel'dovich approximation was used in N-body simulations to compute the cosmic web.

Universe (Heß et al., 2013; Sorce et al., 2016) showed that the formation of the voids, walls and filaments is even more apparent in the dark matter. Several computational techniques have been developed for the detection of large-scale structures, which I will discuss more in-depth in Chapter 2.

1.4.1 The filaments of the cosmic web

One component of the cosmic web is the cosmic filament. Cosmic filaments are long, thread-like structures composed of galaxies, dark matter, and gas that span vast distances in the Universe (of order $\sim$ Mpc), connecting clusters and superclusters of galaxies. These filaments are believed to form from the gravitational collapse of overdense regions and serve as highways for matter and energy to flow through (e.g. Dolag et al., 2006; Cautun et al., 2014). The average filament is thought to

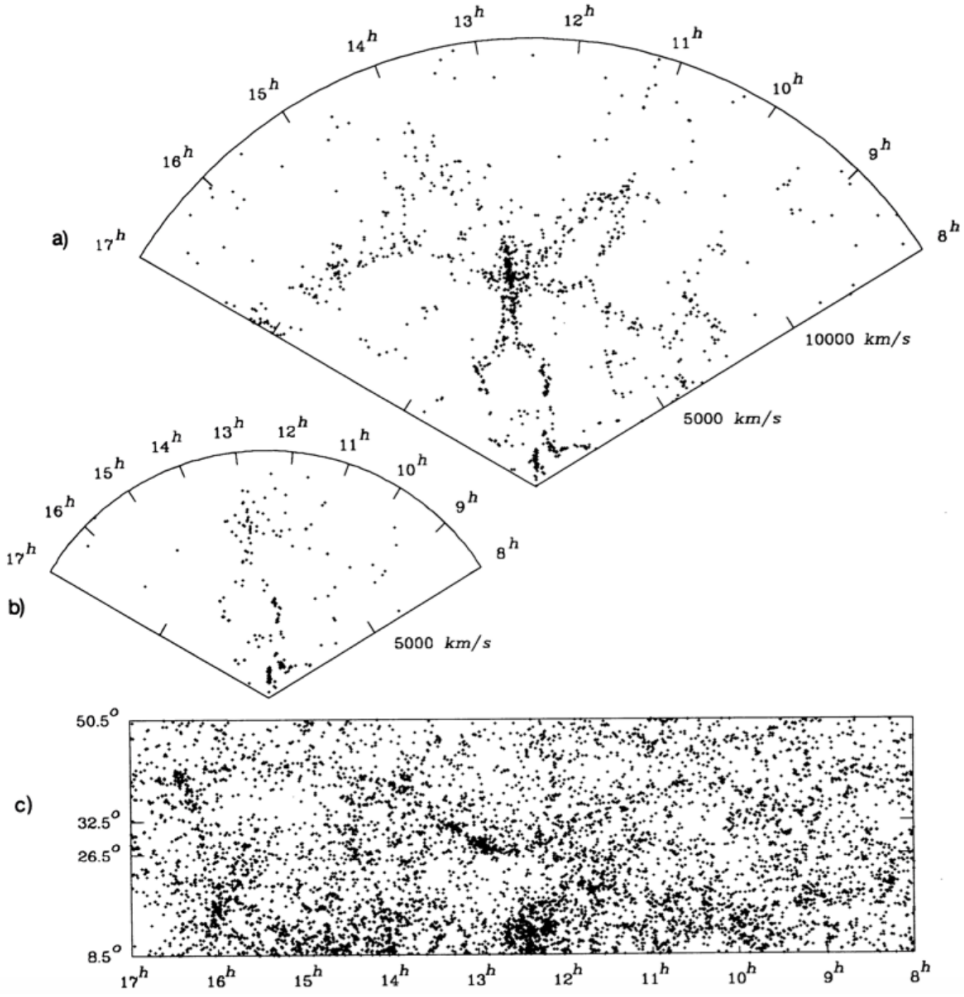

Figure 1.14: Map of the Coma cluster as presented in de Lapparent et al. (1986). This was the first time the cosmic web was observed.

span tens of megaparsecs in length, with a typical width of a few Mpc (Bond et al., 2010; Galárraga-Espinosa et al., 2024; Wang et al., 2024). Depending on its length, a cosmic filament can contain anywhere from a few hundred to several thousand galaxies. This will affect its properties, such as its density and the amount of dark matter it contains (Bonjean et al., 2018; Gheller and Vazza, 2019; Malavasi et al., 2020). In terms of its gas content, within filaments, gas can be found in several phases. These phases include the hot, ionised gas that fills the intracluster medium in galaxy clusters, as well as cooler, denser gas. Short filaments are characterised by being puffier and denser, with a significant presence of hot gas. In contrast, long filaments are described as having more contributions from the cooler and diffuse

intergalactic medium gas, which corresponds to primordial gas that has not been heated by baryonic processes (Galárraga-Espinosa et al., 2020; Galárraga-Espinosa et al., 2021). While short and long filaments share a common region of warm-hot intergalactic medium phase, overall their gas compositions are distinct. The presence of dense gas in filaments, particularly in short filaments, could play a role in star formation for galaxies located at the cores of these filaments, potentially providing a reservoir of star-forming material for the galaxies to accrete from (Klar and Mücket, 2012; Gheller and Vazza, 2019; Galárraga-Espinosa et al., 2021).

Various methods have been proposed to detect and study the cosmic filaments, both directly and indirectly, across different redshift ranges. For high redshifts, these include using observations of fluorescent Lyman-α emission from the filaments (Cantalupo et al., 2014). For low redshifts, methods have been propsosed via detecting the extended disks of galaxies that are formed through filamentary accretion of gas (Danovich et al., 2012), and utilising intensity mapping to trace HI in the intergalactic medium (Tramonte et al., 2019).

One method of indirectly detecting the cosmic web at high redshift is through observations in the Lyman-α emission (Hogan and Weymann, 1987; Gould and Weinberg, 1996). The Lyman-α forest is a spectral feature caused by the absorption of radiation by intervening gas atoms along the line of sight from a bright background source. As the radiation travels, it gets redshifted due to the expansion of the Universe and is absorbed out of the line of sight by intervening hydrogen gas at the Lyman-α wavelength, creating what is known as the Lyman-α forest. The Lyman-α emission line allows for the identification of Lyman-α emitters (LAEs) and Lyman-α blobs (LABs). LAEs are galaxies that exhibit strong Lyman-α emission lines in their spectra, indicating the presence of ionised hydrogen gas (Rhoads and Malhotra, 2001; Yamada et al., 2012). LABs, on the other hand, are large and extended regions of intense Lyman-α emission that can span several hundred kpc across (Cen and Zheng, 2013). In the context of cosmic filaments, both LAEs and LABs could potentially trace the presence of ionised gas in said filaments. There have been several detection of LABs (Martin et al., 2016; Umehata et al., 2019;

Kikuta et al., 2019; Elias et al., 2020) which found that their sizes spread way beyond the virial radius of haloes and were aligned such that they could be tracing the cosmic filaments feeding into a quasar host galaxy.

For low redshifts, a method of indirectly detecting the cosmic web is through the observation of extended disks. Extended disks are detected through the grazing incidence of quasar sightlines around galaxies, allowing for the detection of co-rotating extended disks. These extended disks can extend out to distances of up to 100 kpc, providing a larger volume for the interception of quasar sightlines compared to the filaments alone. This grazing incidence technique, as proposed by Stewart et al. (2011) and Ho and Martin (2020), provides strong evidence for recent filamentary accretion and the presence of the cosmic web.

Also at low redshift, any attempts trying to trace cosmic filaments via neutral hydrogen (HI) have proved impossible, since the current telescopes cannot reach the sensitivity required for such a detection in HI emission directly (Kooistra et al., 2017), or via the 21-cm intensity mapping technique of Tramonte et al. (2019).

1.4.2 Other components of the cosmic web

Another component of the cosmic web is voids, which These are large, empty regions with very low galaxy density, spanning tens of megaparsecs. Voids are characterised by a lack of galaxies and are surrounded by interconnected walls (Colberg et al., 2005; Aragón-Calvo and Szalay, 2013). These voids play a crucial role in the overall structure of the cosmic web, as they create pathways for matter to flow along the filaments and bring about the formation of galaxies and galaxy clusters. To detect voids in the cosmic web, astronomers often use galaxy surveys to identify regions with a low galaxy density and large separations between galaxies (Kauffmann and Fairall, 1991; Hoyle and Vogeley, 2004; Hoyle et al., 2005).

Walls, also known as sheets, are also a part of the cosmic web. They are large, flat structures that two-dimensional structures that lie between filaments, containing galaxies. They are believed to form filaments at their intersections and can also extend for tens of megaparsecs in length and also have a thickness of

several megaparsecs (Babul and Starkman, 1992; Lee, 2004). To detect walls in the cosmic web, one has to rely on techniques which involve identifying regions of high galaxy density and large-scale clustering patterns that indicate the presence of walls in the cosmic web. Moreover, the detection of cosmic sheets, especially in galaxy surveys, is challenging due to the lower brightness galaxies that form them, which are sparsely distributed, their planar nature and reduced contrast with respect to the background density (Tempel and Libeskind, 2013).

Galaxy clusters are another important component of the cosmic web. Galaxy clusters are dense regions containing hundreds to thousands of galaxies, bound together by gravity, within the cosmic web, located at the intersection of filaments (hence also known as nodes), (see Kravtsov and Borgani, 2012 for a review). The gravitational pull of galaxy clusters can influence the motion, shape, and structure of individual galaxies within them (Alberts and Noble, 2022). Additionally, the presence of a dense cluster environment can trigger various physical processes that affect galaxy properties, such as star formation rates (see Section 1.5.2), morphologies (Dressler, 1980; Moore et al., 1998b), and gas content (Pratt et al., 2010). To detect clusters, several observational techniques can be employed, across different wavelengths. One of the methods is via X-ray emission from hot, ionised gas within the cluster, which can be detected and used to identify the presence of a galaxy cluster (Rosati et al., 2002; Cavagnolo et al., 2008; Ilić et al., 2015). Furthermore, the Sunyaev-Zeldovich (SZ) effect (Sunyaev and Zeldovich, 1972) is another method used to detect galaxy clusters. The SZ effect occurs when the CMB radiation passing through a galaxy cluster is scattered by the hot gas within the cluster. Hence, along the line of sight of a cluster, the CMB will appear fainter at lower frequencies and brighter at higher frequencies (Birkinshaw, 1999). Furthermore, observing clusters in visible light can be done to detect the light emitted by galaxies within the clusters (intracluster light; Montes, 2019). Cluster detection can be done via radio measurements. This can be done via the radio emission from the relativistic electrons in galaxy clusters, which are accelerated by magnetic fields within the cluster. (Giovannini et al., 1999; Bacchi et al., 2003;

Ferrari et al., 2008). Finally, another common method for detecting galaxy clusters is through the observation of their gravitational lensing effects, which cause the distortion of light from background objects as it passes through the gravitational field of the cluster. This distortion can be measured and used to identify the presence of a galaxy cluster (Hoekstra, 2003; Hoekstra, 2007).

1.5 The environment of a galaxy

By understanding the nature of the cosmic web, we can probe deeper into its effect on galaxy formation and evolution. Whilst the effect of the local environment on galaxies (i.e. clusters) has been well-researched (e.g. Dressler, 1980; Davis and Geller, 1976; Balogh et al., 2004; Peng et al., 2012; Robotham et al., 2013; Treyer et al., 2018; Davies et al., 2019), the effects of the filamentary large-scale structure are not as well understood, as it represents a different density environment and it is harder to quantify (see Figure 1.15 for a schematic of what we mean by different environments in terms of position). Morphology, stellar mass, colour, star formation rate (SFR) and specific star formation rate (sSFR) could all be sensitive to the larger-scale environment, especially with respect to the filaments.

1.5.1 Effects on the stellar mass of a galaxy

In terms of galaxy properties, there have been several studies looking at the stellar masses and colours (which are correlated with their star formation) of galaxies in relation to several components of the cosmic web. The most widely accepted result is that the massive, red, quiescent galaxies are closer to the spine of the filaments. This was shown in several studies, such as Alpaslan et al. (2015) and Kraljic et al. (2017) using the Galaxy and Mass Assembly survey (GAMA; Driver et al., 2009), Laigle et al. (2017) using the COSMOS2015 catalogue (Laigle et al., 2016), Chen et al. (2017) using the SDSS survey, Malavasi et al. (2017) using the VIMOS Public Extragalactic Redshift Survey (VIPERS; Moutard et al., 2016), Luber et al. (2019) using the COSMOS HI Large Extragalactic Survey (CHILES; Fernández et al., 2016) or Bonjean et al. (2020) using the WISExSCOS catalogue (Bilicki et al., 2016).

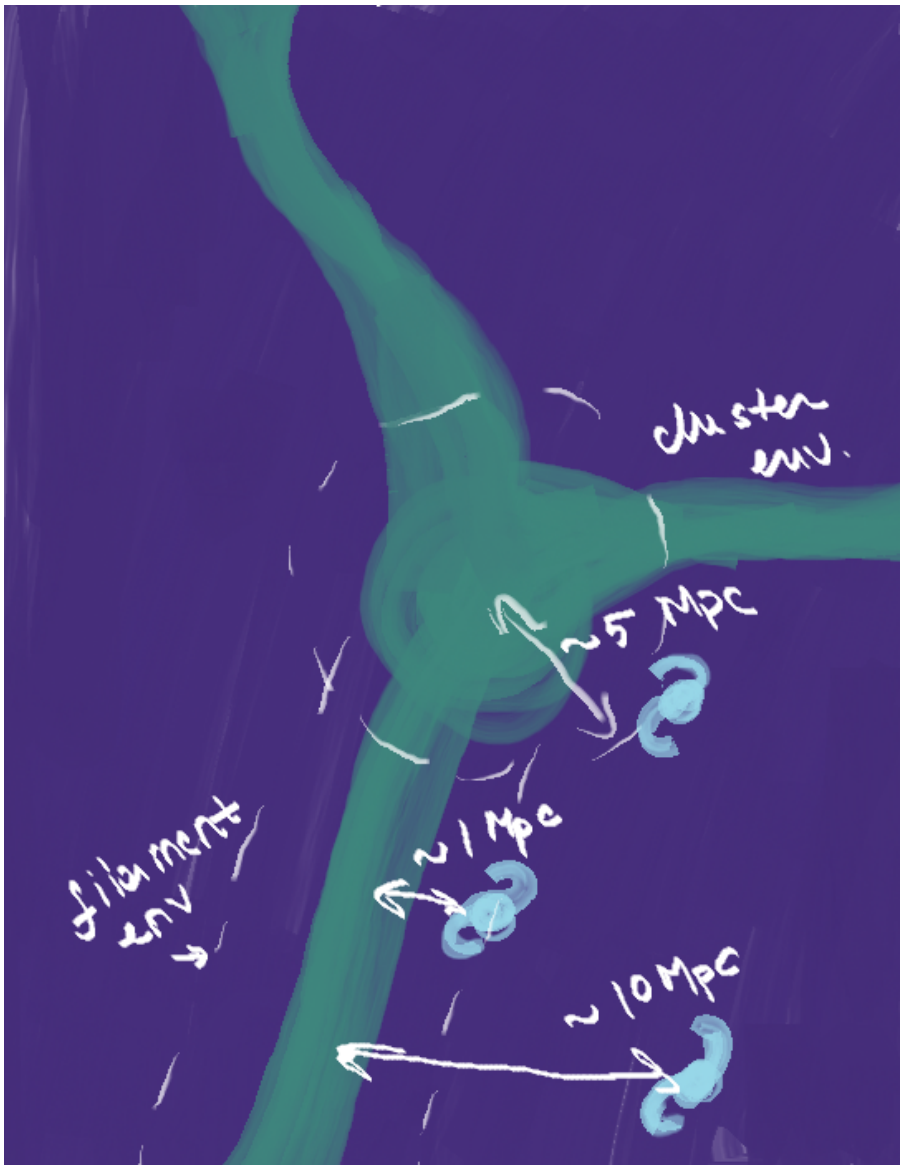

Figure 1.15: A cartoon graphic of several filaments meeting in a node, all representing different environments in which galaxies can exist.

These studies have been conducted across different redshift ranges, from the local universe, up to redshift $z \sim 0.7$. Whilst observed in a multitude of studies, the physical mechanisms behind this result are yet to be fully understood. One possible explanation could be related to the age of structures. Most clusters/filaments we observe at $z < 0.7$ probably formed earlier and had more time to acquire matter. Therefore, they are more likely to host the most massive galaxies.

1.5.2 Effects on the star formation rate of a galaxy

As we discussed in Section 1.2, there is a link between the star formation of galaxies and their environment. Specifically, we discussed how star formation can be stopped by internal processes (SNe and AGN feedback). In terms of high density environments (cluster), the quenching of star-formation occurs via several mechanisms, such as gas stripping via ram-pressure stripping (Gunn and Gott, 1972; Poggianti et al., 2017), harassment (Moore et al., 1996) or starvation/strangulation (Larson et al., 1980; McCarthy et al., 2008; Feldmann and Mayer, 2015). However, the link between star formation in galaxies and the filaments of the cosmic web is not clear neither when it comes to observations, nor in simulations.

In terms of observations, Darvish et al. (2014) found evidence for an increase in the number of star forming galaxies along the filaments close to clusters at redshifts around $z \approx 0.8 - 0.9$, which could be caused by either mild galaxy-galaxy interactions or by intrinsic effects and/or due to a boost in the SFR of star-forming galaxies in filaments; independent of selection biases such as the Hα flux limits or the dependence on the environment of the SFR-Mass relation. Similarly, Vulcani et al. (2019) show using the GAs Stripping Phenomena in galaxies with MUSE (GASP; Poggianti et al., 2017) programme that four of their galaxies which are within filaments show an enhancement in star formation in the low-z universe ($z < 0.07$).

However, the situation may be further complicated by the proximity of a galaxy to the nodes of the filaments. Martínez et al. (2016) showed using the SDSS survey, that the fraction of galaxies with a lower sSFR increases towards the nodes of the filaments and it decreases outwards for redshifts between $0.05 < z < 0.15$. This could be explained by the effect of massive clusters speeding up the quenching of such galaxies, through a range of physical mechanisms mentioned above such as mergers, (Kormendy and Ho, 2013), strangulation (e.g. Kereš et al., 2005; Dekel and Birnboim, 2006; Peng et al., 2015) and ram-pressure stripping (e.g. Gunn and Gott, 1972; Ebeling et al., 2014; Boselli et al., 2022). Also using the SDSS, Kuutma et al. (2017) showed that there is a decrease in SFR towards the filament spine up to redshift $z = 0.2$, which suggest an increase in the merger rate due to the

increase of number density of satellite galaxies within filament spines or a cut-off in the external gas supply. At fixed mass, Kraljic et al. (2017) showed using the GAMA survey (Driver et al., 2009), that in the redshift range $0.03 < z < 0.25$, the star forming galaxies have lower sSFR the closer they are to a filament. This could also be explained by a possible cut-off of the external gas supply from the filaments. Cooke et al. (2023) found that there are no correlations between the larger-scale environment of a galaxy on the star forming main sequence (SFMS) and its star formation and there are other parameters driving it, such as the bulge growth.

In terms of simulations, Kotecha et al. (2022) found that, using The Three Hundred project (Cui et al., 2018) at $z = 0$, filaments closer to clusters tend to delay the quenching of the galaxies that reside within them. However, Xu et al. (2020) find in the EAGLE simulation (Schaye et al., 2015) that at $z = 0$ there is a stellar mass threshold (of $M_\star \approx 10^{10.5} M_\odot$) for which the sSFR at galaxies with a lower stellar mass than the threshold is lower in nodes than in filaments. Furthermore, they also find that at higher redshifts, this dependency on the environment disappears. This effect at the lower mass end is attributed to the different fraction of active SF galaxies ($\log(\mathrm{sSFR}[\mathrm{yr}^{-1}]) > 11.0$)) in different environments - there are more active SF galaxies in voids than in knots/filaments. At the higher mass end, there is no significant difference in the active SF fraction in different environments, which causes this change in behaviour. Malavasi et al. (2022) find in the IllustrisTNG simulation (Pillepich et al., 2018) that for low redshift ($z = 0$), the SFR in galaxies decreases as they approach filaments and nodes. They also notice that the result is slightly dependent on mass, as there is evidence for galaxies at lower masses to have lower sSFR. These studies imply that SFR related quantities are affected by the effects of the cosmic web. On the other hand, Hasan et al. (2023a) find using the IllustrisTNG simulation (Pillepich et al., 2018), that at $z = 0$, for high mass galaxies ($M_\star > 10^{10.5} M_\odot$), the star formation is not affected by position with respect to filaments, whilst low mass galaxies are more likely to have their star formation affected by the environment.

There are two opposite proposed models that may explain some of these processes: the Cosmic Web Detachment (CWD) or the Cosmic Web Enhancement. On one hand, Aragón-Calvo et al. (2019) argue that in the CWD model, galaxies detach from their primordial filaments and their source of cold gas is then severed - a process that will cause quenching. This implies that looking for galaxies in present-time voids or walls could be a way to find galaxies which are still connected to their primordial filaments and are still star-forming. Its effects should be noticeable on the star formation history of a galaxy, such that any starburst events followed by a decline in SFR imply the detachment. On the other hand, Vulcani et al. (2019) argue for the Cosmic Web Enhancement effect, where the cool gas in the filaments enhances the star formation. These filaments aid in the cooling of gas which in turn, causes the increase in star formation in the dense regions of the circumgalactic medium.

Kuutma et al. (2017) also showed that for a fixed environmental density level, there was a higher elliptical-to-spiral ratio towards the filament spines. As elliptical galaxies are more likely to have a lower star formation than spiral galaxies, this could also be related to the cut-off of the gas supply as explained by the CWD model.

1.5.3 Effects on angular momentum and galaxy spins

A key property of galaxies is their angular momentum, which could improve our understanding of their morphology and its dependence on the environment. As strong evidence of the alignment of the angular momentum vector of the galaxies and their associated filament is yet to be found, I explore this topic in Chapters 3 and 6 of this thesis. The theoretical considerations of the tidal torque theory (TTT; Peebles, 1969; White, 1984), relate the spin angular momentum of a proto-galaxy to its tidal interactions with the surrounding matter. These tidal forces arise due to the uneven distribution of matter and the gravitational pull exerted by nearby galaxies, galaxy clusters, and the cosmic web itself. The gravitational tidal forces act on a protogalactic cloud or proto-galaxy and induce rotation within the cloud. This rotation arises from the differential gravitational forces experienced by different parts of the cloud, causing it to develop a net angular momentum.

As the protogalactic cloud collapses under its self-gravity to form a galaxy, the angular momentum acquired through tidal torquing becomes imprinted in the galactic system (Catelan and Theuns, 1996a; Catelan and Theuns, 1996b). This angular momentum determines the rotational motion of the forming galaxy and influences its subsequent evolution, including the formation of galactic disks and the distribution of stars within the galaxy (Barnes and Efstathiou, 1987). As galaxies accrete matter along the filaments of the cosmic web, and the gravitational interactions with neighbouring structures lead to the transfer and redistribution of angular momentum (Porciani et al., 2002).

Since the first study on this topic in a hydrodynamical simulation by Hahn et al. (2010), who reported that massive disk galaxies were aligned with the filaments, several other hydrodynamical simulation studies carried out do not agree with this result. The most significant prediction in the current literature is that low-mass galaxies tend to be rotationally aligned with their closest filaments, whilst high-mass galaxies have a tendency towards mis-alignment. Simulations such as those by Aragón-Calvo et al. (2007), Dubois et al. (2014), and Codis et al. (2015) and Kraljic et al. (2020) confirm this result, whilst Ganeshaiah Veena et al. (2018) also predict alignment between the angular momentum vector of the dark matter haloes and the filaments of the cosmic web. Whilst the simulations mentioned above find hints of a spin transition from alignment to mis-alignment - for example, Kraljic et al. (2020) find a spin transition for a stellar mass of $\sim 10^{10} M_{\odot}$, other simulations such as Ganeshaiah Veena et al. (2018) find no such transition and report a preference for overall mis-alignment at all masses.

Observational evidence for a spin-alignment at a certain stellar mass is lacking. Krolewski et al. (2019) reports no spin alignment using the Mapping Nearby Galaxies at Apache Point Observatory (MaNGA; Bundy et al., 2015) integral-field survey, whilst Welker et al. (2020) find a spin transition within a stellar-mass interval of $10^{10.4} M_{\odot} - 10^{10.9} M_{\odot}$ using the Sydney-AAO (Australian Astronomical Observatory) Multi-object survey (SAMI; Croom et al., 2012).

In the context of HI, studies such as Kleiner et al. (2017) and Crone Odekon et al. (2018) have investigated the link between HI in galaxies and the large-scale structures, with different results regarding the correlation between position of the galaxy and its HI content, and how it is fuelled by the filaments. The former found that massive galaxies ($\log M_\star > 11 M_\odot$) have increased HI-to-stellar-mass ratios closer to filaments, implying that said galaxies replenish some of their gas from the intra-filamentary medium. However, the latter argues that low-mass galaxies ($\log M_\star < 10.5 M_\odot$) show an HI deficiency closer to filament spines due to a cut-off from their gas supply by said filaments. There are other properties of HI selected galaxies that can be investigated as a function of distance to large-scale structures, such as the angular momentum of a galaxy. The overall picture of the relationship between the spin vector of a galaxy and its alignment with the filaments of the cosmic web in which it may reside is complicated. There have been a few studies using HI galaxies which tried to propose a more cohesive picture of this spin-filament alignment. Kraljic et al. (2020) find a possible spin transition threshold in HI mass at $M_{\rm HI} = 10^{9.5} M_\odot$ using the SIMBA (Davé et al., 2019) simulation. Blue Bird et al. (2020), using the COSMOS HI Large Extragalactic Survey (CHILES; Fernández et al., 2016), find that the spins of their galaxies in their HI-selected sample tend to be aligned with the cosmic web. However, their study does not find any significant mass transition between the aligned and the mis-aligned spin. In addition to a mass dependence, the type of the galaxy has also been shown to relate to the filaments. Kraljic et al. (2021) using the MaNGA integral-field survey find that the spins of late-type galaxies (LTGs) are preferentially aligned to their closest filament, whilst S0 type galaxies have a preferential perpendicular alignment to their closest filament. The result regarding the elliptical/S0 galaxies has been previously identified in studies such as Tempel et al. (2013) using SDSS and Pahwa et al. (2016) using the 2MASS Redshift Survey. Scd types have also been shown to have a preferential parallel alignment, whilst Sab galaxies have been shown to have a preferential perpendicular alignment (Hirv, A. et al., 2017). There are, however, studies which find no particular preference for alignment for spiral galaxies (Pahwa

et al., 2016; Krolewski et al., 2019), or they find a perpendicular preference for alignment for these galaxies (Lee and Erdogdu, 2007).

1.6 Structure of Thesis

In this thesis, I explore how we can compute and analyse the cosmic web, and how it can broaden our understanding of galaxy formation and evolution. In Chapter 2, I discuss the challenges of quantifying the cosmic web in observations and the different algorithms that can be used. I focus on DISPERSE, which is the algorithm I chose to do all the analysis done for this work. The following chapters are all based on journal papers that I have written and have been/will be published. Chapter 3 discusses the relationship between the spin vector of a galaxy and the direction of the filaments of the cosmic web in which it may reside (the spin-filament alignment). This is a complicated relation, with many results from both simulations and observations disagreeing to different degrees. In Chapter 4, I investigate whether past mergers can be the disruptor in the spin-filament alignment. Such a merger history can be investigated by measuring the star formation histories (SFHs) of the galaxies as a function of their spin alignment with the filaments. In Chapter 5, I explored how galaxy positions relate to cosmic filaments using photometric redshifts. These redshift uncertainties lead to different possible cosmic web configurations. To address this, I developed a method that iteratively assesses the likelihood of a galaxy's position within the cosmic web, resulting in the most probable configuration. Furthermore, I also studied how distances impact the understanding of the connection between the cosmic web and galaxy characteristics such as stellar mass and specific star formation rate (sSFR). Chapter 6 delves into the discovery of an elongated structure of 14 HI dwarf galaxies which trace a cosmic filament and are aligned with it. I summarise my results and conclusions in Chapter 7 and present avenues for future work.

You are a naughty Euclidean, sometimes you dabble in metric perturbations.

Casey Cragg

2 Filament-finding techniques

Contents

2.1 Introduction

In recent years, multiple methods have been developed to detect and classify the different components of the cosmic web.

In order to conduct any filament analysis using galaxy surveys, we need to know all three coordinates that describe the position of the galaxies: right ascension (RA), declination (Dec) and redshift (z). There are two ways of obtaining the redshift observationally: via spectroscopy or via photometry (Fernández-Soto et al., 2001). The most accurate way to measure the redshift of a galaxy is by using spectroscopy. However, spectroscopic redshifts surveys are a time-costly process and usually the number of galaxies with known spectra is limited and often biased to certain galaxy populations, e.g. above a certain magnitude or stellar mass limit, and

those galaxies with emission lines. Hence, this poses a challenge for implementing the catalogue-based filament analysis. The less accurate method of photometric redshifts ('photo-z's') require the measurement of the flux of a galaxy by using broader filters, which will provide an approximate shape of the SED. The main advantage of this method lays in numbers: many more redshifts can be measured from imaging surveys, with a broader range in magnitudes and to higher redshifts (e.g. Carrasco Kind and Brunner, 2014; Duncan et al., 2018b; Hatfield et al., 2022).

Galaxy surveys as a way to compute the cosmic web turns out to be most useful at lower redshifts. However, for high redshift, observing cosmic web filaments of the cosmic web can be done via the Lyman-α forest, as discussed in Section 1.4.1. This is linked to the cold accretion mode, which is believed to be the dominating mode of accretion onto galaxies at these redshifts. (Kereš et al., 2005; Dekel and Birnboim, 2006). The Ly-α forest provides a means to map the distribution of cold gas which flows from the filaments into the haloes and galaxies. Theoretically, they could be detected both directly, via Ly-α emission (e.g. Faucher-Giguère et al., 2010; Rosdahl and Blaizot, 2012), or indirectly, via Ly-α absorption in quasar-galaxy pairs, for example (Ho and Martin, 2020). As these filaments have a narrow size and low density (compared to the central galaxies), the streams are difficult to directly detect observationally. However, there are numerous observational studies of the CGM and the IGM around massive high redshift galaxies, both in absorption (e.g. Prochaska et al., 2014; Bouché et al., 2016; Fumagalli et al., 2017) and in emission (e.g. Steidel et al., 2000; Cantalupo et al., 2014; Umehata et al., 2019; Daddi et al., 2021; Ramakrishnan et al., 2024), which attempt to do such detections. Hence, deriving precise filament properties from observations is highly challenging, especially in the IGM, due to their low density, small size, and ambiguous chemical and ionisation compositions.

For the purposes of this chapter, we will only focus on methods using galaxy catalogues at low redshifts.

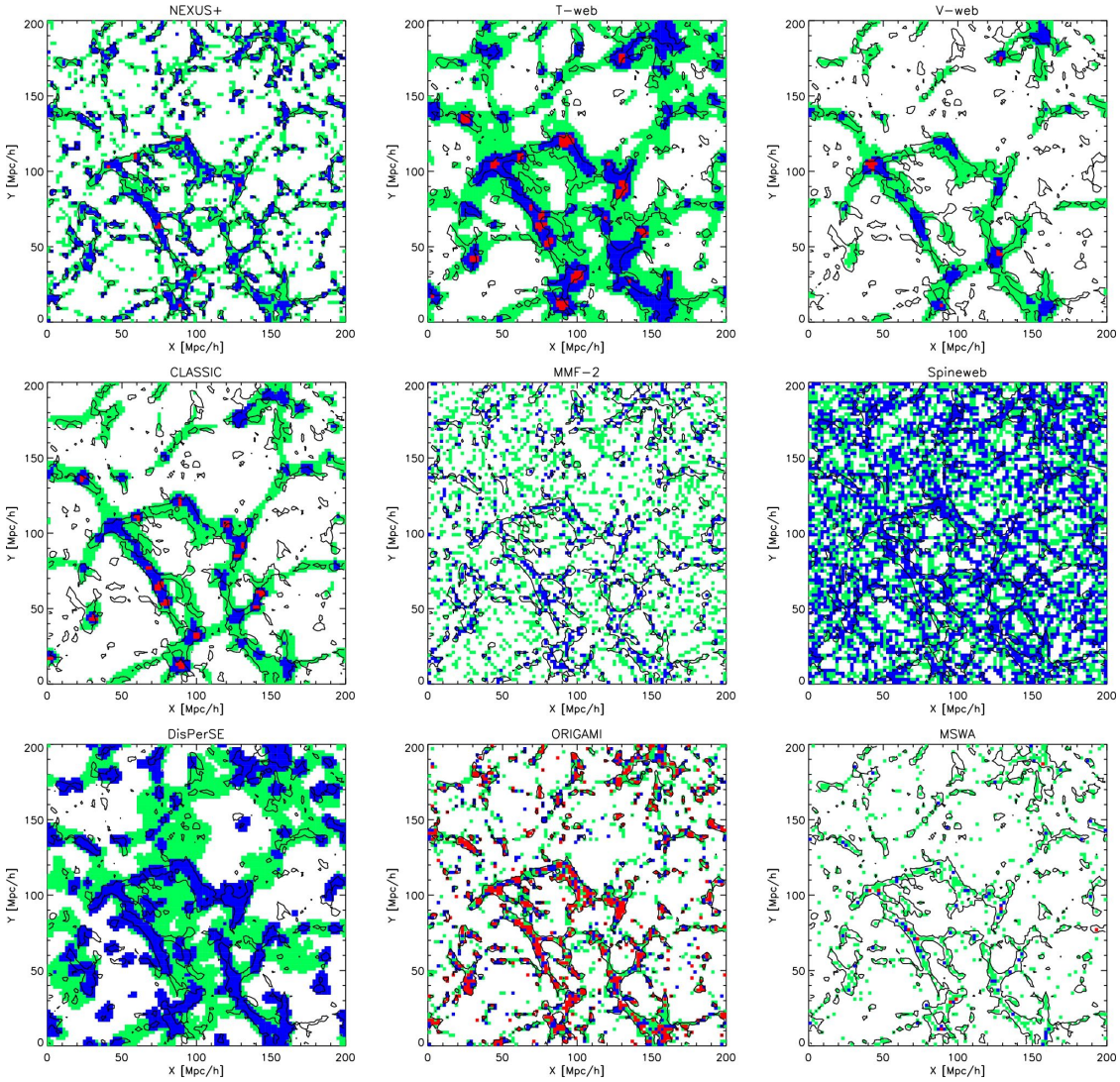

Figure 2.1: An example of how the cosmic web can be recovered by different filament-finding algorithms, for the same data. The colours indicate different parts of the network being identified: knots (red), filaments (blue), walls (green) and voids (white). Each panel has a set of solid black lines which indicate contours of over and under dense regions, with respect to the mean. Reproduced from Libeskind et al. (2017).

2.1.1 Computing the cosmic web

In terms of quantifying the cosmic web, there have been significant developments in the computational techniques required to identify and analyse such structures. Each of these techniques have different goals and different implementations. They can be grouped into five main categories: graph and percolation techniques, stochastic methods, geometric or scale-space multiscale Hessian-based methods, topological methods and phase-space methods.

Topological analysis techniques include the watershed transform and persistent homology, which identify and classify the different structures of the cosmic web based on their topological properties (Colberg et al., 2008; Sousbie, 2011). A topological feature is represented by a peak or a trough in the density field (in the case of the cosmic web, in the distribution of galaxies or the dark matter distribution), indicating a denser (underdense) region such as a cluster/filament (void). Examples of algorithms that use these techniques are SKELETON (Novikov et al., 2006; Sousbie et al., 2008), SPINEWEB (Aragón-Calvo et al., 2010) and DISPERSE (Sousbie, 2011; Sousbie et al., 2011).

Other methods rely on the identification of density peaks or overdensities in the distribution of galaxies, which can be used to detect clusters, filaments, voids, and walls. For example, the friends-of-friends algorithm is a commonly used method that identifies clusters by linking galaxies that are within a certain distance of each other (Huchra and Geller, 1982). Similarly, the Voronoi tessellation technique is used to detect and classify cosmic web structures based on the density fluctuations in galaxy distributions (Bermejo et al., 2024). In this category, Hessian-based methods are included, with algorithms such as T-WEB (Forero-Romero et al., 2009), V-WEB (Hoffman et al., 2012) and CLASSIC (Kitaura et al., 2012) being used. The Hessian methods can be combined with scale-space methods (which work by repeatedly filtering the density field at different scales to identify structures of different sizes) in algorithms such as MMF-2 (Aragón-Calvo et al., 2007; Aragón-Calvo and Yang, 2014) and NEXUS+ (Cautun et al., 2013a).

In the other two categories mentioned above, we also have graph and percolation techniques, which are some of the earliest methods used to quantify the cosmic web (e.g. Zel'dovich et al., 1982). They are based on the idea of graph theory, where galaxies or points in the cosmic web are represented as nodes, and the connections between them as edges. These graph techniques are used in algorithms such as Adapted Minimal Spanning Tree (Alpaslan et al., 2014). Other methods are represented by stochastic methods, which involve sampling particular geometrical distributions (i.e. connected, aligned cylinders for filaments) via Bayesian methods

or otherwise, to locate structures. Examples include algorithms such as FINE (González and Padilla, 2010) and Bisous (Stoica et al., 2005; Stoica et al., 2007; Tempel et al., 2014; Tempel et al., 2016). For the phase-space methods, which use the information from both position and velocity of galaxies to infer the density field, we have ORIGAMI (Falck et al., 2012; Falck and Neyrinck, 2015) and MSWA (Ramachandra and Shandarin, 2017).

Additionally, machine learning algorithms have been developed to detect and classify the cosmic web structures. For example, the Deep Density Displacement Model (D3M) uses a deep learning approach to identify and classify different components of the cosmic web based on the density and velocity fields of galaxies (He et al., 2019).

Figure 2.1 shows the difference between some of the algorithms mentioned above on the same test data in Libeskind et al. (2017). As can be seen, some of them perform better in terms of finding filaments, whilst others focus on walls/sheets or voids.

For the rest of this section, we will focus on DISPERSE, which is the algorithm of choice for the analysis in the following chapters of this work.

2.2 DiSPerSE

The Discrete Persistent Structure Extractor (DISPERSE; Sousbie, 2011; Sousbie et al., 2011) is a topological algorithm based on discrete Morse theory (Milnor, 1963). The discrete Morse theory refers to the mathematical framework used to analyse and classify the topology of discrete data sets, such as the distribution of galaxies in the cosmic web. It subsequently discerns one-dimensional and two-dimensional ascending manifolds as the filaments and walls of the cosmic web. Instead of employing the concept of a smoothing scale, it integrates topological persistence, enabling the assignment of a significance level to each topologically connected pair of critical points. This process effectively emulates an adaptive smoothing approach contingent upon the local noise level. The skeleton of the cosmic web is then computed using the Delaunay Tessellation Field Estimator (DTFE; Schaap and van

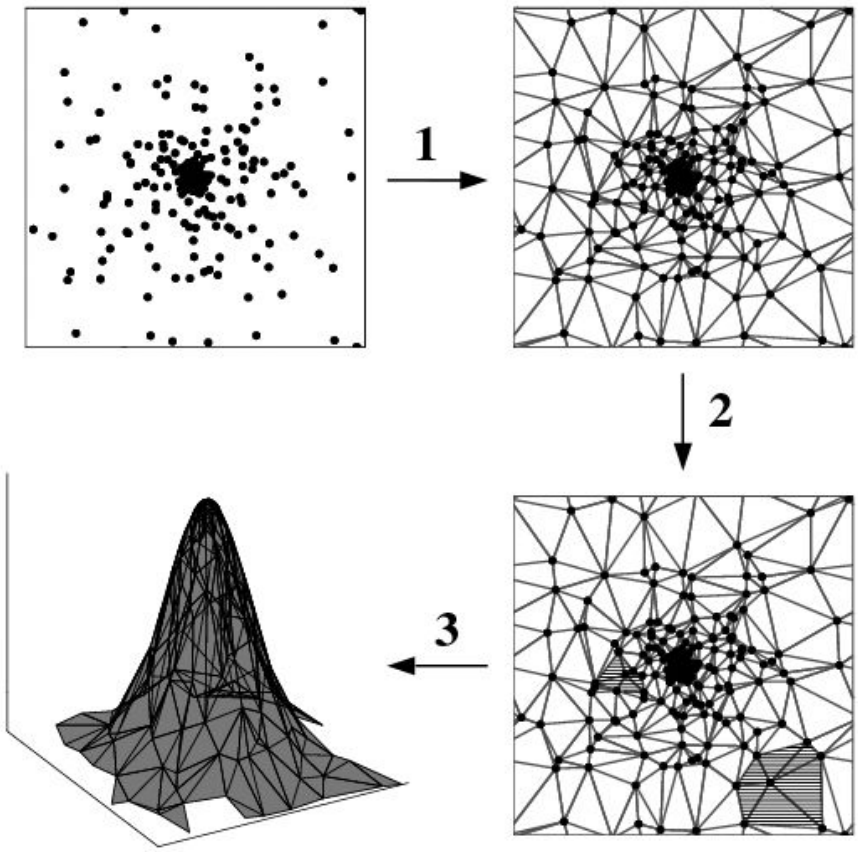

Figure 2.2: Summary of the DTFE method: For a point distribution - in this case, a galaxy catalogue (*top left*), a corresponding Delaunay tessellation is constructed (*top right*), from which the density at the position of the sampling points is estimated (*bottom right*) and by assuming that the density varies linearly within each Delaunay triangle, it result in a volume-covering continuous density field (*bottom left*). Figure reproduced from van de Weygaert and Schaap (2009).

de Weygaert, 2000), which connects nearby particles to form simplices (triangles in 2D or tetrahedra in 3D), creating a network of connections between the galaxies and generates a density field (as can be seen in Figure 2.2). As the filaments are string-like structures connecting the galaxy clusters and bordering the voids, the DTFE can easily detect the variations in the field due to the structures.

DISPERSE has been used to compute the filaments in studies such as Galárraga-Espinosa et al. (2020) for the Illustris-TNG simulation (Nelson et al., 2019), in Laigle et al. (2017) for the Horizon-AGN simulation (Dubois et al., 2014) and in Kraljic et al. (2020) for the SIMBA simulation (Davé et al., 2019). DISPERSE has also been used to compute filaments from observations such as the CHILES survey by Luber

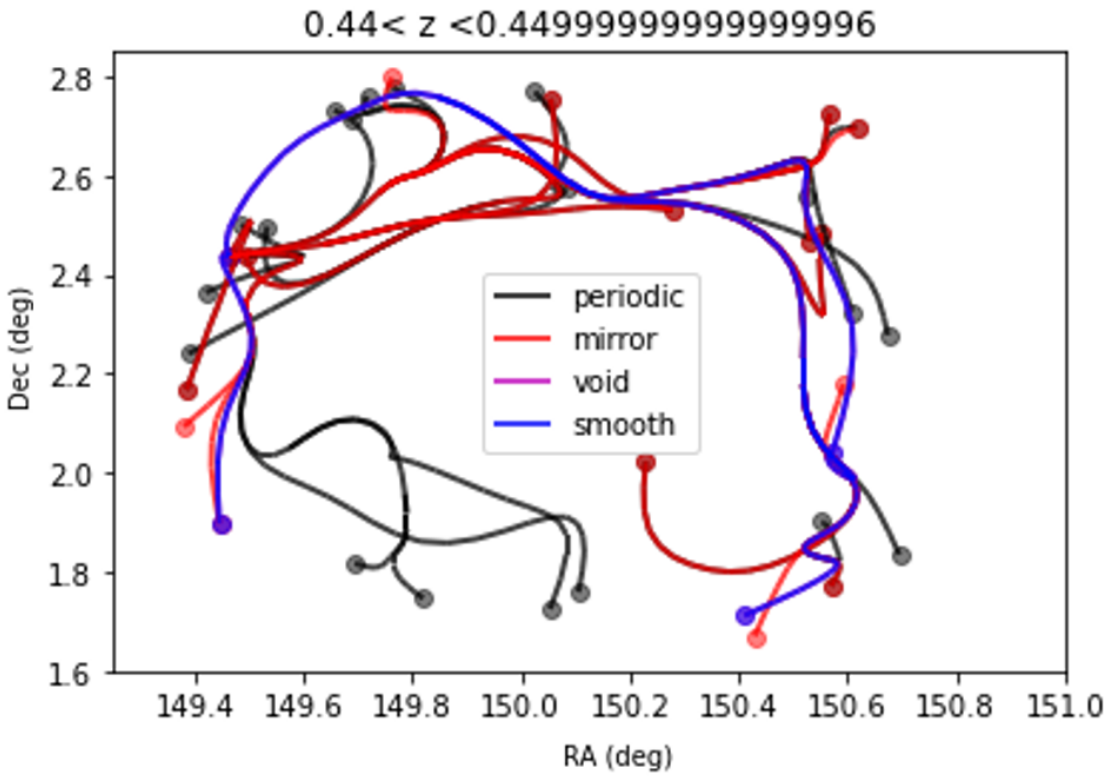

Figure 2.3: Comparison between the four BCs listed above (in black: periodic BCS, red: mirror BCs, purple: void BCs and blue: smooth BCs) using the 3D DTFE on a set of galaxies from a slice of redshift of $0.44 < z < 0.45$.

et al. (2019), the Galaxy And Mass Assembly survey (GAMA; Driver et al., 2009) by Kraljic et al. (2017) and SDSS by Winkel et al. (2021). To find the filaments, the critical points of the density field are identified: we obtain maxima, minima and saddle points. The filaments themselves are computed by connecting a maximum point to a saddle point. As an algorithm, DISPERSE can also return the walls, voids and clusters if needed. The distribution of the filaments is dependent on two important parameters: the boundary conditions (BCs) and the significance level.

2.2.1 Boundary Conditions

The distribution of the filaments is dependent on the chosen boundary conditions. DISPERSE runs with four boundary conditions:

- periodic: normal periodic conditions;
- mirror: the particles outside the field mirror the particles on the edge;

- void: there are no boundary particles added;
- smooth: particles are added to the boundaries based of an interpolated density estimation.

An illustration on how the choice of BCs affects the filament distribution can be seen in Figure 2.3. As can be seen, the problem of choosing BCs becomes relevant for the edges of our field - as the centre of the field is not significantly affected on average. In the case of simulations, we usually have access to the BCs set on the simulation box itself - usually the periodic BCs. However, when it comes to observations, it is a different story. In most cases, it is more advantageous to use either periodic or mirror BCs, as void BCs will struggle with the field-edges and in turn, affect the whole field.

2.2.2 Persistence and thresholds

The other parameter, the significance level, deals with the level at which a structure is picked up as a filament or not. The significance level is described by a threshold in a persistence diagram. Persistence is a parameter computed as the absolute value of the difference between the function values at the critical points where a topological feature is created and destroyed. In other words, persistence is measuring the density contrast between critical points defining a filament. A persistence diagram is then the persistence of a pair of critical points (represented as a ratio for DTFE) on the y-axis and with the x-axis as the value at the lowest critical point of the two (the background density). An example of a persistence diagram is shown in Figure 2.4, in which the 3D DTFE is run on a set of galaxies from a slice of redshift of $0.3 < z < 0.5$. Depending on the chosen boundary condition, a different number of voids (blue points) and collapsed structures (red points) can be identified. As such, it is important to keep in mind what significance parameter to choose based on the BC used. Figure 2.4 shows how void BCs struggle to find voids, but find a lot more collapsed structures (such as walls and filaments). Meanwhile, choosing

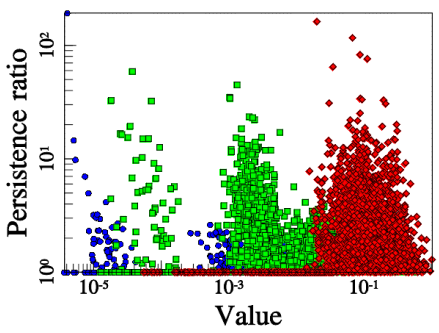

(a) Persistence ratio computed with periodic boundary conditions.

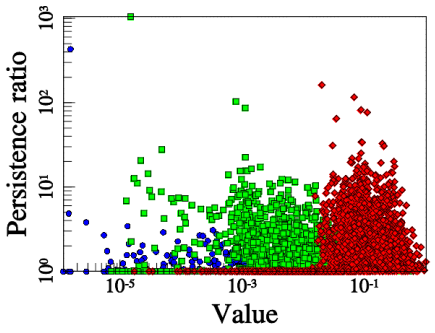

(b) Persistence ratio computed with mirror boundary conditions.

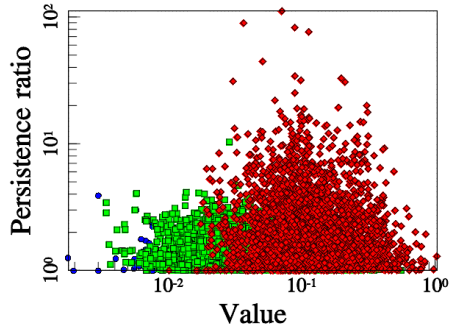

(c) Persistence ratio computed with void boundary conditions.

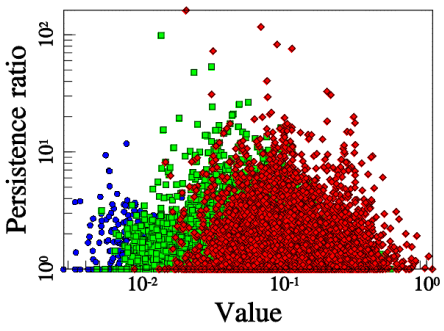

(d) Persistence ratio computed with smooth boundary conditions.

Figure 2.4: The persistence ratio obtained by running DISPERSE with a threshold of 3.5σ on a slice of photometric redshift of $0.3 < z < 0.5$, where the blue points represent minima/1-saddle points in the density field (voids), the green points represent 1-saddle/2-saddle points and the red points represent maxima/2-saddle points (collapsed structures).

periodic or mirror BCs ensure that we also find voids, as well as a more balanced number of filaments, walls and clusters.

The persistence diagram can also be used to find a suitable threshold. The choice of threshold heavily influences the computed filaments, since a low threshold will pick out structures that might not be filaments, whilst a high threshold might smooth out existing structures. An example can be seen in Figure 2.5 for three different significance levels: 5σ, 7.5σ and 10σ. As we deal with discrete distributions, the language used is in terms of Poisson distributions. Here, the significance of persistence pairs, σ, refers to the measure of statistical significance expressed in units

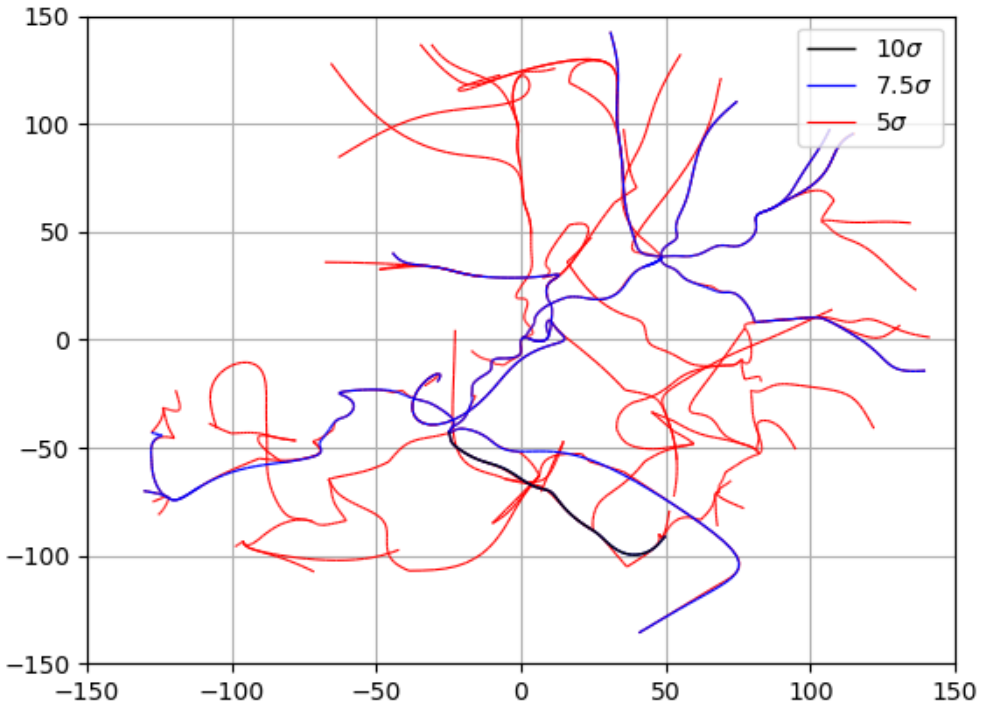

Figure 2.5: Comparison of three different filament networks obtained from a set of test particles with three significant levels (5σ, 7.5σ and 10σ). This shows how significance level strongly affects the structures that get picked as filaments - in this case, 5σ picks too many spurious filaments, whilst 10σ only picks one principal filament.

of standard deviation, analogous to the Gaussian distribution. More specifically, σ deals with Poisson noise, such that higher σ levels indicate a lower probability that the observed feature is due to noise, thereby providing a more reliable identification of true topological features in the data. Going back to the concept of persistence, it represents the range of density thresholds over which a filament connecting two critical points remains significant relative to the noise controlled by σ. As can be seen, for different σ we will have different filament networks. For the lowest sigma in this example, we find many structures - some of which are spurious. At the other end, for the highest σ, we only pick one spine of the main filament. In order to obtain a balanced view of the filament network in this instance, we choose the middle ground - which is 7.5σ. Similarly to the BCs, choosing an appropriate σ will depend on what type of data DISPERSE is run on, as there will be differences between

running it on simulations or observations. On the one hand, in simulations we have access to haloes and dark matter particles, as well as fairly complete coverage. As such, using a higher σ is more preferable - usually anything between 5σ to 10σ, depending on what part of the network structure we are interested in - see Figure 2.6 for an example of running DISPERSE on a halo and its close environment with 10σ (top) versus running DISPERSE on a halo catalogue in a bigger field with 7.5σ (bottom). On the other hand, the story is different for observations, where we only have access to galaxy distributions, which are incomplete tracers of the large scale structure. As such, using a lower σ is usually preferred. Usually, anything between 2σ to 4σ can be used to compute filament networks from galaxy catalogues.

Critical Points

DISPERSE offers several ways to output the critical points used to compute the filaments:

- original - no critical points are removed,
- boundary removed - the arcs and nodes that lay on the boundary or outside the domain of definition, such as nodes/arcs at infinity generated by boundary conditions are removed
- outside removed - the artificial arcs and nodes generated by the boundary conditions, such as arcs/nodes at infinity are removed but the boundaries themselves are kept.

Figure 2.7 shows the difference between the three types of critical points. The boundary removed and the outside removed matched in each run of each slice. As can be seen in Figure 2.7, without removing the boundary, we get several spurious points (which are just edges of the field). Therefore, using either boundary removed or outside removed is preferred. The critical points generated by DISPERSE come with a flag, which is used to define whether a critical point is a minima/maxima or a saddle point at the intersection of filaments. As it will be discussed in Section

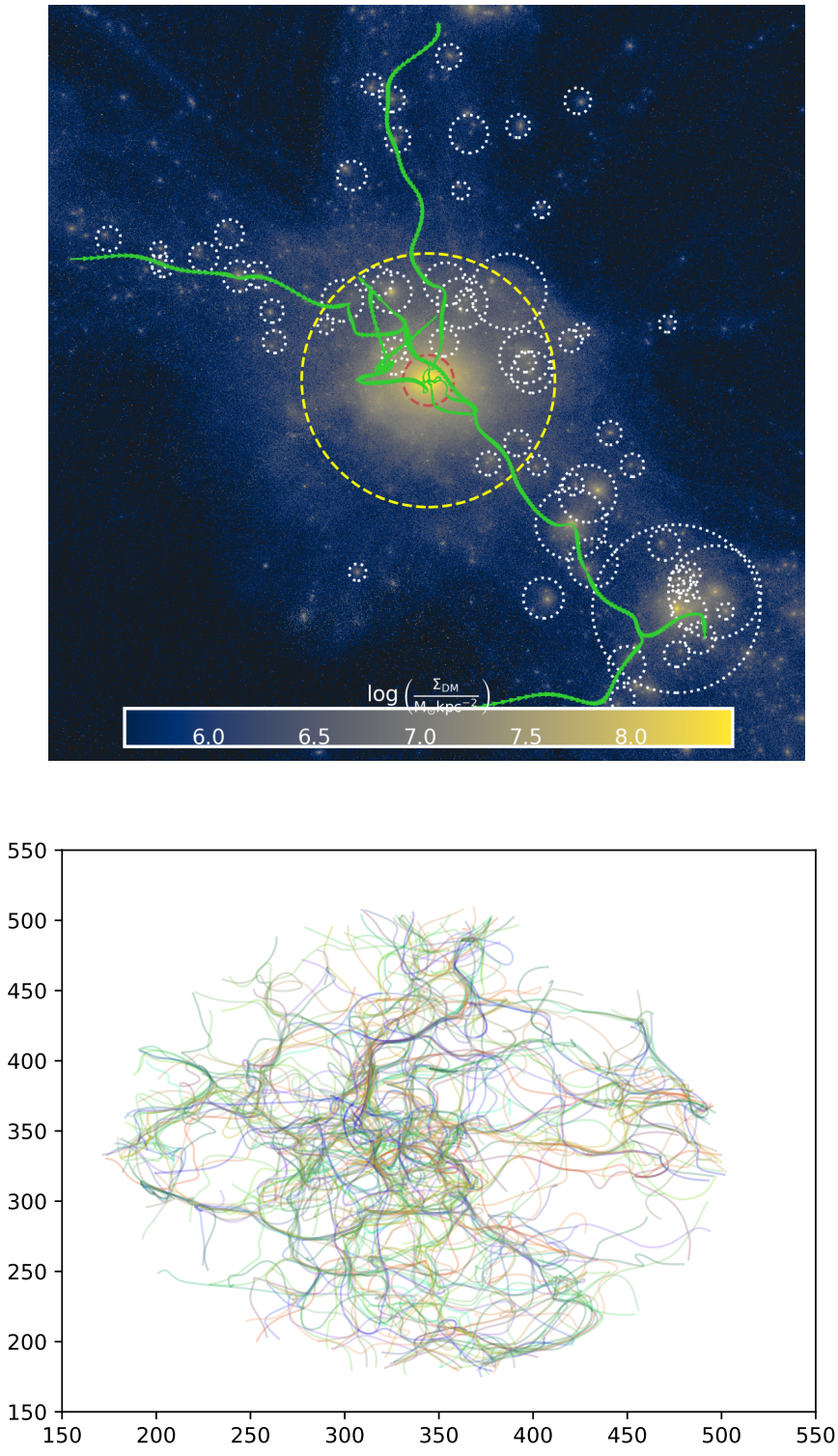

Figure 2.6: Example of two filament networks from simulations using DISPERSE. An example of a halo and its close environment, using dark matter particles to compute the filament network, where the persistence level is set to $\sigma = 10$ (*top*). An example of several filament networks obtained by sampling a halo catalogue 100 times, where the persistence level is set to $\sigma = 7.5$ (*bottom*).

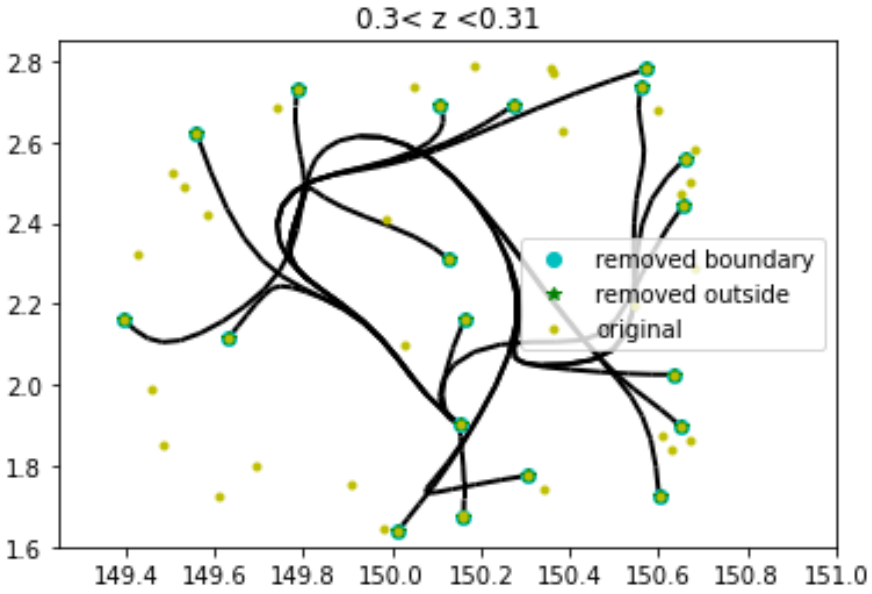

Figure 2.7: Comparison between the critical points obtained by running the 3D DTFE on a slice of redshift of $0.3 < z < 0.31$ for original distribution (yellow points), for the boundary removed (turquoise points) and for the outside removed (green points).

2.2.3, the most important critical points are the ones which intersect filaments, since they are proxies for the nodes of the cosmic web.

2.2.3 Methods and applications

Distance to the closest filament

To calculate the distance from a galaxy to the spine of the closest filament, the skeleton generated by DISPERSE can be used, as it consists of a network of points which form small segments to assemble the filament network. The midpoint of each segment can be crossmatched with a galaxy sample. This provides the physical separation - for which the 3D position of the filament point can be used - between each galaxy and its closest filament, as illustrated in Figure 2.8. This method does not provide the true exact distance to the filament, as it would require computing the right angle between a line going through the point. However, the length of the filament segments are on average ~ 1 Mpc. In the extreme case of the galaxy lying within 1 Mpc of the filament this would result in an uncertainty of the order unity, however the fractional uncertainty obviously decreases for a galaxy that resides

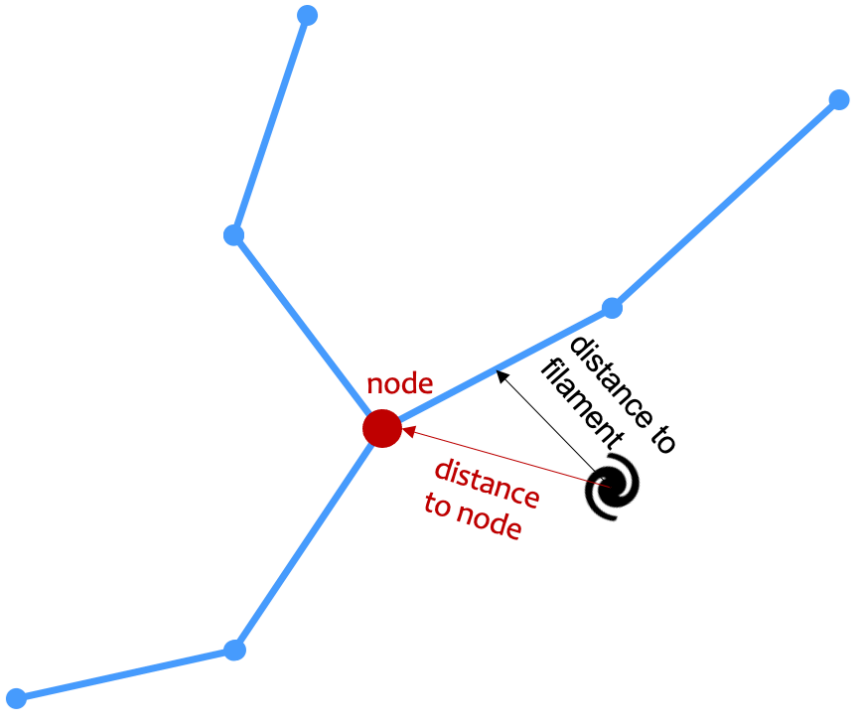

Figure 2.8: A schematic showing the two distances (distance-to-filament and distance-to-node) we use to characterise the relationship between galaxies and the filaments.

at a greater distance to the filament: for a galaxy 5 Mpc from the filament, the uncertainty on the distance is ~ 1 per cent due to this assumption, i.e. a negligible source of uncertainty given the uncertainty around the filament distribution itself.

Distance to the closest node

Similar to the distance-to-filament, the distance from a galaxy to its closest node using a similar method as above can be computed. I define a node as the intersection of at least three segments from the filament distribution obtained from DISPERSE (see Figure 2.8). The nodes can be assumed as a proxy for clusters, since the overlapping of the filaments can be approximated as a higher density point. However, we must be cautious when taking the nodes as proxies for clusters. Cornwell et al. (2024) have shown that, when used on simulations, DISPERSE finds 68% of their groups are identified as nodes. In order to account for all the nodes, I use a 3D histogram in which I input the filament network and control the bin size in order to find where the segments intersect such that the ratio between a segment and the bin

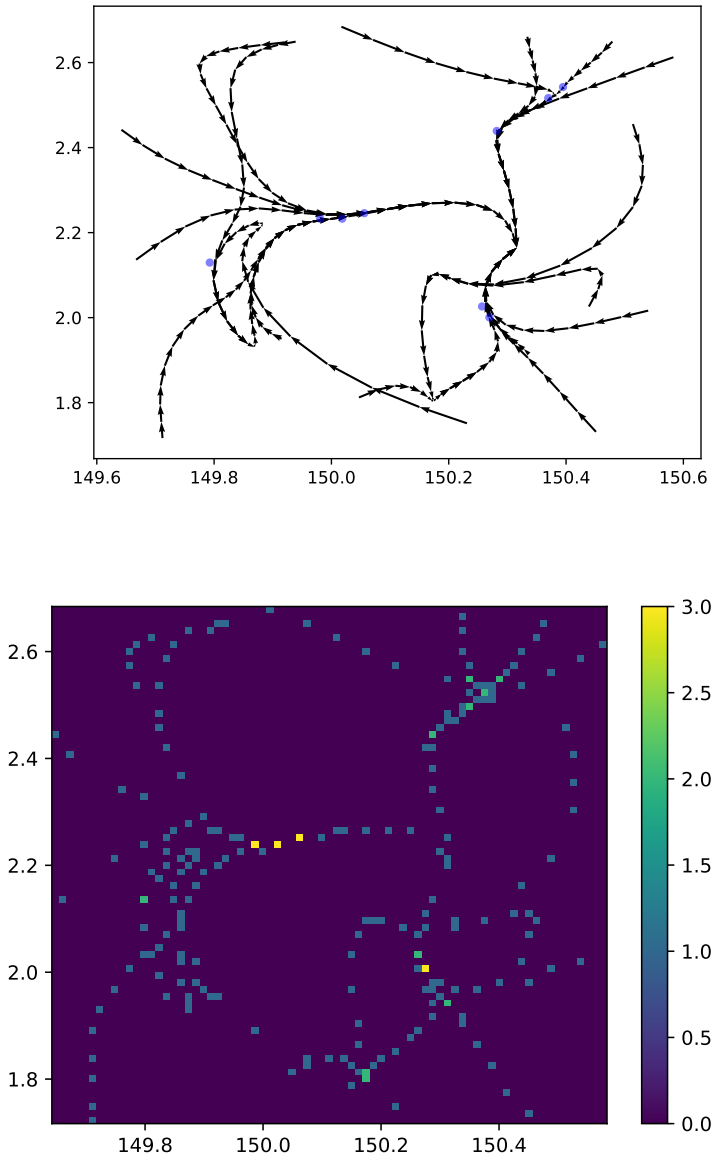

Figure 2.9: Example of an iteration of a filament network in a redshift sub-slice (upper figure) along with the corresponding 2D-histogram for the intersections (lower figure). The blue dots represent the nodes on the upper plot, whilst the colour bar on the lower plot represents the number of filaments intersecting in that bin.

size is between 2:1 and 1:1. An example can be seen in Figure 2.9. With the graph network method I use, I find on average between 2 to 4 times more nodes as DISPERSE does. One reason is due to the binning in the 3D histogram, as two adjacent bins would be two different nodes - when it practice, they are just one. As such, the disadvantage of this method is that it can recover nodes which are not clusters. However, it does recover all of the DISPERSE nodes.

Resampling on Photometric Redshift Slices

When using photometric redshifts, the filamentary structures obtained will have uncertainties associated with them. The probability associated with each photometric redshift can be used to compute a probability distribution for the filaments. When using redshift slices, as some galaxies might not be part of a slice due to their probability distribution, a jack-knife technique can be used on each slice multiple times to calculate a probability distribution for the filamentary structure. As a consequence, for each redshift slice in which I compute a filament network, I can have a number of possible filament distributions. This is discussed in more detail on actual data in Chapter 5.

The gas is not ionised because it is unionised.

Casey Cragg

3 Galaxies in the local universe: The spin-filament alignment of HI galaxies

Contents

3.1 Introduction

As discussed in the previous chapters, on the largest scales, the Universe contains a network-like distribution of galaxies, gas and dark matter - the cosmic web (Bond et al., 1996). This cosmic web affects the galaxies that reside within it via several mechanisms, and with different effects on different properties, such as mass, star formation or angular momentum.

In the case of angular momentum, as previously shown in 1.5.3, there is not a consensus on how it relates to the filaments of the cosmic web. Studies such as Ganeshaiah Veena et al. (2018) predict alignment between the angular momentum vector of the dark matter haloes and the filaments of the cosmic web. Some simulations also find hints of a spin transition from alignment to mis-alignment. For example, Kraljic et al. (2020) find a spin transition for a stellar mass of $\sim 10^{10} M_{\odot}$, whilst other simulations such as Ganeshaiah Veena et al. (2018) find no such transition and report a preference for overall mis-alignment at all masses.

However, it is not as straight-forward to obtain observational evidence for a spin-alignment at a certain stellar mass. Krolewski et al. (2019) reports no spin alignment using the Mapping Nearby Galaxies at Apache Point Observatory (MaNGA; Bundy et al., 2015) integral-field survey, whilst Welker et al. (2020) find a spin transition within a stellar-mass interval of $10^{10.4} M_{\odot} - 10^{10.9} M_{\odot}$ using the Sydney-AAO (Australian Astronomical Observatory) Multi-object survey (SAMI, Croom et al., 2012). Concentrating on the HI gas, Kraljic et al. (2020) find a possible spin transition threshold in HI mass at $M_{\rm HI} = 10^{9.5} M_{\odot}$ using the SIMBA (Davé et al., 2019) simulation. Blue Bird et al. (2020), using the COSMOS HI Large Extragalactic Survey (CHILES, Fernández et al. 2016), find that the spins of their galaxies in their HI-selected sample tend to be aligned with the cosmic web. However, their study does not find any significant mass transition between the aligned and the mis-aligned spin.

For this chapter, I aim to to elucidate the link between the spin of galaxies and the large scale structure. In order to do it, I use a HI galaxy sample provided by the MeerKAT International GigaHertz Tiered Extragalactic Exploration (MIGHTEE; Jarvis et al., 2016) Early Science data release to compute the 3D spin vector of an HI-selected galaxy sample, using optically-selected galaxies from the COSMOS and XMM-LSS fields, to relate this to the filaments of the cosmic web. The sample I use is the largest HI sample to date used to conduct a study like this, which enables me to make stronger statistical statements than in the previous study of Blue Bird et al. (2020). This allows me to compute the angular momentum using

position angles and inclinations from the HI moments, which was not possible in studies discussed in Section 1.5.3, such as Kleiner et al. (2017) or Crone Odekon et al. (2018), since they used single-dish surveys with large numbers of detections, but without the power to sufficiently resolve kinematics for the sources.

3.2 Data

The MIGHTEE survey is one of the eight Large Survey Projects (LSPs) which are being undertaken by MeerKAT (Jonas, 2009). MeerKAT consists of an array of 64 offset-Gregorian dishes, where each dish consists of a main reflector with a diameter of 13.5 m and a sub-reflector with a diameter of 3.8 m. MeerKAT's three band receivers, UHF–band ($580 < \nu < 1015$ MHz), L–band ($900 < \nu < 1670$ MHz) and S–band ($1750 < \nu < 3500$ MHz) all collect data in spectral mode. The MIGHTEE survey has three major components: radio continuum (Heywood et al., 2021), polarisation (Taylor et al., 2024) and spectral line (Maddox et al., 2021). For this work, I use the spectral line information in the L–band Early Science data release with 4096 channels with a channel width of 209 kHz, which corresponds to 44 km s^{-1} at $z = 0$.

MIGHTEE-HI (Maddox et al., 2021) is the HI emission part of the MIGHTEE survey. Its initial data products, as part of the Early Science release, were obtained using the `ProcessMeerKAT` calibration pipeline. This pipeline is a parallelised `CASA`[1]-based (McMullin et al., 2007) pipeline whose calibration routines and strategies are standard (i.e. flagging, delay, bandpass, and complex gain calibration). It performs spectral-line imaging using `CASA`'s `TCLEAN` task. The continuum subtraction was done in two domains. Visibility domain subtraction was performed using the standard `CASA` routines `UVSUB` and `UVCONTSUB`. This process was followed by an image plane based continuum subtraction using per-pixel median filtering, which was applied to the resulting data cubes (see Figure 3.1 for a visualisation of one HI data cube) to reduce the impact of the direction-dependent artefacts. The summary of the data used in this chapter is shown in Table 3.1.

[1] http://casa.nrao.edu

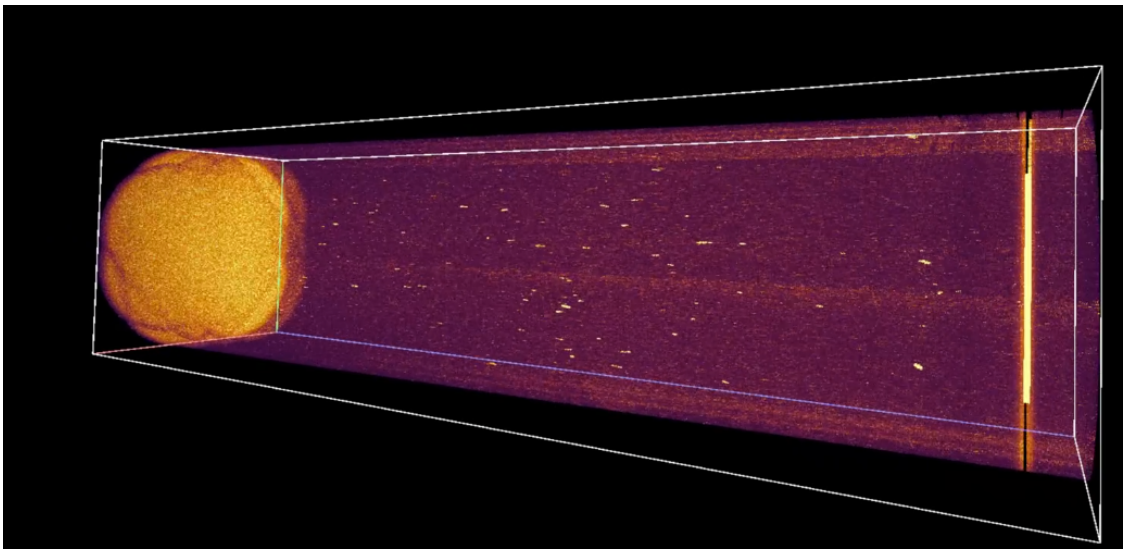

Figure 3.1: A 3D visualisation of the HI data cube in the COSMOS field. The three axes are RA, Dec and frequency channels, where the yellow blobs represent the HI galaxies.

Table 3.1: Short summary of the MIGHTEE-HI Early Science data products used in this chapter.

Area covered	$\sim 1\,\mathrm{deg}^2$ COSMOS field $\sim 3\,\mathrm{deg}^2$ XMM-LSS field
Frequency range	$1320 - 1410\,\mathrm{MHz}$
Redshift range	$0.02 - 0.09$
Channel width	$209\,\mathrm{kHz}$
Median $\mathrm{H_I}$ channel rms noise	$85\ \mu\mathrm{Jy\ beam}^{-1}$
N_{HI} sensitivity (3σ)	$1.6 \times 10^{20}\ \mathrm{cm}^{-2}$ (per channel)
Synthesised beam	$14.5" x 11"$ COSMOS field $12" x 10"$ XMM-LSS field
HI mass lower limit (Fig. 3.3)	$\sim 10^{6.7} M_\odot (z = 0.02)$ $\sim 10^{8.5} M_\odot (z = 0.09)$

There are ~ 270 galaxies in the full Early Science HI catalogue. An example of a galaxy with the HI contours overplotted can be seen in Figure 3.2. In this chapter, I use a reduced sample of 77 galaxies taken from Ponomareva et al. (2021). The kinematic modelling of these galaxies is done by using ^{3D}Barolo (1.6.1), a tool for fitting 3D tilted-ring models to the MIGHTEE-HI emission-line data-cubes (Di Teodoro and Fraternali, 2015). The number of galaxies in this sample is lower than the full Early Science catalogue due to two factors. The first is that accurate kinematically measured inclination and position angles for 183 galaxies could not be

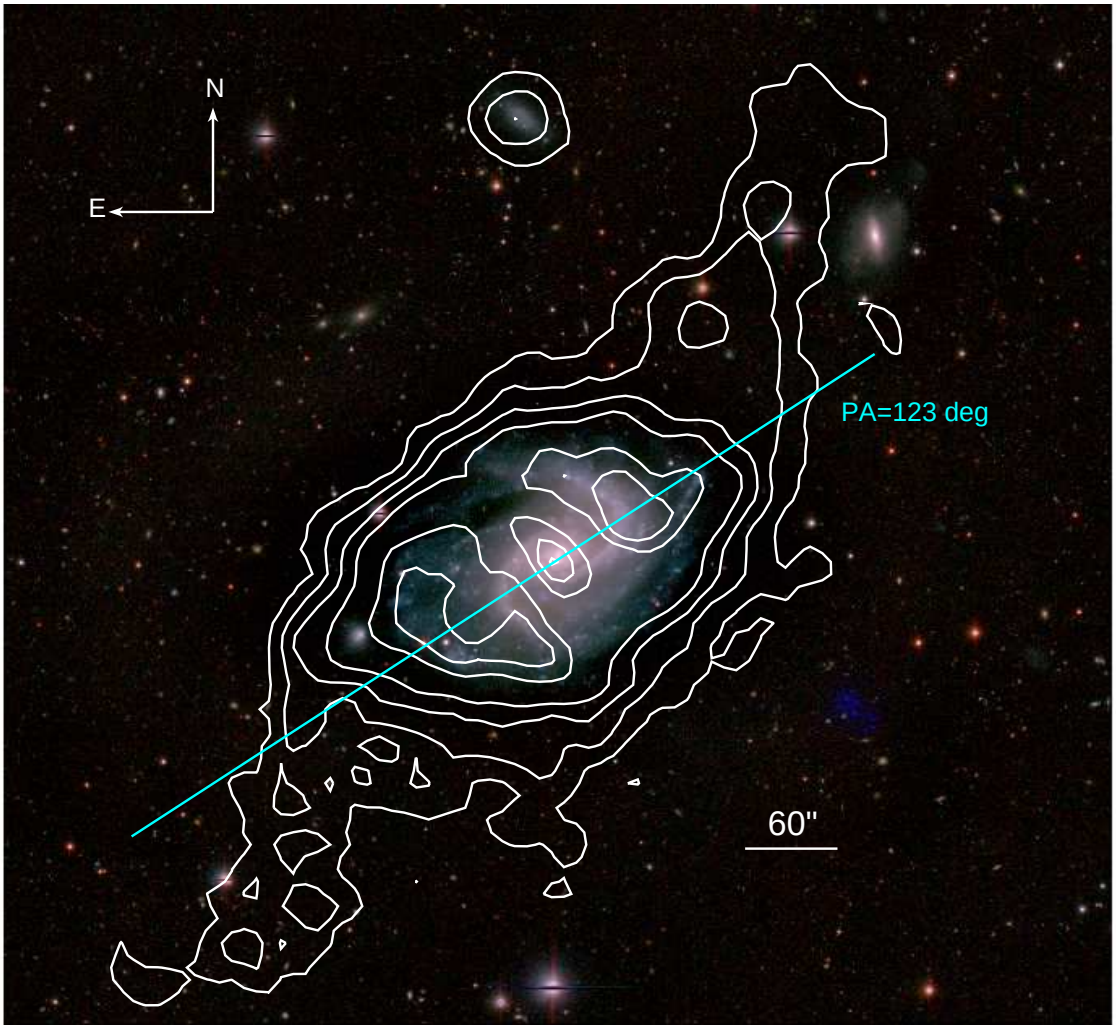

Figure 3.2: MIGHTEE-HI HI total intensity contours, overplotted on the HSC grY image of NGC 895. The HI contours have been smoothed to $20x20$ arcsec, and are based on ~ 20 h of on-source integration. The scale-bar shows 60 arcsec, while the synthesised beam is $11x9$ arcsec. The position angle from the modelling (see text) is marked in cyan. Figure reproduced from Maddox et al. (2021).

obtained due to insufficient signal-to-noise (the kinematic modelling in Ponomareva et al., 2021 requires $> 3.5\sigma$ per resolution element) and/or not being sufficiently spatially or spectrally resolved in the MIGHTEE data cube (the kinematic modelling requires at least three resolution elements, both spatially and spectrally). The second factor is that the redshift range I chose ($0.02 < z < 0.09$) means I remove a further 10 galaxies from the sample. I adopt this cut due to the small number of spectroscopic redshifts for galaxies within the COSMOS and XMM-LSS fields at $z < 0.02$, which do not provide enough information to identify the filamentary

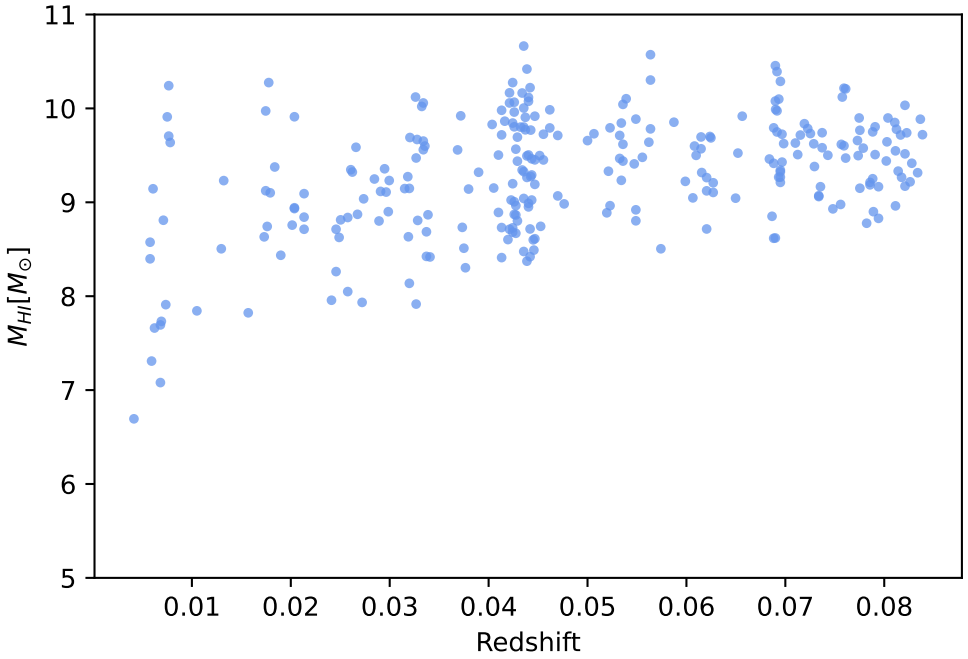

Figure 3.3: HI masses as a function of redshift for the MIGHTEE-HI Early Science HI detections.

structures in such a small comoving volume.

3.3 Methods

3.3.1 The Cosmic Web

In this work, I use DISPERSE to determine the skeleton of the cosmic web based on the distribution of galaxies from the COSMOS and XMM-LSS fields. These are two of the most widely studied extragalactic fields accessible from the southern hemisphere and have been the subject of a large number of multi-wavelength surveys over the past decade. Here, I use the imaging data described in Adams et al. (2021), which includes optical and near-infrared imaging from the HyperSuprimeCam Strategic Survey Programme DR1 (HSC; Aihara et al., 2018) and near-infrared imaging is sourced from the UltraVISTA survey in the COSMOS field (McCracken et al., 2012) and the VISTA Deep Extragalactic Observations (VIDEO; Jarvis et al., 2013) Survey in the XMM-LSS field. Spectroscopic redshifts from a variety of

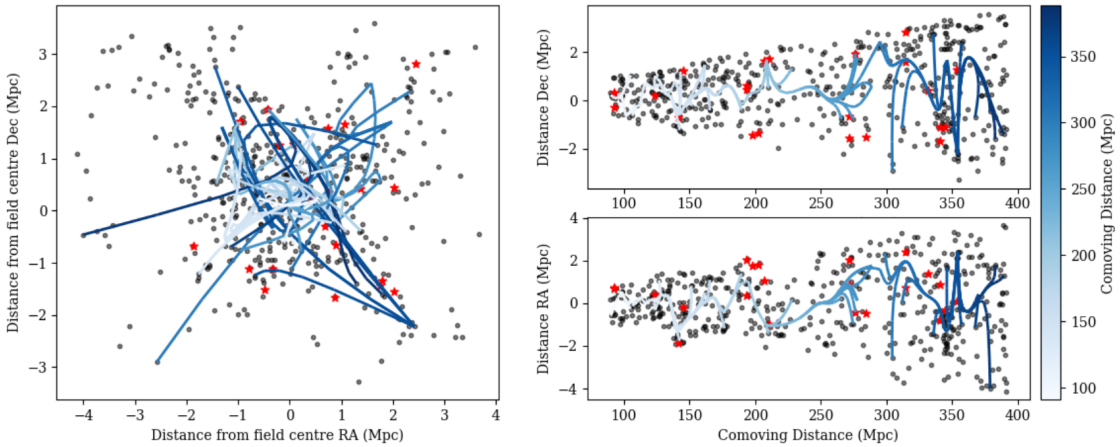

Figure 3.4: The filament distribution projected in 2D obtained by running DISPERSE with mirror boundary conditions for the COSMOS catalogue in a redshift interval $0.02 < z < 0.09$. Left: Angular distance in right ascension versus angular distance in declination. Top right: Radial comoving distance versus angular distance in declination. Bottom right: Radial comoving distance versus angular distance in right ascension of the filament distribution overlaid on top of the galaxies in the optical sample. The red stars represent the HI galaxies detected by MIGHTEE. The colour bar represents the radial comoving distance in Mpc.

surveys have been compiled by the HSC team[2]. In this catalogue, there are spectra from the VIMOS VLT Deep Survey (VVDS; Le Fèvre et al., 2013), z-COSMOS (Lilly et al., 2009), Sloan Digital Sky Survey DR-12 (SDSS-DR12; Alam et al., 2015), 3D-HST (Skelton et al., 2014; Momcheva et al., 2016), Primus (Coil et al., 2011; Cool et al., 2013), and the Fiber-Multi Object Spectrograph (FMOS; Silverman et al., 2015). From these, there is an additional selection for only those with high-quality flags (> 95% confidence) to ensure secure redshifts are being used. Together, these provide a spectroscopic sample of 22409 in COSMOS and 35125 in XMM-LSS for a redshift interval of $0.0 < z < 6.0$. These spectroscopic data provide the accurate redshifts for the filament finding and the imaging data provide the spectral baseline to derive stellar mass estimates of the galaxies within the sample.

I use spectroscopic redshifts over the redshift range $0.02 < z < 0.09$, from the range of surveys mentioned above. Within this range, there are 500 spectroscopic redshifts in the COSMOS field, and 2197 spectroscopic redshifts in the XMM-LSS field. Note that the heterogeneous nature of the spectroscopic redshifts across

[2] https://hsc-release.mtk.nao.ac.jp/doc/index.php/dr1_specz/

these fields may results in biases in some relations. For this reason, I restricted the analysis to those relations that should be largely invariant to the heterogeneous nature of the spectroscopic redshifts, i.e. those concerning the alignment of the galaxies' spin axis with the direction of the filaments.

Following Luber et al. (2019), I split the sample into slices of equal redshifts $\Delta z = 0.01$ from $z = 0.02$ to $z = 0.09$. As the errors from the spectroscopic redshifts vary between $\delta z = 0.0001$ to $\delta z = 0.0009$, depending where are they acquired from, this ensures that our filament slices are robust. I choose a threshold of 3.5σ, motivated by the comparisons in Sousbie (2011) and use the mirror boundary conditions to aid comparison with previous work (e.g. Blue Bird et al., 2020). Figure 3.4 shows an example for the filament network converted into 3D Cartesian coordinates for mirror boundary conditions along with the galaxies used to compute it. The choice of the significance level ensures that the filaments are robust and that the big structures are picked up without washing out some of the relevant finer structures.

3.3.2 Spin of the galaxy

In order to compute the 3D spin of a galaxy, I followed the treatment in Lee and Erdogdu (2007). They use a thin-disk approximation, such that the spin unit vector of a galaxy can be characterised in local spherical coordinates as:

$$\hat{L}_r = \cos i \tag{3.1}$$

$$\hat{L}_\theta = \sin i \sin \mathrm{PA} \tag{3.2}$$

$$\hat{L}_\phi = \sin i \cos \mathrm{PA} \tag{3.3}$$

where PA is the position angle and i is the inclination angle of the galaxy. The values for both the PAs and the i's were measured using 3D kinematic modelling with ^{3D}Barolo (1.6.1), a tool for fitting 3D tilted-ring models to the MIGHTEE-HI emission-line data-cubes (Di Teodoro and Fraternali, 2015). An example of a position-velocity diagram obtained using ^{3D}Barolo on the MIGHTEE-HI data can be seen in Figure 3.5.

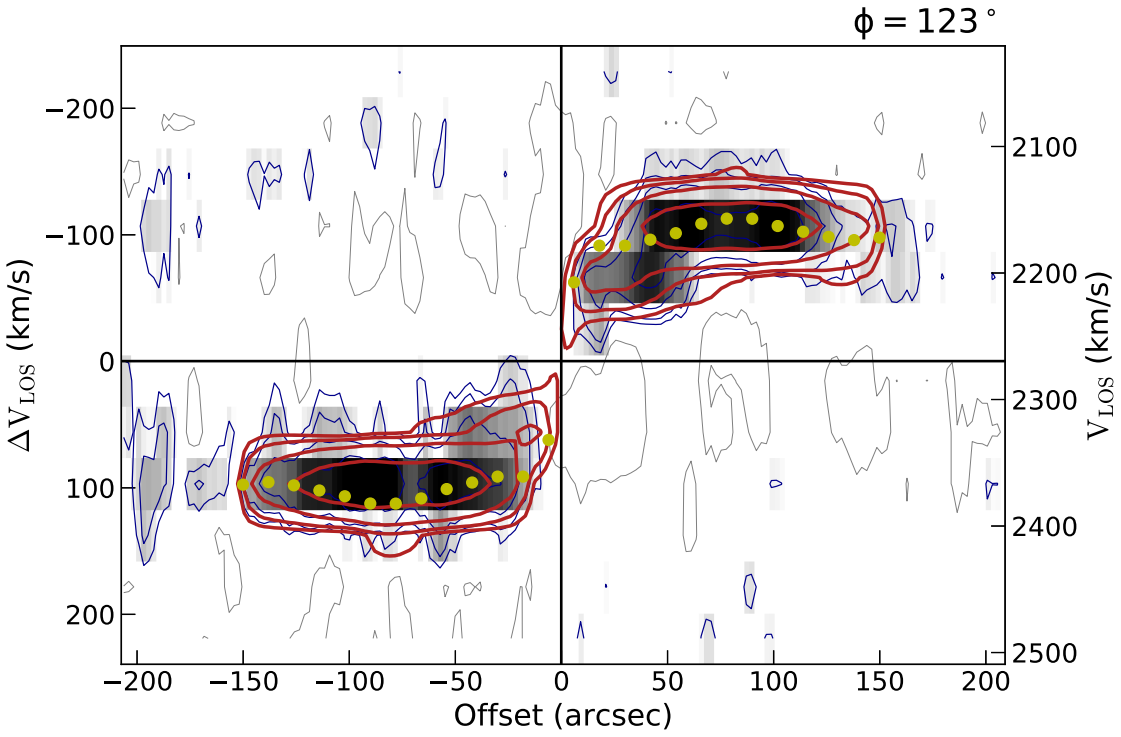

Figure 3.5: Position-velocity (PV) diagram of NGC 895, using HI data from MIGHTEE-HI, is shown in grey scale and blue contours. The 3D kinematic model (see text) is shown with red contours, and the resulting rotation curve of the galaxy, projected on the data, is shown with yellow dots. Reproduced from Maddox et al. (2021).

The inclination angle is defined as $i = 0$ if face-on and $i = \pi/2$ if edge-on, whilst the PA is measured from the north counterclockwise to the receding side of a galaxy.

The unit spin vector is converted into Cartesian coordinates, with the spherical vector related to the Cartesian vector by:

$$\begin{bmatrix} \hat{L}_x \\ \hat{L}_y \\ \hat{L}_z \end{bmatrix} = \begin{bmatrix} \sin\alpha\cos\beta & \cos\alpha\cos\beta & -\sin\beta \\ \sin\alpha\sin\beta & \cos\alpha\sin\beta & \cos\beta \\ \cos\alpha & -\sin\alpha & 0 \end{bmatrix} \begin{bmatrix} \hat{L}_r \\ \hat{L}_\theta \\ \hat{L}_\phi \end{bmatrix}, \tag{3.4}$$

where $\alpha = \pi/2 - \mathrm{DEC}$ and $\beta = \mathrm{RA}$, with DEC and RA corresponding to declination and right ascension, respectively. Figure 3.6a illustrates the unit spin vector along with the angles used for its calculation and the direction of rotation for the galaxy. There is a sign ambiguity which arises in $\hat{L}_r$, which has been shown in Trujillo et al. (2006). Following past work (Lee and Erdogdu, 2007; Kraljic et al., 2021), I choose to take the positive sign in $\hat{L}_r$. Kraljic et al. (2021) has shown that if the sign of $\hat{L}_r$ is flipped in Equation 3.4, the overall effect of a galaxy being either aligned or mis-aligned does not change due to the symmetry.

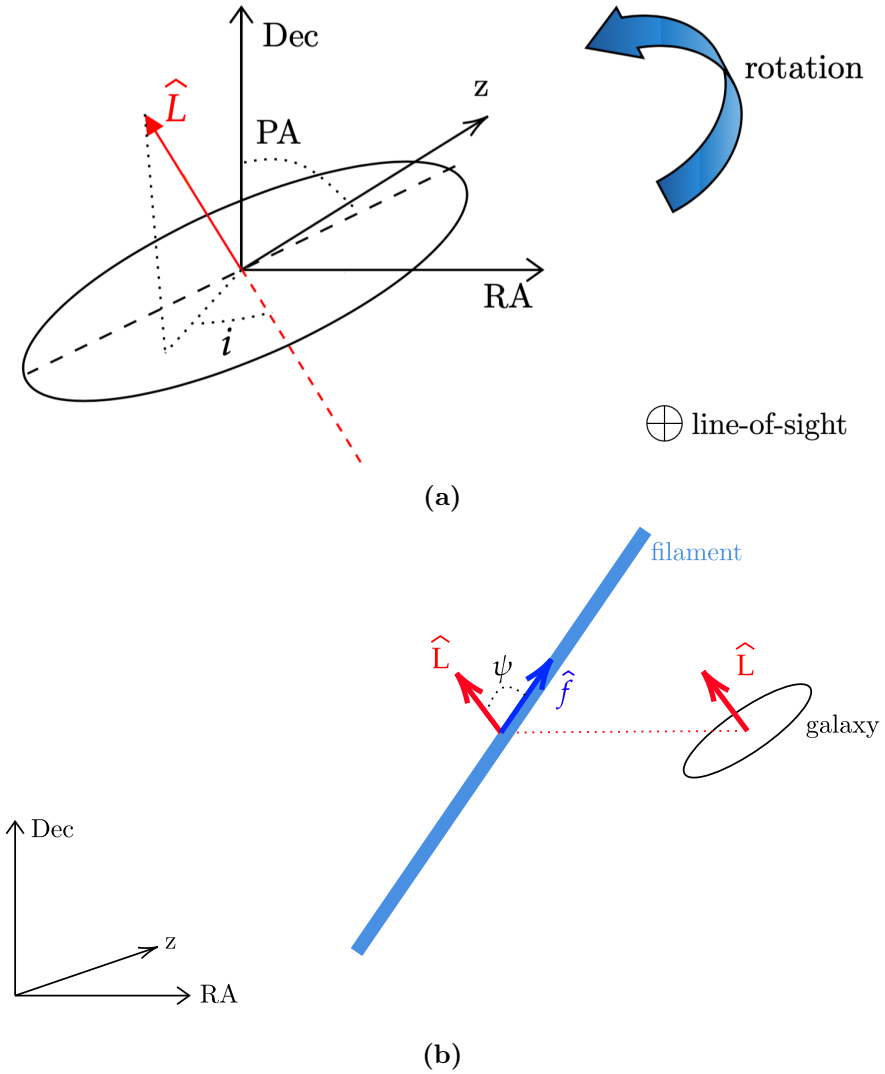

Figure 3.6: Schematic of a galaxy and its closest filament in (RA, Dec, z) coordinates. Illustration of the position angle (PA), the inclination (i), the unit spin vector ($\hat{L}$) and the direction of rotation for a galaxy (*top*). Illustration of a galaxy and its unit spin vector next to its closest filament vector along with the angle ψ between them (*bottom*).

3.3.3 Angle between galaxy and filament

To calculate the angle between the spin galaxy vector and the filament, I cross-match the galaxy with the closest filament, which is defined by a starting point $f_1(\mathrm{RA}_1, \mathrm{Dec}_1, z_1)$ and an end point $f_2(\mathrm{RA}_2, \mathrm{Dec}_2, z_2)$, where z is the redshift centred on the midpoint of the filament segment. To calculate the spherical components

of the filament vector I then write:

$$f_{\rm RA} = f_2({\rm RA}_2) - f_1({\rm RA}_1), \tag{3.5}$$

$$f_{\rm Dec} = f_2({\rm Dec}_2) - f_1({\rm Dec}_1), \tag{3.6}$$

$$f_z = f_2(z_2) - f_1(z_1), \tag{3.7}$$

where $f_{\rm RA}$ is the vector-component along RA, defined by the beginning and the end point, $f_{\rm Dec}$ is the vector-component along Dec and f_z is the vector-component along redshift.

The filament vector is then converted into Cartesian coordinates in order to compute the dot product between the spin vector of the galaxy **L** and the filament vector **f**. To find the cosine of the angle between the galaxy spin vector and the filament vector, ψ, I divide the dot product by the modulus of the filament vector, as the spin vector is already normalised to 1:

$$\cos\psi = \frac{f_x \cdot \hat{L}_x + f_y \cdot \hat{L}_y + f_z \cdot \hat{L}_z}{|\mathbf{f}|}, \tag{3.8}$$

where f_x, f_y, f_z are the Cartesian components of the filament vector **f** and $\hat{L}_x$, $\hat{L}_y$, $\hat{L}_z$ are defined as before. Figure 3.6b shows a schematic of the two vectors and ψ. To analyse the orientation of the galaxy spin relative to the spine of the filament I take the absolute value of the cosine, which gives us the acute value of the angle ψ independent of the direction of the normalised filament vector $\hat{f}$. Following the convention in Kraljic et al. (2020), for $|\cos\psi| < 0.5$ the two are considered mis-aligned, whilst for $|\cos\psi| > 0.5$ they are considered aligned.

Table 3.2: A table of the coordinates, masses and distances-to-filament for the MIGHTEE-HI galaxies used in this study.

RA [deg]	**Dec [deg]**	**z**	$\mathbf{log_{10}\,\frac{M_\star}{M_\odot}}$	$\mathbf{log_{10}\,\frac{M_{HI}}{M_\odot}}$	$\boldsymbol{d_{\rm fil}}$ **[Mpc]**	$\mathbf{|\cos\psi|}$
150.547	2.022	0.021	9.228	8.713	6.621	0.867
150.595	2.422	0.021	8.763	8.842	6.607	0.339
150.313	2.306	0.028	8.611	9.248	23.887	0.384

Continued on next page

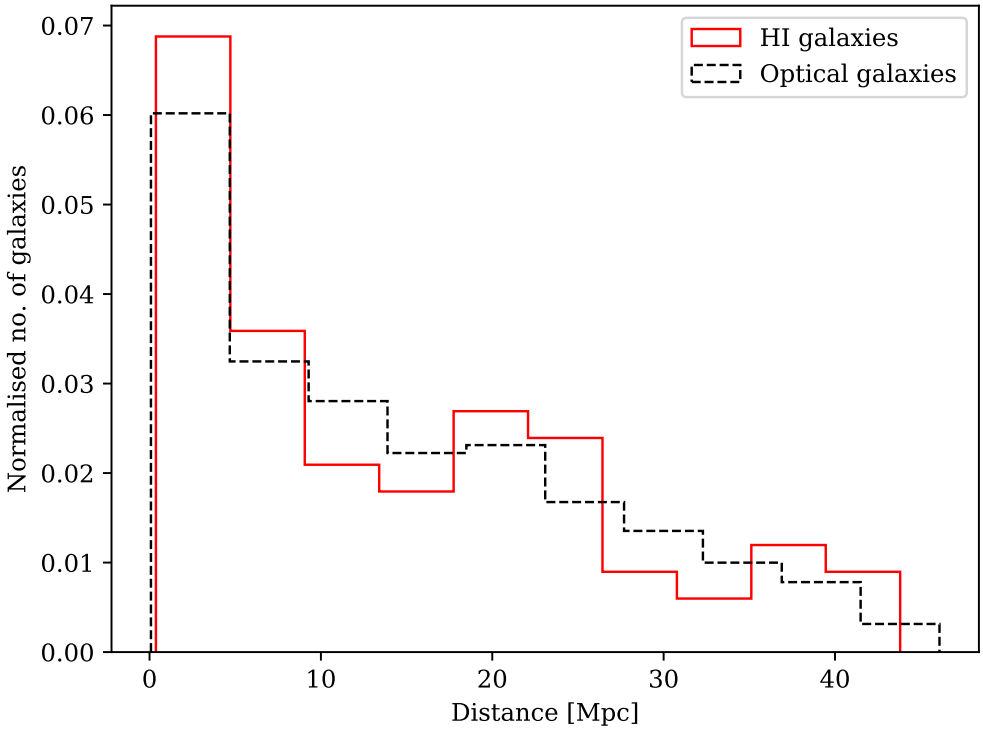

Figure 3.7: Normalised histogram of both the HI galaxies (red solid line) and the optical galaxies (black dashed line) from the COSMOS and XMM-LSS fields in the redshift range of $0.02 < z < 0.09$ as a function of distance from the cosmic web obtained using mirror boundary conditions on DISPERSE.

Table 3.2: A table of the coordinates, masses and distances-to-filament for the MIGHTEE-HI galaxies used in this study. (Continued)

RA [deg]	Dec [deg]	z	$\log_{10} \frac{M_\star}{M_\odot}$	$\log_{10} \frac{M_{\rm HI}}{M_\odot}$	$d_{\rm fil}$ [Mpc]	$\lvert\cos\psi\rvert$
149.336	1.919	0.032	10.14	9.69	0.946	0.893
150.039	2.713	0.033	9.458	9.472	28.682	0.456
150.23	2.395	0.044	10.416	9.274	11.376	0.208
150.746	2.343	0.044	10.926	9.769	4.393	0.753
150.652	1.772	0.045	7.942	8.744	19.748	0.827
150.652	1.81	0.046	9.224	9.725	25.232	0.529
150.43	2.686	0.047	9.24	9.712	1.351	0.207
149.847	2.694	0.048	9.681	8.983	10.83	0.424
150.321	2.06	0.062	9.459	9.317	10.826	0.275

Continued on next page

Table 3.2: A table of the coordinates, masses and distances-to-filament for the MIGHTEE-HI galaxies used in this study. (Continued)

RA [deg]	Dec [deg]	z	$\log_{10} \frac{M_\star}{M_\odot}$	$\log_{10} \frac{M_{\rm HI}}{M_\odot}$	$d_{\rm fil}$ [Mpc]	$\lvert\cos\psi\rvert$
150.574	1.857	0.062	10.189	9.671	0.449	0.432
150.026	2.636	0.063	8.874	9.208	16.123	0.711
150.016	1.881	0.065	9.096	9.524	36.483	0.22
150.265	2.515	0.072	9.934	9.837	0.381	0.915
150.595	2.755	0.072	9.417	9.785	7.523	0.373
150.375	2.285	0.076	10.363	9.617	10.432	0.131
149.977	2.005	0.078	10.361	9.577	15.139	0.77
150.279	1.904	0.078	10.25	9.767	14.865	0.034
150.06	2.007	0.079	10.204	8.9	2.636	0.503
150.131	2.431	0.081	8.976	8.962	44.805	0.93
34.558	−4.829	0.032	8.904	9.273	4.036	0.639
34.947	−4.809	0.032	8.783	9.146	37.281	0.558
34.497	−4.276	0.033	8.821	9.652	38.714	0.367
35.089	−4.967	0.033	10.395	9.56	21.729	0.237
35.208	−5.487	0.033	9.227	10.02	1.85	0.931
36.012	−4.16	0.033	10.32	10.058	6.886	0.598
36.198	−4.779	0.033	8.935	10.121	1.911	0.865
35.703	−4.886	0.037	9.057	9.921	7.516	0.115
36.345	−4.922	0.037	8.442	9.558	8.133	0.447
34.299	−4.411	0.038	8.073	9.141	28.772	0.807
36.053	−4.998	0.04	9.724	9.829	12.295	0.301
34.76	−4.446	0.041	9.274	9.718	10.453	0.638
35.137	−5.435	0.041	10.01	9.98	19.117	0.342
35.273	−4.498	0.041	10.232	9.503	18.242	0.766
33.887	−4.769	0.042	10.148	10.058	25.095	0.16
34.564	−4.266	0.042	10.171	10.166	4.78	0.601
34.601	−5.465	0.042	9.246	9.844	25.105	0.856
34.614	−4.205	0.042	10.278	9.864	25.138	0.616
34.437	−4.199	0.043	9.832	9.961	4.953	0.438
34.886	−4.246	0.043	9.627	9.804	22.314	0.87

Continued on next page

Table 3.2: A table of the coordinates, masses and distances-to-filament for the MIGHTEE-HI galaxies used in this study. (Continued)

RA [deg]	Dec [deg]	z	$\log_{10} \frac{M_\star}{M_\odot}$	$\log_{10} \frac{M_{\rm HI}}{M_\odot}$	$d_{\rm fil}$ [Mpc]	$\lvert\cos\psi\rvert$
36.011	−4.693	0.043	11.024	10.164	20.365	0.755
33.935	−4.928	0.044	9.14	10.004	9.736	0.033
34.371	−5.141	0.044	9.618	9.801	6.239	0.096
34.949	−4.858	0.044	9.642	9.772	2.175	0.637
35.214	−4.951	0.044	9.926	10.42	0.927	0.6
35.961	−4.846	0.044	8.57	10.117	4.129	0.817
36.016	−4.551	0.044	10.185	10.221	7.041	0.516
36.017	−4.803	0.044	10.301	10.664	2.601	0.968
36.123	−4.677	0.044	8.55	9.504	18.036	0.42
36.161	−4.572	0.044	9.614	9.905	18.22	0.11
36.231	−4.293	0.044	10.759	10.076	4.051	0.519
35.884	−4.824	0.045	8.699	9.191	3.004	0.595
36.233	−5.322	0.053	9.508	9.844	0.704	0.826
36.27	−4.707	0.053	9.883	9.712	20.311	0.29
34.261	−5.328	0.054	9.12	10.043	37.32	0.018
36.402	−5.003	0.054	9.589	10.103	30.434	0.683
36.296	−4.915	0.055	10.151	8.803	6.793	0.171
36.405	−5.428	0.055	10.185	9.886	23.204	0.304
34.041	−5.316	0.056	10.463	10.572	2.494	0.218
34.259	−4.748	0.056	10.171	9.64	40.554	0.834
34.285	−4.23	0.056	9.514	10.302	41.877	0.473
34.001	−4.737	0.069	9.91	10.099	8.617	0.686
34.452	−4.545	0.069	10.1	9.989	2.51	0.55
35.4	−4.422	0.069	9.264	10.039	4.958	0.701
35.782	−5.484	0.069	10.652	10.392	2.383	0.61
35.903	−4.476	0.069	8.95	9.749	2.086	0.706
36.065	−4.698	0.069	9.609	10.078	3.743	0.631
36.125	−4.604	0.069	10.735	10.455	33.28	0.027
36.073	−4.286	0.073	8.76	9.732	25.437	0.569
35.444	−4.606	0.076	10.085	10.017	2.797	0.909

Continued on next page

Table 3.2: A table of the coordinates, masses and distances-to-filament for the MIGHTEE-HI galaxies used in this study. (Continued)

RA [deg]	Dec [deg]	z	$\log_{10} \frac{M_\star}{M_\odot}$	$\log_{10} \frac{M_{\rm HI}}{M_\odot}$	$d_{\rm fil}$ [Mpc]	$\lvert\cos\psi\rvert$
35.624	−4.887	0.08	10.332	9.904	33.848	0.759
35.476	−4.673	0.081	10.427	10.132	13.726	0.09
36.229	−5.43	0.081	9.025	9.778	25.489	0.303

3.4 Results

3.4.1 Spin alignment as a function of distance-to-filament

As can be seen in Figure 3.7, all of the HI-selected galaxies in the sample lie within ~ 40 Mpc of their associated closest filament - with the majority of the sample within 10 Mpc (36 out of 77 HI-selected galaxies). For the HI-selected galaxy sample, 50% of the galaxies are within 10.6 Mpc, whilst 50% of the optical galaxies used to compute the cosmic web are within 11.6 Mpc. Using the method described in Section 3.3.3, I calculated the spin axis for the 77 galaxies in the sample and the cosine of the angle between the spin axis of each galaxy and its closest filament. The results can be seen in Table 3.3 and Figure 3.8, where I separate the sample into different distance ranges. I use these distance ranges as bins for which I calculate the means and the medians, to highlight the overall trend. Whilst the errors on the means (medians) are computed using the standard errors, it is more difficult to calculate the errors on the individual $\langle|\cos\psi|\rangle$ values. This is due to the nature of the filament-finding algorithm which does not provide any information on the uncertainty in the length or direction of the filaments. Hence, in order to be able to provide an estimate of the uncertainty for $\cos\psi$, I determined the filament distribution by randomly omitting 5 per cent of the optical galaxies and computing a new network 100 times. I then used the new network to find the closest filament to the galaxy and to recalculate $\cos(\psi)$. Therefore, for each galaxy, I generated 101 values for the cos-angle, which allows the standard deviation on each $\cos(\psi)$ value to be determined. These are shown in Figure 3.8. I truncate the error bars where the formal uncertainty gives a value above $|\cos\psi| = 1$ and below $|\cos\psi| = 0$.

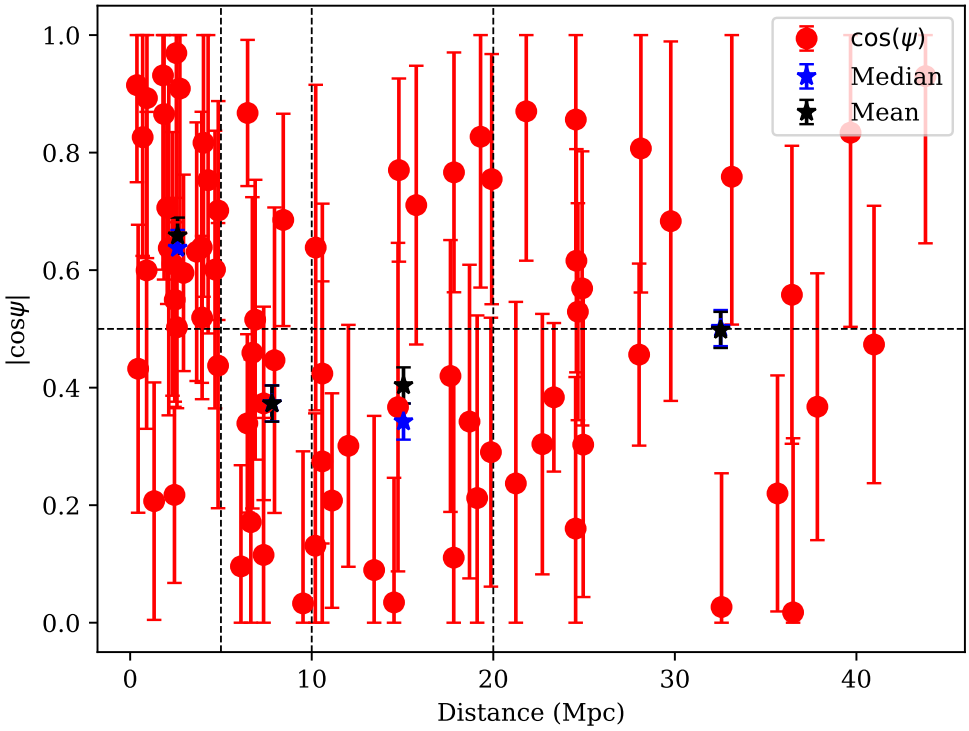

Figure 3.8: $|\cos\psi|$ for the galaxy sample as a function of distance to the closest filament computed with mirror boundary conditions. The black horizontal dotted line represents the spin value 0.5, whilst the vertical dotted lines mark the 5 Mpc, 10 Mpc and 20 Mpc distance cuts respectively. The blue and black stars represent the medians and the means obtained by splitting the sample in distance bins of 5 Mpc, 10 Mpc and 20 Mpc, respectively. Uncertainties on the individual values of $\cos\psi$ are determined using the method outlined in Section 3.4.1.

Clearly the result is noisier where there is a lack of a larger numbers of objects at largerdistances to the filaments, however there is a clear result for alignment for the galaxies within 5 Mpc of their closest filament.

I use the Mann-Whitney U test (Mann and Whitney, 1947) on the distributions with different distance ranges to compare their medians, shown in Table 3.4. I find significant evidence for alignment between the spin axis of the HI-selected galaxies and their closest identified filaments. For example, for the galaxies within 5 Mpc of their closest filament I find $\langle|\cos\psi|\rangle = 0.66 \pm 0.04$, whereas those galaxies that lie $>$ 5 Mpc away from their nearest filament give a mean alignment of $\langle|\cos\psi|\rangle = 0.44 \pm 0.04$, with a Mann-Whitney test giving a $p-$value of 5×10^{-4},

providing strong evidence that the two distributions are significantly different. The trend continues for the distributions of the galaxies within 10 Mpc of their closest filament and further away from 10 Mpc of their nearest filament, with a Mann-Whitney $p-$value of $3.1 \cdot 10^{-2}$. The only distribution without a statistically significant $p-$value is for the galaxies within 20 Mpc of their closest filaments and those beyond 20 Mpc. This is likely due to the low number of galaxies which are beyond 20 Mpc from their closest filament.

This is in agreement with the results obtained by Blue Bird et al. (2020), who used only 10 galaxies (which were within 10 Mpc of their closest filament) and also found that galaxy spins tend to be aligned with the filaments of the cosmic web.

Table 3.3: The mean of the cosine of the angle between the HI spin of the galaxy and its closest filament $\cos\psi$ and the p-values for the Kolmogorov-Smirnov test for different distance ranges.

Distance Cut	$\langle\lvert\cos\psi\rvert\rangle$	$\mathbf{p_{KS}}$
$0\,\mathrm{Mpc} < d < 5\,\mathrm{Mpc}$	0.66 ± 0.04	$5 \cdot 10^{-2}$
$5\,\mathrm{Mpc} < d < 10\,\mathrm{Mpc}$	0.37 ± 0.08	$9 \cdot 10^{-2}$
$10\,\mathrm{Mpc} < d < 20\,\mathrm{Mpc}$	0.40 ± 0.06	$4 \cdot 10^{-3}$
$d > 20\,\mathrm{Mpc}$	0.50 ± 0.06	10^{-9}
full range	0.51 ± 0.03	10^{-19}

To verify the result, I shuffled the PAs and the i's in the sample. With this shuffled galaxy sample, I cross-matched it with the filamentary structures and then recalculated the cosine of the angles. I repeated this process 2000 times and used a Kolmogorov-Smirnov test (Noether, 1978) to determine whether the measured alignments are consistent with the null-hypothesis of a randomly oriented spin vector for the galaxy sample, which I show in Table 3.3. The $p-$values for the whole sample for the KS test is 10^{-19}. Thus I can strongly reject the null hypothesis of the spin axis of galaxies being randomly oriented with respect to the orientation of the filaments.

There are not many studies investigating the link between the distance of the galaxy from the filament and $|\cos\psi|$. Krolewski et al. (2019) do not find any connection between the distance to the filament and the spin of galaxies using

the MaNGA integral-field survey. However, the distance cuts they use are much smaller than the ones used in this paper: 0.3 Mpc, 1.0 Mpc and 1.8 Mpc. I can explore larger ranges in the study due to MeerKAT's field of view. The mean of $|\cos\psi|$ for all their cuts is in the range $\langle|\cos\psi|\rangle = 0.62$ to $\langle|\cos\psi|\rangle = 0.67$, which is in accordance with the results, since for the closest galaxies to the filaments, the alignment is stronger. A key difference in methodology is that they use 2D angles, which could cause a confusion between filaments and walls, leading to the walls dominating the effect (Welker et al., 2020).

Table 3.4: A comparison between the $\cos\psi$ distributions for different distance cuts using the p-values for the Mann-Whitney U test.

Distribution 1	Distribution 2	p_{MW}
$d < 5$ Mpc	$d > 5$ Mpc	10^{-4}
$d < 5$ Mpc	5 Mpc $< d <$ 10 Mpc	$2 \cdot 10^{-3}$
$d < 10$ Mpc	$d > 10$ Mpc	$3.1 \cdot 10^{-2}$
$d < 10$ Mpc	10 Mpc $< d <$ 20 Mpc	$1.7 \cdot 10^{-2}$
$d < 20$ Mpc	$d > 20$ Mpc	$4.3 \cdot 10^{-1}$

3.4.2 Spin alignment as a function of HI Mass

A better understanding of the HI content of a galaxy is vital in understanding galaxy evolution. As HI extends to larger radii than stars in galaxies, it is more easily perturbed during tidal interactions and hence, more sensitive to external influences (Yun et al., 1994).

In this section, I therefore investigate how $|\cos\psi|$ depends on the HI-mass of the galaxies. In Figure 3.9[3], the relationship between $|\cos\psi|$ as a function of HI mass is shown. The black vertical dotted line marks $M_{\rm HI} = 10^{9.78} M_\odot$, which represents the median of $M_{\rm HI}$ for the sample. This value is close to $10^{9.5} M_\odot$, at which the spin transition was observed in the simulation performed by Kraljic et al. (2020), which overall agrees with the findings, as the lower left corner of Figure 3.9 is less populated compared to the other regions.

[3]I choose not to show the uncertainties on each value of $\cos\psi$ in the remaining figures for clarity, but note that Figure 3.8 does show these estimated uncertainties.

However, I find $\langle|\cos\psi|\rangle = 0.52 \pm 0.04$ for galaxies with $\log_{10}(M_{\rm HI}/M_\odot) < 9.78$, which is consistent with that of the full sample, where $\langle|\cos\psi|\rangle = 0.51 \pm 0.03$. For the sample with a $\log_{10}(M_{\rm HI}/M_\odot) > 9.78$, I find $\langle|\cos\psi|\rangle = 0.50 \pm 0.04$, with the Mann-Whitney U test p-value of 0.4. Therefore, I find no statistical difference in the spin alignment of galaxies with HI mass less than or greater than the median value of $10^{9.78}\,\mathrm{M}_\odot$.

Therefore, similar to the study by Blue Bird et al. (2020), I find no evidence for a spin transition at an HI mass of $\sim 10^{9.5}\,\mathrm{M}_\odot$. Additionally, I performed a correlation test between HI mass and $|\cos\psi|$ to verify the relationship between the parameters. Using Kendall's Tau (Kendall, 1938) and Spearman Rank correlation (Glasser and Winter, 1961), I find no evidence for a correlation: a τ of -0.06 with an associated p-value of 0.5 and a Spearman Rank coefficient of -0.08 with an associated p-value of 0.5.

3.4.3 Spin alignment as a function of other factors

In addition to distance-to-filament and HI mass, I investigate other key properties relating galaxies to their environment: the HI-to-stellar mass ratio and the baryon fraction. I used the ancillary data extracted by the MIGHTEE-HI team for the $ugrizYJHK_s$ photometry. The SED fitting code LEPHARE (Arnouts et al., 1999; Ilbert et al., 2006) was then used to derive the stellar mass. Given that the galaxies already have redshift from the HI, the redshift values are fixed and then LEPHARE was run with the COSMOS SED template (Ilbert et al., 2009), as well as the Bruzual and Charlot (2003) template. For dust, the Calzetti et al. (2000) extinction law was applied with E(B-V) $= 0.0, 0.05, 0.1, 0.2, 0.3$. The uncertainty in stellar mass for each galaxy that was adopted is ~ 0.1 dex (Adams et al., 2021).

HI – stellar mass ratio

The stellar mass of a galaxy has been found to be linked to both the environment and the intrinsic properties of the galaxy - for example, galaxies with a higher stellar mass tend to be in dense environments (e.g. Dressler, 1980; Davis and

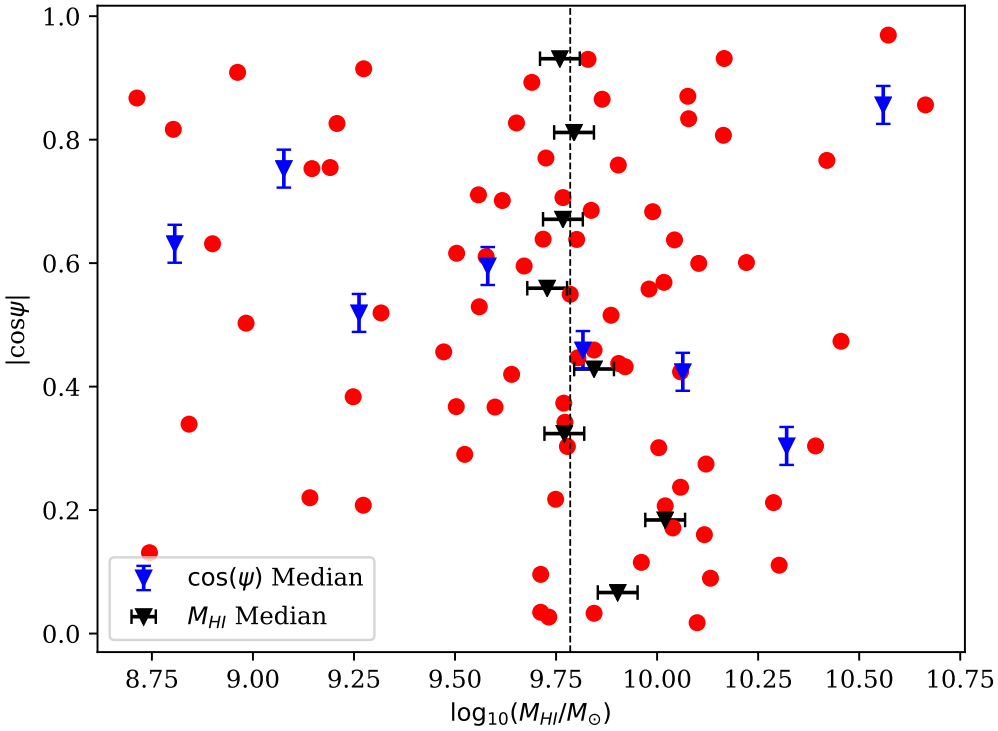

Figure 3.9: $|\cos\psi|$ for the galaxy sample as a function of HI mass computed with mirror boundary conditions. The vertical black dashed line represents the median of the HI mass for the sample. The 77 galaxies were firstly split in 8 bins of $|\cos\psi|$, then they were split in 8 bins of HI mass. The black triangles represent the median of the HI mass for each bin of $|\cos\psi|$ whilst the blue triangles represent the medians of $|\cos\psi|$ for each bin of $M_{\rm H\,I}$.

Geller, 1976; Balogh et al., 2004; Vulcani et al., 2011; Peng et al., 2012; Robotham et al., 2013; Treyer et al., 2018; Davies et al., 2019).

To determine if there is a difference in the behaviour in the alignment of the spin axis of a galaxy to its nearest filament, I split the sample according to its HI-to-stellar mass ratio at the median of the sample ($\log_{10}(M_{\rm HI}/M_\star) = 0.11$). For $\log_{10}(M_{\rm HI}/M_\star) < 0.11$, I find $\langle|\cos\psi|\rangle = 0.58 \pm 0.04$, which is significantly higher than that for the sample with $\log_{10}(M_{\rm HI}/M_\star) > 0.11$, $\langle|\cos\psi|\rangle = 0.44 \pm 0.05$ with a Mann-Whitney U test p-value of 0.012. Figure 3.10 shows the behaviour of the $|\cos\psi|$ as a function of $\log_{10}(M_{\rm HI}/M_\star)$ - where I see a dearth of galaxies at low values of $|\cos\psi|$ for $\log_{10}(M_{\rm HI}/M_\star) < -0.5$. Thus, I find evidence for the spin changing from aligned to mis-aligned for the galaxies below and above the median

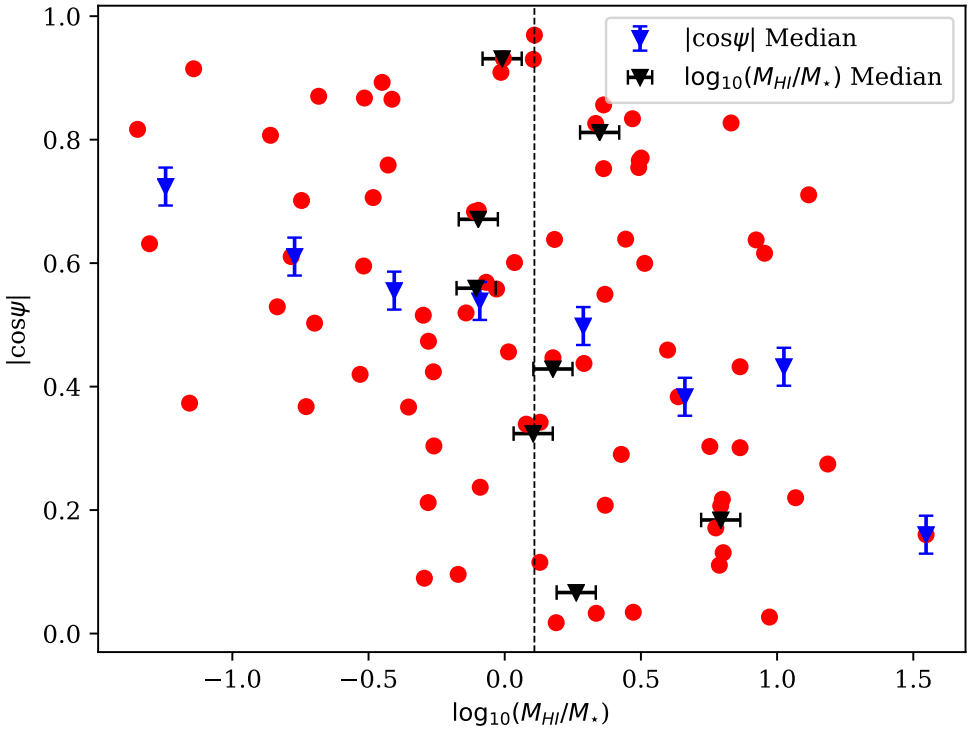

Figure 3.10: $|\cos\psi|$ for the galaxy sample as a function of log HI-to-stellar mass ratio computed with mirror boundary conditions. The 77 galaxies were firstly split in 8 bins of $|\cos\psi|$, then they were split in 8 bins of $M_{\rm HI}/M_\star$. The black triangles represent the medians of log HI-to-stellar mass ratio for each bin whilst the blue triangles represent the medians of $|\cos\psi|$ for each bin. The width of the bins is denoted by the width (height) of the error bars for the blue (black) points.

of the HI-to-stellar mass ratio $\log_{10}(M_{\rm HI}/M_\star) = 0.11$, respectively. Furthermore, the KS test ($p = 7.5 \cdot 10^{-3}$) suggests that for $\log_{10}(M_{\rm HI}/M_\star) < 0.11$, the distribution of $|\cos\psi|$ is not consistent with being drawn from an underlying random galaxy spin alignment distribution.

Both the Kendall Tau and Spearman Rank tests also suggest a correlation between the HI-to-stellar mass ratio and the $|\cos\psi|$: a τ of -0.209 with an associated p-value of 0.007 and a Spearman Rank coefficient of -0.311 with an associated p-value of 0.006.

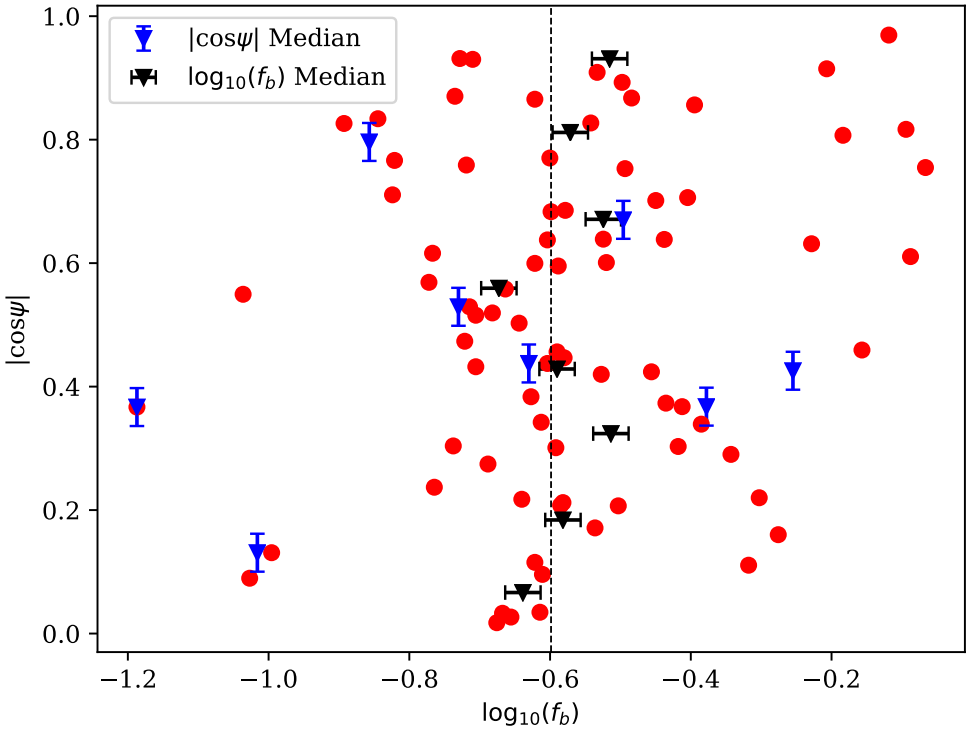

Figure 3.11: $|\cos\psi|$ as a function of the log of the baryon mass fraction $f_b = M_{\rm baryon}/M_{\rm dyn}$. The vertical black dashed line represents the median f_b for the sample. The 77 galaxies were firstly split in 8 bins of $|\cos\psi|$, then they were split in 8 bins of f_b. The black triangles represent the medians of the baryon mass fraction for each bin whilst the blue triangles represent the medians of $|\cos\psi|$ for each bin. The width of the bins is denoted by the width (height) of the error bars for the black (blue) points.

Baryonic mass versus dynamical mass

Finally, I explore the effect of the dark matter, through the dynamical mass and the baryon mass fraction. I calculate the dynamical mass $M_{\rm dyn}$ as:

$$M_{\rm dyn} = \frac{R}{G} V_{\rm rot}^2, \tag{3.9}$$

where $V_{\rm rot}$ is the rotational velocity of the galaxy and R is the radius at which the rotational velocity is measured from the resolved HI rotation curves, which tend to extend much further than the stellar disk into the dark matter halo (see Ponomareva et al., 2021, for details). I then define the baryon mass fraction as $f_b = M_{\rm baryon}/M_{\rm dyn}$, where $M_{\rm baryon} = 1.4 \cdot M_{\rm HI} + M_\star$. The factor of 1.4 is included to

account for the primordial abundance of metals and helium (Arnett, 1999), however it does not include the molecular gas component.

Table 3.5: The mean of the cosine of the angle between the HI spin of the galaxy and its closest filament $\cos\psi$ and comparison parameters: HI Mass $M_{\rm HI}$, HI-to-stellar mass ratio $M_{\rm HI}/M_\star$ and baryon mass fraction f_b.

Parameter	Cut	$\langle\lvert\cos\psi\rvert\rangle$	p_{MW}
$\log_{10}\left(\frac{M_{\rm HI}}{M_\odot}\right)$	< 9.78	0.52 ± 0.04	0.40
	> 9.78	0.50 ± 0.05	
$\log_{10}\left(\frac{M_{\rm HI}}{M_\star}\right)$	< 0.11	0.58 ± 0.04	0.01
	> 0.11	0.44 ± 0.05	
$\log_{10}(f_b)$	< -0.598	0.47 ± 0.05	0.13
	> -0.598	0.55 ± 0.04	

Following the same method as above, I split the galaxy sample at the median of the baryon mass fraction, $\log_{10}(f_b) = -0.6$. Here, the average value of $|\cos\psi|$ tends to be marginally mis-aligned for galaxies with a lower baryon mass fraction: $\langle|\cos\psi|\rangle = 0.47 \pm 0.05$, whilst for the higher baryon mass fraction, it tends towards alignment: $\langle|\cos\psi|\rangle = 0.55 \pm 0.04$. Figure 3.11 shows $|\cos\psi|$ as a function of the baryon mass fraction - it can be seen that for the lower baryon mass fraction there is a spread in $\cos\psi$, whilst for the highest baryon mass fraction ($\log_{10}(f_b) > -0.2$), the galaxies all tend to be aligned. This implies that galaxies with high stellar and/or HI mass tend to retain their alignment with the filament, whilst the galaxies with a higher dark matter fraction are less likely to be aligned with the filaments. However, I find no evidence for a correlation using both the Kendall's Tau $\tau = 0.07$ and the Spearman Rank coefficient (0.11), with associated p-values of 0.38 and 0.36, respectively. Similarly to the $M_{\rm HI}/M_\star$, I notice a spin transition at the median value of the baryon mass fraction $\log_{10}(f_b) = -0.6$, from $\langle|\cos\psi|\rangle = 0.47 \pm 0.05$ to $\langle|\cos\psi|\rangle = 0.55 \pm 0.04$, although the Mann-Whitney U p-value of 0.132 shows that this is not significant given the current sample. Therefore, galaxies with a lower dark matter content are more likely to be aligned, but for the rest of the galaxies the alignment is consistent with being random. This will require more data and future analysis to see if such a trend persists.

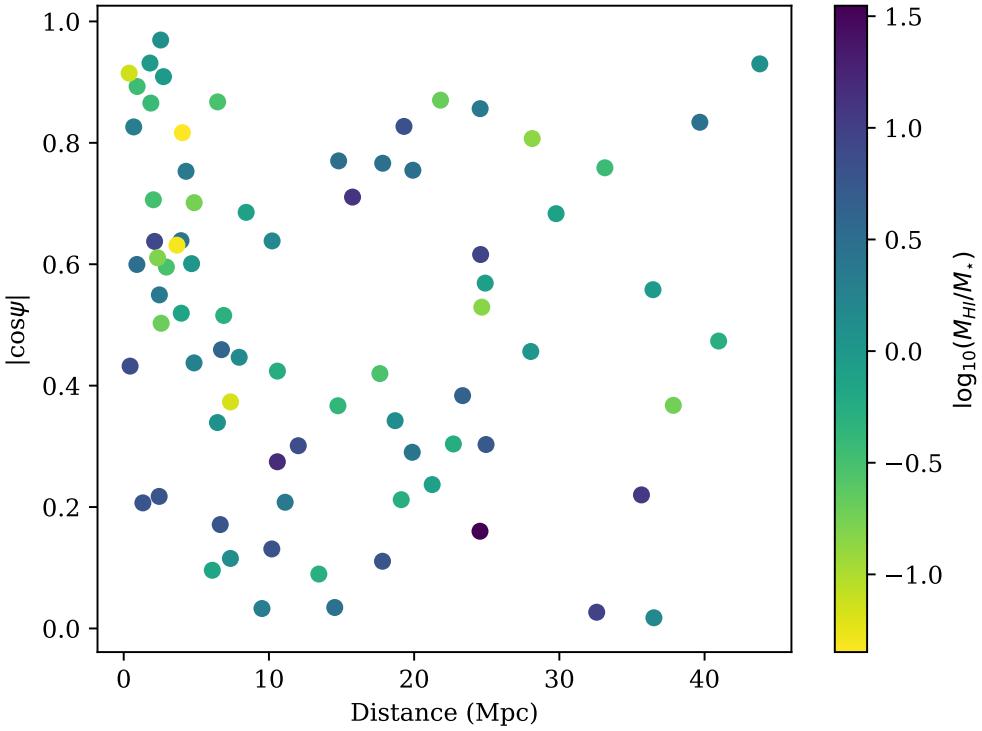

Figure 3.12: $|\cos\psi|$ as a function of distance as presented in Figure 3.7, with the HI-stellar mass ratio $\log_{10}(M_{\rm HI}/M_\star)$ overlaid as a colourmap.

3.4.4 Discussion

Taken together, the results suggest that the stellar mass of a galaxy has a strong influence on the spin of the galaxy in relation to the filaments. In Figure 3.12, I show the $M_{\rm HI}/M_\star$ ratio as a function of the distance from the nearest filament. It shows that those galaxies with the lowest $M_{\rm HI}/M_\star$ ratio, and therefore the highest stellar mass, given that the sample is selected on HI mass, tend to be aligned. The stellar mass being an important influence on the spin would be consistent with several simulations (Dubois et al., 2014; Kraljic et al., 2020), where they find a transition at a stellar mass of $M_\star \sim 10^{10}\,{\rm M}_\odot$, from aligned to mis-aligned. Furthermore, Welker et al. (2020) found a similar spin transition between lower mass and higher mass galaxies using the SAMI survey around $10^{10.4}M_\odot - 10^{10.9}M_\odot$. To understand whether there is a bias, such that galaxies with higher stellar mass tend to be found in denser environments and closer to the filaments, I checked their position with

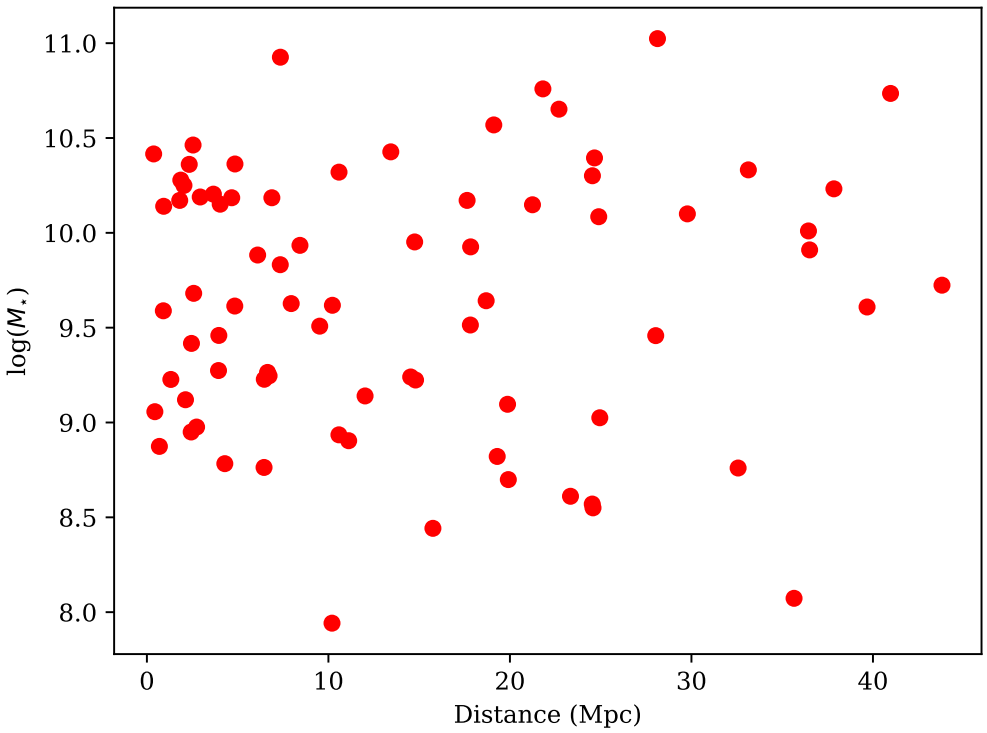

Figure 3.13: The stellar mass for the galaxy sample as a function of distance to the closest filament computed with mirror boundary conditions.

respect to their closest filament. As can be seen in Figure 3.13, the stellar mass of the galaxies is randomly distributed, therefore I find no evidence that this could be the reason for the results on the spin-alignment between galaxies and their closest filaments. Due to the fact that the sample is HI selected, comparisons with other studies selected on stellar mass would be biased and uninformative for this study.

I also investigate whether the dark matter content affects the relation between the spin-axis of the galaxy and the orientation of its nearest filament by determining the baryonic mass fraction. I find that for the highest baryonic mass fractions the galaxies tend to align with the nearest filament. However, I find no evidence for a general trend of alignment with baryonic mass fraction. Both of these reinforce the evidence from the $M_{\rm HI}/M_\star$ ratio, that the stellar mass is a key factor in determining whether a galaxy is aligned with its nearest filament or not.

I also note that some of the trends that I do find could also be linked with the

morphology of the galaxies - as the baryon mass fraction varies depending whether a galaxy is elliptical or spiral. As mentioned before, Kraljic et al. (2021) found a dependence on the shape of the galaxy and its alignment with the filament - S0 type galaxies are more likely to be mis-aligned. Other environmental factors, such as the gas inflows around the filaments or galaxy mergers in the filament regions could also influence the alignment of the spin of the galaxies. Welker et al. (2014) have shown that galaxies that have undergone fewer mergers are more likely to be aligned with the filaments, whilst galaxies that have undergone mergers along the filaments are more likely to have their spins swung to mis-alignment - especially for major mergers. Given that it is more likely for the more massive galaxies to have undergone a merger in the past, the fact that in the HI-selected sample it is those galaxies with a relatively larger stellar mass which tend to be more aligned, appears to be at odds with this finding from simulations. However, it is difficult to interpret the results in this context due to the fact that the sample is HI-selected and dominated by relatively low-stellar mass objects and contains very few objects with masses above the mass where the spin transition appears in observations and simulations (Welker et al., 2020). However, gas-rich mergers are expected to increase the amount of neutral gas in galaxies (Ellison et al., 2018) and this may provide an explanation of the results, where those galaxies which are misaligned do have higher HI mass fractions compared to their stellar mass. Such a merger history may also be apparent in the stellar populations of the galaxies and thus a fruitful future line of enquiry would be to investigate whether the aligned and misaligned populations exhibit different star formation histories, ongoing enhanced star formation or morphological evidence of a merger event happening. I return to this point in Chapter 4.

It is difficult to fully explore this with the current sample due to the limited number of objects, as I do not have the number statistics, or the filament constraints. However, it will be possible as the MIGHTEE survey expands to the full 20 deg^2 area, substantially increasing the sample size I would have to work with. For the $5\,\mathrm{deg}^2$ in the COSMOS + XMM-LSS Early Science data, which is not to full depth and was taken with a coarser channel width than will be done for the rest of the

survey, there are about 50 detections per square degree. For the full MIGHTEE survey, there will be around ~ 1000 detections at $z < 0.1$ (Maddox et al., 2021), as such I will be able to investigate sub-samples of the galaxies in relation to their filaments, binning with respect to morphology, age and also the actual spin and angular momentum of the galaxies within the sample.

Table 3.6: The coefficients and p-values for the two correlation tests, Kendall's Tau and Spearman Rank, for each parameter against the $|\cos\psi|$.

Parameter	**Kendall's Tau**		**Spearman Rank**	
	τ	**p-value**	**coefficient**	**p-value**
Distance	-0.144	0.065	-0.205	0.074
$M_{\rm HI}$	-0.058	0.452	-0.083	0.472
$M_{\rm HI}/M_\star$	-0.209	0.007	-0.311	0.006
f_b	0.069	0.377	0.107	0.355

3.5 Conclusions

In this chapter, I presented a study of the 3D spins of 77 HI galaxies identified with the MIGHTEE-HI survey, and their link to the filaments of the cosmic web. The large-scale filaments are computed using DISPERSE and optical galaxies from the COSMOS and XMM-LSS fields. I took into consideration several parameters that might affect the alignment between the galaxies and the filaments and found that:

- distance-to-filament: galaxies closer ($< 5\,$Mpc) to the spine of the filament tend to be aligned with their nearest filament.
- HI content of galaxy: no spin transition was found using the HI mass of the galaxy for mirror boundary conditions for $\log_{10}(M_{\rm HI}/M_\odot) < 9.78$.
- HI-to-stellar mass ratio of galaxy: I find a preference for alignment for the galaxies with a lower HI-to-stellar mass ratio and overall throughout the sample, as well as a spin transition.

- baryon mass fraction of galaxy: I find those galaxies with the highest baryon mass fraction to exhibit alignment with their nearest filament. However, I find no trend across the range of baryonic mass fraction probed.

Overall, I find the compelling evidence that the neutral gas fraction relative to the stellar mass of a galaxy is clearly related to the alignment of the galaxy spin vector and the nearest filament. Furthermore, galaxies show greater evidence for alignment the closer they are to the filament, suggesting that there is an interplay between the galaxy spin axis and the filament. I suggest that this is due to those galaxies which have undergone a recent gas-rich merger have their spin-orientation disrupted with respect to the filament, whereas those galaxies which have not undergone a recent merger tend to retain their alignment and their evolution is dictated by secular processes. Such a scenario could be investigated further by measuring the star-formation histories of the galaxies as a function of their spin alignment with the filaments, as I discuss in Chapter 4.

She had a MCMC approach to conversations - she went on random tangents.

Casey Cragg

4 Galaxies in the local universe: Star formation histories of HI galaxies

Contents

4.1 Introduction

A fundamental constituent of galaxies is gas, which plays a pivotal role in shaping their dynamics and evolution. Specifically, neutral hydrogen (HI) reservoirs within galaxies act as key players in the stellar birth process, providing the raw material for star formation. These HI-rich regions serve as the birthplaces of new stellar generations, contributing significantly to the overall enrichment of the interstellar medium with heavier elements. The relationship between neutral hydrogen and

stars is fundamental in determining a galaxy's morphology and star formation rates. Galaxies with higher HI content tend to exhibit higher star formation rates, as the abundance of gas fuels the formation of new stars (Saintonge and Catinella, 2022). Furthermore, the HI$-M_\star$ relation shows that more massive galaxies contain more HI, up to a certain mass where the relation experiences a turnover, indicating a saturation point in HI content (Maddox et al., 2015). As such, it is important to investigate how HI links to stellar mass and what processes affect this.

In the previous chapter, I found that the HI-to-stellar mass ratio of a galaxy is related to the spin-filament alignment, such that galaxies which are misaligned have higher HI-to-stellar mass ratios. One possible explanation for this effect is the occurrence of gas-rich mergers in these galaxies, which, in turn, could cause the mis-alignment in the spin-filament angle, whilst increasing the mass of the HI gas in the galaxies. As mergers have been associated with the presence of starbursts in galaxies in both observations (e.g. Lin et al., 2010; Chou et al., 2013; Robotham et al., 2014) and simulations (e.g. Renaud et al., 2014; Moreno et al., 2019; Cenci et al., 2024), one way to investigate this theory is by computing the SFHs of these galaxies and checking for any bursts.

In this chapter, I present an investigation of the star formation histories (SFHs) of 237 (out of 270) galaxies from the MeerKAT International GigaHertz Tiered Extragalactic Exploration (MIGHTEE; Jarvis et al., 2016) Early Science release using multi-wavelength photometry. I use a sub-sample of 66 of these galaxies, where I have accurate kinematics and good photometry, to analyse the link between the spin-filament alignment, the HI content and SFH of the galaxies, as a follow-up from the work presented in Chapter 3.

4.2 Data and Methods

For this work, I use the MIGHTEE-HI survey Early Release data, as described in the Data section of Chapter 3. There are 270 galaxies in the full Early Science HI catalogue. I used the ancillary data extracted by the MIGHTEE-HI team for the $ugrizYJHK_s$ photometry as detailed in (Maddox et al., 2021). Furthermore, I

crossmatched these galaxies with the Herschel Extragalactic Legacy Project Shirley et al. (HELP; 2019) in order to obtain mid-to-far infrared data. As a consequence of the lack of full photometry for some of the galaxies, and because I am restricted to the $0.02 < z < 0.09$ redshift interval for the filaments, the sample was reduced to 237 galaxies. Within this sample, I retained 66 out of the 77 the galaxies used in Tudorache et al. (2022) to study the spin-filament alignment of the galaxies with the filaments of the cosmic web, due to the same reason (lack of photometry in some bands) as for the full sample.

4.2.1 SED fitting of galaxies

There are several different algorithms that can perform SED fitting in order to obtain information from photometry. Known as template fitting, it involves fitting observed photometric data with theoretical templates or model spectra. The fitting can be done in several ways, by using prior knowledge about the expected properties of the galaxy, such as stellar population models and dust attenuation, to derive probability distributions for the physical parameters. SED fitting techniques have been used to extract valuable information about the age, composition, and physical conditions of galaxies based on their observed photometric data (Bolzonella et al., 2000; Ilbert et al., 2006; Walcher et al., 2011).

BAGPIPES[1] (Carnall et al., 2018) is a PYTHON tool that uses Bayesian inference to fit SEDs to galaxies and provide redshifts and galaxy properties from spectroscopic and/or photometric data from the ultraviolet to the microwave regime. Specifically, it is an algorithm that uses a nested sampling approach with MULTINEST (Feroz and Hobson, 2008; Feroz et al., 2009) to fit parameters in a model galaxy spectrum. To describe a model galaxy spectrum, BAGPIPES uses a luminosity per unit rest-frame wavelength $L_\lambda(\lambda)$ given at a specific redshift z, which is built from four components. These four components are simple stellar population model (SSP), the star formation history (SFR(t), which is obtained by summing over SFH components), the transmission function of the ionised ISM (which accounts for

[1] http://bagpipes.readthedocs.io

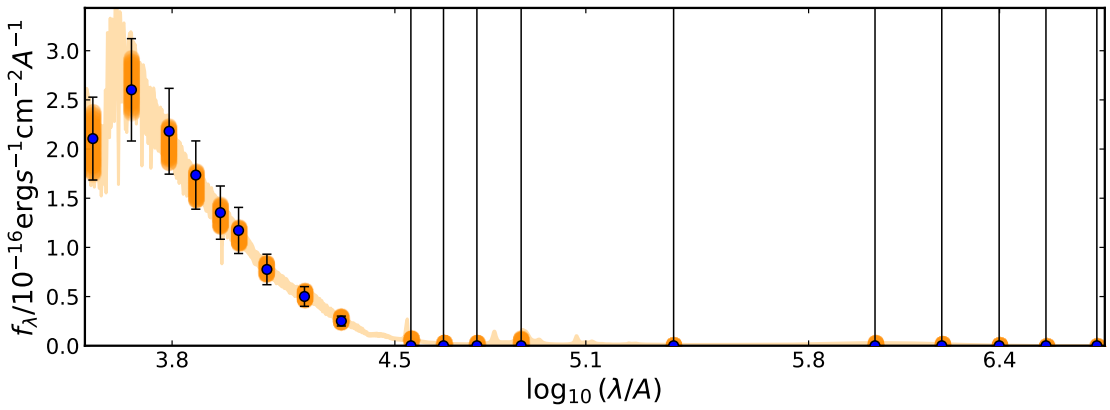

Figure 4.1: An example of the photometric output of one of the MIGHTEE-HI Early Science galaxies using the available photometric filters.

emission/absorption lines) and the transmission function of the neutral ISM (which accounts for dust attenuation and emission). The SSPs are pre-defined, and are a function of wavelength λ, the age of the stellar population, the metallicity of the stellar population and an initial stellar mass function (here, the Kroupa, 2001 IMF is used). For the SFHs, BAGPIPES provides a framework for computing both parametric and non-parametric SFHs, such as delta functions, constant, exponentially declining, delayed exponentially declining, log-normal, double-power law or any custom input (see Carnall et al., 2018 for all the functional forms). Hence, the luminosity will be a sum of these components over several age bins. The luminosity can then be converted into a flux, which is then used to fit the photometry fluxes of a galaxy.

For the sample of galaxies used here, given that I already have spectroscopic redshifts from HI measurements, I fix the redshift values and run BAGPIPES with the Bruzual and Charlot (2003) stellar population model. For dust, I apply the Calzetti et al. (2000) extinction law with priors on E(B-V) $= (0.0, 2.0)$. Similarly, I keep the priors for all other properties as uniform. A summary of the priors used can be seen in Table 4.1.

In the Bayesian inference framework, the statistical distribution of a set of parameters, $\boldsymbol{\theta}$, given some data, $\boldsymbol{d}$, is given by Bayes theorem:

$$\mathcal{P}(\boldsymbol{\theta}|\boldsymbol{d},\mathcal{M}) = \frac{\mathcal{L}(\boldsymbol{d}|\boldsymbol{\theta},\mathcal{M})\Pi(\boldsymbol{\theta}|\mathcal{M})}{\mathcal{Z}(\boldsymbol{d}|\mathcal{M})} \tag{4.1}$$

Table 4.1: A description of each of the parameters used for each SFH model, as well as the priors used to fit the SFH models.

Model	Parameter	Prior distribution
Exponential	Age	uniform $\in [0.1, 15.0]$
	τ	uniform $\in [0.3, 10.0]$
	$\log M_*$	uniform $\in [1.0, 15.0]$
	$\log Z$	uniform $\in [0.0, 2.5]$
Constant	Age_{min}	uniform $\in [0.1, 15.0]$
	Age_{max}	uniform $\in [0.1, 15.0]$
	τ	uniform $\in [0.3, 10.0]$
	$\log M_*$	uniform $\in [1.0, 15.0]$
	$\log Z$	uniform $\in [0.0, 2.5]$
Lognormal	t_{max}	uniform $\in [0.1, 15]$
	FWHM	uniform $\in [0.3, 10.0]$
	$\log M_*$	uniform $\in [1.0, 15.0]$
	$\log Z$	uniform $\in [0.0, 2.5]$
Delayed	Age	uniform $\in [0.1, 15.0]$
	τ	uniform $\in [0.3, 10.0]$
	$\log M_*$	uniform $\in [1.0, 15.0]$
	$\log Z$	uniform $\in [0.0, 2.5]$
Double-power law	α	uniform $\in [0.1, 1000]$
	β	uniform $\in [0.1, 1000]$
	τ	uniform $\in [0.3, 10.0]$
	$\log M_*$	uniform $\in [1.0, 15.0]$
	$\log Z$	uniform $\in [0.0, 2.5]$
Burst	Age	uniform $\in [0.1, 15.0]$
	τ	uniform $\in [0.3, 10.0]$
	$\log M_*$	uniform $\in [1.0, 15.0]$
	$\log Z$	uniform $\in [0.0, 2.5]$

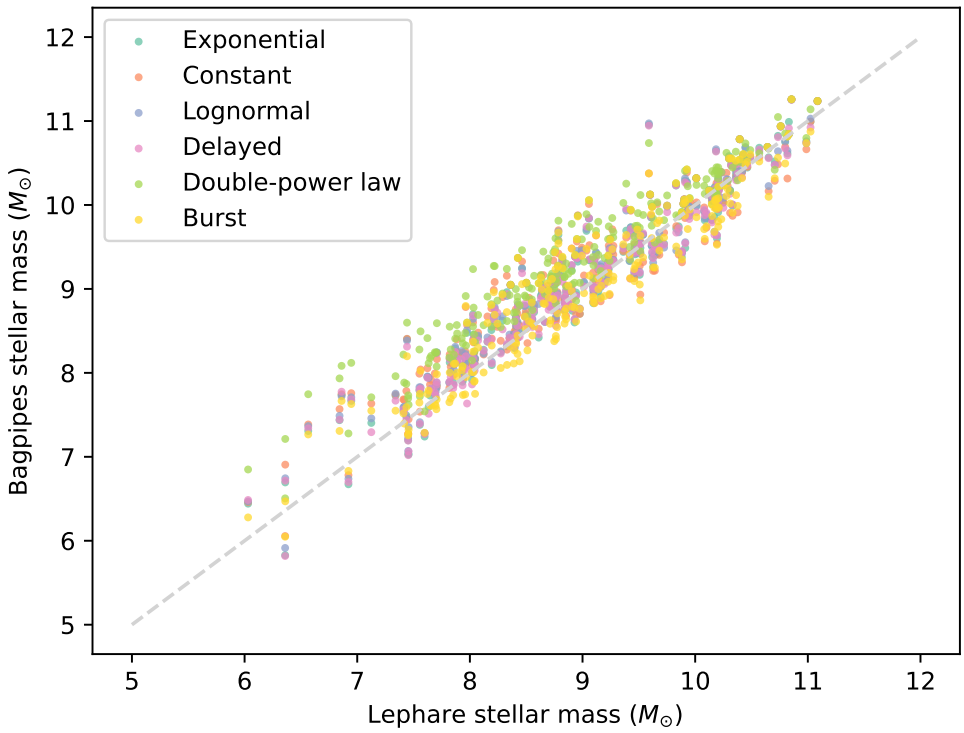

Figure 4.2: A scatter plot illustrating the stellar mass obtained from LePhare (see text) compared to the stellar masses from six different SFH models from Bagpipes.

where $\mathcal{P}(\boldsymbol{\theta}|\boldsymbol{d},\mathcal{M})$ is the posterior probability, $\mathcal{L}(\boldsymbol{d}|\boldsymbol{\theta},\mathcal{M})$ is the likelihood, $\Pi(\boldsymbol{\theta}|\mathcal{M})$ represents the priors and $\mathcal{Z}(\boldsymbol{d}|\mathcal{M})$ is the evidence. As Bagpipes uses a Bayesian inference approach to compute the SFHs and the stellar masses, I can also compute the log of the evidence ($\log \mathcal{Z}(\boldsymbol{d}|\mathcal{M}_i)$) for each model i and for each galaxy. I can then use the Bayes' factor and the Jeffrey scale to also verify which model fits each galaxy better. The Bayes' factor is defined as:

$$\log_{10} B_{01} = \log_{10} \mathcal{Z}(\boldsymbol{d}|\mathcal{M}_0) - \log_{10} \mathcal{Z}(\boldsymbol{d}|\mathcal{M}_1), \tag{4.2}$$

where $\mathcal{M}_0$ and $\mathcal{M}_1$ are two of the models I am comparing. I take $\log_{10} B_{01} < 1$ as "not significant", $1 < \log_{10} B_{01} < 2.5$ as "significant", $2.5 < \log_{10} B_{01} < 5$ as "strong", and $\log_{10} B_{01} > 5$ as "decisive" (Jeffreys, 1998).

4.3 Results

4.3.1 Galaxy SED models comparisons

As described in Section 4.2.1, BAGPIPES provides several models which can be fit to a galaxy in order to infer its SFH. I choose to use six of them for the galaxy sample: the exponential SFH, the constant SFH, the log-normal SFH, the delayed SFH, the double-power law SFH and the burst SFH.

The MIGHTEE-HI full Early Science release catalogue ancillary data also provides stellar masses. The SED fitting code LEPHARE (Arnouts et al., 1999; Ilbert et al., 2006) was used to derive the stellar mass. The uncertainty in stellar mass for each galaxy that I adopted in Chapter 3 was ~ 0.1 dex (Adams et al., 2021). I use these stellar masses in order to compare with the different stellar masses obtained with the six BAGPIPES models. This can be seen in Figure 4.2. I also fit a line through each of the points in each model and compare their R-squared statistic, which can be seen in Table 4.2. I also calculated the scatter $\sigma = |M_*(\text{Bagpipes}) - M_*(\text{LePhare})|$ between the stellar masses from the BAGPIPES models and the LEPHARE stellar masses and found that the lowest average scatter is found in the exponentially-delayed model ($\sigma = 0.21$), whilst the highest is found in the double-power law model ($\sigma = 0.39$).

Table 4.2: A table of the R-squared linear fit obtained by comparing the stellar masses obtained by LEPHARE and the stellar masses obtained by BAGPIPES for each SFH.

Model	R-squared
Exponential	0.927
Constant	0.902
Lognormal	0.927
Delayed	0.929
Double-power law	0.925
Burst	0.898

Another approach to compare between the models is by using the Bayesian framework described in Section 4.2.1. I calculate the Bayes' factor for each galaxy

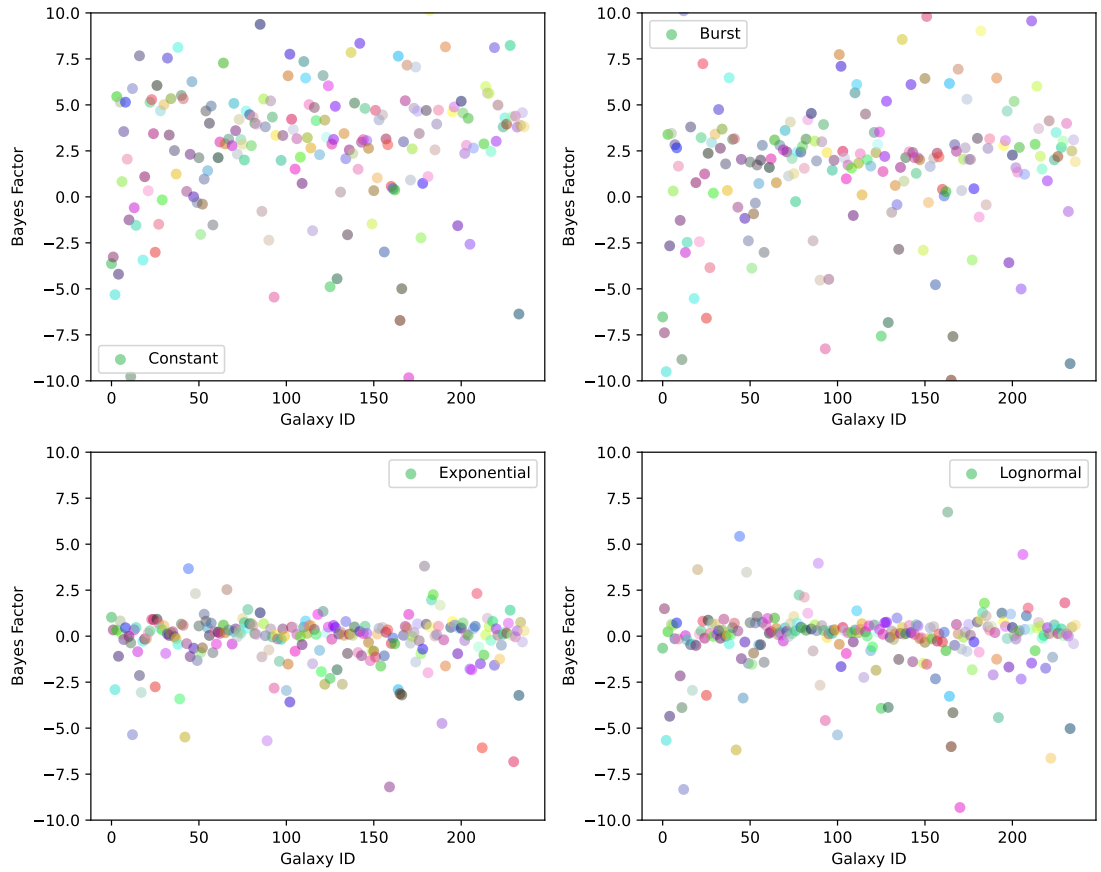

Figure 4.3: A scatter plot of the Bayes' factor calculated for all 237 galaxies in the sample for the exponentially-delayed SFH model compared with the constant SFH (*top left*), burst SFH (*top right*), exponential SFH (*bottom left*) and lognormal SFH (*bottom right*). I use different colours for each galaxy (keeping them the same across models) in order to check if anomalous galaxies (i.e. $\log_{10} B_{01}$ is orders of magnitude higher/lower than in the rest of the sample) are the same across each model.

and for each model in pairs of two and proceed to draw a comparison between all of them. When comparing the SFH models between each other for each galaxy, I find that BAGPIPES cannot differentiate between the exponential SFH, the lognormal SFH and the exponentially-delayed SFH model. This is illustrated in Figure 4.3, where I show the Bayes' factor for each galaxy in the sample, with respect to the exponentially-delayed SFH model. As can be seen, for the comparison with the exponential SFH and the lognormal SFH, the points are clustering around 0.0, whilst for the constant SFH and the burst SFH the points are scattered around (not shown in the figure is the double-power law SFH model, which shows the same behaviour). As the data is not good enough for me to be able to differentiate

between the models, for the rest of the discussion I will only show the full results for the exponentially-delayed SFH model for the sake of clarity. However, I will show medians for the other SFH models in order to verify if they show the same statistical trends when it comes to the analysis.

In Table 4.3, I show the main parameters (stellar mass, SFR, sSFR, peak time of star formation and dust absorption) computed by BAGPIPES for all 237 galaxies using the exponentially-delayed SFH model. I will refer to the values in this table for most of the analysis in the following sections. Figure 4.4 shows the 1D posteriors of all the parameters of a galaxy fitted with the exponentially-delayed SFH model, as well as the galaxy properties I am interested in. Figure 4.5 shows an example of the corner plot of another galaxy fitted with the same model.

Table 4.3: Fitted parameters for the exponentially-delayed model on the MIGHTEE-HI galaxies. The rows in bold represent the galaxies where I could also compute the spin-filament alignment from Chapter 3.

ID	$\log_{10}(\frac{M_\star}{M_\odot})$	$\log_{10}$SFR $[M_\odot/\mathrm{yr}]$	$\log_{10}$sSFR [1/yr]	t_{form} [Gyr]	A_V [mag]
0	$5.82^{+0.09}_{-0.06}$	$0.0^{+0.0}_{-0.0}$	$-8.96^{+0.14}_{-0.19}$	$12.49^{+0.25}_{-0.52}$	$0.0^{+0.0}_{-0.0}$
1	$7.02^{+0.05}_{-0.04}$	$0.01^{+0.0}_{-0.0}$	$-8.9^{+0.08}_{-0.1}$	$12.59^{+0.15}_{-0.21}$	$0.03^{+0.0}_{-0.0}$
2	$6.7^{+0.05}_{-0.04}$	$0.0^{+0.0}_{-0.0}$	$-9.05^{+0.09}_{-0.1}$	$12.31^{+0.19}_{-0.28}$	$0.01^{+0.0}_{-0.0}$
3	$6.49^{+0.12}_{-0.19}$	$0.0^{+0.0}_{-0.0}$	$-9.37^{+0.47}_{-0.23}$	$11.17^{+1.46}_{-1.43}$	$0.35^{+0.4}_{-0.22}$
4	$7.06^{+0.06}_{-0.06}$	$0.01^{+0.0}_{-0.0}$	$-9.04^{+0.07}_{-0.1}$	$12.31^{+0.18}_{-0.28}$	$0.0^{+0.0}_{-0.0}$
5	$7.44^{+0.18}_{-0.17}$	$0.02^{+0.02}_{-0.01}$	$-9.15^{+0.42}_{-0.35}$	$11.95^{+0.84}_{-1.55}$	$0.24^{+0.27}_{-0.16}$
6	$7.39^{+0.04}_{-0.05}$	$0.01^{+0.0}_{-0.0}$	$-9.37^{+0.1}_{-0.1}$	$11.15^{+0.45}_{-0.59}$	$0.01^{+0.0}_{-0.0}$
7	$8.56^{+0.11}_{-0.18}$	$0.1^{+0.09}_{-0.05}$	$-9.56^{+0.46}_{-0.34}$	$10.04^{+1.93}_{-2.09}$	$0.89^{+0.44}_{-0.41}$
8	$7.77^{+0.18}_{-0.15}$	$0.04^{+0.03}_{-0.01}$	$-9.13^{+0.39}_{-0.33}$	$11.83^{+0.79}_{-1.47}$	$0.23^{+0.3}_{-0.16}$
9	$7.44^{+0.12}_{-0.11}$	$0.01^{+0.0}_{-0.0}$	$-9.36^{+0.22}_{-0.23}$	$10.86^{+0.9}_{-1.49}$	$0.0^{+0.0}_{-0.0}$
10	$\mathbf{7.85^{+0.1}_{-0.2}}$	$\mathbf{0.01^{+0.0}_{-0.0}}$	$\mathbf{-9.69^{+0.31}_{-0.16}}$	$\mathbf{8.96^{+1.7}_{-1.32}}$	$\mathbf{0.01^{+0.01}_{-0.01}}$
11	$7.51^{+0.14}_{-0.11}$	$0.04^{+0.01}_{-0.01}$	$-8.9^{+0.19}_{-0.19}$	$12.4^{+0.25}_{-0.31}$	$0.01^{+0.0}_{-0.0}$
12	$9.27^{+0.04}_{-0.03}$	$0.08^{+0.01}_{-0.01}$	$-10.39^{+0.07}_{-0.08}$	$6.77^{+0.58}_{-0.99}$	$0.09^{+0.01}_{-0.01}$
13	$7.19^{+0.11}_{-0.11}$	$0.01^{+0.0}_{-0.0}$	$-9.14^{+0.17}_{-0.18}$	$11.77^{+0.44}_{-0.74}$	$0.0^{+0.0}_{-0.0}$
14	$7.27^{+0.04}_{-0.05}$	$0.01^{+0.0}_{-0.0}$	$-9.17^{+0.13}_{-0.13}$	$11.49^{+0.37}_{-0.54}$	$0.0^{+0.0}_{-0.0}$
15	$8.46^{+0.08}_{-0.04}$	$0.19^{+0.02}_{-0.03}$	$-9.18^{+0.09}_{-0.16}$	$11.57^{+0.29}_{-0.66}$	$0.05^{+0.01}_{-0.01}$

Continued on next page

Table 4.3: Fitted parameters for the exponentially-delayed model on the MIGHTEE-HI galaxies. The rows in bold represent the galaxies where I could also compute the spin-filament alignment from Chapter 3. (Continued)

ID	$\log_{10}(\frac{M_\star}{M_\odot})$	$\log_{10}$SFR $[M_\odot/\mathrm{yr}]$	$\log_{10}$sSFR [1/yr]	t_{form} [Gyr]	A_V [mag]
16	$7.82^{+0.06}_{-0.05}$	$0.06^{+0.01}_{-0.01}$	$-9.02^{+0.11}_{-0.12}$	$12.06^{+0.21}_{-0.35}$	$0.07^{+0.01}_{-0.01}$
17	$9.46^{+0.03}_{-0.03}$	$0.11^{+0.02}_{-0.02}$	$-10.41^{+0.1}_{-0.12}$	$5.4^{+0.48}_{-0.39}$	$1.13^{+0.38}_{-0.26}$
18	$8.11^{+0.08}_{-0.08}$	$0.08^{+0.01}_{-0.01}$	$-9.24^{+0.15}_{-0.15}$	$11.29^{+0.51}_{-0.71}$	$0.01^{+0.0}_{-0.0}$
19	$10.33^{+0.11}_{-0.15}$	$4.4^{+3.39}_{-2.95}$	$-9.69^{+0.38}_{-0.57}$	$8.86^{+2.07}_{-1.67}$	$0.95^{+0.41}_{-0.54}$
20	$9.58^{+0.03}_{-0.04}$	$0.85^{+0.1}_{-0.06}$	$-9.65^{+0.09}_{-0.07}$	$8.56^{+0.65}_{-0.7}$	$0.11^{+0.01}_{-0.01}$
21	$8.64^{+0.06}_{-0.06}$	$0.25^{+0.03}_{-0.04}$	$-9.24^{+0.11}_{-0.12}$	$11.17^{+0.4}_{-0.59}$	$0.07^{+0.01}_{-0.01}$
22	$8.97^{+0.14}_{-0.15}$	$0.46^{+0.34}_{-0.14}$	$-9.3^{+0.36}_{-0.31}$	$10.71^{+1.13}_{-1.73}$	$0.32^{+0.37}_{-0.23}$
23	$\mathbf{9.21^{+0.06}_{-0.06}}$	$\mathbf{0.59^{+0.1}_{-0.07}}$	$\mathbf{-9.44^{+0.13}_{-0.11}}$	$\mathbf{9.95^{+0.68}_{-0.78}}$	$\mathbf{0.08^{+0.01}_{-0.01}}$
24	$8.85^{+0.06}_{-0.06}$	$0.43^{+0.06}_{-0.06}$	$-9.22^{+0.12}_{-0.12}$	$10.97^{+0.42}_{-0.53}$	$0.08^{+0.01}_{-0.01}$
25	$9.33^{+0.03}_{-0.03}$	$0.12^{+0.02}_{-0.02}$	$-10.26^{+0.11}_{-0.11}$	$5.66^{+0.54}_{-0.43}$	$0.68^{+0.18}_{-0.16}$
26	$7.73^{+0.18}_{-0.13}$	$0.07^{+0.03}_{-0.02}$	$-8.89^{+0.26}_{-0.33}$	$11.89^{+0.36}_{-0.95}$	$0.17^{+0.22}_{-0.13}$
27	$8.77^{+0.06}_{-0.06}$	$0.35^{+0.05}_{-0.05}$	$-9.23^{+0.12}_{-0.12}$	$11.0^{+0.41}_{-0.58}$	$0.0^{+0.0}_{-0.0}$
28	$8.84^{+0.13}_{-0.16}$	$0.27^{+0.18}_{-0.08}$	$-9.41^{+0.37}_{-0.26}$	$10.15^{+1.39}_{-1.76}$	$0.32^{+0.32}_{-0.21}$
29	$8.82^{+0.06}_{-0.06}$	$0.3^{+0.05}_{-0.04}$	$-9.35^{+0.12}_{-0.13}$	$10.46^{+0.55}_{-0.7}$	$0.03^{+0.01}_{-0.0}$
30	$\mathbf{10.16^{+0.13}_{-0.15}}$	$\mathbf{5.72^{+4.19}_{-1.83}}$	$\mathbf{-9.43^{+0.4}_{-0.25}}$	$\mathbf{10.23^{+1.41}_{-1.68}}$	$\mathbf{0.4^{+0.38}_{-0.25}}$
31	$8.72^{+0.06}_{-0.06}$	$0.2^{+0.03}_{-0.03}$	$-9.42^{+0.12}_{-0.11}$	$9.79^{+0.65}_{-0.86}$	$0.18^{+0.04}_{-0.03}$
32	$8.76^{+0.06}_{-0.06}$	$0.37^{+0.05}_{-0.04}$	$-9.19^{+0.12}_{-0.11}$	$10.87^{+0.35}_{-0.47}$	$0.08^{+0.01}_{-0.01}$
33	$\mathbf{10.29^{+0.1}_{-0.18}}$	$\mathbf{6.06^{+5.42}_{-2.11}}$	$\mathbf{-9.52^{+0.47}_{-0.24}}$	$\mathbf{9.31^{+2.03}_{-1.75}}$	$\mathbf{0.8^{+0.38}_{-0.3}}$
34	$9.91^{+0.14}_{-0.16}$	$3.48^{+3.12}_{-1.1}$	$-9.38^{+0.43}_{-0.29}$	$10.23^{+1.43}_{-1.75}$	$0.41^{+0.41}_{-0.26}$
35	$\mathbf{9.1^{+0.05}_{-0.05}}$	$\mathbf{0.35^{+0.05}_{-0.04}}$	$\mathbf{-9.55^{+0.11}_{-0.1}}$	$\mathbf{8.89^{+0.73}_{-0.84}}$	$\mathbf{0.36^{+0.07}_{-0.06}}$
36	$10.67^{+0.1}_{-0.17}$	$13.38^{+10.07}_{-5.22}$	$-9.54^{+0.39}_{-0.29}$	$9.2^{+1.89}_{-1.65}$	$0.71^{+0.37}_{-0.32}$
37	$9.37^{+0.04}_{-0.05}$	$0.5^{+0.06}_{-0.05}$	$-9.67^{+0.1}_{-0.07}$	$8.31^{+0.9}_{-0.71}$	$0.07^{+0.01}_{-0.01}$
38	$9.66^{+0.04}_{-0.06}$	$0.77^{+0.08}_{-0.06}$	$-9.76^{+0.06}_{-0.07}$	$7.91^{+1.24}_{-0.82}$	$0.37^{+0.04}_{-0.04}$
39	$9.97^{+0.02}_{-0.02}$	$4.75^{+0.18}_{-0.19}$	$-9.29^{+0.04}_{-0.04}$	$10.48^{+0.18}_{-0.15}$	$0.11^{+0.0}_{-0.0}$
40	$9.51^{+0.16}_{-0.13}$	$2.02^{+1.13}_{-0.59}$	$-9.2^{+0.29}_{-0.3}$	$10.87^{+0.77}_{-1.41}$	$0.23^{+0.26}_{-0.16}$
41	$9.95^{+0.13}_{-0.17}$	$3.23^{+2.98}_{-0.83}$	$-9.44^{+0.43}_{-0.24}$	$9.89^{+1.55}_{-1.87}$	$0.34^{+0.4}_{-0.22}$
42	$9.63^{+0.01}_{-0.01}$	$0.2^{+0.02}_{-0.01}$	$-10.34^{+0.05}_{-0.03}$	$5.17^{+0.3}_{-0.2}$	$1.81^{+0.14}_{-0.22}$
43	$8.62^{+0.07}_{-0.07}$	$0.29^{+0.05}_{-0.05}$	$-9.15^{+0.13}_{-0.14}$	$11.08^{+0.37}_{-0.53}$	$0.02^{+0.0}_{-0.0}$
44	$\mathbf{9.96^{+0.03}_{-0.03}}$	$\mathbf{2.7^{+0.15}_{-0.15}}$	$\mathbf{-9.52^{+0.05}_{-0.05}}$	$\mathbf{9.01^{+0.32}_{-0.43}}$	$\mathbf{0.47^{+0.04}_{-0.04}}$

Continued on next page

Table 4.3: Fitted parameters for the exponentially-delayed model on the MIGHTEE-HI galaxies. The rows in bold represent the galaxies where I could also compute the spin-filament alignment from Chapter 3. (Continued)

ID	$\log_{10}(\frac{M_\star}{M_\odot})$	$\log_{10}$SFR $[M_\odot/\mathrm{yr}]$	$\log_{10}$sSFR [1/yr]	t_{form} [Gyr]	A_V [mag]
45	$9.25^{+0.05}_{-0.05}$	$0.23^{+0.04}_{-0.04}$	$-9.89^{+0.09}_{-0.12}$	$7.59^{+1.13}_{-0.87}$	$0.09^{+0.02}_{-0.01}$
46	$10.48^{+0.05}_{-0.02}$	$0.68^{+0.09}_{-0.08}$	$-10.65^{+0.05}_{-0.07}$	$7.26^{+0.28}_{-1.5}$	$0.36^{+0.03}_{-0.03}$
47	$8.18^{+0.18}_{-0.1}$	$0.08^{+0.02}_{-0.02}$	$-9.26^{+0.18}_{-0.29}$	$10.73^{+0.61}_{-1.2}$	$0.01^{+0.01}_{-0.01}$
48	$10.04^{+0.02}_{-0.02}$	$2.77^{+0.12}_{-0.14}$	$-9.6^{+0.04}_{-0.05}$	$8.6^{+0.35}_{-0.38}$	$0.49^{+0.04}_{-0.03}$
49	$8.92^{+0.06}_{-0.07}$	$0.06^{+0.01}_{-0.01}$	$-10.14^{+0.11}_{-0.13}$	$6.88^{+1.58}_{-1.03}$	$0.01^{+0.01}_{-0.01}$
50	$7.29^{+0.14}_{-0.28}$	$0.01^{+0.0}_{-0.0}$	$-9.53^{+0.47}_{-0.26}$	$9.89^{+2.27}_{-1.85}$	$0.0^{+0.0}_{-0.0}$
51	$9.06^{+0.01}_{-0.02}$	$0.0^{+0.0}_{-0.0}$	$-18.64^{+3.79}_{-3.82}$	$1.55^{+0.66}_{-0.5}$	$0.06^{+0.0}_{-0.01}$
52	$9.91^{+0.13}_{-0.14}$	$1.33^{+1.12}_{-1.02}$	$-9.76^{+0.33}_{-0.75}$	$8.75^{+1.99}_{-2.16}$	$0.67^{+0.4}_{-0.37}$
53	$7.63^{+0.06}_{-0.07}$	$0.13^{+0.02}_{-0.02}$	$-8.51^{+0.1}_{-0.12}$	$12.94^{+0.06}_{-0.11}$	$0.01^{+0.0}_{-0.0}$
54	$\mathbf{6.72^{+0.23}_{-0.17}}$	$\mathbf{0.0^{+0.0}_{-0.0}}$	$\mathbf{-9.19^{+0.31}_{-0.35}}$	$\mathbf{11.53^{+0.83}_{-1.8}}$	$\mathbf{0.01^{+0.02}_{-0.01}}$
55	$\mathbf{8.89^{+0.07}_{-0.11}}$	$\mathbf{0.17^{+0.04}_{-0.03}}$	$\mathbf{-9.64^{+0.18}_{-0.15}}$	$\mathbf{8.86^{+1.37}_{-1.14}}$	$\mathbf{0.03^{+0.01}_{-0.0}}$
56	$8.06^{+0.15}_{-0.17}$	$0.04^{+0.01}_{-0.01}$	$-9.48^{+0.28}_{-0.25}$	$10.11^{+1.43}_{-1.86}$	$0.05^{+0.01}_{-0.01}$
57	$\mathbf{8.42^{+0.16}_{-0.17}}$	$\mathbf{0.15^{+0.09}_{-0.05}}$	$\mathbf{-9.24^{+0.35}_{-0.3}}$	$\mathbf{11.42^{+0.97}_{-1.7}}$	$\mathbf{0.21^{+0.3}_{-0.15}}$
58	$\mathbf{9.34^{+0.05}_{-0.08}}$	$\mathbf{0.0^{+0.02}_{-0.0}}$	$\mathbf{-12.59^{+1.73}_{-4.67}}$	$\mathbf{3.84^{+1.6}_{-1.66}}$	$\mathbf{0.04^{+0.02}_{-0.02}}$
59	$\mathbf{9.0^{+0.05}_{-0.06}}$	$\mathbf{0.23^{+0.03}_{-0.03}}$	$\mathbf{-9.63^{+0.12}_{-0.09}}$	$\mathbf{9.0^{+0.98}_{-0.86}}$	$\mathbf{0.1^{+0.01}_{-0.01}}$
60	$9.89^{+0.05}_{-0.06}$	$1.33^{+0.21}_{-0.23}$	$-9.76^{+0.12}_{-0.13}$	$7.96^{+0.9}_{-0.61}$	$0.08^{+0.01}_{-0.01}$
61	$8.31^{+0.1}_{-0.11}$	$0.06^{+0.02}_{-0.01}$	$-9.52^{+0.2}_{-0.18}$	$9.86^{+1.23}_{-1.46}$	$0.02^{+0.01}_{-0.01}$
62	$7.89^{+0.09}_{-0.12}$	$0.02^{+0.0}_{-0.0}$	$-9.59^{+0.21}_{-0.16}$	$9.42^{+1.39}_{-1.23}$	$0.0^{+0.0}_{-0.0}$
63	$9.49^{+0.01}_{-0.01}$	$2.0^{+0.04}_{-0.03}$	$-9.19^{+0.02}_{-0.01}$	$11.84^{+0.06}_{-0.04}$	$1.23^{+0.06}_{-0.08}$
64	$7.56^{+0.14}_{-0.15}$	$0.08^{+0.03}_{-0.02}$	$-8.69^{+0.29}_{-0.25}$	$12.43^{+0.24}_{-0.4}$	$0.15^{+0.19}_{-0.1}$
65	$7.78^{+0.15}_{-0.13}$	$0.03^{+0.01}_{-0.01}$	$-9.28^{+0.22}_{-0.27}$	$11.0^{+0.78}_{-1.52}$	$0.02^{+0.01}_{-0.01}$
66	$9.67^{+0.08}_{-0.1}$	$2.02^{+0.47}_{-0.33}$	$-9.36^{+0.18}_{-0.16}$	$10.53^{+0.82}_{-0.83}$	$0.11^{+0.02}_{-0.02}$
67	$\mathbf{8.92^{+0.08}_{-0.09}}$	$\mathbf{0.22^{+0.04}_{-0.04}}$	$\mathbf{-9.57^{+0.15}_{-0.16}}$	$\mathbf{9.31^{+1.17}_{-1.19}}$	$\mathbf{0.03^{+0.01}_{-0.0}}$
68	$9.65^{+0.02}_{-0.02}$	$5.72^{+0.31}_{-0.37}$	$-8.89^{+0.04}_{-0.05}$	$12.13^{+0.07}_{-0.1}$	$0.1^{+0.01}_{-0.01}$
69	$8.91^{+0.06}_{-0.08}$	$0.15^{+0.03}_{-0.03}$	$-9.74^{+0.15}_{-0.16}$	$8.28^{+1.23}_{-0.9}$	$0.02^{+0.01}_{-0.01}$
70	$10.29^{+0.15}_{-0.18}$	$7.43^{+6.22}_{-2.28}$	$-9.44^{+0.44}_{-0.27}$	$10.38^{+1.54}_{-1.96}$	$0.4^{+0.37}_{-0.26}$
71	$9.33^{+0.14}_{-0.16}$	$0.88^{+0.63}_{-0.29}$	$-9.38^{+0.38}_{-0.31}$	$10.64^{+1.28}_{-2.09}$	$0.32^{+0.31}_{-0.22}$
72	$8.04^{+0.13}_{-0.15}$	$0.03^{+0.01}_{-0.01}$	$-9.6^{+0.26}_{-0.26}$	$9.44^{+1.48}_{-1.66}$	$0.05^{+0.02}_{-0.01}$
73	$\mathbf{8.61^{+0.07}_{-0.09}}$	$\mathbf{0.1^{+0.02}_{-0.01}}$	$\mathbf{-9.62^{+0.17}_{-0.13}}$	$\mathbf{9.17^{+1.08}_{-1.18}}$	$\mathbf{0.12^{+0.02}_{-0.02}}$

Continued on next page

Table 4.3: Fitted parameters for the exponentially-delayed model on the MIGHTEE-HI galaxies. The rows in bold represent the galaxies where I could also compute the spin-filament alignment from Chapter 3. (Continued)

ID	$\log_{10}(\frac{M_\star}{M_\odot})$	$\log_{10}$SFR $[M_\odot/\mathrm{yr}]$	$\log_{10}$sSFR [1/yr]	t_{form} [Gyr]	A_V [mag]
74	$9.03^{+0.12}_{-0.14}$	$0.32^{+0.24}_{-0.1}$	$-9.53^{+0.36}_{-0.22}$	$9.87^{+1.63}_{-1.67}$	$0.45^{+0.33}_{-0.28}$
75	$\mathbf{7.78^{+0.12}_{-0.17}}$	$\mathbf{0.02^{+0.01}_{-0.01}}$	$\mathbf{-9.39^{+0.27}_{-0.22}}$	$\mathbf{10.45^{+1.15}_{-1.53}}$	$\mathbf{0.01^{+0.01}_{-0.01}}$
76	$8.16^{+0.19}_{-0.13}$	$0.08^{+0.03}_{-0.02}$	$-9.26^{+0.26}_{-0.3}$	$11.1^{+0.81}_{-1.67}$	$0.0^{+0.0}_{-0.0}$
77	$7.81^{+0.17}_{-0.16}$	$0.04^{+0.03}_{-0.01}$	$-9.25^{+0.38}_{-0.3}$	$11.19^{+0.99}_{-1.71}$	$0.23^{+0.31}_{-0.16}$
78	$9.79^{+0.09}_{-0.11}$	$2.22^{+0.47}_{-0.37}$	$-9.45^{+0.19}_{-0.16}$	$10.1^{+0.95}_{-1.1}$	$0.11^{+0.02}_{-0.02}$
79	$7.93^{+0.16}_{-0.16}$	$0.06^{+0.04}_{-0.02}$	$-9.17^{+0.35}_{-0.3}$	$11.44^{+0.83}_{-1.42}$	$0.21^{+0.25}_{-0.15}$
80	$8.39^{+0.11}_{-0.16}$	$0.07^{+0.02}_{-0.02}$	$-9.56^{+0.25}_{-0.18}$	$9.51^{+1.43}_{-1.67}$	$0.02^{+0.03}_{-0.01}$
81	$8.64^{+0.06}_{-0.07}$	$0.52^{+0.07}_{-0.07}$	$-8.92^{+0.12}_{-0.12}$	$12.09^{+0.2}_{-0.28}$	$0.09^{+0.01}_{-0.01}$
82	$9.06^{+0.12}_{-0.16}$	$0.39^{+0.3}_{-0.1}$	$-9.47^{+0.4}_{-0.24}$	$10.08^{+1.62}_{-1.79}$	$0.35^{+0.37}_{-0.21}$
83	$9.32^{+0.05}_{-0.06}$	$0.6^{+0.09}_{-0.09}$	$-9.55^{+0.12}_{-0.12}$	$9.49^{+0.78}_{-0.82}$	$0.06^{+0.01}_{-0.01}$
84	$9.45^{+0.0}_{-0.0}$	$1.78^{+0.01}_{-0.01}$	$-9.2^{+0.0}_{-0.01}$	$11.81^{+0.01}_{-0.02}$	$1.64^{+0.03}_{-0.03}$
85	$9.24^{+0.08}_{-0.07}$	$1.48^{+0.26}_{-0.24}$	$-9.07^{+0.14}_{-0.16}$	$11.7^{+0.35}_{-0.51}$	$0.14^{+0.03}_{-0.02}$
86	$10.57^{+0.05}_{-0.05}$	$0.27^{+0.24}_{-0.26}$	$-11.13^{+0.3}_{-1.61}$	$4.8^{+1.74}_{-1.19}$	$0.3^{+0.14}_{-0.08}$
87	$\mathbf{9.01^{+0.16}_{-0.14}}$	$\mathbf{0.66^{+0.46}_{-0.21}}$	$\mathbf{-9.18^{+0.38}_{-0.31}}$	$\mathbf{11.4^{+0.88}_{-1.49}}$	$\mathbf{0.22^{+0.31}_{-0.15}}$
88	$\mathbf{8.23^{+0.13}_{-0.15}}$	$\mathbf{0.06^{+0.04}_{-0.01}}$	$\mathbf{-9.45^{+0.35}_{-0.25}}$	$\mathbf{10.21^{+1.42}_{-1.78}}$	$\mathbf{0.28^{+0.3}_{-0.17}}$
89	$\mathbf{9.95^{+0.02}_{-0.03}}$	$\mathbf{1.83^{+0.12}_{-0.12}}$	$\mathbf{-9.69^{+0.05}_{-0.05}}$	$\mathbf{8.09^{+0.47}_{-0.45}}$	$\mathbf{0.68^{+0.09}_{-0.07}}$
90	$10.91^{+0.07}_{-0.08}$	$0.0^{+0.0}_{-0.0}$	$-15.39^{+1.9}_{-3.8}$	$4.01^{+2.63}_{-2.69}$	$0.18^{+0.0}_{-0.0}$
91	$7.8^{+0.17}_{-0.15}$	$0.05^{+0.03}_{-0.02}$	$-9.11^{+0.33}_{-0.35}$	$11.64^{+0.67}_{-1.54}$	$0.21^{+0.29}_{-0.15}$
92	$8.64^{+0.1}_{-0.12}$	$0.13^{+0.03}_{-0.02}$	$-9.53^{+0.2}_{-0.17}$	$9.45^{+1.29}_{-1.26}$	$0.13^{+0.03}_{-0.03}$
93	$11.23^{+0.0}_{-0.0}$	$0.0^{+0.0}_{-0.0}$	$-23.1^{+1.98}_{-1.11}$	$0.8^{+0.13}_{-0.13}$	$0.18^{+0.0}_{-0.0}$
94	$10.11^{+0.13}_{-0.15}$	$4.07^{+3.03}_{-1.45}$	$-9.52^{+0.39}_{-0.28}$	$9.7^{+1.72}_{-1.86}$	$0.66^{+0.38}_{-0.31}$
95	$\mathbf{9.53^{+0.08}_{-0.06}}$	$\mathbf{2.23^{+0.29}_{-0.37}}$	$\mathbf{-9.18^{+0.11}_{-0.15}}$	$\mathbf{11.18^{+0.35}_{-0.62}}$	$\mathbf{0.06^{+0.01}_{-0.01}}$
96	$10.48^{+0.04}_{-0.04}$	$5.42^{+0.72}_{-0.72}$	$-9.74^{+0.09}_{-0.09}$	$8.18^{+0.66}_{-0.64}$	$0.08^{+0.01}_{-0.01}$
97	$\mathbf{9.38^{+0.06}_{-0.09}}$	$\mathbf{0.58^{+0.12}_{-0.08}}$	$\mathbf{-9.62^{+0.16}_{-0.12}}$	$\mathbf{8.91^{+1.16}_{-1.15}}$	$\mathbf{0.03^{+0.0}_{-0.0}}$
98	$7.53^{+0.15}_{-0.13}$	$0.01^{+0.01}_{-0.0}$	$-9.4^{+0.31}_{-0.26}$	$10.56^{+1.29}_{-1.77}$	$0.25^{+0.29}_{-0.16}$
99	$\mathbf{9.91^{+0.04}_{-0.04}}$	$\mathbf{3.41^{+0.29}_{-0.24}}$	$\mathbf{-9.37^{+0.07}_{-0.07}}$	$\mathbf{10.18^{+0.35}_{-0.46}}$	$\mathbf{0.28^{+0.03}_{-0.03}}$
100	$\mathbf{10.27^{+0.01}_{-0.01}}$	$\mathbf{2.17^{+0.14}_{-0.1}}$	$\mathbf{-9.93^{+0.04}_{-0.03}}$	$\mathbf{6.59^{+0.27}_{-0.22}}$	$\mathbf{1.66^{+0.21}_{-0.23}}$
101	$10.66^{+0.03}_{-0.03}$	$1.48^{+0.3}_{-0.32}$	$-10.49^{+0.09}_{-0.12}$	$5.7^{+0.89}_{-0.8}$	$0.17^{+0.04}_{-0.02}$
102	$10.5^{+0.01}_{-0.01}$	$0.5^{+0.11}_{-0.11}$	$-10.8^{+0.1}_{-0.12}$	$4.25^{+0.39}_{-0.29}$	$0.47^{+0.07}_{-0.06}$

Continued on next page

Table 4.3: Fitted parameters for the exponentially-delayed model on the MIGHTEE-HI galaxies. The rows in bold represent the galaxies where I could also compute the spin-filament alignment from Chapter 3. (Continued)

ID	$\log_{10}(\frac{M_\star}{M_\odot})$	$\log_{10}$SFR $[M_\odot/\mathrm{yr}]$	$\log_{10}$sSFR [1/yr]	t_{form} [Gyr]	A_V [mag]
103	$8.83^{+0.12}_{-0.17}$	$0.29^{+0.21}_{-0.09}$	$-9.36^{+0.38}_{-0.26}$	$10.13^{+1.3}_{-1.63}$	$0.24^{+0.3}_{-0.17}$
104	$8.92^{+0.13}_{-0.15}$	$0.36^{+0.25}_{-0.11}$	$-9.38^{+0.34}_{-0.26}$	$10.01^{+1.29}_{-1.62}$	$0.24^{+0.29}_{-0.17}$
105	$8.54^{+0.1}_{-0.1}$	$0.03^{+0.01}_{-0.01}$	$-10.0^{+0.2}_{-0.2}$	$7.36^{+1.6}_{-1.2}$	$0.59^{+0.13}_{-0.13}$
106	$8.56^{+0.14}_{-0.16}$	$0.14^{+0.11}_{-0.05}$	$-9.41^{+0.37}_{-0.32}$	$10.9^{+1.4}_{-2.27}$	$0.26^{+0.32}_{-0.18}$
107	$\mathbf{10.02^{+0.01}_{-0.0}}$	$\mathbf{0.0^{+0.0}_{-0.0}}$	$\mathbf{-17.01^{+0.19}_{-0.13}}$	$\mathbf{6.74^{+0.06}_{-0.08}}$	$\mathbf{0.33^{+0.0}_{-0.0}}$
108	$7.82^{+0.12}_{-0.16}$	$0.02^{+0.01}_{-0.01}$	$-9.51^{+0.36}_{-0.23}$	$10.36^{+1.65}_{-1.87}$	$0.31^{+0.3}_{-0.2}$
109	$8.82^{+0.03}_{-0.02}$	$0.16^{+0.02}_{-0.01}$	$-9.62^{+0.08}_{-0.06}$	$9.13^{+0.55}_{-0.81}$	$0.22^{+0.02}_{-0.03}$
110	$\mathbf{8.84^{+0.11}_{-0.1}}$	$\mathbf{0.76^{+0.12}_{-0.14}}$	$\mathbf{-8.95^{+0.15}_{-0.21}}$	$\mathbf{12.28^{+0.29}_{-0.58}}$	$\mathbf{0.52^{+0.06}_{-0.06}}$
111	$8.63^{+0.06}_{-0.08}$	$0.11^{+0.02}_{-0.02}$	$-9.6^{+0.16}_{-0.13}$	$9.35^{+1.17}_{-1.11}$	$0.05^{+0.01}_{-0.01}$
112	$8.09^{+0.15}_{-0.15}$	$0.05^{+0.03}_{-0.02}$	$-9.36^{+0.3}_{-0.31}$	$10.92^{+1.18}_{-2.27}$	$0.26^{+0.29}_{-0.18}$
113	$\mathbf{7.89^{+0.12}_{-0.12}}$	$\mathbf{0.04^{+0.01}_{-0.01}}$	$\mathbf{-9.27^{+0.21}_{-0.22}}$	$\mathbf{10.99^{+0.72}_{-1.27}}$	$\mathbf{0.11^{+0.03}_{-0.03}}$
114	$8.37^{+0.12}_{-0.1}$	$0.21^{+0.04}_{-0.04}$	$-9.05^{+0.17}_{-0.19}$	$11.83^{+0.33}_{-0.6}$	$0.07^{+0.01}_{-0.01}$
115	$\mathbf{10.39^{+0.01}_{-0.0}}$	$\mathbf{0.0^{+0.0}_{-0.0}}$	$\mathbf{-15.26^{+1.23}_{-0.99}}$	$\mathbf{6.6^{+0.18}_{-0.18}}$	$\mathbf{2.0^{+0.0}_{-0.0}}$
116	$\mathbf{8.52^{+0.08}_{-0.11}}$	$\mathbf{0.08^{+0.02}_{-0.01}}$	$\mathbf{-9.64^{+0.2}_{-0.16}}$	$\mathbf{8.86^{+1.45}_{-1.19}}$	$\mathbf{0.08^{+0.02}_{-0.02}}$
117	$8.08^{+0.12}_{-0.16}$	$0.03^{+0.01}_{-0.01}$	$-9.55^{+0.27}_{-0.2}$	$9.56^{+1.44}_{-1.53}$	$0.09^{+0.04}_{-0.03}$
118	$9.5^{+0.05}_{-0.05}$	$0.75^{+0.09}_{-0.07}$	$-9.63^{+0.09}_{-0.09}$	$8.77^{+0.81}_{-0.81}$	$0.25^{+0.03}_{-0.03}$
119	$9.1^{+0.06}_{-0.06}$	$0.15^{+0.04}_{-0.04}$	$-9.93^{+0.17}_{-0.18}$	$7.59^{+0.98}_{-0.96}$	$0.09^{+0.03}_{-0.02}$
120	$9.37^{+0.06}_{-0.06}$	$1.03^{+0.14}_{-0.13}$	$-9.35^{+0.11}_{-0.12}$	$10.65^{+0.57}_{-0.78}$	$0.22^{+0.04}_{-0.03}$
121	$8.41^{+0.12}_{-0.22}$	$0.09^{+0.02}_{-0.02}$	$-9.48^{+0.32}_{-0.21}$	$9.88^{+1.56}_{-1.7}$	$0.06^{+0.02}_{-0.01}$
122	$10.25^{+0.03}_{-0.03}$	$0.41^{+0.12}_{-0.12}$	$-10.63^{+0.13}_{-0.16}$	$5.09^{+0.87}_{-0.64}$	$0.41^{+0.11}_{-0.07}$
123	$8.46^{+0.11}_{-0.17}$	$0.1^{+0.06}_{-0.03}$	$-9.5^{+0.37}_{-0.27}$	$9.92^{+1.74}_{-1.92}$	$0.84^{+0.4}_{-0.34}$
124	$7.94^{+0.23}_{-0.13}$	$0.06^{+0.02}_{-0.01}$	$-9.2^{+0.24}_{-0.34}$	$11.3^{+0.73}_{-1.74}$	$0.13^{+0.04}_{-0.03}$
125	$\mathbf{10.32^{+0.0}_{-0.0}}$	$\mathbf{0.0^{+0.0}_{-0.0}}$	$\mathbf{-23.18^{+1.88}_{-1.22}}$	$\mathbf{0.78^{+0.16}_{-0.12}}$	$\mathbf{0.34^{+0.01}_{-0.01}}$
126	$\mathbf{9.3^{+0.1}_{-0.13}}$	$\mathbf{0.58^{+0.17}_{-0.12}}$	$\mathbf{-9.53^{+0.22}_{-0.2}}$	$\mathbf{9.74^{+1.24}_{-1.51}}$	$\mathbf{0.45^{+0.17}_{-0.19}}$
127	$\mathbf{7.95^{+0.12}_{-0.16}}$	$\mathbf{0.03^{+0.01}_{-0.01}}$	$\mathbf{-9.54^{+0.29}_{-0.19}}$	$\mathbf{9.59^{+1.51}_{-1.51}}$	$\mathbf{0.04^{+0.07}_{-0.03}}$
128	$\mathbf{8.94^{+0.08}_{-0.08}}$	$\mathbf{0.26^{+0.05}_{-0.04}}$	$\mathbf{-9.53^{+0.16}_{-0.15}}$	$\mathbf{9.66^{+0.96}_{-1.23}}$	$\mathbf{0.12^{+0.02}_{-0.02}}$
129	$\mathbf{10.78^{+0.0}_{-0.0}}$	$\mathbf{0.0^{+0.0}_{-0.0}}$	$\mathbf{-23.33^{+2.26}_{-1.15}}$	$\mathbf{0.85^{+0.17}_{-0.15}}$	$\mathbf{0.13^{+0.0}_{-0.0}}$
130	$\mathbf{9.51^{+0.04}_{-0.04}}$	$\mathbf{0.58^{+0.05}_{-0.07}}$	$\mathbf{-9.74^{+0.07}_{-0.09}}$	$\mathbf{8.08^{+0.77}_{-0.56}}$	$\mathbf{0.17^{+0.03}_{-0.02}}$
131	$\mathbf{9.0^{+0.09}_{-0.08}}$	$\mathbf{0.27^{+0.05}_{-0.04}}$	$\mathbf{-9.58^{+0.16}_{-0.14}}$	$\mathbf{9.39^{+0.96}_{-1.17}}$	$\mathbf{0.09^{+0.02}_{-0.01}}$

Continued on next page

Table 4.3: Fitted parameters for the exponentially-delayed model on the MIGHTEE-HI galaxies. The rows in bold represent the galaxies where I could also compute the spin-filament alignment from Chapter 3. (Continued)

ID	$\log_{10}(\frac{M_\star}{M_\odot})$	$\log_{10}$SFR $[M_\odot/\mathrm{yr}]$	$\log_{10}$sSFR [1/yr]	t_{form} [Gyr]	A_V [mag]
132	$\mathbf{10.27^{+0.03}_{-0.03}}$	$\mathbf{1.78^{+0.3}_{-0.23}}$	$\mathbf{-10.02^{+0.09}_{-0.1}}$	$\mathbf{6.93^{+0.61}_{-0.65}}$	$\mathbf{0.14^{+0.02}_{-0.02}}$
133	$7.34^{+0.14}_{-0.17}$	$0.02^{+0.0}_{-0.0}$	$-9.1^{+0.26}_{-0.25}$	$11.62^{+0.62}_{-1.05}$	$0.03^{+0.03}_{-0.02}$
134	$8.78^{+0.07}_{-0.08}$	$0.23^{+0.04}_{-0.03}$	$-9.41^{+0.15}_{-0.14}$	$10.57^{+0.63}_{-0.9}$	$0.05^{+0.01}_{-0.01}$
135	$10.17^{+0.04}_{-0.06}$	$0.01^{+0.03}_{-0.01}$	$-12.08^{+0.57}_{-2.03}$	$4.31^{+1.99}_{-1.34}$	$0.18^{+0.02}_{-0.03}$
136	$7.67^{+0.08}_{-0.14}$	$0.01^{+0.0}_{-0.0}$	$-9.56^{+0.23}_{-0.16}$	$9.25^{+1.42}_{-1.4}$	$0.02^{+0.03}_{-0.01}$
137	$9.88^{+0.05}_{-0.05}$	$1.82^{+0.17}_{-0.15}$	$-9.62^{+0.08}_{-0.08}$	$8.51^{+0.75}_{-0.75}$	$0.29^{+0.03}_{-0.03}$
138	$8.75^{+0.13}_{-0.11}$	$0.22^{+0.06}_{-0.05}$	$-9.4^{+0.21}_{-0.23}$	$10.06^{+0.91}_{-1.59}$	$0.01^{+0.01}_{-0.0}$
139	$8.8^{+0.1}_{-0.21}$	$0.21^{+0.05}_{-0.04}$	$-9.5^{+0.29}_{-0.17}$	$9.53^{+1.35}_{-1.37}$	$0.12^{+0.03}_{-0.02}$
140	$10.38^{+0.0}_{-0.0}$	$2.2^{+0.02}_{-0.02}$	$-10.03^{+0.01}_{-0.01}$	$6.05^{+0.11}_{-0.05}$	$1.98^{+0.01}_{-0.03}$
141	$9.47^{+0.08}_{-0.08}$	$1.75^{+0.27}_{-0.25}$	$-9.23^{+0.15}_{-0.14}$	$10.93^{+0.47}_{-0.59}$	$0.08^{+0.01}_{-0.01}$
142	$8.92^{+0.07}_{-0.06}$	$0.44^{+0.06}_{-0.05}$	$-9.28^{+0.11}_{-0.12}$	$10.67^{+0.45}_{-0.65}$	$0.16^{+0.02}_{-0.02}$
143	$9.63^{+0.05}_{-0.06}$	$0.52^{+0.12}_{-0.13}$	$-9.91^{+0.14}_{-0.17}$	$7.44^{+1.09}_{-0.88}$	$0.15^{+0.04}_{-0.03}$
144	$8.03^{+0.08}_{-0.14}$	$0.03^{+0.01}_{-0.01}$	$-9.62^{+0.21}_{-0.17}$	$8.55^{+1.56}_{-1.06}$	$0.16^{+0.08}_{-0.07}$
145	$8.42^{+0.14}_{-0.09}$	$0.22^{+0.04}_{-0.04}$	$-9.07^{+0.14}_{-0.22}$	$11.4^{+0.36}_{-0.75}$	$0.08^{+0.02}_{-0.02}$
146	$8.79^{+0.05}_{-0.04}$	$0.83^{+0.09}_{-0.08}$	$-8.88^{+0.08}_{-0.08}$	$11.82^{+0.14}_{-0.17}$	$0.19^{+0.03}_{-0.02}$
147	$\mathbf{9.58^{+0.11}_{-0.15}}$	$\mathbf{1.0^{+0.7}_{-0.42}}$	$\mathbf{-9.59^{+0.38}_{-0.3}}$	$\mathbf{9.07^{+1.8}_{-1.7}}$	$\mathbf{0.62^{+0.36}_{-0.33}}$
148	$9.42^{+0.03}_{-0.02}$	$2.04^{+0.11}_{-0.13}$	$-9.11^{+0.05}_{-0.05}$	$11.13^{+0.16}_{-0.21}$	$0.56^{+0.07}_{-0.05}$
149	$10.59^{+0.02}_{-0.03}$	$0.0^{+0.02}_{-0.0}$	$-14.21^{+1.93}_{-3.59}$	$2.75^{+1.08}_{-1.07}$	$0.0^{+0.0}_{-0.0}$
150	$\mathbf{10.75^{+0.02}_{-0.02}}$	$\mathbf{3.16^{+0.95}_{-0.73}}$	$\mathbf{-10.25^{+0.11}_{-0.11}}$	$\mathbf{9.82^{+0.3}_{-0.28}}$	$\mathbf{0.26^{+0.05}_{-0.05}}$
151	$\mathbf{10.13^{+0.04}_{-0.08}}$	$\mathbf{1.28^{+0.13}_{-0.14}}$	$\mathbf{-10.02^{+0.07}_{-0.06}}$	$\mathbf{7.31^{+1.81}_{-1.03}}$	$\mathbf{0.34^{+0.05}_{-0.03}}$
152	$\mathbf{8.25^{+0.08}_{-0.11}}$	$\mathbf{0.04^{+0.01}_{-0.01}}$	$\mathbf{-9.64^{+0.18}_{-0.16}}$	$\mathbf{8.43^{+1.41}_{-1.1}}$	$\mathbf{0.05^{+0.05}_{-0.03}}$
153	$8.91^{+0.12}_{-0.1}$	$0.32^{+0.08}_{-0.06}$	$-9.4^{+0.19}_{-0.21}$	$9.99^{+0.85}_{-1.5}$	$0.06^{+0.02}_{-0.02}$
154	$\mathbf{9.29^{+0.04}_{-0.03}}$	$\mathbf{1.18^{+0.08}_{-0.1}}$	$\mathbf{-9.21^{+0.06}_{-0.08}}$	$\mathbf{10.8^{+0.25}_{-0.36}}$	$\mathbf{0.46^{+0.07}_{-0.05}}$
155	$8.27^{+0.13}_{-0.16}$	$0.08^{+0.02}_{-0.02}$	$-9.37^{+0.23}_{-0.24}$	$10.07^{+1.11}_{-1.51}$	$0.05^{+0.03}_{-0.03}$
156	$9.05^{+0.0}_{-0.01}$	$0.0^{+0.0}_{-0.0}$	$-20.78^{+2.82}_{-2.72}$	$1.18^{+0.43}_{-0.31}$	$0.03^{+0.01}_{-0.01}$
157	$\mathbf{8.4^{+0.09}_{-0.11}}$	$\mathbf{0.05^{+0.01}_{-0.01}}$	$\mathbf{-9.68^{+0.2}_{-0.18}}$	$\mathbf{8.71^{+1.51}_{-1.1}}$	$\mathbf{0.05^{+0.01}_{-0.01}}$
158	$\mathbf{9.91^{+0.12}_{-0.19}}$	$\mathbf{2.55^{+2.02}_{-0.98}}$	$\mathbf{-9.52^{+0.43}_{-0.29}}$	$\mathbf{10.27^{+1.76}_{-2.03}}$	$\mathbf{0.62^{+0.36}_{-0.35}}$
159	$10.07^{+0.01}_{-0.01}$	$0.0^{+0.0}_{-0.0}$	$-16.91^{+0.27}_{-0.18}$	$6.64^{+0.08}_{-0.09}$	$1.69^{+0.01}_{-0.01}$
160	$7.86^{+0.14}_{-0.14}$	$0.02^{+0.0}_{-0.01}$	$-9.68^{+0.23}_{-0.36}$	$9.08^{+1.55}_{-1.53}$	$0.0^{+0.0}_{-0.0}$

Continued on next page

Table 4.3: Fitted parameters for the exponentially-delayed model on the MIGHTEE-HI galaxies. The rows in bold represent the galaxies where I could also compute the spin-filament alignment from Chapter 3. (Continued)

ID	$\log_{10}(\frac{M_\star}{M_\odot})$	$\log_{10}$SFR $[M_\odot/\mathrm{yr}]$	$\log_{10}$sSFR [1/yr]	t_{form} [Gyr]	A_V [mag]
161	$7.86^{+0.14}_{-0.12}$	$0.02^{+0.0}_{-0.01}$	$-9.63^{+0.23}_{-0.28}$	$9.5^{+1.43}_{-1.6}$	$0.0^{+0.0}_{-0.0}$
162	$8.75^{+0.13}_{-0.11}$	$0.08^{+0.03}_{-0.04}$	$-9.82^{+0.18}_{-0.4}$	$7.78^{+1.45}_{-1.32}$	$0.04^{+0.05}_{-0.03}$
163	$10.64^{+0.01}_{-0.01}$	$0.33^{+0.01}_{-0.0}$	$-11.11^{+0.01}_{-0.01}$	$5.85^{+0.12}_{-0.13}$	$1.99^{+0.0}_{-0.01}$
164	$9.71^{+0.03}_{-0.03}$	$0.24^{+0.05}_{-0.05}$	$-10.33^{+0.11}_{-0.13}$	$5.58^{+0.43}_{-0.46}$	$0.42^{+0.09}_{-0.06}$
165	$10.69^{+0.0}_{-0.0}$	$0.0^{+0.0}_{-0.0}$	$-16.38^{+0.72}_{-0.42}$	$6.44^{+0.09}_{-0.1}$	$1.13^{+0.0}_{-0.0}$
166	$10.93^{+0.0}_{-0.01}$	$0.0^{+0.0}_{-0.0}$	$-21.33^{+3.13}_{-1.97}$	$1.05^{+0.25}_{-0.2}$	$0.07^{+0.0}_{-0.0}$
167	$8.67^{+0.13}_{-0.11}$	$0.1^{+0.02}_{-0.03}$	$-9.69^{+0.21}_{-0.3}$	$8.49^{+1.5}_{-1.3}$	$0.08^{+0.03}_{-0.02}$
168	$8.74^{+0.18}_{-0.17}$	$0.41^{+0.21}_{-0.11}$	$-9.12^{+0.3}_{-0.3}$	$11.55^{+0.7}_{-1.36}$	$0.17^{+0.19}_{-0.12}$
169	$9.54^{+0.05}_{-0.07}$	$0.87^{+0.12}_{-0.11}$	$-9.61^{+0.13}_{-0.11}$	$9.08^{+0.96}_{-0.89}$	$0.08^{+0.01}_{-0.01}$
170	$10.56^{+0.01}_{-0.01}$	$0.0^{+0.0}_{-0.0}$	$-16.69^{+0.63}_{-0.32}$	$6.28^{+0.07}_{-0.1}$	$1.61^{+0.01}_{-0.01}$
171	$\mathbf{10.92^{+0.13}_{-0.14}}$	$\mathbf{20.54^{+15.71}_{-9.42}}$	$\mathbf{-9.61^{+0.38}_{-0.36}}$	$\mathbf{9.35^{+1.86}_{-2.03}}$	$\mathbf{0.96^{+0.33}_{-0.4}}$
172	$10.11^{+0.12}_{-0.15}$	$3.65^{+2.92}_{-1.3}$	$-9.55^{+0.37}_{-0.25}$	$9.63^{+1.73}_{-1.78}$	$0.62^{+0.35}_{-0.34}$
173	$8.23^{+0.12}_{-0.13}$	$0.06^{+0.01}_{-0.01}$	$-9.49^{+0.22}_{-0.2}$	$10.0^{+1.11}_{-1.55}$	$0.19^{+0.12}_{-0.11}$
174	$10.25^{+0.03}_{-0.04}$	$0.39^{+0.08}_{-0.06}$	$-10.66^{+0.09}_{-0.09}$	$5.76^{+1.05}_{-0.95}$	$0.44^{+0.06}_{-0.06}$
175	$\mathbf{7.86^{+0.15}_{-0.17}}$	$\mathbf{0.03^{+0.01}_{-0.01}}$	$\mathbf{-9.35^{+0.29}_{-0.27}}$	$\mathbf{10.69^{+1.08}_{-1.73}}$	$\mathbf{0.08^{+0.04}_{-0.03}}$
176	$8.43^{+0.14}_{-0.16}$	$0.09^{+0.03}_{-0.02}$	$-9.49^{+0.28}_{-0.22}$	$10.02^{+1.34}_{-1.74}$	$0.07^{+0.02}_{-0.02}$
177	$9.38^{+0.03}_{-0.03}$	$0.0^{+0.0}_{-0.0}$	$-15.42^{+2.78}_{-3.65}$	$2.67^{+1.29}_{-1.03}$	$0.03^{+0.01}_{-0.01}$
178	$9.08^{+0.1}_{-0.07}$	$0.15^{+0.04}_{-0.06}$	$-9.92^{+0.19}_{-0.31}$	$7.62^{+0.97}_{-1.04}$	$0.05^{+0.02}_{-0.01}$
179	$10.47^{+0.01}_{-0.01}$	$0.0^{+0.0}_{-0.0}$	$-16.79^{+0.37}_{-0.24}$	$6.45^{+0.08}_{-0.11}$	$1.28^{+0.0}_{-0.0}$
180	$9.03^{+0.13}_{-0.17}$	$0.44^{+0.34}_{-0.12}$	$-9.38^{+0.39}_{-0.27}$	$10.5^{+1.44}_{-1.89}$	$0.31^{+0.33}_{-0.22}$
181	$9.85^{+0.1}_{-0.06}$	$0.22^{+0.13}_{-0.17}$	$-10.5^{+0.25}_{-0.78}$	$5.39^{+0.77}_{-1.2}$	$0.24^{+0.18}_{-0.07}$
182	$9.45^{+0.06}_{-0.06}$	$0.83^{+0.11}_{-0.11}$	$-9.53^{+0.12}_{-0.12}$	$9.56^{+0.75}_{-0.9}$	$0.12^{+0.02}_{-0.02}$
183	$\mathbf{9.53^{+0.07}_{-0.07}}$	$\mathbf{1.36^{+0.2}_{-0.19}}$	$\mathbf{-9.4^{+0.13}_{-0.14}}$	$\mathbf{10.43^{+0.65}_{-0.9}}$	$\mathbf{0.1^{+0.02}_{-0.01}}$
184	$9.72^{+0.03}_{-0.04}$	$1.11^{+0.1}_{-0.08}$	$-9.67^{+0.07}_{-0.06}$	$8.36^{+0.67}_{-0.59}$	$0.29^{+0.03}_{-0.03}$
185	$8.2^{+0.07}_{-0.05}$	$0.24^{+0.04}_{-0.03}$	$-8.82^{+0.11}_{-0.11}$	$12.24^{+0.15}_{-0.19}$	$0.15^{+0.03}_{-0.02}$
186	$8.76^{+0.12}_{-0.1}$	$0.5^{+0.09}_{-0.09}$	$-9.07^{+0.17}_{-0.2}$	$11.52^{+0.37}_{-0.68}$	$0.08^{+0.02}_{-0.01}$
187	$8.79^{+0.14}_{-0.16}$	$0.26^{+0.2}_{-0.09}$	$-9.37^{+0.38}_{-0.31}$	$10.39^{+1.32}_{-2.1}$	$0.36^{+0.32}_{-0.25}$
188	$9.45^{+0.06}_{-0.04}$	$1.5^{+0.15}_{-0.15}$	$-9.28^{+0.08}_{-0.11}$	$10.87^{+0.34}_{-0.51}$	$0.22^{+0.03}_{-0.02}$
189	$10.59^{+0.02}_{-0.02}$	$6.3^{+0.39}_{-0.36}$	$-9.79^{+0.05}_{-0.05}$	$7.57^{+0.47}_{-0.43}$	$0.13^{+0.01}_{-0.01}$

Continued on next page

Table 4.3: Fitted parameters for the exponentially-delayed model on the MIGHTEE-HI galaxies. The rows in bold represent the galaxies where I could also compute the spin-filament alignment from Chapter 3. (Continued)

ID	$\log_{10}(\frac{M_\star}{M_\odot})$	$\log_{10}$SFR $[M_\odot/\mathrm{yr}]$	$\log_{10}$sSFR [1/yr]	t_{form} [Gyr]	A_V [mag]
190	$9.48^{+0.04}_{-0.03}$	$2.39^{+0.2}_{-0.2}$	$-9.11^{+0.07}_{-0.07}$	$11.36^{+0.19}_{-0.25}$	$0.22^{+0.03}_{-0.02}$
191	$10.57^{+0.05}_{-0.03}$	$2.01^{+0.26}_{-0.31}$	$-10.28^{+0.07}_{-0.09}$	$9.08^{+0.41}_{-0.81}$	$0.17^{+0.02}_{-0.02}$
192	$9.38^{+0.01}_{-0.02}$	$1.46^{+0.05}_{-0.04}$	$-9.21^{+0.03}_{-0.02}$	$11.6^{+0.08}_{-0.09}$	$0.92^{+0.07}_{-0.07}$
193	$10.95^{+0.0}_{-0.0}$	$0.57^{+0.0}_{-0.0}$	$-11.19^{+0.0}_{-0.0}$	$5.72^{+0.07}_{-0.07}$	$2.0^{+0.0}_{-0.0}$
194	$8.89^{+0.03}_{-0.03}$	$0.83^{+0.07}_{-0.07}$	$-8.97^{+0.07}_{-0.07}$	$11.82^{+0.14}_{-0.17}$	$0.32^{+0.05}_{-0.04}$
195	$9.06^{+0.1}_{-0.1}$	$0.54^{+0.12}_{-0.09}$	$-9.33^{+0.18}_{-0.18}$	$10.65^{+0.74}_{-1.08}$	$0.07^{+0.01}_{-0.01}$
196	$9.35^{+0.15}_{-0.15}$	$1.21^{+0.78}_{-0.35}$	$-9.27^{+0.34}_{-0.26}$	$10.95^{+0.97}_{-1.61}$	$0.22^{+0.31}_{-0.15}$
197	$9.19^{+0.08}_{-0.07}$	$1.12^{+0.16}_{-0.16}$	$-9.14^{+0.12}_{-0.15}$	$11.37^{+0.35}_{-0.54}$	$0.11^{+0.02}_{-0.02}$
198	$\mathbf{10.23^{+0.02}_{-0.04}}$	$\mathbf{0.0^{+0.0}_{-0.0}}$	$\mathbf{-17.04^{+3.4}_{-3.81}}$	$\mathbf{1.65^{+1.16}_{-0.62}}$	$\mathbf{0.67^{+0.06}_{-0.05}}$
199	$\mathbf{9.97^{+0.07}_{-0.06}}$	$\mathbf{2.89^{+0.41}_{-0.36}}$	$\mathbf{-9.51^{+0.12}_{-0.12}}$	$\mathbf{9.59^{+0.68}_{-0.92}}$	$\mathbf{0.11^{+0.02}_{-0.01}}$
200	$7.68^{+0.12}_{-0.17}$	$0.06^{+0.03}_{-0.02}$	$-8.93^{+0.32}_{-0.28}$	$11.9^{+0.48}_{-0.78}$	$0.14^{+0.18}_{-0.1}$
201	$9.16^{+0.1}_{-0.09}$	$0.46^{+0.1}_{-0.09}$	$-9.5^{+0.18}_{-0.19}$	$9.75^{+1.0}_{-1.41}$	$0.07^{+0.01}_{-0.01}$
202	$\mathbf{8.16^{+0.09}_{-0.1}}$	$\mathbf{0.03^{+0.01}_{-0.01}}$	$\mathbf{-9.68^{+0.16}_{-0.2}}$	$\mathbf{8.46^{+1.29}_{-1.12}}$	$\mathbf{0.18^{+0.09}_{-0.08}}$
203	$\mathbf{8.58^{+0.17}_{-0.15}}$	$\mathbf{0.14^{+0.04}_{-0.03}}$	$\mathbf{-9.42^{+0.25}_{-0.26}}$	$\mathbf{10.07^{+1.25}_{-1.72}}$	$\mathbf{0.03^{+0.02}_{-0.01}}$
204	$\mathbf{8.13^{+0.12}_{-0.14}}$	$\mathbf{0.06^{+0.03}_{-0.02}}$	$\mathbf{-9.38^{+0.31}_{-0.25}}$	$\mathbf{10.56^{+1.27}_{-1.45}}$	$\mathbf{0.27^{+0.31}_{-0.18}}$
205	$\mathbf{10.12^{+0.01}_{-0.01}}$	$\mathbf{0.0^{+0.0}_{-0.0}}$	$\mathbf{-19.64^{+3.35}_{-3.47}}$	$\mathbf{1.25^{+0.49}_{-0.32}}$	$\mathbf{0.62^{+0.02}_{-0.03}}$
206	$\mathbf{9.83^{+0.02}_{-0.03}}$	$\mathbf{1.24^{+0.09}_{-0.1}}$	$\mathbf{-9.74^{+0.05}_{-0.06}}$	$\mathbf{7.85^{+0.48}_{-0.38}}$	$\mathbf{0.14^{+0.01}_{-0.01}}$
207	$\mathbf{8.85^{+0.06}_{-0.07}}$	$\mathbf{0.13^{+0.02}_{-0.02}}$	$\mathbf{-9.72^{+0.12}_{-0.14}}$	$\mathbf{8.44^{+1.07}_{-0.85}}$	$\mathbf{0.07^{+0.02}_{-0.01}}$
208	$9.74^{+0.05}_{-0.06}$	$1.48^{+0.16}_{-0.14}$	$-9.57^{+0.1}_{-0.09}$	$9.21^{+0.69}_{-0.81}$	$0.23^{+0.03}_{-0.03}$
209	$10.11^{+0.03}_{-0.03}$	$3.18^{+0.21}_{-0.18}$	$-9.61^{+0.06}_{-0.05}$	$8.75^{+0.52}_{-0.52}$	$0.39^{+0.04}_{-0.03}$
210	$9.12^{+0.06}_{-0.06}$	$0.82^{+0.12}_{-0.11}$	$-9.21^{+0.12}_{-0.12}$	$10.92^{+0.38}_{-0.53}$	$0.13^{+0.02}_{-0.02}$
211	$10.28^{+0.02}_{-0.02}$	$0.89^{+0.15}_{-0.16}$	$-10.34^{+0.08}_{-0.1}$	$5.75^{+0.86}_{-0.56}$	$0.21^{+0.04}_{-0.03}$
212	$\mathbf{10.81^{+0.02}_{-0.01}}$	$\mathbf{11.38^{+0.38}_{-0.35}}$	$\mathbf{-9.75^{+0.03}_{-0.03}}$	$\mathbf{7.72^{+0.23}_{-0.33}}$	$\mathbf{0.1^{+0.0}_{-0.0}}$
213	$\mathbf{9.37^{+0.07}_{-0.06}}$	$\mathbf{0.34^{+0.08}_{-0.09}}$	$\mathbf{-9.84^{+0.15}_{-0.19}}$	$\mathbf{7.68^{+1.12}_{-0.85}}$	$\mathbf{0.12^{+0.03}_{-0.02}}$
214	$9.86^{+0.04}_{-0.06}$	$1.49^{+0.19}_{-0.2}$	$-9.69^{+0.11}_{-0.1}$	$8.24^{+0.93}_{-0.73}$	$0.1^{+0.02}_{-0.01}$
215	$\mathbf{8.18^{+0.16}_{-0.15}}$	$\mathbf{0.09^{+0.06}_{-0.03}}$	$\mathbf{-9.23^{+0.35}_{-0.32}}$	$\mathbf{10.89^{+0.94}_{-1.71}}$	$\mathbf{0.23^{+0.3}_{-0.16}}$
216	$8.35^{+0.1}_{-0.12}$	$0.14^{+0.03}_{-0.03}$	$-9.22^{+0.19}_{-0.17}$	$10.81^{+0.66}_{-0.87}$	$0.07^{+0.02}_{-0.02}$
217	$\mathbf{8.55^{+0.09}_{-0.14}}$	$\mathbf{0.08^{+0.02}_{-0.02}}$	$\mathbf{-9.65^{+0.22}_{-0.2}}$	$\mathbf{8.62^{+1.38}_{-1.22}}$	$\mathbf{0.09^{+0.04}_{-0.03}}$
218	$9.64^{+0.06}_{-0.06}$	$2.98^{+0.39}_{-0.33}$	$-9.16^{+0.11}_{-0.11}$	$11.12^{+0.31}_{-0.47}$	$0.16^{+0.02}_{-0.02}$

Continued on next page

Table 4.3: Fitted parameters for the exponentially-delayed model on the MIGHTEE-HI galaxies. The rows in bold represent the galaxies where I could also compute the spin-filament alignment from Chapter 3. (Continued)

ID	$\log_{10}(\frac{M_\star}{M_\odot})$	$\log_{10}$SFR $[M_\odot/\mathrm{yr}]$	$\log_{10}$sSFR [1/yr]	t_{form} [Gyr]	A_V [mag]
219	$\mathbf{10.19^{+0.03}_{-0.04}}$	$\mathbf{1.01^{+0.17}_{-0.15}}$	$\mathbf{-10.18^{+0.07}_{-0.09}}$	$\mathbf{6.55^{+1.05}_{-0.81}}$	$\mathbf{0.23^{+0.04}_{-0.03}}$
220	$9.01^{+0.11}_{-0.09}$	$0.51^{+0.07}_{-0.08}$	$-9.29^{+0.13}_{-0.18}$	$10.59^{+0.56}_{-0.96}$	$0.11^{+0.02}_{-0.01}$
221	$8.31^{+0.14}_{-0.17}$	$0.09^{+0.1}_{-0.04}$	$-9.35^{+0.49}_{-0.34}$	$10.28^{+1.5}_{-2.13}$	$0.97^{+0.43}_{-0.34}$
222	$10.56^{+0.03}_{-0.03}$	$2.04^{+0.22}_{-0.21}$	$-10.25^{+0.06}_{-0.06}$	$7.05^{+0.62}_{-0.7}$	$0.37^{+0.04}_{-0.04}$
223	$10.48^{+0.06}_{-0.08}$	$2.32^{+0.25}_{-0.27}$	$-10.11^{+0.08}_{-0.08}$	$8.01^{+1.42}_{-1.46}$	$0.29^{+0.04}_{-0.03}$
224	$8.41^{+0.13}_{-0.17}$	$0.08^{+0.02}_{-0.02}$	$-9.49^{+0.27}_{-0.22}$	$9.53^{+1.38}_{-1.52}$	$0.07^{+0.03}_{-0.03}$
225	$\mathbf{9.19^{+0.11}_{-0.17}}$	$\mathbf{0.47^{+0.39}_{-0.13}}$	$\mathbf{-9.52^{+0.41}_{-0.21}}$	$\mathbf{9.4^{+1.92}_{-1.55}}$	$\mathbf{0.47^{+0.37}_{-0.29}}$
226	$9.32^{+0.12}_{-0.15}$	$0.83^{+0.57}_{-0.24}$	$-9.39^{+0.34}_{-0.25}$	$10.1^{+1.27}_{-1.9}$	$0.3^{+0.29}_{-0.22}$
227	$10.01^{+0.05}_{-0.04}$	$5.48^{+0.49}_{-0.5}$	$-9.27^{+0.08}_{-0.09}$	$10.56^{+0.27}_{-0.42}$	$0.29^{+0.04}_{-0.03}$
228	$8.68^{+0.21}_{-0.15}$	$0.28^{+0.07}_{-0.07}$	$-9.24^{+0.26}_{-0.31}$	$10.67^{+0.83}_{-1.69}$	$0.18^{+0.04}_{-0.03}$
229	$10.17^{+0.11}_{-0.14}$	$4.45^{+2.99}_{-1.25}$	$-9.53^{+0.34}_{-0.23}$	$9.3^{+1.58}_{-1.66}$	$0.49^{+0.36}_{-0.25}$
230	$\mathbf{9.54^{+0.02}_{-0.02}}$	$\mathbf{2.61^{+0.1}_{-0.1}}$	$\mathbf{-9.13^{+0.03}_{-0.03}}$	$\mathbf{11.45^{+0.11}_{-0.13}}$	$\mathbf{1.44^{+0.24}_{-0.19}}$
231	$9.4^{+0.13}_{-0.16}$	$0.81^{+0.45}_{-0.32}$	$-9.51^{+0.36}_{-0.27}$	$9.38^{+1.7}_{-1.74}$	$1.43^{+0.29}_{-0.34}$
232	$9.42^{+0.05}_{-0.08}$	$0.63^{+0.09}_{-0.08}$	$-9.63^{+0.13}_{-0.1}$	$8.26^{+1.0}_{-0.8}$	$0.23^{+0.04}_{-0.03}$
233	$11.25^{+0.0}_{-0.0}$	$0.0^{+0.0}_{-0.0}$	$-22.99^{+1.48}_{-0.92}$	$0.69^{+0.11}_{-0.08}$	$0.89^{+0.01}_{-0.0}$
234	$\mathbf{8.74^{+0.11}_{-0.18}}$	$\mathbf{0.15^{+0.04}_{-0.03}}$	$\mathbf{-9.55^{+0.26}_{-0.18}}$	$\mathbf{9.06^{+1.46}_{-1.34}}$	$\mathbf{0.05^{+0.02}_{-0.02}}$
235	$9.43^{+0.05}_{-0.06}$	$0.55^{+0.08}_{-0.08}$	$-9.68^{+0.1}_{-0.12}$	$8.11^{+0.95}_{-0.69}$	$0.17^{+0.03}_{-0.02}$
236	$\mathbf{9.26^{+0.06}_{-0.06}}$	$\mathbf{1.46^{+0.2}_{-0.18}}$	$\mathbf{-9.1^{+0.11}_{-0.11}}$	$\mathbf{11.21^{+0.3}_{-0.39}}$	$\mathbf{0.12^{+0.02}_{-0.01}}$

4.3.2 SFHs as tracers of mergers

As discussed in Chapter 3, the HI-to-stellar mass ratio of a galaxy is related to the spin-filament alignment, such that galaxies which are misaligned have higher HI-to-stellar mass ratios. As gas-rich mergers are expected to increase the amount of neutral gas in galaxies (Ellison et al., 2018), this could suggest that galaxies which have recently undergone such a merger might have their spin-orientation disrupted with respect to the filament, whereas those galaxies which have not undergone a recent merger will tend to retain their alignment and their evolution is dictated by secular processes.

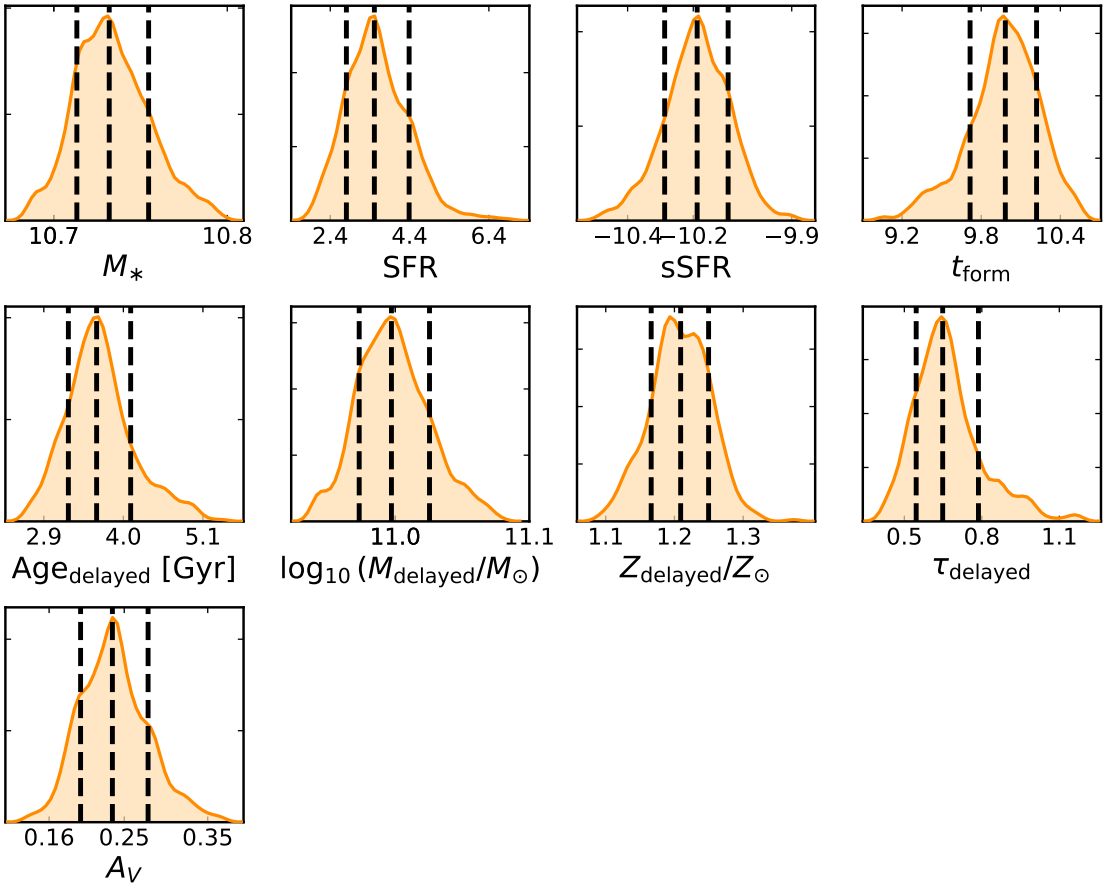

Figure 4.4: An example of the posteriors of one of the MIGHTEE-HI Early Science galaxies using the available photometric filters, fitted with an exponentially-delayed SFH model.

First of all, I check if there are any galaxies within the sample showing evidence of undergoing mergers. I only find 7 galaxies (of which only 4 are within 10 Mpc of a filament), which are randomly distributed in terms of the spin-filament alignment (they don't have a preference for either aligned or misaligned). Then, I continue to investigate this theory using the SFHs obtained from fitting photometry in BAGPIPES. An example of the SFR as a function of time (redshift) for one of the galaxies can be seen in Figure 4.6 for each SFH. I choose to focus on the exponentially-delayed SFH model, as discussed in the section above (however, tables for all correlations are shown in Appendix A). I took the 66 galaxies from Chapter 3 and I split them into aligned and misaligned, based on their spin-filament alignment. I visually inspected each of the SFHs for any disruptions, such as

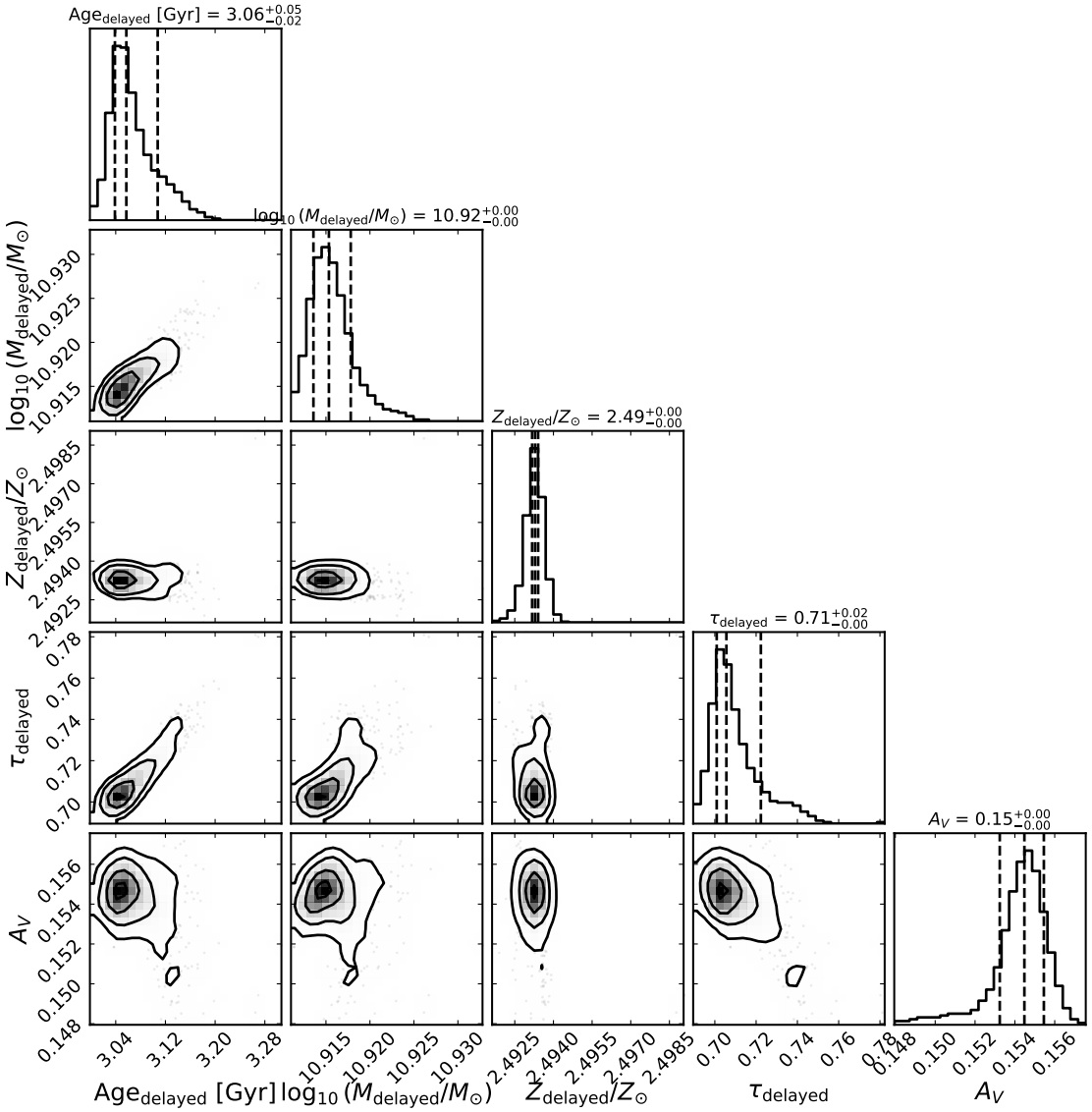

Figure 4.5: An example of a corner plot of one of the MIGHTEE-HI Early Science galaxies using the available photometric filters, fitted with an exponentially-delayed SFH model.

bumps in the SFR. I did not find any major differences between the aligned sample and the misaligned sample. Then, I tested if there is any correlation between the spin-filament alignment angle and the time it took for the HI galaxies to reach their peak star formation. As can be seen in Figure 4.7, there is no strong trend between the two parameters, independent of the SFH model I choose. Additionally, I performed correlation tests between $|\cos\psi|$ and $t(z_{\rm form})$ by using Kendall's Tau (Kendall, 1938) and Spearman Rank (Glasser and Winter, 1961) tests. For the

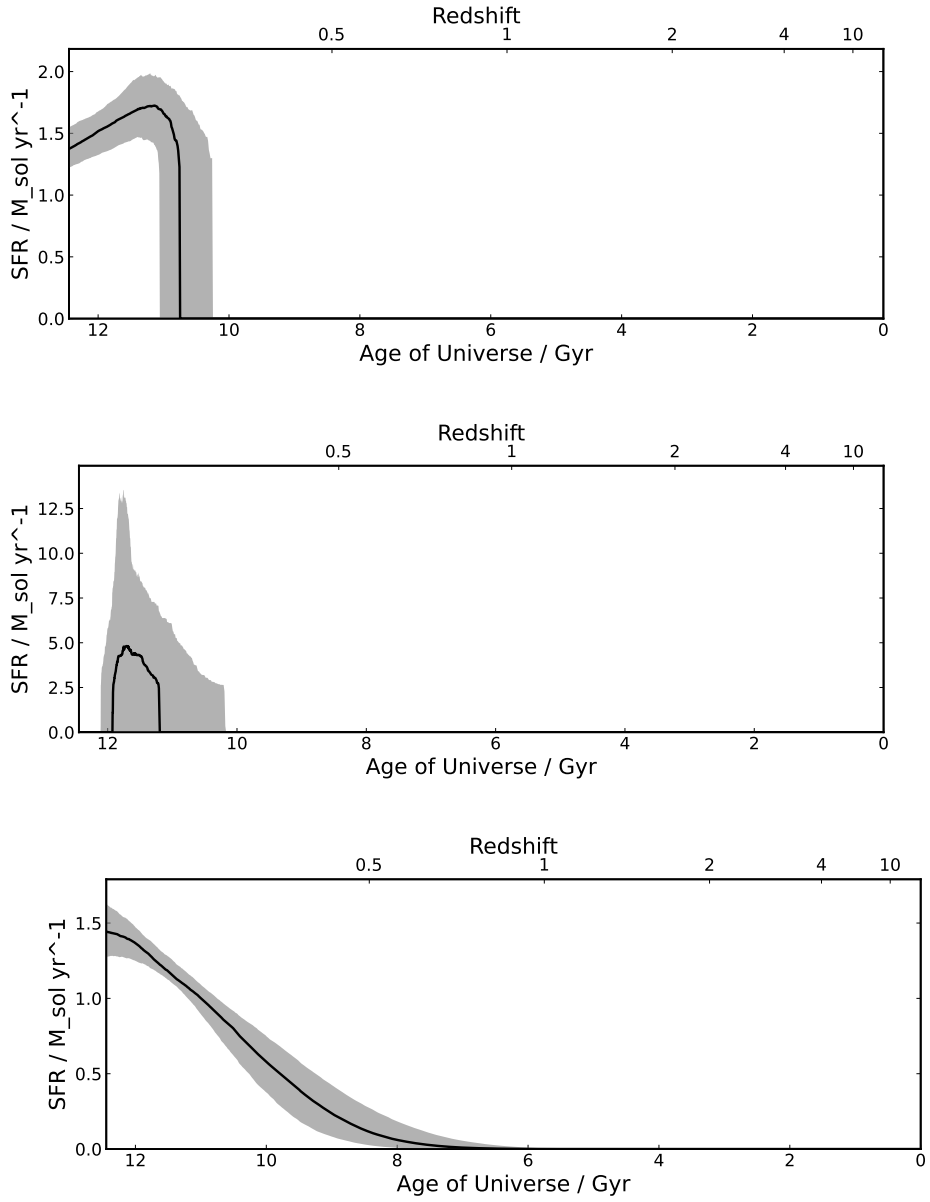

Figure 4.6: An example of several SFHs of one of the MIGHTEE-HI Early Science galaxies using the available photometry. The shaded area represents the error bars, calculated from the 16th and 84th percentiles. From top to bottom: exponential SFH, constant SFH and lognormal SFH. The burst case is not displayed here as for the chosen galaxy, a burst could not be fit to its spectrum.

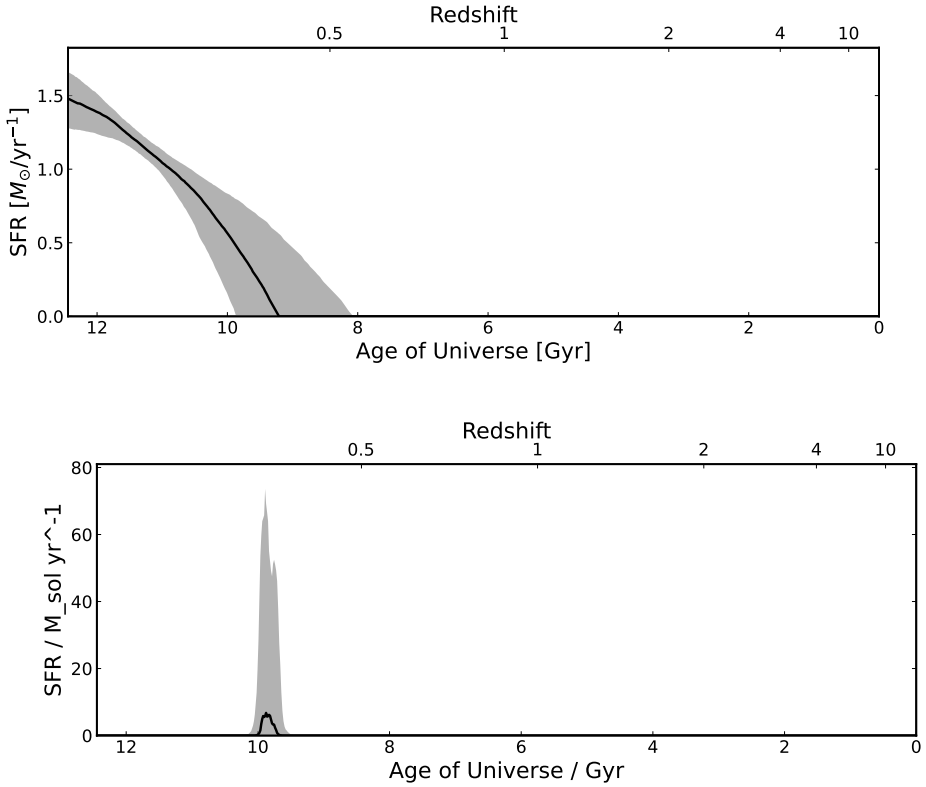

Figure 4.6: An example of several SFHs of one of the MIGHTEE-HI Early Science galaxies using the available photometry. The shaded area represents the error bars, calculated from the 16th and 84th percentiles. From top to bottom: exponentially-delayed SFH and double-power law SFH. The burst case is not displayed here as for the chosen galaxy, a burst could not be fit to its spectrum (cont.).

exponentially-delayed SFH, I obtain a τ of 0.098 with an associated p-value of 0.261 and a Spearman Rank coefficient of 0.148 with an associated p-value of 0.251, showing that there is no evidence for a correlation.

Another way to look at the link between the spin-filament alignment and the HI is by using the gas depletion time. By using the computed SFR from the SFHs with the $M_{\rm HI}$ measured from the 21cm line, the gas depletion time is calculated as:

$$t_{\rm dep} = \frac{\rm SFR}{M_{\rm HI}}. \tag{4.3}$$

In Figure 4.8, I plot the SFR-$M_{\rm HI}$ relation, with the galaxies which are within $d_{\rm fil} < 10$ Mpc of a filament, split into aligned and misaligned on top. As can be seen, there is no evident trend, as both aligned and misaligned galaxies fall across

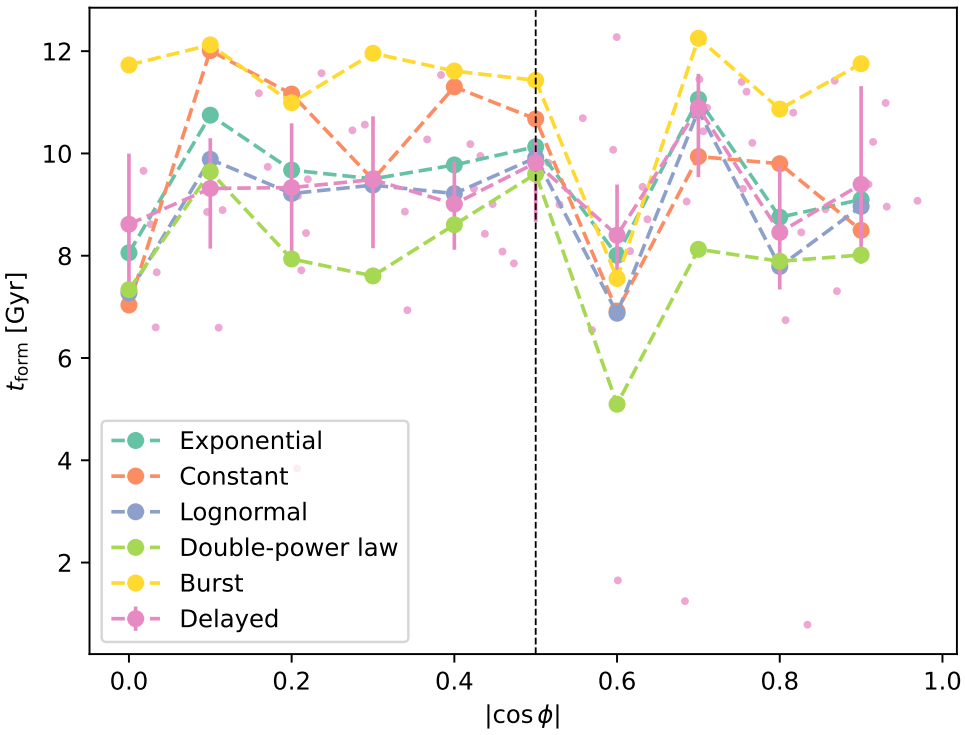

Figure 4.7: A scatter plot illustrating the spin-filament cos-angle $|\cos\psi|$ of a galaxy as a function of $t(z_{\rm form})$ for the exponentially-delayed SFH, with all the other SFHs plotted as running medians. The vertical dotted line represents $|\cos\psi| = 0.5$, where I split the sample as being either aligned (≥ 0.5) or misaligned (≤ 0.5) with respect to their closest filament. The error bars on the medians (for clarity, I only show the exponentially-delayed SFH) are calculated by using the 16th and 84th percentile values of $t(z_{\rm form})$.

different depletion timescales. By running a 2D KS test (see Section 3.4.1), I find a p-value of 0.158, which confirms that it is not a statistically significant result.

Furthermore, for the full sample, I investigate if there is any link between the distance-to-filament and the peak of star formation, $t(z_{\rm form})$. As can be seen in Figure 4.10, there seems to be a preference for younger galaxies to be closer to filaments, whilst older ones are further. However, when I run the two correlation tests, I do not find this result to be statistically significant independent of the model used for the SFH. For the exponentially-delayed SFH, I obtain a τ of -0.063 with an associated p-value of 0.177 and a Spearman Rank coefficient of -0.095 with an associated p-value of 0.171. Similarly, when investigating a link between the gas depletion time and the distance-to-filament, there is no correlation - as can

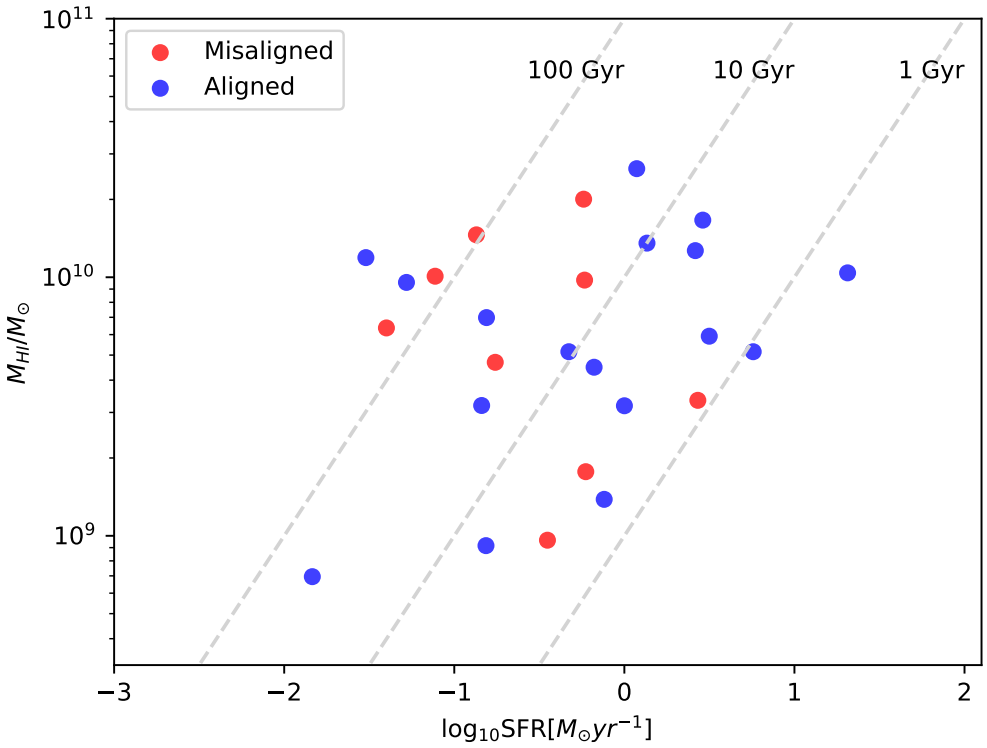

Figure 4.8: A scatter plot illustrating SFR as a function of $M_{\rm HI}$ for the exponentially-delayed SFH, with the galaxies within $d_{\rm fil} < 10$ Mpc of a filament, split into aligned (blue points) and misaligned (red points). The diagonal dashed lines represent lines of constant gas depletion times.

be seen in Figure 4.9. This follows from above, as for this sample, the timescales of star formation in a galaxy do not seem to have any link to its position with respect to the cosmic filaments.

I also investigate if there is a link between stellar mass and distance-to-filament. As can be seen in Figure 4.11, for the exponentially-delayed SFH, I obtain a τ of 0.041 with an associated p-value of 0.372 and a Spearman Rank coefficient of 0.064 with an associated p-value of 0.351, which is not statistically significant. The lack of a correlation between stellar mass and distance-to-filament is surprising, as it is expected for stellar mass to correlate with proximity to filament (e.g. Alpaslan et al., 2015; Laigle et al., 2017; Bonjean et al., 2020, or Chapter 5 of this thesis). This could be attributed to low number statistics, or the fact that the sample is HI-selected, which makes it biased towards certain stellar masses.

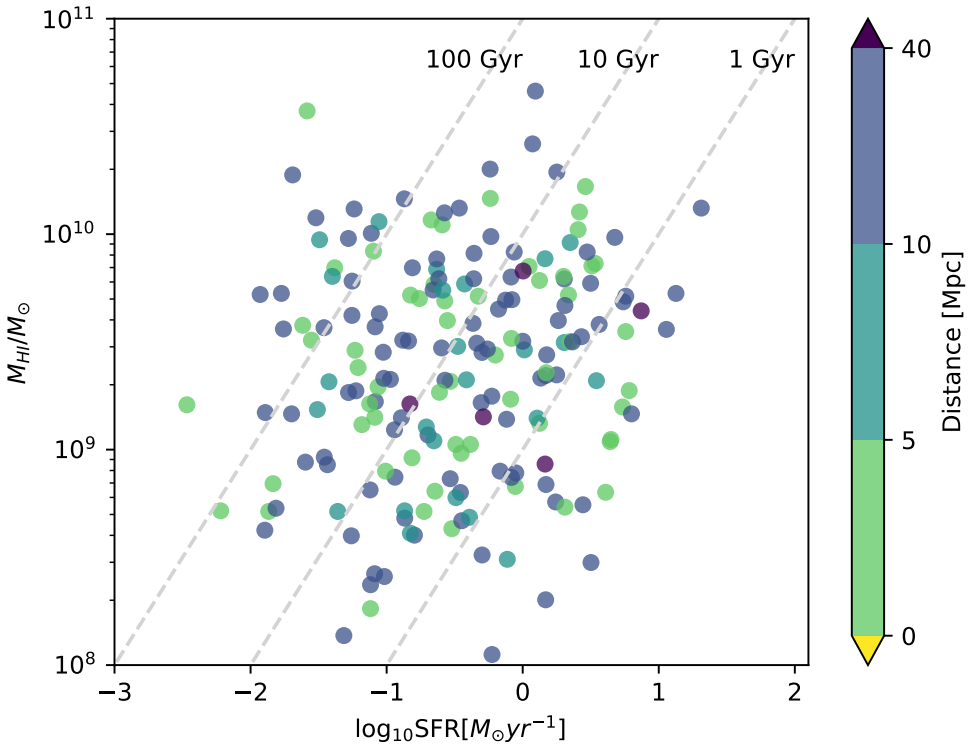

Figure 4.9: A scatter plot illustrating SFR as a function of $M_{\rm HI}$ for the exponentially-delayed SFH. The diagonal dashed lines represent lines of constant gas depletion times, whilst the colour bar shows the distance-to-filament for each galaxy, which is split in three distance bins: 5 Mpc, 10 Mpc and 40 Mpc.

4.3.3 HI properties as function of SFHs

As I do not find any strong correlations with respect to a galaxy's position and spin-angle with respect to the filament in the sub-sample, I investigate further links between the full HI galaxy sample and the time when the galaxies reached their peak star formation, as inferred by BAGPIPES for each SFH. Specifically, I am running these tests since HI serves as the raw material for the build-up of stellar mass in galaxies; however the processes involved in the conversion of HI to stars is complex and not well understood (Maddox et al., 2021).

First, I look into the HI mass as a function of the peak time of star formation, $t(z_{\rm form})$. As can be seen in Figure 4.12, all SFHs show a similar trend - a flat line independent of the value of $M_{\rm HI}$. Using two correlation tests (Kendall's Tau and Spearman Rank), I do not find any correlation, with a τ of -0.015 with an

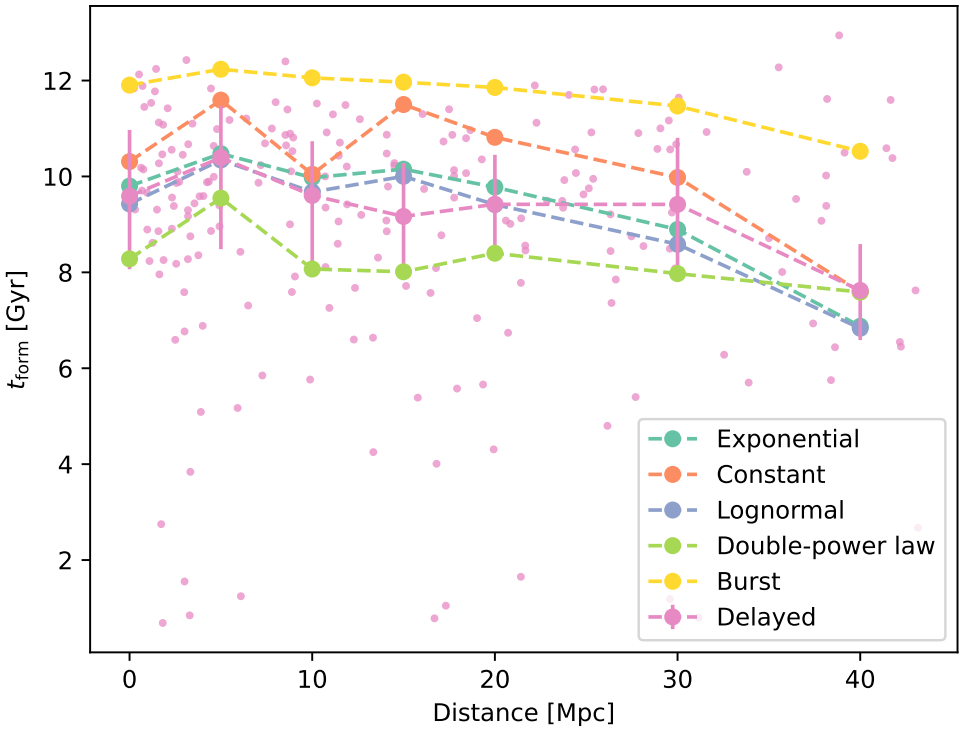

Figure 4.10: A scatter plot illustrating the distance to the closest filament of a galaxy as a function of the peak of the star formation of a galaxy for the exponentially-delayed SFH, with all the other SFHs plotted as running medians. The error bars on the medians (for clarity, I only show the exponentially-delayed SFH) are calculated by using the 16th and 84th percentile values of $t(z_{\rm form})$).

Table 4.4: The coefficients and p-values for the two correlation tests, Kendall's Tau and Spearman Rank, for each parameter against the $t(z_{\rm form})$ for the delayed SFH.

Parameter	**Kendall's Tau**		**Spearman Rank**	
	τ	**p-value**	**coefficient**	**p-value**
Distance	-0.063	0.177	-0.095	0.171
$\lvert\cos\psi\rvert$	0.098	0.261	0.148	0.251
$M_{\rm HI}$	-0.015	0.751	-0.026	0.711
M_*	-0.402	10^{-16}	-0.573	10^{-16}
$M_{\rm HI}/M_*$	0.345	10^{-16}	0.509	10^{-16}

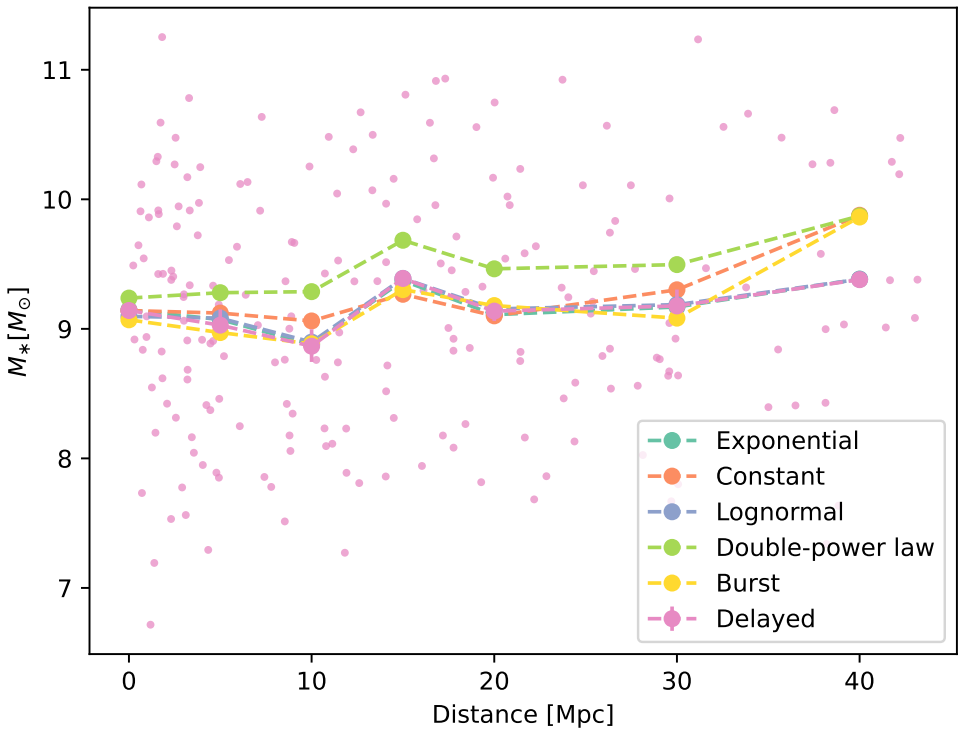

Figure 4.11: A scatter plot illustrating the distance to the closest filament of a galaxy as a function of stellar mass for the exponentially-delayed SFH, with all the other SFHs plotted as running medians. The error bars on the medians (for clarity, I only show the exponentially-delayed SFH) are calculated by using the 16th and 84th percentile values of stellar mass).

associated p-value of 0.751 and a Spearman Rank coefficient of -0.026 with an associated p-value of 0.711 for the exponentially-delayed SFH.

Then, I investigated the HI-to-stellar mass ratio of a galaxy as a function of $t(z_{\rm form})$ to check how the shape of the SFH and the age of the stellar population is affected. As can be seen in Figure 4.13, there is a positive correlation between the two parameters. This is also confirmed by the two correlation tests, in which I obtain a τ of 0.345 with an associated p-value of 10^{-16} and a Spearman Rank coefficient of 0.509 with an associated p-value of 10^{-16} for the exponentially-delayed SFH. With the exception of the double-power law SFH, all the other SFHs show similar values of the correlation tests.

As $M_{\rm HI}$ does not show a correlation with $t(z_{\rm form})$ but $M_{\rm HI}/M_*$ does, I also

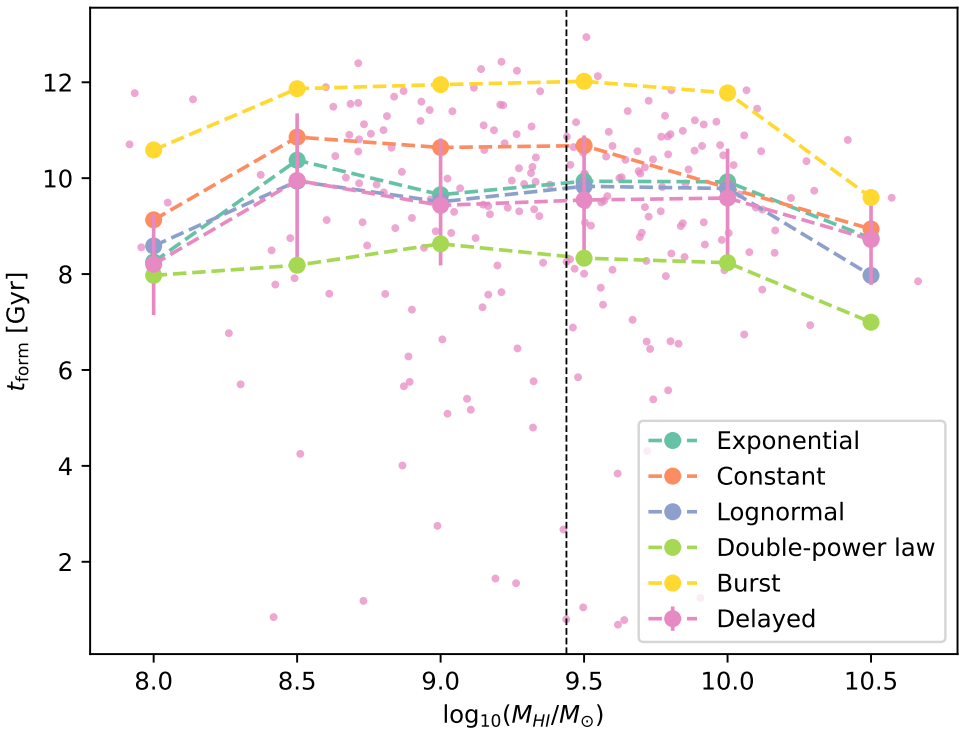

Figure 4.12: A scatter plot illustrating the HI mass of a galaxy as a function of $t(z_{\rm form})$ for the exponentially-delayed SFH, with all the other SFHs plotted as running medians. The dotted vertical line represents the median $M_{\rm HI}$ value of the sample. The error bars on the medians (for clarity, I only show the exponentially-delayed SFH) are calculated by using the 16th and 84th percentile values of $t(z_{\rm form})$.

investigated if there is any relationship between the stellar mass of a galaxy M_* and $t(z_{\rm form})$. As can be seen in Figure 4.14, there is a strong anti-correlation between the time a galaxy reached its peak star-formation and its stellar mass. This is also confirmed by the correlation tests, where I obtained a τ of -0.402 with an associated p-value of 10^{-16} and a Spearman Rank coefficient of -0.573 with an associated p-value of 10^{-16} for the exponentially-delayed SFH. Similar to the $M_{\rm HI}/M_*$ case, this is seen across all the SFHs with the exception of the double-power law SFH.

As I have calculated the HI depletion time in the section above, in Figure 4.15, I show an example for the exponentially-delayed SFH, split in terms the stellar mass (colour bar), the mid point being represented by the median stellar mass of the sample. As shown in Pan et al. (2023), using LEPHARE-based SFRs (which

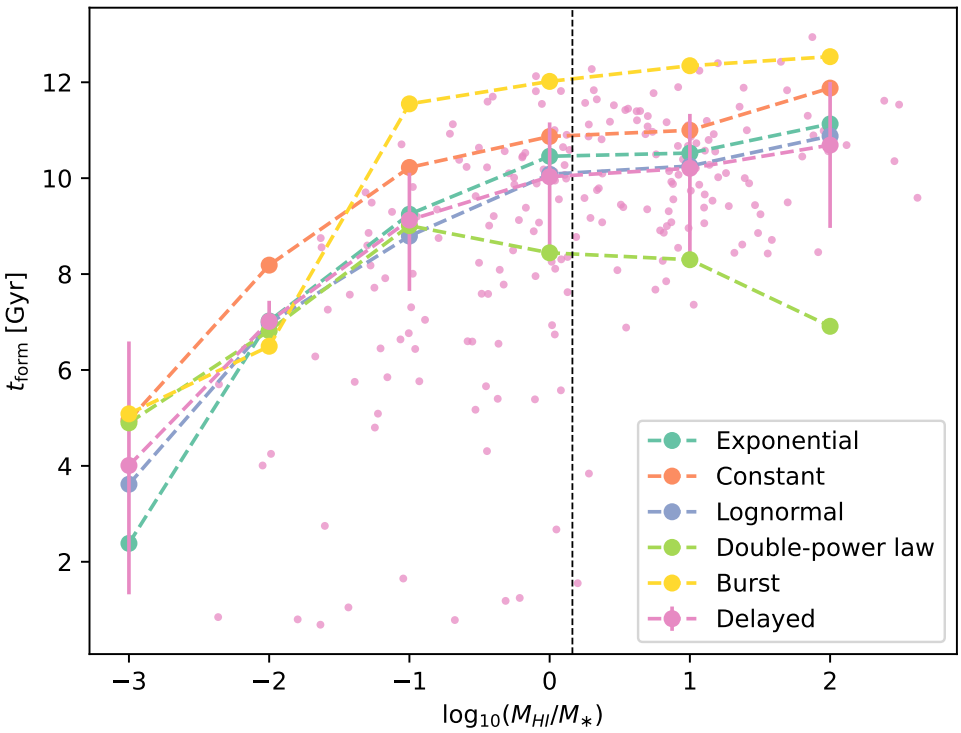

Figure 4.13: A scatter plot illustrating the HI-to-stellar mass fraction of a galaxy ($\frac{M_{\rm HI}}{M_\star}$) as a function of the time when it reached peak star formation for the exponentially-delayed SFH, with all the other SFHs plotted as running medians. The error bars on the medians (for clarity, I only show the exponentially-delayed SFH) are calculated by using the 16th and 84th percentile values of $t(z_{\rm form})$.

assumes an exponential SFH) for the MIGHTEE-HI Early Science sample, most of the galaxies have a depletion time in the range of 1 to 100 Gyr. As can be seen, lower HI mass galaxies tend to have a higher gas depletion time, whilst higher HI mass galaxies tend to have a lower gas depletion time.

In Figure 4.16, I repeat the process, but I split the sample in terms of the HI-to-stellar mass ratio. As can be seen, galaxies with higher HI-to-stellar mass ratios have longer depletion times, whilst galaxies with lower HI-to-stellar mass ratios have shorter depletion times.

Then, in Figure 4.17, I split the sample based on the peak time of star formation for each galaxy (at the median). In this case, no correlation can be seen, as the points are randomly distributed across different timescales of depletion.

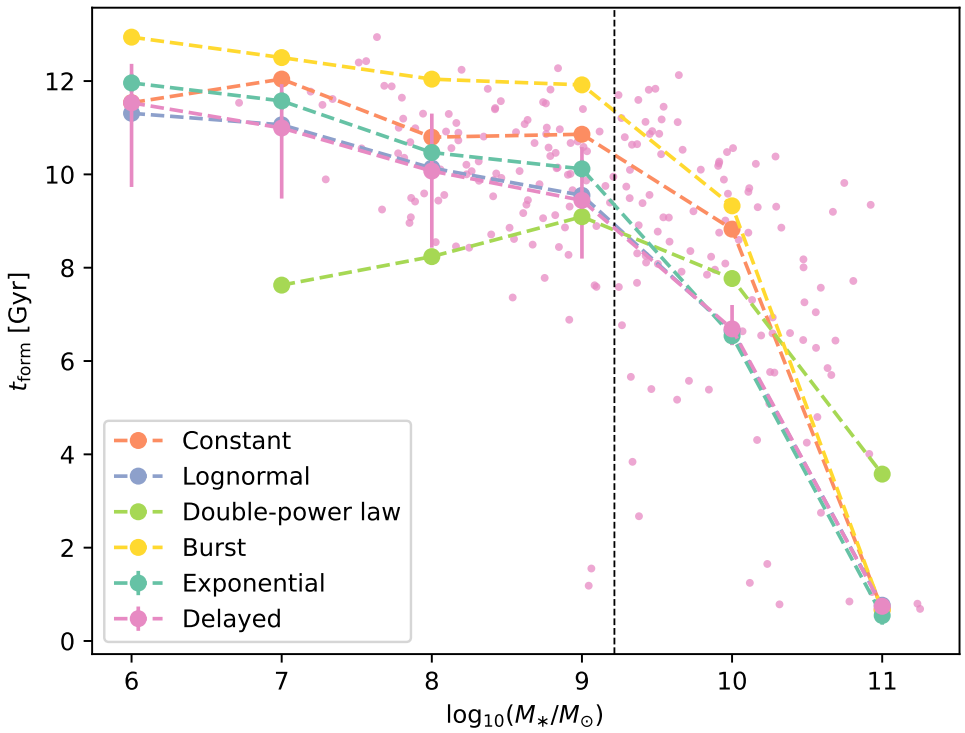

Figure 4.14: A scatter plot illustrating the stellar mass $M_\star$ of a galaxy as a function of the time when it reached its peak star-formation for the exponentially-delayed SFH, with all the other SFHs plotted as running medians. The error bars on the medians (for clarity, I only show the exponentially-delayed SFH) are calculated by using the 16th and 84th percentile values of $t(z_{\rm form})$.

4.3.4 Discussion

Spin-filament alignment and SFHs

I do not find evidence of recent star-formation that could indicate mergers in galaxies which have their spin misaligned with their closest filament. I also do not find any evidence for a correlation between the time when a galaxy reached its peak star formation and the spin-filament alignment cos-angle. There are two possibilities which could explain this result: either mergers do not explain the link between the HI-to-stellar mass ratio and the spin-filament alignment or the photometric data is not good enough to infer accurate SFHs from which mergers could be traced.

For the former case, it is possible that the HI-to-stellar mass ratio is actually a secondary correlation with the spin-filament alignment. As seen in Figure 4.7,

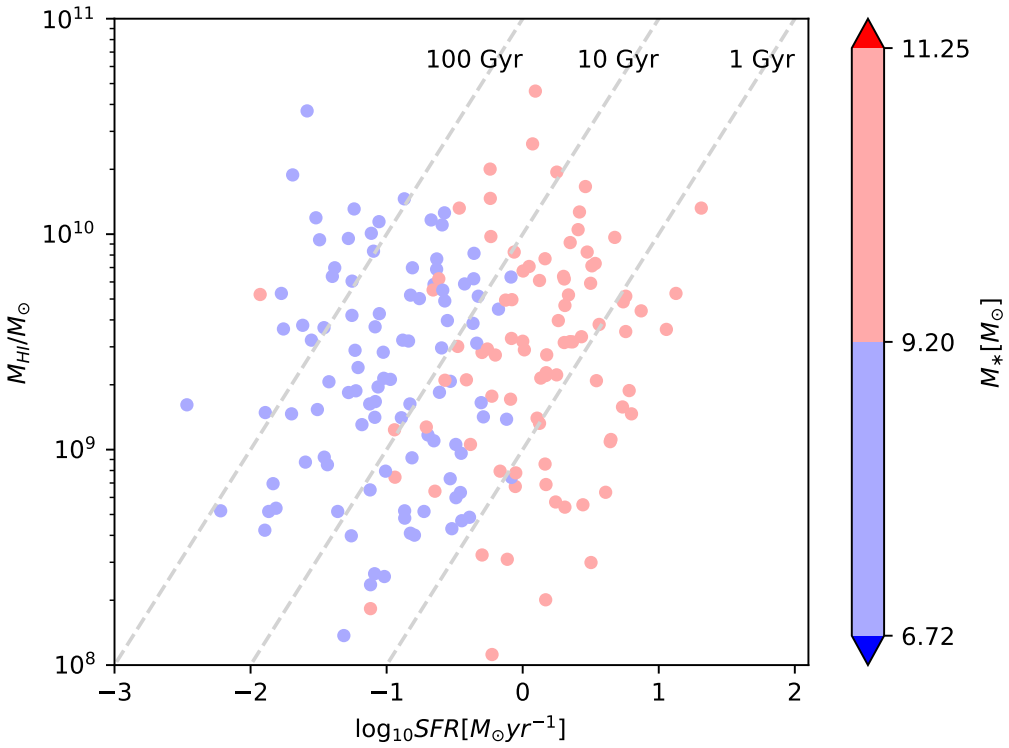

Figure 4.15: A scatter plot illustrating SFR as a function of $M_{\rm HI}$ for the exponentially-delayed SFH. The diagonal dashed lines represent lines of constant gas depletion times, whilst the colour bar shows the stellar mass for each galaxy, which is split at the median value of the whole sample.

the HI-to-stellar mass ratio correlates with the peak of star formation. This could imply that the quantity to which the spin-filament alignment is related to could actually be the age of the galaxy, with the HI-to-stellar mass ratio as a proxy. In this case, it would imply that the spin of a galaxy has either been imprinted during its formation (White, 1984; Lee and Pen, 2000; Lee and Erdogdu, 2007; Moon and Lee, 2024) or merger events are not the primary mechanism for the generation of the spin transition (Forero-Romero et al., 2014; Lee and Moon, 2022). Furthermore, it is also possible that some mergers would not leave the signature expected in the SFR, even if they have occurred. For example, at low redshift, rich galaxy mergers can exert a minimal impact on the galaxies' SFR (Li et al., 2023) or fail to trigger starbursts due to short timescales (Di Matteo et al., 2008; Cortijo-Ferrero et al., 2017) or a clumpy, turbulent interstellar medium (Perret et al., 2014).

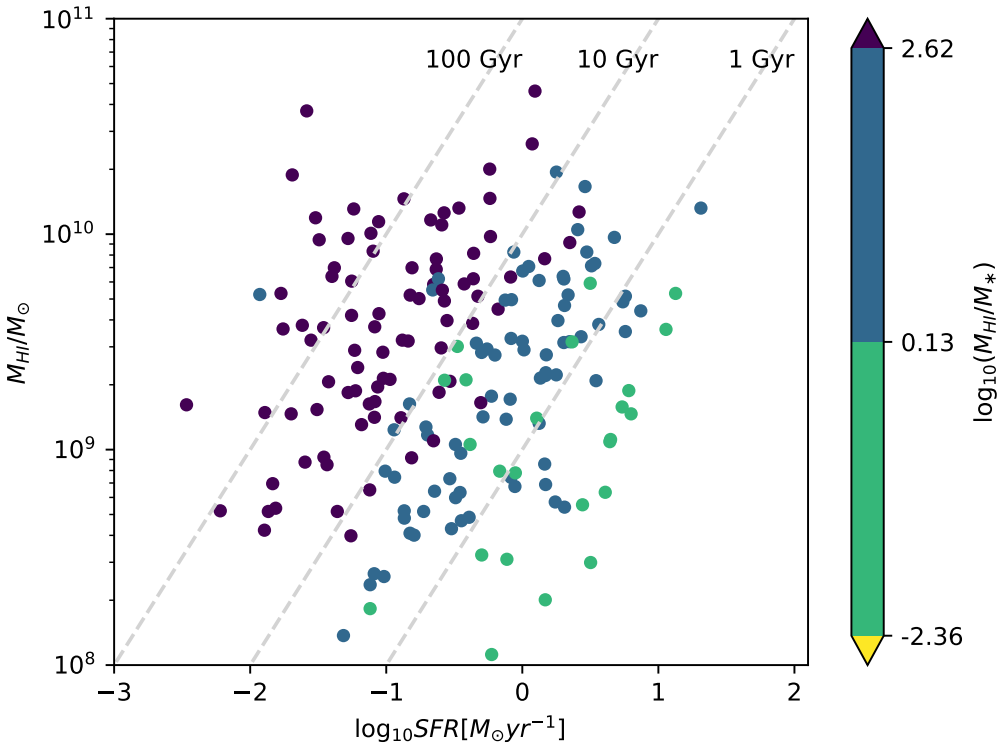

Figure 4.16: A scatter plot illustrating SFR as a function of $M_{\rm HI}$ for the exponentially-delayed SFH. The diagonal dashed lines represent lines of constant gas depletion times, whilst the colour bar shows the HI-to-stellar mass ratio for each galaxy, which is split at the median value of the whole sample.

For the latter case, inferring SFHs from photometric data can be difficult. The observed photometry may be dominated by the light from recently-formed stars, even if the actual galaxy mass is dominated by older stars that are not as easily seen in the observed light. This can lead to an underestimation of the age of the galaxy and the contribution of older stars to the total mass (Conroy et al., 2009; Conroy, 2013). It has been shown that in order to recover SFHs more accurately, spectroscopic data will always be required (Nersesian et al., 2024). This is because spectroscopy allows for the analysis of individual spectral lines, which can provide diagnostic information about the number of stars in a given mass range. Using methods such as spectro-photometric fitting (e.g. Bruzual and Charlot, 2003; Gallazzi and Bell, 2009; Cappellari, 2023), which combines both spectroscopic and photometric data, can provide more reliable estimates of SFHs by taking into account the full spectrum of

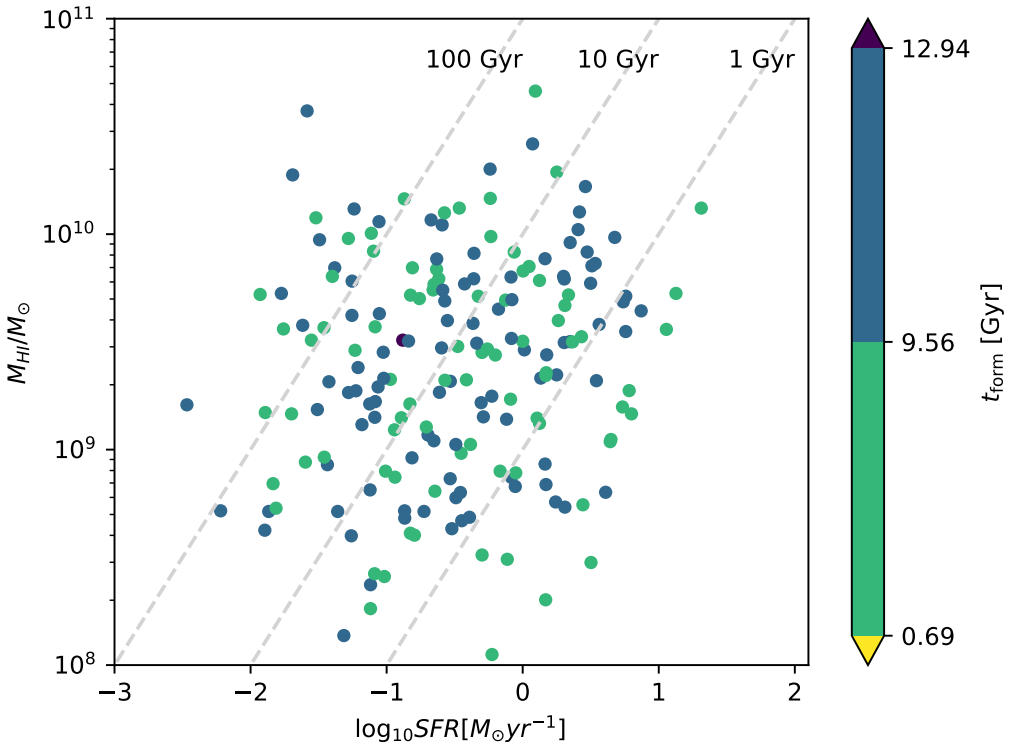

Figure 4.17: A scatter plot illustrating SFR as a function of $M_{\rm HI}$ for the exponentially-delayed SFH. The diagonal dashed lines represent lines of constant gas depletion times, whilst the colour bar shows the peak time of star formation for each galaxy, which is split at the median value of the whole sample.

the galaxy and considering a range of possible SFHs. Furthermore, the assumption of a simple and parameterised SFH can introduce additional uncertainties in the models. By assuming a specific functional form for the SFH, such as constant or exponentially declining, one may be unable to model bursts of star formation, rejuvenation, sudden episodes of quenching or other non-standard star formation activity accurately (Simha et al., 2014; Leja et al., 2019; Iyer et al., 2019).

Also in terms of the filaments, I investigate if there is any link between the distance-to-filament of a galaxy and the time when it reached its peak star formation. Whilst Figure 4.10 shows a tendency of older galaxies to be further from the filaments, this is not statistically significant. Other studies find that older galaxies tend, in fact, to be found more preferentially in clusters as opposed to filaments/voids (e.g. Bernardi et al., 2006; Smith et al., 2012b; Chen et al., 2017).

HI galaxy properties and SFHs

In terms of HI properties, whilst I found no correlation between the time when a galaxy reached its peak star formation and its $M_{\rm HI}$, I found that $M_{\rm HI}/M_*$ is correlated with the time when a galaxy reached its peak star formation, independent of the star formation pathway. This implies that older galaxies have less HI - which could be explained by the fact that they have already used the bulk of their cold gas reservoir in order to form stars. This has been also observed in the Survey of Ionisation in Neutral Gas Galaxies (SINGG; Meurer et al., 2006), in which Hanish et al. (2006) observed that the most massive galaxies have a larger fraction of their mass locked up in stars compared with HI, while the opposite is true for less massive galaxies. Hence, lower mass galaxies are not as evolved because they have converted less of their ISM into stars than high mass galaxies, so they will have more gas available. The higher HI-to-stellar mass ratio in a galaxy is then an indicator of how quickly a galaxy's SFH reached its peak: dwarf galaxies or very late types have not formed most of their stars yet, and that is why the SFH peaks at a later times. The stellar mass of a galaxy being anti-correlated with the time when it reached its peak star formation is not entirely surprising, given the result from the HI-to-stellar mass ratio. It follows that galaxies with higher stellar masses have likely formed stars earlier in their evolution and have used up a larger portion of their gas reservoirs.

This is also reflected in the correlations found with the gas depletion time. I show that gas-rich galaxies with higher HI mass fractions have longer gas depletion times. This means that they can sustain star formation at their current rate for a longer period of time before their gas is completely depleted. This is consistent with the idea that gas-rich galaxies have a higher potential for ongoing star formation and can replenish their gas reservoirs through accretion from their immediate surroundings (i.e. their CGM; Jaskot et al., 2015; Lutz et al., 2017), even if I find no relation to the larger-scale environment (the filaments). Furthermore, the observed correlation between stellar mass and gas depletion time suggests that more massive galaxies not only have higher gas masses but also a more efficient utilisation of their gas reservoirs for star formation. As dwarf galaxies form in

lower potential wells, the gas will experience a lower gravitational pull, allowing more gas to escape or not allowing it to collapse, preventing efficient replenishment. At the other end, the massive galaxies have a higher density of gas in the central regions, which facilitates star formation (Saintonge et al., 2012; Parkash et al., 2018; Saintonge and Catinella, 2022). For the peak time of star formation, I find no correlation with the gas depletion time, which suggests that it is independent of the gas depletion time. Instead, the peak time of star formation is likely influenced by other factors such as galaxy interactions, mergers, and the availability of cold gas in the surrounding environment (Leroy et al., 2008; Popping et al., 2014; Somerville et al., 2015; Díaz-García and Knapen, 2020).

4.4 Conclusions

In this chapter, I make use of the star formation histories of 237 galaxies from the MIGHTEE-HI Early Release data in order to investigate links between the HI content of galaxies, the large-scale structures of the cosmic web and star formation. In terms of the spin-filament alignment and SFHs, the main findings are:

- By using BAGPIPES, an Bayesian inference-based SED fitting code, I find that most of the galaxies are best described by either a delayed-exponentially declining or an exponentially declining model for the SFHs;
- By visually inspecting the SFHs of a sub-sample, I do not find any signs of recent episodes of star formation in the misaligned galaxies; furthermore, for the 66 galaxies sub-sample where I could calculate the spin-filament alignment cos-angle, $|\cos\psi|$ does not correlate with the peak time of star formation $t(z_{\rm form})$;
- I find no significant trend between the gas depletion time and the spin-filament alignment cos-angle, $|\cos\psi|$;
- I find that there is a trend for older HI galaxies to be further from the filament for all SFHs - however, this trend is not statistically significant.

As discussed, these conclusions could be explained in two ways: either the photometric data is not good enough to constrain SFHs such that a merger history would be observed; or mergers are not the cause for the split in the spin-filament alignment, such that the HI-to-stellar mass ratio is a secondary correlation to another parameter, such as age. Therefore, the hypothesis that SFHs can be used to explain the difference in the spin-filament alignment as a function of HI-to-stellar mass ratio cannot be excluded.

In terms of the HI properties with respect to the SFHs, the main findings are:

- I do not find any strong correlation between the HI mass of galaxies and the time of the peak of star formation for any of the SFHs;
- I find strong correlations between the HI-to-stellar mass ratio and the time of the peak of star formation (positive correlation) and stellar mass and the time of the peak of star formation (anti-correlation) for all the SFHs except for the double-power law SFH;
- For the gas depletion time, I find correlations between depletion time and HI-to-stellar mass ratio and stellar mass of a galaxy, but I find no correlation between depletion time and peak time of star formation for a galaxy.

These correlations are consistent with the picture that smaller, gas-rich galaxies have a higher depletion time due to a shallower potential well and less efficient star formation, whilst more massive galaxies have already depleted their gas and formed stars efficiently.

I am going to call my child riz but in italic letters after the optical filters.

Casey Cragg

5

Galaxies at higher redshift: Links between galaxy properties and filaments

Contents

5.1 Introduction

Davis et al. (1982) and de Lapparent et al. (1986) presented the earliest observational evidence of the cosmic web, finding a web-like distribution of galaxies. 21st century galaxy redshift surveys, such as the Sloan Digital Sky Survey (SDSS; York et al., 2000), 2dF Galaxy Redshift Survey (2dFGRS; Colless et al., 2001) and 2MASS Redshift Survey (2MRS; Huchra et al., 2012) have now traced it over much larger scales to greater fidelity.

By understanding the nature of the cosmic web, we can probe deeper into its effect on galaxy formation and evolution. The effect of the filamentary large-scale structure is not as well understood. Morphology, stellar mass, colour, star formation rate (SFR) and specific star formation rate (sSFR) are all be sensitive to the larger-scale environment, especially with respect to the filaments. However, in the same way that this picture is uncertain when it comes to angular momentum, it comes with the same challenges when trying to associate the exact effect of the cosmic web on the stellar mass and the SFR of a galaxy. When it comes to stellar mass, the most widely accepted result is that massive, red, quiescent galaxies tend to lie closer to the spine of the filaments (e.g. Alpaslan et al., 2015; Kraljic et al., 2017; Laigle et al., 2017; Chen et al., 2017; Malavasi et al., 2017; Luber et al., 2019). In terms of the star-formation activity in galaxies and the relation to the large-scale environment, the relation is more complicated. As discussed in Chapter 1.5.2, there are two proposed models that may explain some of these processes are the Cosmic Web Detachment (CWD, Aragón-Calvo et al., 2019) and the Cosmic Web Enhancement (Vulcani et al., 2019). This is reflected in the different results obtained across both simulations and observations, such that some show that galaxies close to filaments are more likely to be quenched (Martínez et al., 2016; Kuutma et al., 2017; Kraljic et al., 2017; Malavasi et al., 2022), whilst other studies show that galaxies close to filaments are more likely to experience episodes of star formations (Darvish et al., 2014; Vulcani et al., 2019).

For this chapter, I use optically-selected galaxies from the COSMOS and XMM-LSS fields with photometric redshifts (and spectroscopic redshifts where available),

to find the filaments of the cosmic web and investigate how they influence the properties of the galaxies.

5.2 Data

5.2.1 COSMOS and XMM-LSS fields

The COSMOS (Scoville et al., 2007) and XMM-LSS fields are two of the most widely studied extragalactic fields accessible from the southern hemisphere. Over the past decade, they have been the subject of a large number of multi-wavelength surveys. The COSMOS field spans across $\sim 2\,\mathrm{deg}^2$, with its centre at $10^{\mathrm{h}}00^{\mathrm{m}}28.6^{\mathrm{s}}$ in RA and $02°12'21.0''$ in Dec (J2000 coordinates). The XMM-LSS field that I use spans $\sim 4.5\,\mathrm{deg}^2$, centred at $02^{\mathrm{h}}22^{\mathrm{m}}00^{\mathrm{s}}$ in RA and $-04°48'00''$ in Dec.

Imaging at visible wavelengths is provided by the HyperSuprimeCam Strategic Survey Programme DR3 (HSC; Aihara et al., 2022) and near-infrared imaging is sourced from the UltraVISTA survey in the COSMOS field (McCracken et al., 2012) and the VISTA Deep Extragalactic Observations (VIDEO; Jarvis et al., 2013) Survey in the XMM-LSS field. For COSMOS, I use the photometry in 11 filters: *ugrizy*, NB0921 (HSC) and $\mathrm{YJHK_s}$ (VISTA). Similarly, for XMM-LSS I use 10 filters - the same as above, with the exception of NB0921.

5.2.2 Hierarchical Bayesian redshift catalogue

I utilise the photometric redshift catalogue over the COSMOS and XMM-LSS fields from Hatfield et al. (2022) and Stylianou et al. (in prep), encompassing more than 2.7 million galaxies within the COSMOS and XMM-LSS fields, within a redshift interval of $0.0 < z < 9.0$. In the COSMOS field, it covers an area of $\sim 1.8\,\mathrm{deg}^2$ (accounting for masking), whilst in XMM-LSS it covers an area of $\sim 4.33\,\mathrm{deg}^2$ (accounting for the overlapping between the VISTA area and the HSC area). This catalogue comprises photometric redshifts derived through two distinct methods: template fitting using `LePhare` (Arnouts et al., 1999; Ilbert et al., 2006) and a machine learning algorithm 'GPz,' which is based on a sparse Gaussian process (Almosallam et al., 2016b; Almosallam et al., 2016a). These methods

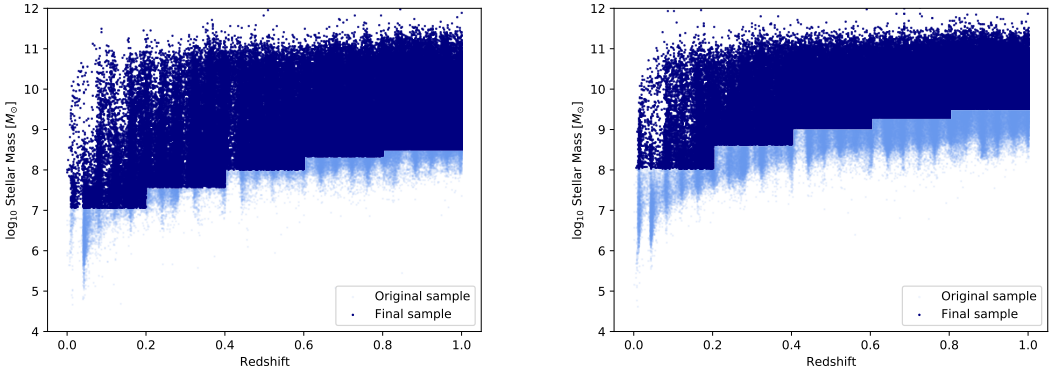

(a) COSMOS **(b)** XMM-LSS

Figure 5.1: Stellar mass versus redshift K_s-band completeness cuts for the COSMOS and XMM-LSS galaxies. The original sample is shown in light blue and the dark blue points represent the final sample I use for this study, split into redshift bins of $\delta z = 0.2$.

produce distinct redshift probability distribution functions (PDFs), and these PDFs are combined using the Hierarchical Bayesian combination (Duncan et al., 2018a; Duncan et al., 2018b). The use of these catalogues ensures that exactly the same methodology for determining photometric redshifts is used for both fields.

Furthermore, both catalogues have been masked to remove any foreground stars and dead pixels. Any background stars have been removed by using a colour-colour diagram same as Jarvis et al. (2010) and following the stellar locus approach of Baldry et al. (2010).

5.2.3 `LePhare`

In order to obtain stellar masses, star formation rates (SFR) and specific star formation rates (sSFR) for the catalogue, I use LePhare. LePhare is an SED fitting code written in Fortran, which is uses template fitting in order to compute redshifts and galaxy properties.

I use imaging at visible wavelengths is provided by the HyperSuprimeCam Strategic Survey Programme DR3 (HSC; Aihara et al., 2022) and the Canada France Hawaii Telescope Legacy Survey (CFHTLS; Lilly et al., 1995) and near-infrared imaging is sourced from the UltraVISTA survey in the COSMOS field (McCracken et al., 2012) and the VISTA Deep Extragalactic Observations (VIDEO;

Jarvis et al., 2013) Survey in the XMM-LSS field. I use the catalogues described in Adams et al., 2021, with updated photometry from Varadaraj et al., 2023, which include imaging from the $u-$band through to K_s band (see Table 5.1, which aggregates the information from Adams et al., 2021 and Varadaraj et al., 2023).

Table 5.1: Summary of the 5σ detection depths within the COSMOS and XMM-LSS fields. The depths are calculated in 2 arcsec diameter circular apertures, placed on empty regions of the image. Sources in the catalogues have a point-source aperture correction applied. The XMM-LSS field is split into three regions of 1.5 deg^2 corresponding to the VISTA VIDEO tiles, and ordered from low to high RA.

Filter	COSMOS	XMM1	XMM2	XMM3
u^*	27.0	25.8	25.8	26.9
g	27.1	-	-	27.0
r	26.7	-	-	26.6
i	26.4	-	-	26.4
G	27.2	27.0	26.4	26.5
R	26.8	26.5	26.1	26.1
I	26.6	26.4	25.4	25.6
NB0921	26.0	-	-	
z	25.9	26.3	24.6	24.8
y	25.5	25.6	24.1	24.1
Y	25.5	25.2	25.1	25.2
J	25.3	24.7	24.7	24.7
H	25.0	24.2	24.3	24.3
K_s	24.8	23.8	23.9	23.9

Given that I already have redshifts for the galaxies, I fix the redshift values and run LePhare with the COSMOS SED template for the galaxies (Ilbert et al., 2009), as well as the Bruzual and Charlot (2003) template. For dust, I apply the Calzetti et al. (2000) extinction law with E(B-V) $= 0.0, 0.05, 0.1, 0.2, 0.3$.

5.2.4 Sample cuts

I selected the sources by applying cuts in the K_s band, to be close as possible to a stellar-mass cut following Adams et al. (2021). For the COSMOS sample, I limit

the sample to galaxies within $K_s = 25$, whilst for the XMM-LSS sample, I limit to a magnitude of $K_s = 23.8$, using a circular aperture with a diameter of $2''$.

In order to have a complete sample in terms of stellar mass, I follow the approach of Pozzetti et al. (2010) and Ilbert et al. (2013). This approach consists of calculating the lowest detectable stellar mass for a galaxy using the equation:

$$\log_{10}(M_{\rm lim}) = \log_{10}(M_*) + 0.4\left(K_s - K_s^{\rm lim}\right), \tag{5.1}$$

where $K_s^{\rm lim} = 25$ for COSMOS and $K_s^{\rm lim} = 23.8$ for XMM-LSS, as mentioned above. For this sample, I bin the galaxies in redshift sub-intervals of $\delta z = 0.2$. For each bin, I calculate the mass in which 90 per cent of the galaxies fall below $M_{\rm lim}$ and I cut the sample based on this limit. I then adopt the upper limit of the redshift interval to ensure uniform selection across the redshift bin. Figure 5.1 shows the original samples (light blue) in the two catalogues and the resulting samples (dark blue) after applying the cuts.

5.3 Methods

5.3.1 The Cosmic Web

Following the same steps as in Chapter 3, I use the filament-finding algorithm DISPERSE to calculate the skeleton of the cosmic web using the distribution of galaxies from the COSMOS and XMM-LSS fields.

For the catalogue, I split the redshift interval $0.0 < z < 1.0$ into smaller sub-slices with redshift widths of $\delta z = 0.01$ and combine these narrow shells into broader shells of $\delta z = 0.2$ - note that the choice of a wider bin for the initial filament finding does not affect the results. This broader bin width is chosen based on the accuracy inferred for the photometric redshifts which is typically $\delta z/(1+z) \lesssim 0.05$ over the redshift range I use (Hatfield et al., 2022). I choose a significance threshold of 3.5σ and mirror boundary conditions to determine the filament distribution. This is motivated by the comparisons in Sousbie (2011) and use the mirror boundary conditions to aid comparison with previous work (e.g. Luber et al., 2019; Blue Bird et al., 2020; Tudorache et al., 2022).

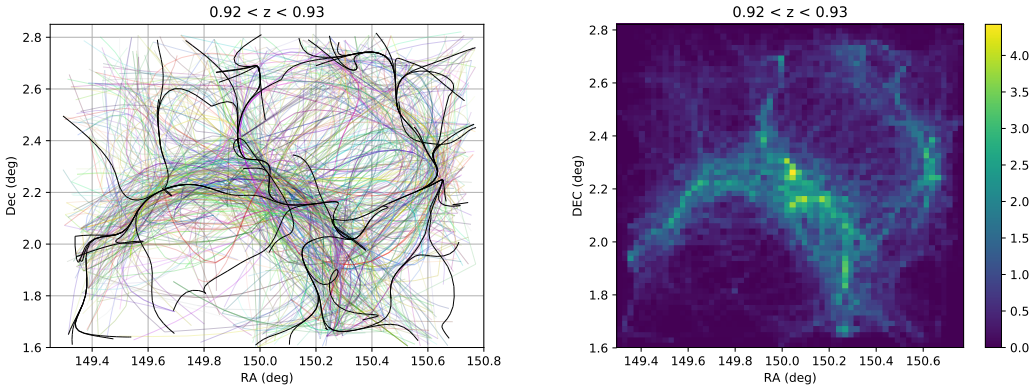

(a) (b)

Figure 5.2: An example of the filament distribution for a redshift slice in the COSMOS field. The figure on the left shows filament distributions obtained with the original catalogue (black line) and the filaments distributions obtained using the MC iterations (coloured lines). The figure on the right shows the same filament distribution as a 2D histogram, binning all the 101 iterations of possible filament distributions.

5.3.2 Resampling on Photometric Redshift Slices

Using the catalogue as described in Section 5.3.1 and the methods described in Chapter 2.2.3, I compute the different possible filament distributions for the associated photo-z errors. For each $\delta z = 0.01$ redshift slice, there will be 101 possible filament distributions, and for each broader redshift bin (of $\delta z = 0.2$) for which I analyse the results, there will be 2020 realisations of the filament distribution. An example of these realisations can be seen in Figure 5.2a for the COSMOS field for a narrow redshift slice of $0.92 < z < 0.93$. Figure 5.2b shows the same narrow redshift slice, but this time, all 101 iterations of the filament distribution are stacked together, highlighting the structures that are common in all the possible distributions. In this specific example, it can be seen that the largest structures (spine of the filament in the centre and top right, voids in the lower left and top right corners) persist throughout all the iterations.

However, an additional possible bias arises when investigating trends with redshift, due to the fact that each redshift slice has a different stellar mass threshold for the galaxies from which to construct the filaments and I return to this in Section 5.4.2.

5.4 Results and Discussion

5.4.1 Stellar Mass Dependence

To investigate the relationship between the galaxy mass and the distance to the filament or the node, I take each galaxy and crossmatch it with the filament network. I do this for each possible filament distribution from the resampled redshifts of the galaxies and crossmatch these filaments with the resampled galaxies. I then define a fraction f_i of galaxies within a distance x Mpc to a filament or node, such that

$$f_i = \frac{N_i(d < x \text{ Mpc})}{N_i(d < 50\text{Mpc})}, \tag{5.2}$$

where the numerator gives the number (N_i) of galaxies that lie within x Mpc of the their nearest filament/node, and I consider three cases for the filaments, where $x = 1, 5$ and 10 Mpc and a single case for the nodes with $x = 10$ Mpc. I reiterate that for the filaments I impose the additional constraint that the galaxy cannot lie within 5 Mpc of a node as defined in Section 2.2.3. For the denominator, I set a cut-off at 50 Mpc to compare to the properties of galaxies that are not within x Mpc of a filament/node. This also ensures that I do not take into account the erroneous filament iterations which introduce larger distances than expected given a redshift slice (i.e. iterations where most of the galaxies were not present in a redshift slice and the corresponding filament network is constructed from very few segments which are unreliable).

In Figure 5.3, I show how f_i (left for distance-to-filament and right for distance-to-node) of the 2020 realisations of the filaments and galaxy distributions changes as a function of redshift up to $z = 1.0$ for different stellar masses (noting that the minimum detectable stellar mass increases with redshift due to the flux-limit of the survey, see Figure. 5.1). The uncertainties are determined from the 16th and 84th percentiles of the fractions in each bin using all of the resampled distributions. As can be seen, there is no significant difference between the relative fractions of galaxy distances to filaments and nodes. The trend across the redshift bins is similar, with a peak at the lower mass end, followed by a steady decrease in the fraction towards

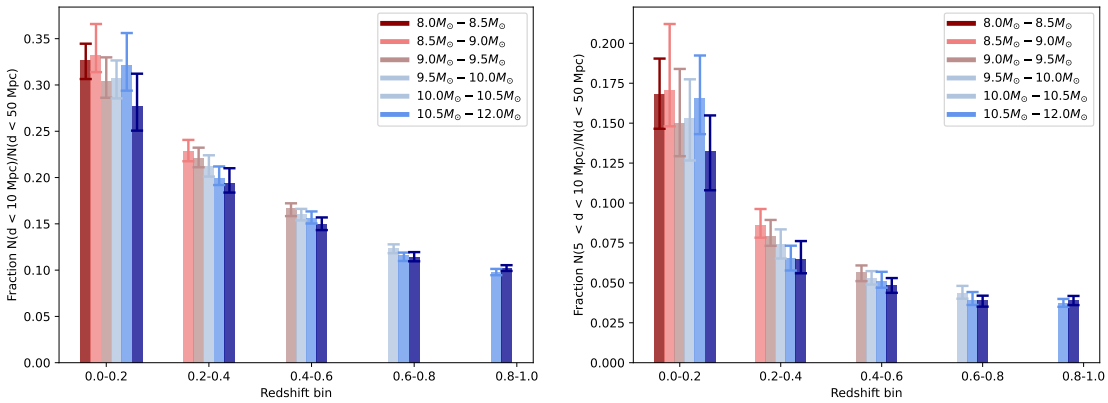

(a) Distance-to-filament **(b)** Distance-to-node

Figure 5.3: The fraction of galaxies within 10 Mpc of their closest filament (left) or node (right) divided by the number of galaxies within a distance of 50 Mpc to the closest filament (left) or node (right), f_i (see Equation 5.2) on the y-axis, split in bins of stellar mass, across redshift bins of $\delta z = 0.2$ on the x-axis. The error bars on the bins are calculated using the 16th and 84th percentiles in the 101 resampled filament networks.

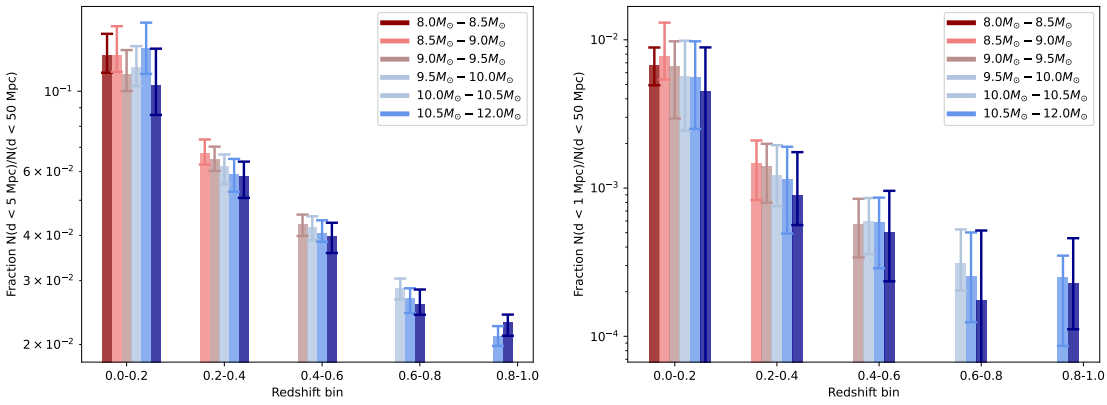

(a) $d_i < 5$ Mpc **(b)** $d_i < 1$ Mpc

Figure 5.4: The fraction of galaxies for 5 Mpc (left) and 1 Mpc (right) distance cuts of their closest filament divided by the number of galaxies within a distance of 50 Mpc to the closest filament, f_i (see Equation 5.2) on the y-axis, split in bins of stellar mass, across redshift bins of $\delta z = 0.2$ on the x-axis. The error bars on the bins are calculated as the 16th and 84th percentiles in the 101 resampled filament networks. For ease of visualisation, the y-axis is plotted on a log scale.

higher masses. However, in the lowest redshift bin, the distribution of galaxies is more uncertain due to the limited volume in this redshift range. In the highest redshift bin, the fraction has a slight upwards trend. However, whilst the error bars are small, given that I only have two bins, I cannot draw a conclusion about the mass distribution with respect to distance to filament.

I also investigate how the fraction of galaxies close to filaments changes using different distance cuts in f_i. As can be seen in Figure 5.4, using a cut at both 5 Mpc and 1 Mpc, I find a similar trend as for the 10 Mpc cut, but with larger uncertainties due to the lower number of galaxies in close proximity to the filaments/nodes.

This result may seem surprising, as one may predict that there should be a higher fraction of massive galaxies in larger overdensities (characterised by the nodes in this work). However, as I am using a flux-limited sample, the sample is always dominated by the lowest mass galaxies that can be detected in each redshift bin. Given that DISPERSE determines the filaments distribution based on density of particles, the more numerous galaxies will contribute more to the identification of filaments, which results in this observed bias in terms of the stellar mass of the galaxy sample and its dependence on the proximity to the filament or node distributions. This will be discussed further in Section 5.4.2.

5.4.2 Influence of galaxy stellar mass in the filament-tracing process

As seen in Figure 5.3 and discussed in Section 5.4.1, I find a higher fraction of low mass galaxies closer to their associated filament/node (excluding cluster galaxies in the nodes). An explanation for this is that it is a result of the filament tracing algorithm, which only takes into account number density - hence it will identify a filament where there are more galaxies. However, if I do not include the more abundant low-mass galaxies, then the most significant and robust structures traced should be preserved without the low-mass galaxies.

In order to test this, I take all the galaxies in the five redshift bins and consider two cases: one, where I remove all the galaxies with a mass $M_* < 9.0 M_\odot$, and a

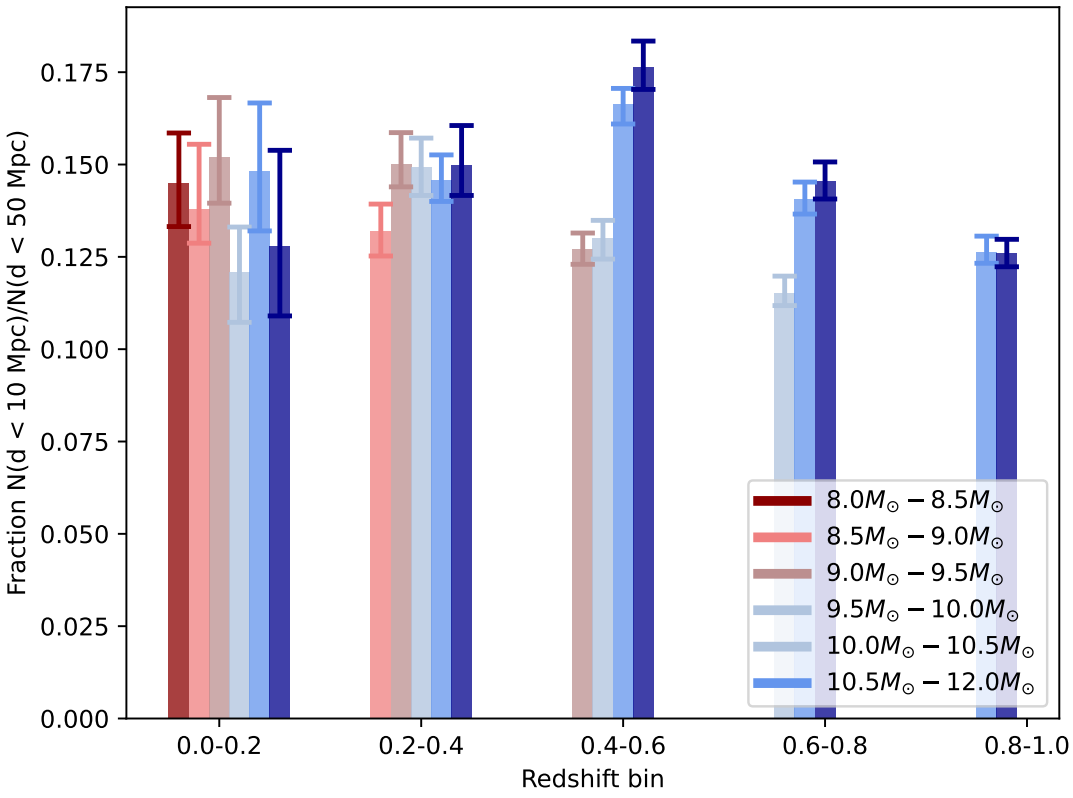

Figure 5.5: The fraction of galaxies within 10 Mpc of their closest filament divided by the number of galaxies within a distance of 50 Mpc to the closest filament, across redshift bins of $\delta z = 0.2$, where the filament distribution was obtained by removing every galaxy with $M_* < 10^{9.0} M_\odot$.

second in which I randomly sample from the low mass galaxies with $M_* < 9.0 M_\odot$ and only keep half of the galaxies. I then regenerate all the resampled filament networks following Sections 5.3.1 and 2.2.3. Using the newly obtained networks, I crossmatch them with the original galaxy catalogue in that redshift bin and calculate the distance-to-filament for each galaxy. I then investigate the mass distribution of galaxies as a function of distance-to-filament for $f_i(d < 10$ Mpc) as before. Figure 5.6 shows that by randomly cutting half of the low-mass galaxies from the filament-finding catalogue I have a similar trend in the lowest and highest redshift bins, however, the number of lower mass galaxies closer to a filament decreases in the other redshift bins. When I cut all the low-mass galaxies, as seen in Figure 5.5, there is no trend with mass in the lowest redshift bin, and for the other redshift bins, I also notice that now I have higher fractions for the more massive galaxies

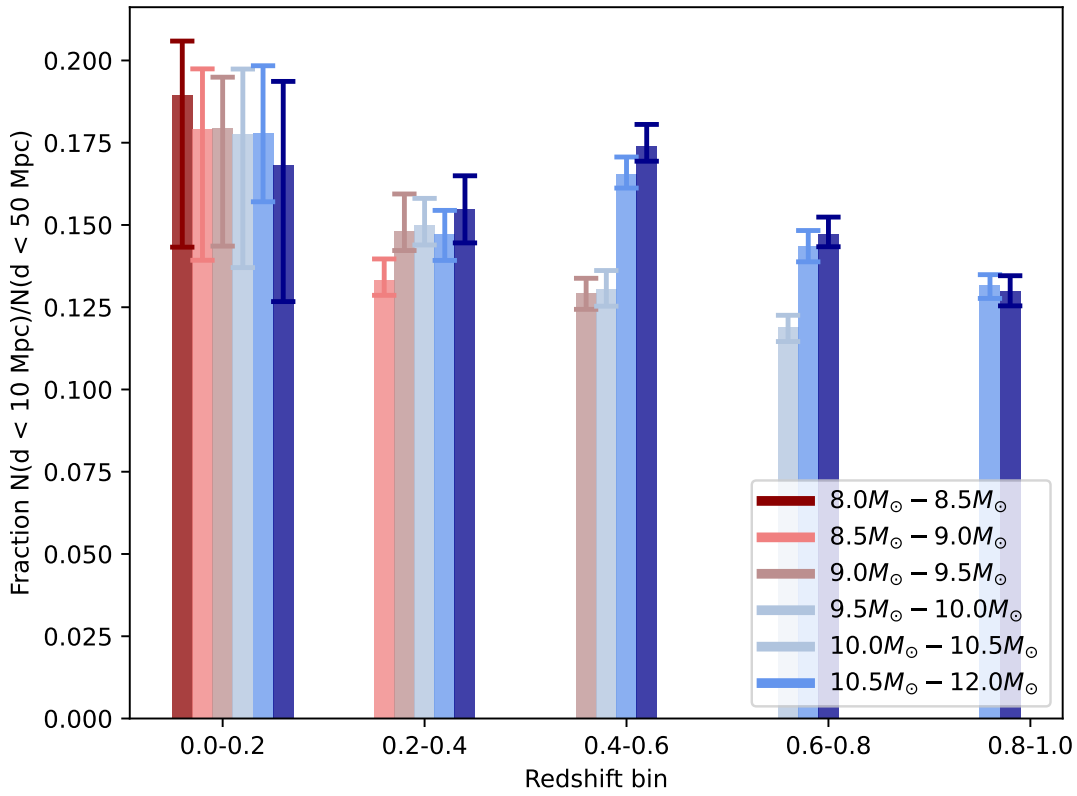

Figure 5.6: The fraction of galaxies within 10 Mpc of their closest filament divided by the number of galaxies within a distance of 50 Mpc to the closest filament, across redshift bins of $\delta z = 0.2$, where the filament distribution was obtained by randomly removing half the galaxies with $M_* < 10^{9.0} M_\odot$.

closer to filaments. I discuss this further in Section 5.4.5.

5.4.3 Specific star formation rate and its relation to filaments

The specific star formation rate (sSFR) is the star formation per unit stellar mass of a galaxy, defined as sSFR $\equiv$ SFR/$M_\star$. I fit a parametric function to the sSFR as a function of redshift:

$$\text{sSFR} = A + \gamma \log_{10}(1+z), \tag{5.3}$$

where A and γ are parameters whose values are taken from Johnston et al. (2015).

To investigate the relationship between the star formation of the galaxies and their closest filament/node, I follow a similar method to the one in Section 5.4.1 for the resampled galaxy redshift distributions. However, in order to disentangle

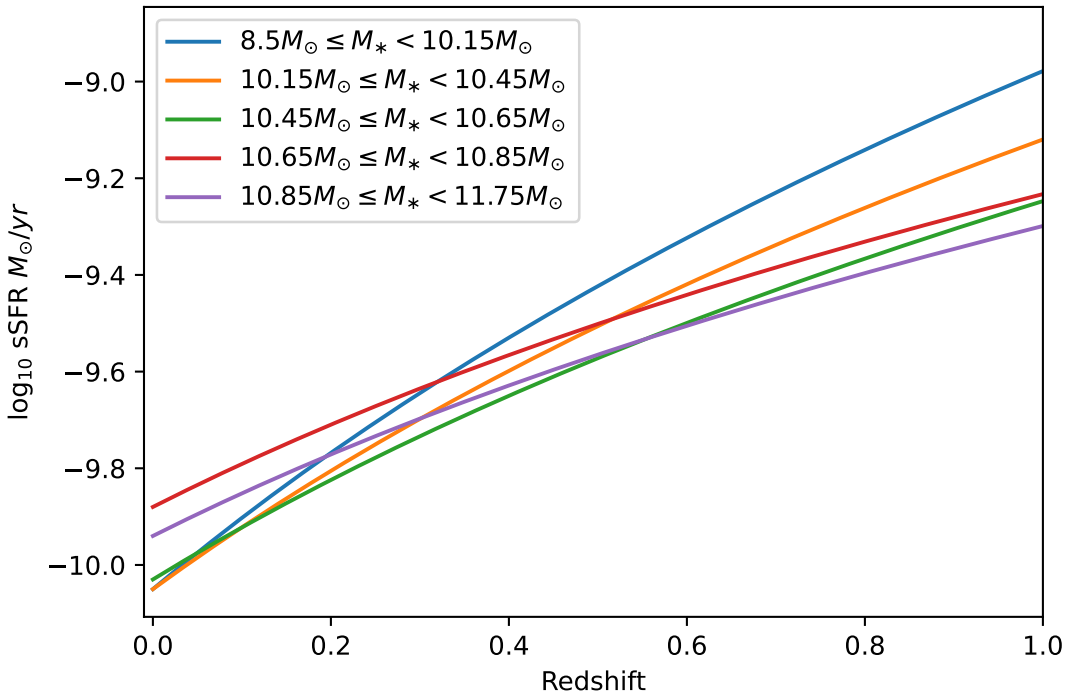

Figure 5.7: The sSFR-z parametric function split in mass bins. Each coloured line represents a different mass bin, extrapolated on the redshift interval $0.0 < z < 1.0$.

the possible effects of the mass, I split the redshift bins into five stellar mass bins: $8.0M_\odot < M_* < 9.5M_\odot$, $9.5M_\odot < M_* < 10.0M_\odot$, $10.0M_\odot < M_* < 10.5M_\odot$ and $10.5M_\odot < M_* < 12.0M_\odot$. These bins and their widths are chosen based on the mass completeness cuts I made in Section 5.2.4 to ensure that I have enough objects within each redshift bin (i.e. choosing a lower mass bin would make a comparison with the higher redshift bin more difficult, whilst choosing a higher mass bin would make the comparison with the lower redshift bin more difficult).

In each constant mass bin, I separate the sample in three categories based on their sSFR: passive galaxies, main sequence galaxies and star forming galaxies. The main sequence galaxies are defined such that they are within $\pm 1\sigma$ of the main sequence described by Equation 5.3. I then calculate the f_i for each galaxy and take the 50th percentile from the resampled galaxy redshift distributions. This can be seen in Figure 5.8 for the filaments (f_f), and in Figure 5.11 for the nodes (f_n). The error bars are determined by using the 16th and 84th percentiles of the fractions in each bin from the resampled distributions. For the filaments, for galaxies in the

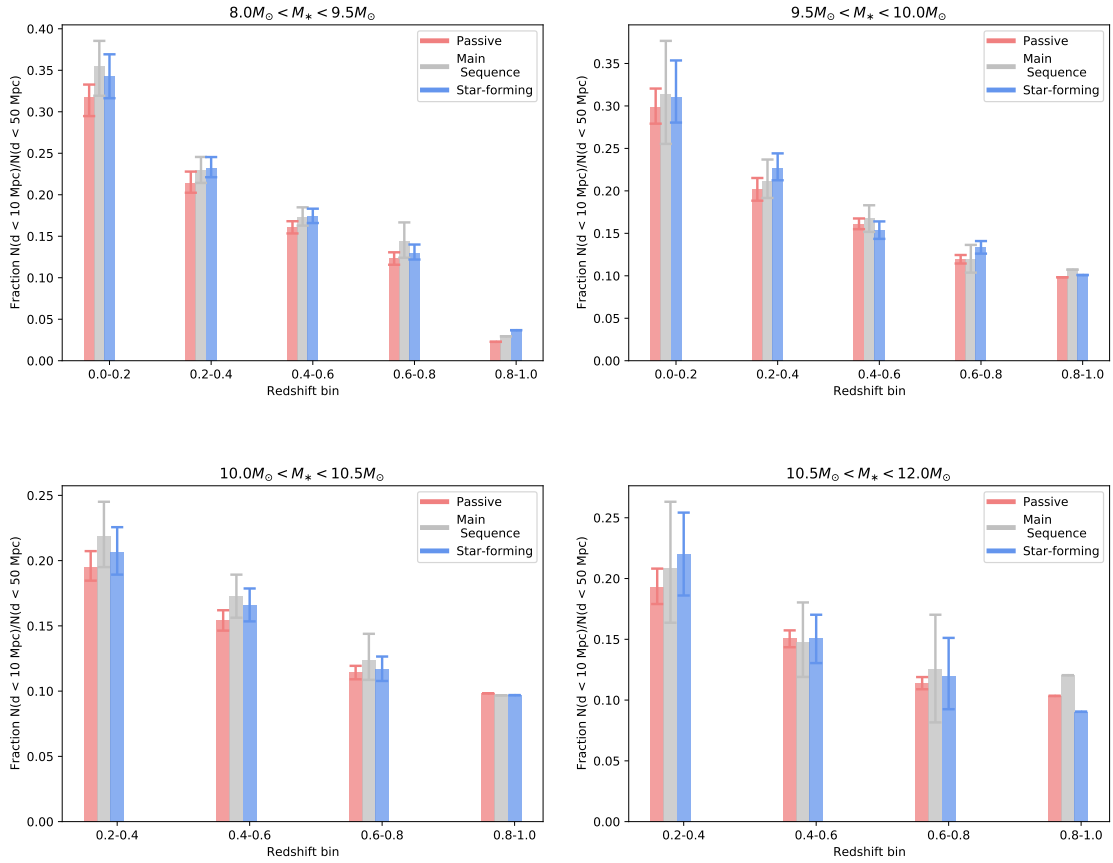

Figure 5.8: The fraction of galaxies within 10 Mpc of their closest filament divided by the number of galaxies with a distance within 50 Mpc (see Equation 5.2, split in bins of star formation, across redshift bins of $\delta z = 0.2$. The main sequence bin corresponds to galaxies within $\pm 1\sigma$ of the sSFR-z relation, whilst the passive/star-forming bins correspond to every below/above it. The error bars are generated by using the 16th and 84th percentiles of the fractions in each bin in each resampled distribution. For the highest redshift bin, the errors are small enough such that the percentiles overlap.

lower mass bins, I find no evidence for a trend between the distance-to-filament and their sSFR, irrespective of redshift. However, at higher mass bins, I find tentative evidence for galaxies that reside close to filaments to be either on or above the main sequence for star formation. I then use the Kolmogorov-Smirnov test (Noether, 1978) to test if the distributions in the fraction of passive, main-sequence and star-forming galaxies close to filaments are statistically indistinguishable from each other. As can be seen in Table 5.2, for the highest redshift bin, there is no statistical significance difference between the different types of galaxy, independent of the mass bin (all p-values are 1.0). However, in the other redshift bins, I rule out the null hypothesis

Table 5.2: The $p-$values for the KS test for the Passive-Main Sequence ($p_{P\text{-}MS}$), Main Sequence-Active ($p_{MS\text{-}A}$) and Passive-Active ($p_{P\text{-}A}$) distributions for the galaxies within 10 Mpc of a filament.

Redshift bin	$\mathbf{8.0M_\odot < M_\star < 9.5M_\odot}$			$\mathbf{9.5M_\odot < M_* < 10.0M_\odot}$		
	$\mathbf{p_{P\text{-}MS}}$	$\mathbf{p_{MS\text{-}A}}$	$\mathbf{p_{P\text{-}A}}$	$\mathbf{p_{P\text{-}MS}}$	$\mathbf{p_{MS\text{-}A}}$	$\mathbf{p_{P\text{-}A}}$
$0.0 < z < 0.2$	10^{-13}	0.078	10^{-11}	0.002	0.078	$7.37\cdot10^{-4}$
$0.2 < z < 0.4$	10^{-11}	0.111	10^{-15}	$1.29\cdot10^{-3}$	10^{-7}	10^{-18}
$0.4 < z < 0.6$	10^{-13}	0.469	10^{-17}	10^{-8}	10^{-11}	10^{-7}
$0.6 < z < 0.8$	10^{-21}	10^{-8}	$1.20\cdot10^{-4}$	$1.29\cdot10^{-3}$	10^{-17}	10^{-28}
$0.8 < z < 1.0$	1.0	1.0	1.0	1.0	1.0	1.0

Redshift bin	$\mathbf{10.0M_\odot < M_\star < 10.5M_\odot}$			$\mathbf{10.5M_\odot < M_\star < 12.0M_\odot}$		
	$\mathbf{p_{P\text{-}MS}}$	$\mathbf{p_{MS\text{-}A}}$	$\mathbf{p_{P\text{-}A}}$	$\mathbf{p_{P\text{-}MS}}$	$\mathbf{p_{MS\text{-}A}}$	$\mathbf{p_{P\text{-}A}}$
$0.0 < z < 0.2$	10^{-13}	0.078	10^{-11}	10^{-19}	10^{-8}	10^{-7}
$0.2 < z < 0.4$	10^{-11}	$1.29\cdot10^{-3}$	10^{-5}	10^{-6}	0.006	10^{-11}
$0.4 < z < 0.6$	10^{-18}	$4.11\cdot10^{-4}$	10^{-13}	$2.24\cdot10^{-4}$	0.281	$6.13\cdot10^{-3}$
$0.6 < z < 0.8$	10^{-12}	$7.37\cdot10^{-4}$	$1.29\cdot10^{-3}$	10^{-12}	0.053	10^{-10}
$0.8 < z < 1.0$	1.0	1.0	1.0	1.0	1.0	1.0

that the distributions in the fraction of galaxies in close proximity to the filaments are drawn from the same underlying distribution. More specifically, I notice that the difference arises more strongly when comparing the passive distributions to the main sequence (shown as $p_{MS\text{-}A}$ in the table, ranging from 10^{-11} to 10^{-21}) and active ones (shown as $p_{P\text{-}A}$ in the table, ranging from 10^{-3} to 10^{-28}).

Following the analysis with stellar mass, I investigate two other distance cuts: 5 Mpc (Figure 5.9) and 1 Mpc (Figure 5.10).

Noting the small-number statistics in the lowest redshift bins for these distance

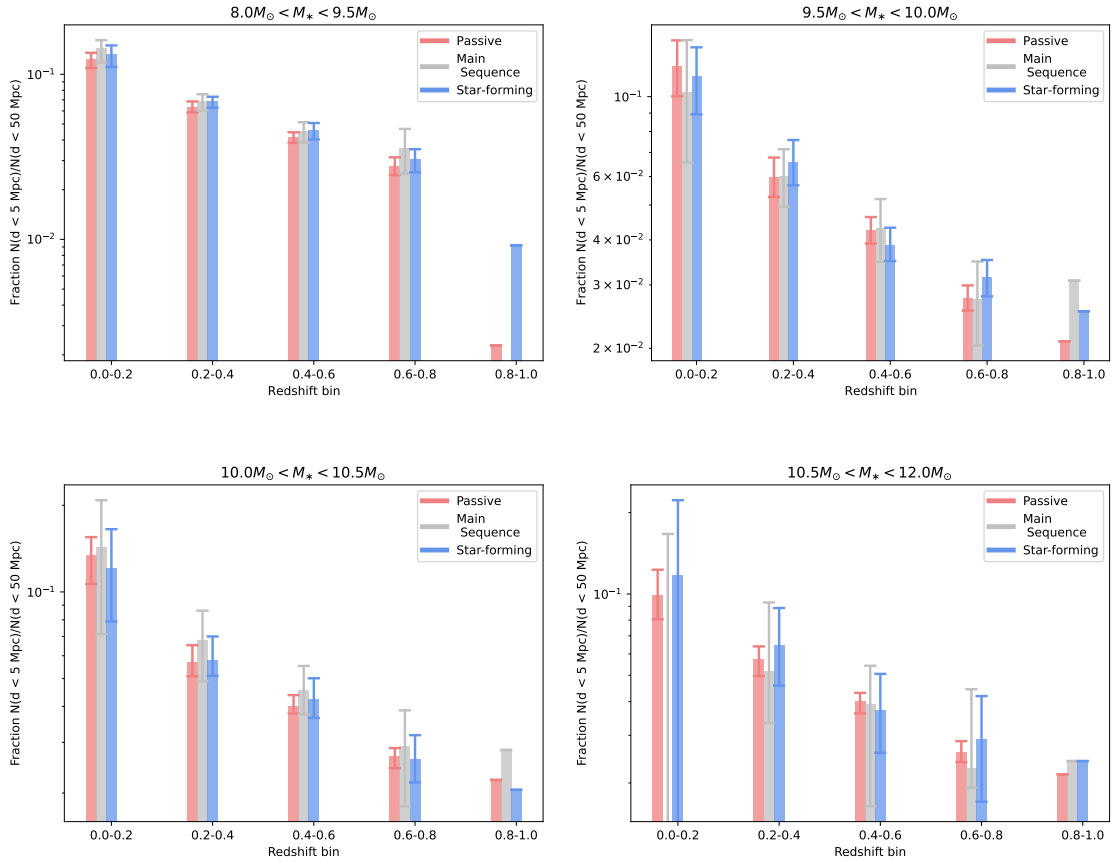

Figure 5.9: The fraction of galaxies within 5 Mpc of their closest filament divided by the number of galaxies with a distance within 50 Mpc (see Equation 5.2, split in terms of their star formation, across redshift bins of $\delta z = 0.2$. The main sequence bin corresponds to galaxies within $\pm 1\sigma$ of the sSFR-z relation, whilst the passive/star-forming bins correspond to every below/above it. The error bars are generated by using the 16th and 84th percentiles of the fractions in each bin in each resampled distribution. For the highest redshift bin, the errors are small enough such that the percentiles overlap.

cuts, I again do not find any strong correlation between the distance to filament and the specific star-formation rate of galaxies. The only relatively robust result is that there is a higher fraction of massive $> 10^{10.5}\,\mathrm{M}_\star$ passive galaxies very close (< 1 Mpc) to filaments at $z > 0.4$ compared to at lower redshift, where the distribution is more even. When looking at the KS test for both these cases (see Table 5.3 for $d < 5$ Mpc and Table 5.4 for $d < 1$ Mpc), I notice a similar trend as in the 10 Mpc sample. Other than the highest redshift bin, I rule out that the distributions in the fraction of galaxies in close proximity to the filaments are drawn from the same underlying distribution. For the 5 Mpc sample, the difference arises more strongly

Table 5.3: The $p-$values for the KS test for the Passive-Main Sequence ($p_{\text{P-MS}}$), Main Sequence-Active ($p_{\text{MS-A}}$) and Passive-Active ($p_{\text{P-A}}$) distributions for the galaxies within 5 Mpc of a filament.

Redshift bin	$\mathbf{8.0M_\odot < M_\star < 9.5M_\odot}$			$\mathbf{9.5M_\odot < M_\star < 10.0M_\odot}$		
	$\mathbf{p_{P\text{-}MS}}$	$\mathbf{p_{MS\text{-}A}}$	$\mathbf{p_{P\text{-}A}}$	$\mathbf{p_{P\text{-}MS}}$	$\mathbf{p_{MS\text{-}A}}$	$\mathbf{p_{P\text{-}A}}$
$0.0 < z < 0.2$	10^{-9}	0.002	0.009	10^{-6}	0.003	0.053
$0.2 < z < 0.4$	10^{-5}	0.036	10^{-7}	0.368	0.001	10^{-6}
$0.4 < z < 0.6$	10^{-8}	0.583	10^{-11}	$1.29 \cdot 10^{4}$	10^{-7}	10^{-7}
$0.6 < z < 0.8$	10^{-12}	10^{-8}	10^{-5}	10^{-5}	10^{-9}	10^{-7}
$0.8 < z < 1.0$	1.0	1.0	1.0	1.0	1.0	1.0

Redshift bin	$\mathbf{10.0M_\odot < M_\star < 10.5M_\odot}$			$\mathbf{10.5M_\odot < M_\star < 12.0M_\odot}$		
	$\mathbf{p_{P\text{-}MS}}$	$\mathbf{p_{MS\text{-}A}}$	$\mathbf{p_{P\text{-}A}}$	$\mathbf{p_{P\text{-}MS}}$	$\mathbf{p_{MS\text{-}A}}$	$\mathbf{p_{P\text{-}A}}$
$0.0 < z < 0.2$	10^{-7}	0.001	0.006	10^{-14}	10^{-7}	10^{-7}
$0.2 < z < 0.4$	10^{-8}	10^{-6}	0.154	10^{-6}	$1.2 \cdot 10^{-4}$	10^{-7}
$0.4 < z < 0.6$	10^{-9}	0.015	10^{-7}	10^{-8}	0.053	10^{-8}
$0.6 < z < 0.8$	10^{-10}	0.001	0.015	10^{-11}	0.015	10^{-8}
$0.8 < z < 1.0$	1.0	1.0	1.0	1.0	1.0	1.0

when comparing the passive distributions to the main sequence (shown as $p_{\text{P-MS}}$ in the table, ranging from 10^{-5} to 10^{-12}) and active ones (shown as $p_{\text{P-A}}$ in the table, ranging from $\sim 10^{-2}$ to 10^{-14}). Similarly for the 1 Mpc sample, the p-values of passive-main sequence distributions $p_{\text{P-MS}}$ range between 10^{-4} to 10^{-38}. However, a slight difference arises in the p-values of passive-active distributions $p_{\text{P-A}}$, where the distributions become more similar for the lower mass bins (p-values being around 0.1 to 0.01), than for the higher mass bins (p-values ranging between $\sim 10^{-2}$ to 10^{-36}).

Similarly for nodes, in Table 5.5, when I use the KS test to check for differences

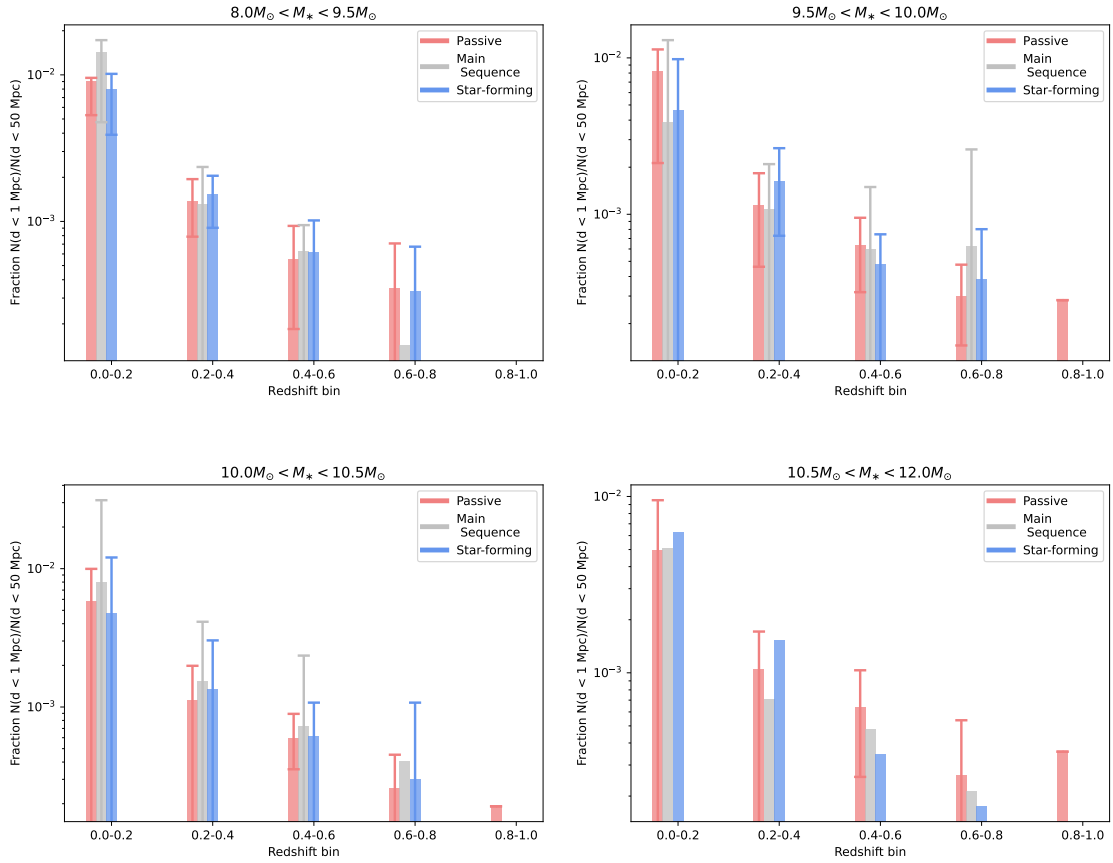

Figure 5.10: The fraction of galaxies within 1 Mpc of their closest filament divided by the number of galaxies with a distance within 50 Mpc (see Equation 5.2, split in terms of their star formation, across redshift bins of $\delta z = 0.2$. The main sequence bin corresponds to galaxies within $\pm 1\sigma$ of the sSFR-z relation, whilst the passive/star-forming bins correspond to every below/above it. The error bars are generated by using the 16th and 84th percentiles of the fractions in each bin in each resampled distribution. For the highest redshift bin, the errors are small enough such that the percentiles overlap.

between the three populations, there is no significant difference in the highest redshift bin, whilst all the other bins have statically different distributions. Without taking into account the highest redshift bin, the difference in $p-$values is considerable - most of the $p_{\text{MS-A}}$ values are of order $\approx 10^2$ (with a few exceptions), whilst both $p_{\text{P-MS}}$ and $p_{\text{P-A}}$ are on average of order 10^{-10} across all mass bins. This could imply that the distance-to-filament/node impacts passive galaxies more than star-forming ones. This could be caused by the fact that the population of galaxies closer to filaments/nodes can be affected by different quenching processes, whilst the main sequence/active galaxies are not. I will revisit the behaviour of passive

Table 5.4: The $p-$values for the KS test for the Passive-Main Sequence ($p_{P\text{-}MS}$), Main Sequence-Active ($p_{MS\text{-}A}$) and Passive-Active ($p_{P\text{-}A}$) distributions for the galaxies within 1 Mpc of a filament.

Redshift bin	$\mathbf{8.0M_\odot < M_\star < 9.5M_\odot}$			$\mathbf{9.5M_\odot < M_\star < 10.0M_\odot}$		
	$\mathbf{p_{P\text{-}MS}}$	$\mathbf{p_{MS\text{-}A}}$	$\mathbf{p_{P\text{-}A}}$	$\mathbf{p_{P\text{-}MS}}$	$\mathbf{p_{MS\text{-}A}}$	$\mathbf{p_{P\text{-}A}}$
$0.0 < z < 0.2$	10^{-7}	10^{-5}	0.015	10^{-19}	10^{-9}	0.024
$0.2 < z < 0.4$	$2.24{\cdot}10^{-4}$	10^{-7}	0.211	10^{-8}	10^{-11}	$2.21{\cdot}10^{-3}$
$0.4 < z < 0.6$	10^{-7}	10^{-5}	0.015	10^{-20}	$2.22{\cdot}10^{-3}$	10^{-11}
$0.6 < z < 0.8$	10^{-13}	10^{-7}	0.154	10^{-20}	10^{-6}	10^{-3}
$0.8 < z < 1.0$	1.0	1.0	1.0	1.0	1.0	1.0

Redshift bin	$\mathbf{10.0M_\odot < M_\star < 10.5M_\odot}$			$\mathbf{10.5M_\odot < M_\star < 12.0M_\odot}$		
	$\mathbf{p_{P\text{-}MS}}$	$\mathbf{p_{MS\text{-}A}}$	$\mathbf{p_{P\text{-}A}}$	$\mathbf{p_{P\text{-}MS}}$	$\mathbf{p_{MS\text{-}A}}$	$\mathbf{p_{P\text{-}A}}$
$0.0 < z < 0.2$	10^{-19}	0.078	10^{-10}	10^{-20}	0.999	10^{-17}
$0.2 < z < 0.4$	10^{-11}	0.003	$1.20{\cdot}10^{-4}$	10^{-27}	0.702	10^{-19}
$0.4 < z < 0.6$	10^{-25}	0.015	10^{-15}	10^{-38}	0.994	10^{-36}
$0.6 < z < 0.8$	10^{-24}	0.469	10^{-16}	10^{-25}	0.999	10^{-24}
$0.8 < z < 1.0$	1.0	1.0	1.0	1.0	1.0	1.0

versus active galaxies in Section 5.4.5.

Furthermore, as can be seen in Figure 5.14 (removing all galaxies with $M_* < 10^9 M_\odot$), when I repeat this analysis for the sSFR, there is no significant change. Similarly, when I do the random mass cut, I do not see any major changes in the sSFR-distance to filament relation. This is a similar result to Zakharova et al. (2023), which showed that excluding for galaxies with $M_* < 10^{9.0} M_\odot$ does not have an impact on galaxy properties as a function of distance to filament.

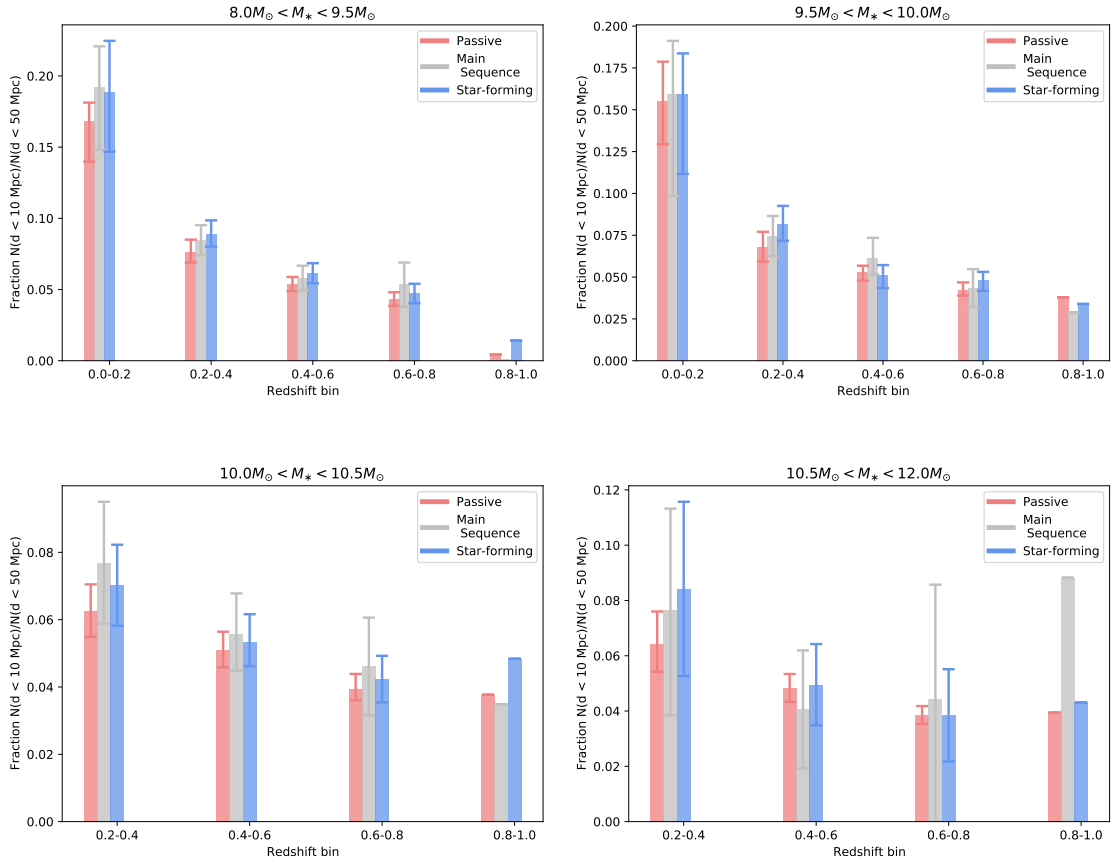

Figure 5.11: The fraction of galaxies within 10 Mpc of their closest node divided by the number of galaxies with a distance within 50 Mpc (see Equation 5.2), split in bins of star formation, across redshift bins of $\delta z = 0.2$.

5.4.4 Effect of node galaxies

For this analysis, I selected galaxies which are at least 5 Mpc away from a node. I made this choice in order to avoid contamination from any galaxies within clusters, which represent a much higher density environment than filaments. As highlighted in Figure 5.11, by applying this cut, any galaxy that is positioned at a distance of $5 < d < 10$ Mpc from a node will have a similar relationship with the galaxies that are within 10 Mpc of a filament. To investigate if this changes at smaller distances to nodes, and if this cut is necessary for the filament analysis, I take the original catalogue and compute the fractions of sSFR for galaxies which are within 5 Mpc of a node, following the method in Section 5.4.3.

As can be seen in Figure 5.12, for the lower redshift bins, I find more passive

Table 5.5: The $p-$values for the KS test for the Passive-Main Sequence ($p_{P\text{-}MS}$), Main Sequence-Active ($p_{MS\text{-}A}$) and Passive-Active ($p_{P\text{-}A}$) distributions for the galaxies within 10 Mpc of a node.

Redshift bin	$\mathbf{8.0M_\odot < M_\star < 9.5M_\odot}$			$\mathbf{9.5M_\odot < M_\star < 10.0M_\odot}$		
	$\mathbf{p_{P\text{-}MS}}$	$\mathbf{p_{MS\text{-}A}}$	$\mathbf{p_{P\text{-}A}}$	$\mathbf{p_{P\text{-}MS}}$	$\mathbf{p_{MS\text{-}A}}$	$\mathbf{p_{P\text{-}A}}$
$0.0 < z < 0.2$	10^{-11}	10^{-11}	0.001	10^{-18}	10^{-11}	10^{-11}
$0.2 < z < 0.4$	10^{-7}	0.024	10^{-17}	$4.11 \cdot 10^{-4}$	$1.20 \cdot 10^{-4}$	10^{-15}
$0.4 < z < 0.6$	10^{-5}	0.006	10^{-11}	10^{-11}	10^{-9}	$6.13 \cdot 10^{-4}$
$0.6 < z < 0.8$	10^{-13}	10^{-8}	10^{-5}	$3.72 \cdot 10^{-4}$	10^{-5}	10^{-11}
$0.8 < z < 1.0$	1.0	1.0	1.0	1.0	1.0	1.0

Redshift bin	$\mathbf{10.0M_\odot < M_\star < 10.5M_\odot}$			$\mathbf{10.5M_\odot < M_\star < 12.0M_\odot}$		
	$\mathbf{p_{P\text{-}MS}}$	$\mathbf{p_{MS\text{-}A}}$	$\mathbf{p_{P\text{-}A}}$	$\mathbf{p_{P\text{-}MS}}$	$\mathbf{p_{MS\text{-}A}}$	$\mathbf{p_{P\text{-}A}}$
$0.0 < z < 0.2$	10^{-13}	0.078	10^{-11}	10^{-19}	10^{-8}	10^{-7}
$0.2 < z < 0.4$	10^{-13}	0.024	10^{-5}	10^{-8}	0.111	10^{-12}
$0.4 < z < 0.6$	10^{-6}	0.036	$3.72 \cdot 10^{-4}$	10^{-11}	$1.20 \cdot 10^{-4}$	$6.13 \cdot 10^{-3}$
$0.6 < z < 0.8$	10^{-11}	10^{-5}	10^{-7}	10^{-11}	$6.14 \cdot 10^{-3}$	10^{-6}
$0.8 < z < 1.0$	1.0	1.0	1.0	1.0	1.0	1.0

galaxies closer to the nodes; whilst for the higher redshift bins, the number of active galaxies increases. This is more noticeable for the lower mass galaxies, where the error bars are also smaller. At higher masses, whilst there seems to be a preference for more star-forming galaxies in the lower redshift bins as well, the error bars overlap quite significantly and I cannot draw a strong conclusion. The difference between blue and red galaxies in cluster environments at different redshifts has been observed before and is known as the Butcher-Oemler effect (Butcher and Oemler, 1978; Butcher and Oemler, 1984). The implication of this effect is that

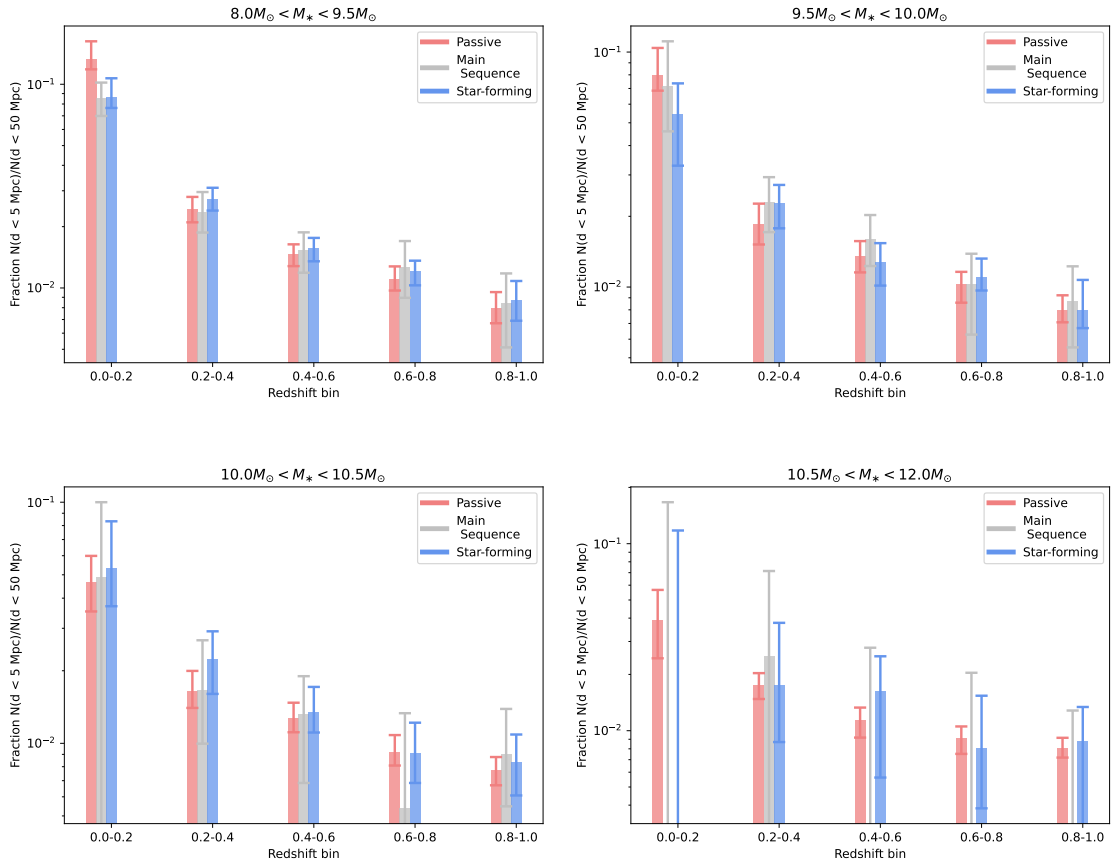

Figure 5.12: The fraction of galaxies within 5 Mpc of their closest nodes divided by the number of galaxies with a distance within 50 Mpc, split in bins of star formation, across redshift bins of $\delta z = 0.2$. The main sequence bin corresponds to galaxies within $\pm 1\sigma$ of the sSFR-z relation, whilst the passive/star-forming bins correspond to every below/above it.

galaxies were more actively forming stars at higher redshift and have been quenched by the high dense environment of the cluster. Similarly to the effect from the filaments, galaxies of lower mass are more easily quenched by their environment when compared to their higher mass counterparts.

5.4.5 Discussion

I investigated the dependence of two galaxy properties as a function of distance to closest filament/node: stellar mass and sSFR.

I found no strong relationship between the stellar mass of a galaxy and its position relative to filaments/nodes. I tested if that is due to the choice of filament-

Table 5.6: The $p-$values for the KS test for the Passive-Main Sequence ($p_{P\text{-}MS}$), Main Sequence-Active ($p_{MS\text{-}A}$) and Passive-Active ($p_{P\text{-}A}$) distributions for the galaxies within 5 Mpc of a node, without cutting any galaxies from the sample.

Redshift bin	$\mathbf{8.0M_\odot < M_\star < 9.5M_\odot}$			$\mathbf{9.5M_\odot < M_\star < 10.0M_\odot}$		
	$\mathbf{p_{P\text{-}MS}}$	$\mathbf{p_{MS\text{-}A}}$	$\mathbf{p_{P\text{-}A}}$	$\mathbf{p_{P\text{-}MS}}$	$\mathbf{p_{MS\text{-}A}}$	$\mathbf{p_{P\text{-}A}}$
$0.0 < z < 0.2$	10^{-39}	0.107	10^{-33}	10^{-5}	10^{-6}	10^{-22}
$0.2 < z < 0.4$	0.036	10^{-8}	10^{-5}	10^{-8}	0.368	10^{-8}
$0.4 < z < 0.6$	$7.3 \cdot 10^{-4}$	0.078	0.003	10^{-8}	10^{-10}	0.036
$0.6 < z < 0.8$	10^{-6}	$4.4 \cdot 10^{-4}$	0.002	$2.2 \cdot 10^{-4}$	10^{-5}	$7.7 \cdot 10^{-4}$
$0.8 < z < 1.0$	0.015	0.111	0.015	$7.3 \cdot 10^{-4}$	0.154	0.009

Redshift bin	$\mathbf{10.0M_\odot < M_\star < 10.5M_\odot}$			$\mathbf{10.5M_\odot < M_\star < 12.0M_\odot}$		
	$\mathbf{p_{P\text{-}MS}}$	$\mathbf{p_{MS\text{-}A}}$	$\mathbf{p_{P\text{-}A}}$	$\mathbf{p_{P\text{-}MS}}$	$\mathbf{p_{MS\text{-}A}}$	$\mathbf{p_{P\text{-}A}}$
$0.0 < z < 0.2$	$3.7 \cdot 10^{-4}$	0.014	$3.8 \cdot 10^{-4}$	10^{-25}	0.022	10^{-12}
$0.2 < z < 0.4$	$4.1 \cdot 10^{-4}$	10^{-5}	10^{-12}	10^{-20}	$2.2 \cdot 10^{-4}$	10^{-6}
$0.4 < z < 0.6$	10^{-6}	$2.3 \cdot 10^{-4}$	0.003	10^{-12}	10^{-8}	10^{-12}
$0.6 < z < 0.8$	10^{-13}	10^{-11}	0.036	10^{-24}	10^{-19}	10^{-5}
$0.8 < z < 1.0$	10^{-11}	$2.2 \cdot 10^{-4}$	$4.1 \cdot 10^{-4}$	10^{-16}	10^{-8}	10^{-7}

tracer by removing the low mass galaxies from the filament tracing - which changed the number density of galaxies and removed some of the smaller scale filaments traced by them. When I redid the analysis I noticed that, for the intermediate redshift bins, by removing some (all) of the low mass galaxies in the filament finding and re-crossmatching to the original catalogue, the fraction of high mass galaxies increased and overtook the lower mass ones, which is consistent with other cosmic web studies (e.g. Alpaslan et al., 2015; Laigle et al., 2017; Malavasi et al., 2017) for the given redshift ranges. In this case, I found that high mass galaxies are

more likely to reside close to the filaments for redshifts $z > 0.4$ (as seen in Figures 5.5 and 5.6). As such, care must be taken when performing such analyses, as using a mass selected sample to compute filaments and then try to extract the mass-filament connection may not give robust results.

Another way to explain this result could be due to the biases of the sample. In order to verify that, I take the Galaxy Stellar Mass Function (GSMF) presented in Adams et al. (2021) and use it to compare it to the galaxies in the sample. I split the galaxies based on the fraction f_f computed earlier, such that the galaxies within $d_f < 10$ Mpc are considered the filament galaxies and the 10 Mpc $< d_f < 50$ Mpc are considered as the field galaxies. I then divide these in mass bins and use these mass bins and the GSMF to explore if there is any excess of low-mass galaxies in the sample or if there is a deficit of high-mass galaxies. The result can be seen in Figure 5.13, which shows the GSMF and how the filament (red points) / field (blue points) are distributed with respect to it in five slices of the redshift interval $0.0 < z < 1.0$. The inset in each plot is a zoom-in for the filament galaxies, which shows that there is a sharper decline towards the higher mass end. This suggests that the sample is deficient in high mass galaxies close to the spine of the filaments.

In terms of the sSFR, I find that the most significant result is that more massive, star-forming galaxies are more likely to be closer to the spine of the filaments or the nodes at lower redshifts. For both the 10 Mpc and the 5 Mpc distance cut, for $z < 0.4$, independent of the mass bin, star forming galaxies will be more likely to be closer to the filament. The only exception is the result for the 1 Mpc distance-to-filament cut at higher masses and higher redshift, which is in agreement with the result from Laigle et al. (2018), where they find that galaxies between redshifts $0.5 < z < 0.9$, with stellar masses of $M_* > 10^{10} M_\odot$ are more likely to be passive if they are closer to a filament. However, in this case, this result must be taken with caution due to the large uncertainties. This result is independent of the mass range of the galaxies used to trace the filament networks, as the result remains when I remove some (all) of the $M_\star < 10^{9.0} M_\odot$ galaxies from the filament tracing and repeating the analysis. From Figure 5.14, it can be seen that for the two higher

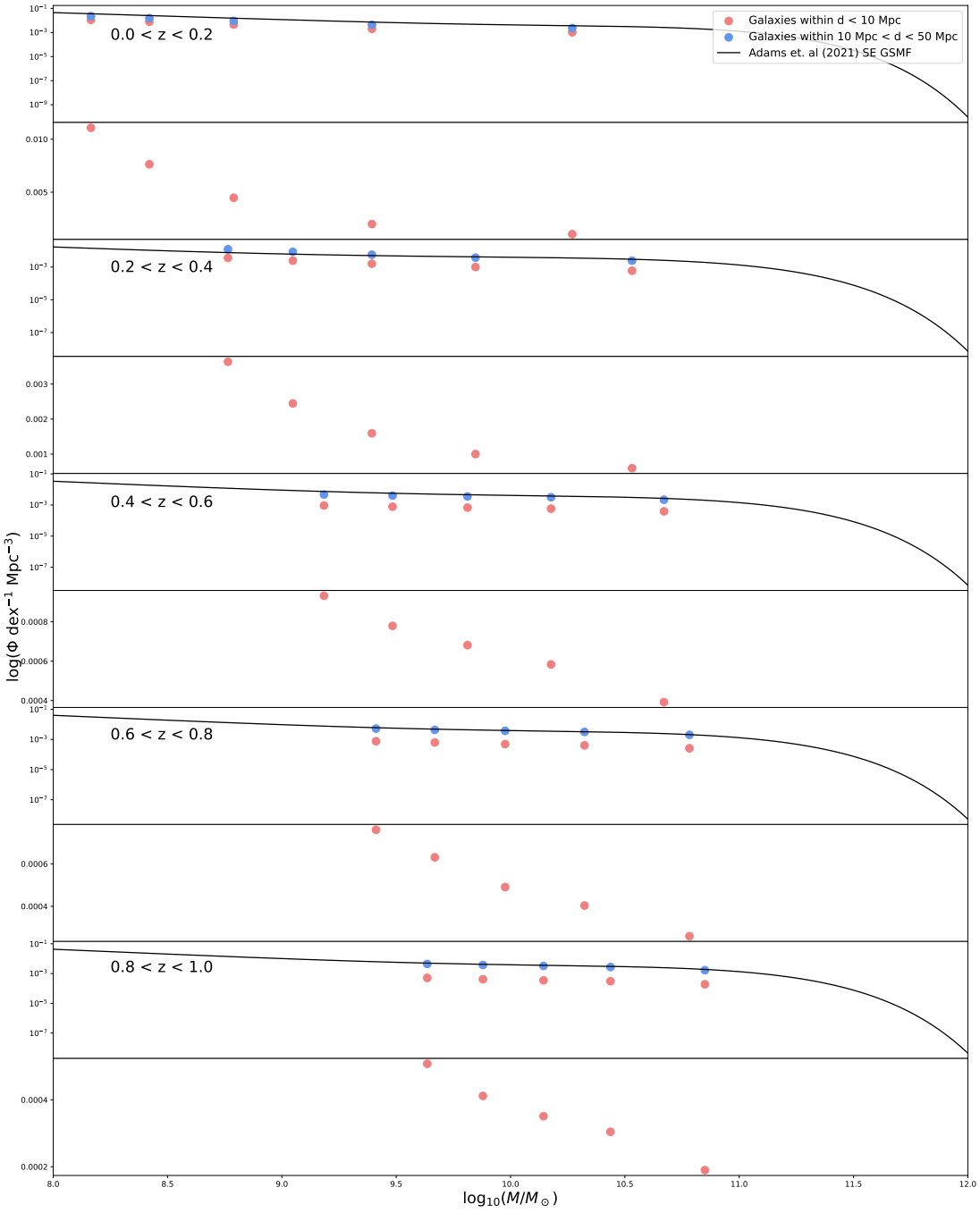

Figure 5.13: The GSMF as presented in Adams et al. (2021) for the five redshift intervals between $0.0 < z < 1.0$. The red points represent the galaxies within 10 Mpc of their closest filament, whilst the blue points represent the galaxies further than 10 Mpc from their closest filament. The inset plots show a zoom-in into the galaxies within 10 Mpc of the filaments.

mass bins ($10.0M_{\odot} < M_{*} < 10.5M_{\odot}$ and $10.5M_{\odot} < M_{*} < 12.0M_{\odot}$), star-forming galaxies are more likely to lie closer to filaments for higher redshift bins ($z > 0.6$ for the former mass bin and $z > 0.4$ for the latter mass bin). As well, from the KS test, I found that the passive galaxies have a more distinct distribution when it comes to distance-to-filament compared with either main-sequence/active galaxies. This implies that they are more susceptible to environmental effects. A similar result has also been reported by Hasan et al. (2023b) in the TNG-100 simulation with regards to nodes. Also in regards to nodes, Darvish et al. (2014) found that the sSFR of galaxies increases along the filaments closer to nodes, which is similar to what I observe in Figure 5.11. The trend observed in this work is mostly visible in the $0.2 < z < 0.4$ redshift bin, which could corresponds to the idea presented in Hasan et al. (2023b) that some of the galaxies specifically at these redshifts are undergoing some "rejuvenation" of their star formation for a brief period of time. This rejuvenation could be caused by several processes, including mergers along the filaments, or streams of gas being funnelled by the filaments into the galaxies. Although finding galaxies undergoing rejuvenation at these redshifts is rare, it is not implausible. In the `SIMBA` simulation, Rodríguez Montero et al. (2019) report a fraction of their galaxies in an intermediate mass bin (corresponding to the high mass bin in this work) which undergo rejuvenation at $z < 0.2$. Tanaka et al. (2023) also report a fraction of 8% of rejuvenated galaxies at $z < 1$ with a bias toward higher stellar masses.

Filaments could also delay quenching in the case of some galaxies - especially filaments which are flowing into clusters/nodes (Kotecha et al., 2022). Furthermore, Darvish et al. (2014) propose a mild-mild galaxy interaction within the filaments as a physical process that could drive the increase in star formation. This could also be explained by the Cosmic Web Enhancement proposed by Vulcani et al. (2019), such that the gas in the the filaments gets cooled down by the flows within said filaments and trigger more star formation in the circumgalactic gas. This has also been reported by Liao and Gao (2019), where they find that gas accreted from the filaments on the galaxy halo favours the gas cooling and star formation enhancement.

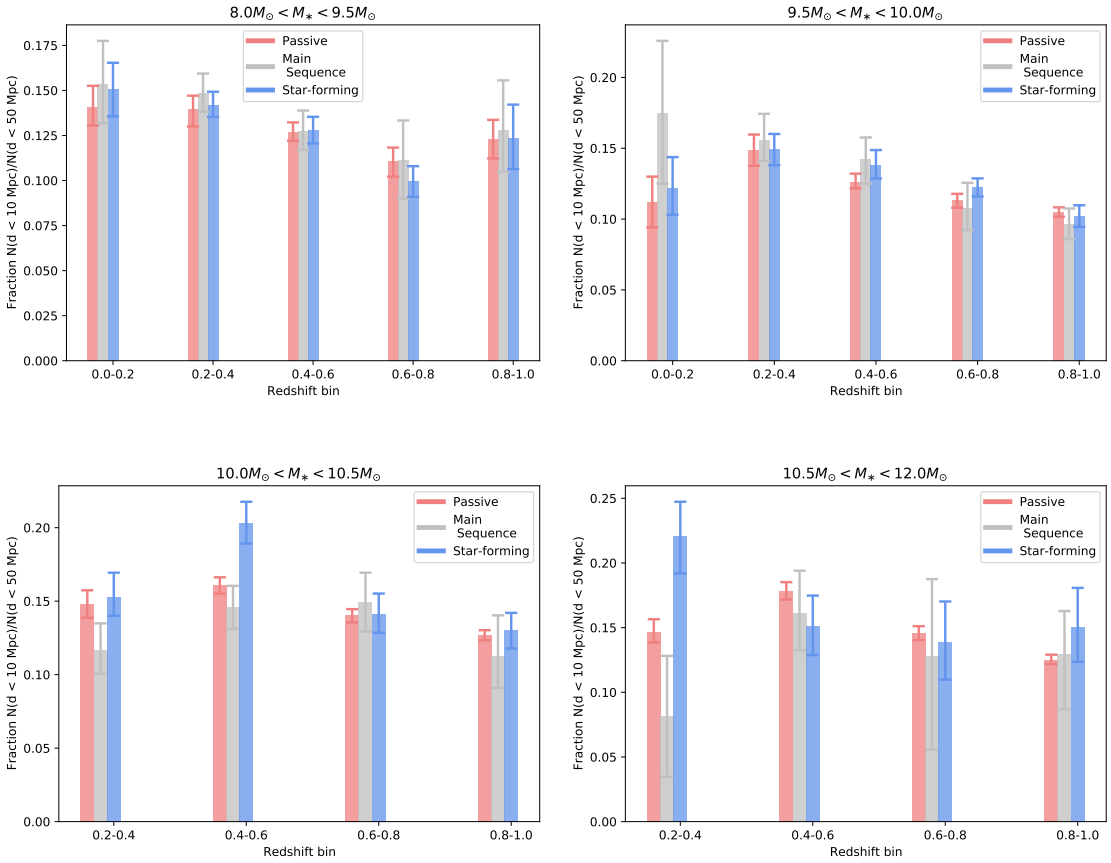

Figure 5.14: The fraction of galaxies within 10 Mpc of their closest filament divided by the number of galaxies with a distance within 50 Mpc, split in bins of star formation, across redshift bins of $\delta z = 0.2$ for the sample where the filament distribution was obtained by removing every galaxy with $M_* < 10^{9.0} M_\odot$. The main sequence bin corresponds to galaxies within $\pm 1\sigma$ of the sSFR-z relation, whilst the passive/star-forming bins correspond to every below/above it.

The result for the 1 Mpc distance-to-filament cut at higher masses and higher redshift is in agreement with the result from Laigle et al. (2018), in which they find that galaxies between redshifts $0.5 < z < 0.9$, with stellar masses of $M_* > 10^{10} M_\odot$ are more likely to be passive if they are closer to a filament. However, this result must be taken cautiously due to the large uncertainties due to the low number statistics.

Another way of looking at this result is by considering why are low-mass galaxies less star-forming by comparison. The quenching of star-formation occurs via several mechanisms, such as gas stripping via ram-pressure stripping (Gunn and Gott, 1972; Poggianti et al., 2017), harassment (Moore et al., 1996) or starvation/strangulation

(Larson et al., 1980; McCarthy et al., 2008; Feldmann and Mayer, 2015) and supernova feedback (Veilleux et al., 2005, and references therein). Low-mass galaxies are more likely to be stripped of their gas than their higher-mass counterparts due to their shallower potential wells. As filaments constitute denser environments, these low-mass galaxies lose their gas reservoir more easily, which makes them less efficient at forming stars within filaments. Meanwhile, the higher-mass galaxies closer to the filaments retain more of their gas, which in turn means they will have more fuel available to form stars in comparison to the low-mass galaxies residing at similar distances in the filaments. Using the SIMBA simulation, Bulichi et al. (2023) find that their satellite galaxies (low-mass in comparison with the higher mass centrals) are more quenched closer to filaments than the central galaxies are. They attribute this mainly to shock-heating from the large-scale structures, as well as some feedback mostly from AGN, but with some minor effects from star formation feedback. A similar result is found observationally by Hoosain et al. (2024), where only low-mass galaxies are more likely to be quenched due to the filaments in the RESOLVE survey and the ECO catalogue (Hutchens et al., 2023).

There are several caveats in terms of the sSFR-distance relationship. There could be other factors that intervene in this relationship. The filament-tracing issue of the filamentary distribution depending on the mass-selected galaxy samples I encounter for the stellar mass-distance analysis can also impact here. This could persist even when I try to disentangle the effect of mass by using constant mass slices.

Physically, I do not take into account the angular momentum of the galaxies and how it could affect both the placement of the galaxies along the filaments and the star formation of said galaxies (e.g. Kraljic et al., 2017; Welker et al., 2020). Tudorache et al. (2022) found evidence for a relationship between the distance to the closest filament of a galaxy and its spin - the spin is more likely to be aligned if a galaxy is closer to a filament. Similarly, the results obtained by Blue Bird et al. (2020), who used only 10 galaxies (which were within 10 Mpc of their closest filament) also found that galaxy spins tend to be aligned with the filaments of the cosmic web. In terms of the link between the stellar mass and the spin, several

simulations (Dubois et al., 2014; Kraljic et al., 2020) find a transition at a stellar mass of $M_\star \sim 10^{10}\,\mathrm{M}_\odot$, from aligned spin to mis-aligned spin. Observationally, Welker et al. (2020) found a similar spin transition between lower mass and higher mass galaxies using the SAMI survey around $10^{10.4}M_\odot - 10^{10.9}M_\odot$. Hence, there is a possibility that there is a link between the two: galaxies with lower stellar mass, which are more likely to have an aligned spin, can reside closer to filaments.

5.5 Conclusions

By mapping the filament distribution of the COSMOS and XMM-LSS fields using the Hatfield et al. (2022) photometric redshift catalogue and the DISPERSE filament-finding algorithm, I investigated the relationship between the cosmic web and two galaxy properties - stellar mass and specific star formation rate - across a redshift range of $0.0 < z < 1.0$. I found that:

1. Photometric redshifts can be used for tracing filaments; but even with a robust way to include the uncertainties associated with each redshift, there will significant ambiguity about the components of the network; however, the main structures of the filaments (spines) and voids are usually preserved in different redshift slices even when taking into account galaxies moving inside and outside said slices because of the uncertainties;

2. More massive, star forming galaxies tend to be closer to the filament spines or the nodes for the $z < 0.4$, independent of the mass cut adopted for the filament network computations for the $d < 10$ Mpc and $d < 5$ Mpc; for the $d < 10$ Mpc cut, I find that passive galaxies are closer to the filaments;

3. By not including the lower mass galaxies ($M_* < 10^{9.0}M_\odot$) into the filament tracing process, I observe a difference in the signal in the $M_\star$-distance-to-filament relationship, especially for the intermediate redshift bins, such that galaxies with $\log M_\star > 10.5M_\odot$ will be closer to filaments for $z > 0.4$ and galaxies with $10.0M_\odot < \log M_\star < 10.5M_\odot$ will be closer to filaments for $z > 0.6$;

4. By excluding the galaxies closest to the nodes of the filament networks (within 5 Mpc), I find that the relationships between the galaxy properties and the distances to nodes and filaments are not distinct; this however changes for galaxies, which are within 5 Mpc of a node, where I can observe a consequence of the Butcher-Oemler effect.

Trying to obtain a general picture of the effect of the filaments, and of the cosmic web itself on galaxy properties is a complex issue. Further studies could be done into different ways of tracing filaments from observations - using filament-finders that are not dependent on the number density, such as geometrical, Hessian matrix based algorithms, such as MMF-2 (Aragón-Calvo et al., 2007) or NEXUS+ (Cautun et al., 2013b) could possibly capture the relationship between the filaments and the stellar mass of the galaxies better. Within DISPERSE itself, it is possible to account for mass weighting (Cornwell et al., 2024), which could improve the results between distance-to-filament and stellar mass. Even when including that, there are other issues that need to be taken into account. Extra care must be taken when using a mass-selected sample to compute filament networks and extract information about stellar mass dependence on the cosmic web, since, as I showed, different mass cuts on the filament networks can lead to different conclusions. This does not mean, however, that cosmic web studies cannot be done with such samples. I recovered a trend between sSFR and distance-to-filament - hence, as long as the effects of stellar mass can be disentangled, recovery of trends between the cosmic web and other galaxy properties can be achieved in observations. As well, understanding the effect of using the same galaxies into the filament tracing and the properties comparison (as opposed to using a different tracer, such as dark matter particles, in simulations) needs to be investigated in more depth. Furthermore, having access to more spectroscopic redshifts can improve the quality of the filament networks themselves.

The only stars the JWST is going to look at are the 50 stars of the flag, long live America.

Casey Cragg

6 Galaxies in the local universe: Detection of a cosmic web filament traced by HI galaxies

Contents

6.1 Introduction

As direct detection of the underlying dark matter distribution is impossible, we have to rely on the galaxies as tracers. As such, we are highly dependent on having a large number of galaxies whose positions we can trust. This also introduces several dependencies, as we use the same galaxies to trace the cosmic web and infer a link

between their properties and the large-scale structures. However, it is predicted that the intergalactic medium is populated by gas in different phases (Tumlinson et al., 2017), hence a way the cosmic web could be traced is via neutral hydrogen (HI). So far, any attempts at doing so have proved impossible, since the current telescopes cannot reach the sensitivity required for such a detection, in HI emission (Kooistra et al., 2017) or via intensity mapping (Tramonte et al., 2019). For this chapter, I discuss the discovery of 14 HI dwarf galaxies in the MIGHTEE-HI survey (Maddox et al., 2021) at $z = 0.03$ in the COSMOS field which form an elongated structure of 1.7 Mpc. This is the first time such a structure has been detected. Simulations have shown that cosmic filaments should be hosting some mildly shock-heated warm gas that is multi-phase in nature and that gas can also exist in filaments in a cooler neutral phase as a result of the radiative cooling (Mandelker et al., 2021; Lu et al., 2024). Therefore, this structure could provide aid into understanding how to obtain direct detections of the filaments of the cosmic web in gas.

6.2 Methods

6.2.1 Data

The MIGHTEE survey is one of the eight Large Survey Projects (LSPs) which are being undertaken by MeerKAT (Jonas, 2009). MeerKAT consists of an array of 64 offset-Gregorian dishes, where each dish consists of a main reflector with a diameter of 13.5 m and a sub-reflector with a diameter of 3.8 m. MeerKAT's three band receivers, UHF–band ($580 < \nu < 1015$ MHz), L–band ($900 < \nu < 1670$ MHz) and S–band ($1750 < \nu < 3500$ MHz) all collect data in spectral mode. The MIGHTEE survey has three major components: radio continuum (Heywood et al., 2021), polarisation (Taylor et al., 2024) and spectral line (Maddox et al., 2021).

MIGHTEE-HI (Maddox et al., 2021) is the HI emission part of the MIGHTEE survey. Unlike the MIGHTEE-HI Early Release data, which was a single 16 h pointing in the COSMOS field, the Data Release 1 data which I use in this chapter has 15 mosaicked pointing with 94.2 h of integration time. The data products were

Table 6.1: Short summary of the MIGHTEE-HI DR 1 data products used in this chapter.

Area covered	$\sim 4\,\mathrm{deg}^2$ COSMOS field
Frequency range	$1290 - 1520\,\mathrm{MHz}$
Redshift range	$0.03 - 0.04$
Channel width	$26.1\,\mathrm{kHz}$
Pixel size	$2\,\mathrm{arcsec}$

produced by using a parallelised CASA[1]-based (McMullin et al., 2007) pipeline whose calibration routines and strategies are standard (i.e. flagging, delay, bandpass, and complex gain calibration), as described in Heywood et al. (submitted). Visibility flagging is conducted using the TRICOLOUR package (Hugo et al., 2022). Each sub-band undergoes imaging via the WSCLEAN software (Offringa et al., 2014), with a pointing-specific mask derived from deep MIGHTEE continuum images (Heywood et al., 2022). The spectral clean component model is smoothed using the SMOPS[2] tool for spectral smoothness. After inversion into the visibility domain, (phase+delay) self-calibration and simultaneous subtraction of the continuum model occur using the CUBICAL package (Kenyon et al., 2018). Pointings are then imaged per-channel with three robustness parameters (0.0, 0.5, and 1.0) using WSCLEAN (Briggs, 1995), and deconvolution masks are generated with a custom PYTHON tool (Heywood et al. submitted). Imaging is repeated within masked regions, and resulting cubes are homogenised to a common angular resolution per channel using a custom PYTHON code and the PYPHER package (Boucaud et al., 2016). These homogenised images are primary beam corrected with the KATBEAM[3] library and linearly mosaicked with variance weighting using the MONTAGE[4] toolkit. Finally, image-plane continuum subtraction is performed along each sightline through the resulting cubes using custom PYTHON code.

For this work, I use the spectral line information in the L–band DR 1 with 32768 channels with a channel width of 26 kHz, which corresponds to $5.5\,\mathrm{km\,s^{-1}}$ at $z = 0$.

[1] http://casa.nrao.edu
[2] https://github.com/Mulan-94/smops
[3] https://github.com/ska-sa/katbeam
[4] http://montage.ipac.caltech.edu/

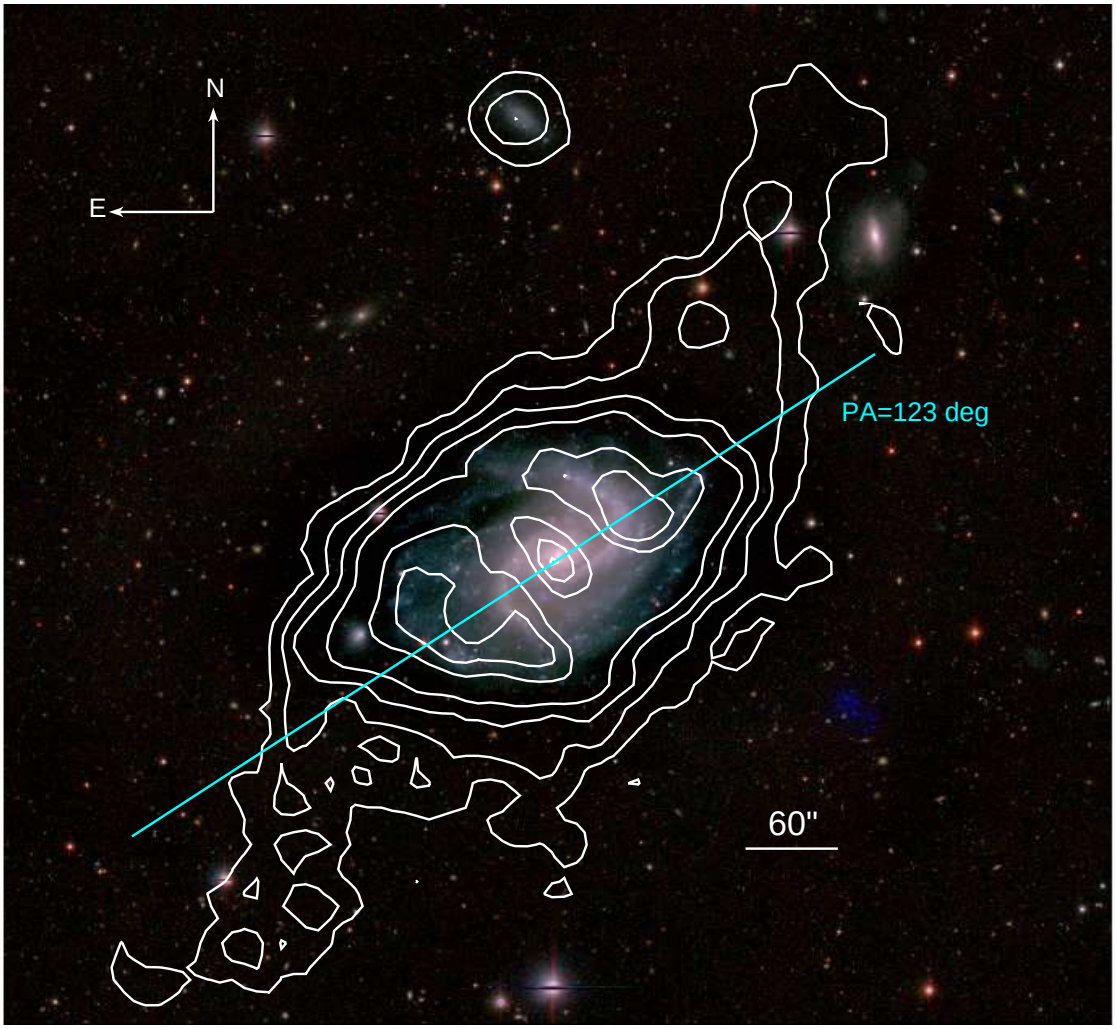

Figure 6.1: The moment-0 contour map of the HI-detected galaxy 22 pair J100222.8+024519 and J100219.8+024543, $z = 0.072266$, overlaid on a 3-colour image from the g, r and i bands of the HSC data (Aihara et al., 2018). The circle in the lower right shows the extent of the restoring beam. Figure reproduced from Heywood et al. (submitted).

6.2.2 Characteristics of the HI galaxies

The HI mass of each galaxy is calculated from the integrated flux S, as:

$$\left(\frac{M_{\rm HI}}{M_\odot}\right) = \frac{2.356 \times 10^5}{1+z}\left(\frac{D_L}{\rm Mpc}\right)^2\left(\frac{S}{\rm Jykms^{-1}}\right), \tag{6.1}$$

where D_L is the cosmological luminosity distance to the source, S is the integrated HI flux density, calculated from the moment-0 (integrated intensity over the spectral line) HI maps. An example of a galaxy with the HI contours overplotted can be seen in Figure 6.1.

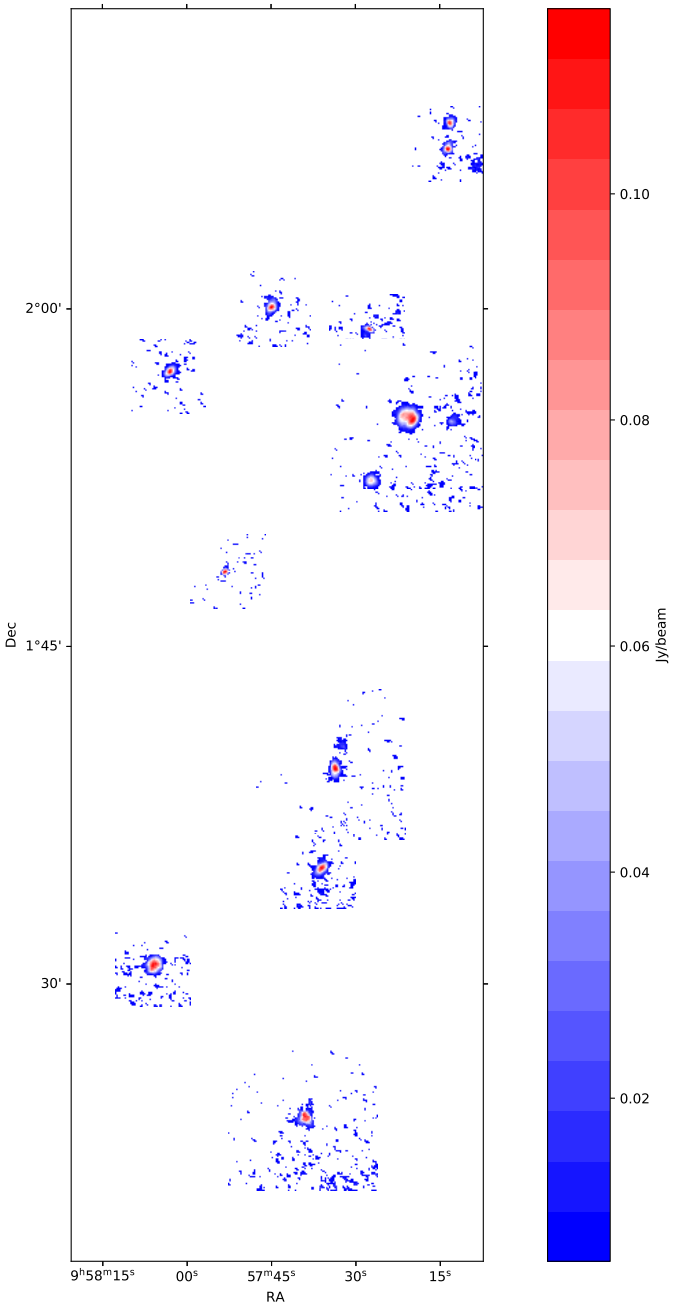

Figure 6.2: The HI galaxies as a function of the resolving beam (colour bar), with masks around each source, plotted on the common coordinate grid of the filament.

The kinematic position and inclinations for the galaxy were obtained by fitting a single ellipse to the outer parts of the moment-1 (intensity-weighted velocity of the spectral line) HI map. The position angle was calculated the same as described in Section 3.3.2 (or by fitting an ellipse where the moment-1 maps were not resolved enough), whilst the inclination i was calculated as:

$$\cos(i) = b/a, \tag{6.2}$$

where b and a are the minor/major axis of the fitted ellipse. For the HI galaxies, I obtained a range on inclinations between 34.874 and 55.736, and position angles between 13.792 and 344.0. In order to do a comparison, optical PAs and i's are also computed, using SDSS DR17 data. The optical PAs and inclinations were measured in exactly the same way, fixing the PA to the kinematic one derived in the previous step.

The velocity dispersion of the structure is computed by comparing the measured systemic velocity of each HI galaxy and its standard deviation, which is obtained kinematically via the same method described in Section 3.3.2.

I also plot the recession velocities as a histogram (see Figure 6.3a for HI only and Figure 6.3b for both the neighbouring optical galaxies and the HI galaxies), it can be seen that the spread is not Gaussian (due to low number of galaxies in the sample), however it is quite narrow.

The structure found is formed of 14 HI galaxies, with a length of ~ 1.7 Mpc and a width of ~ 36 kpc. The HI mass of these galaxies varies between 8.09×10^8 $M_\odot$ and 9.69×10^8 $M_\odot$, the median HI mass of the group being 4.7×10^8 $M_\odot$, and its velocity dispersion being ~ 140 km/s. Unlike the Early Release data, where I able to only find four galaxies within this mass range, with the increased resolution of the DR1 data, I am now able to find fainter, lower HI galaxies. Given their distribution in a straight line, their mass and their velocity spread, it is likely that they are tracing a large-scale filamentary structure.

6.2.3 Cosmic Web characterisation

In this chapter, I use DISPERSE (Sousbie, 2011) again to determine the skeleton of the cosmic web based on the distribution of optical galaxies, using data from SDSS DR17, to verify if the HI structure is indeed embedded into the cosmic web filament at that redshift. I use a redshift slice of width $\delta z = 0.01$ in the interval $0.03 < z < 0.04$, which represents 168 spectroscopically confirmed galaxies. I

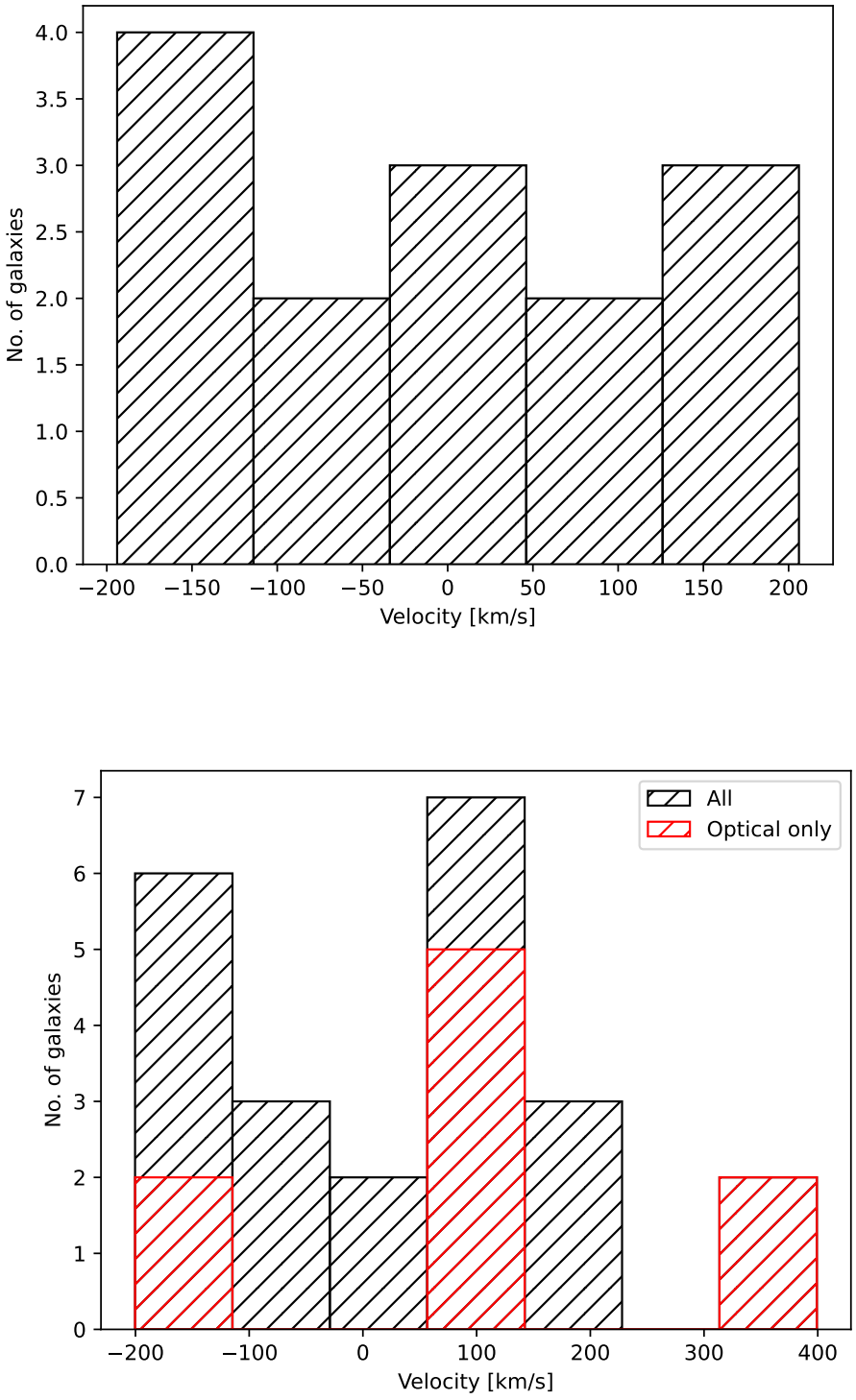

Figure 6.3: A histogram showing the velocity spread of the HI galaxies only (top) and both the HI galaxies and the SDSS optical galaxies (bottom).

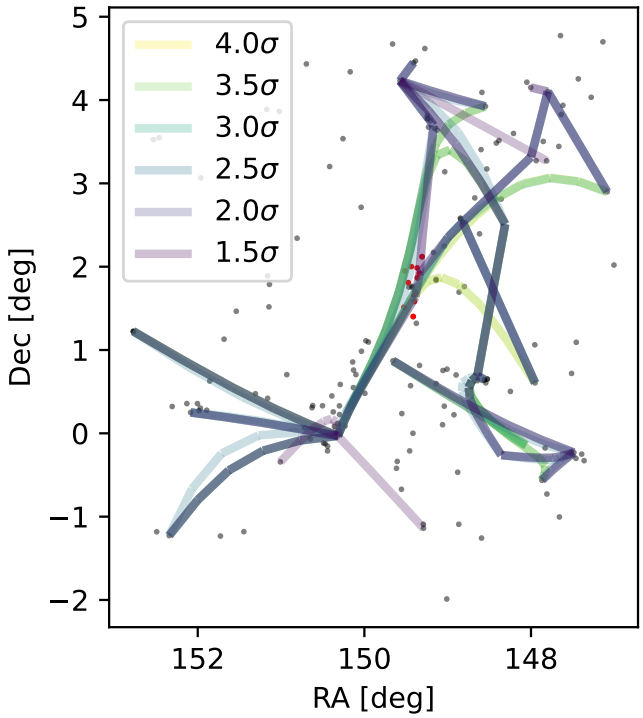

Figure 6.4: The filament distribution projected in 2D obtained by running DISPERSE with mirror boundary conditions for the SDSS catalogue centred around the COSMOS field in a redshift interval $0.03 < z < 0.04$ for different persistence levels. The red dots represent the HI detected galaxies.

use the mirror boundary conditions in DISPERSE to aid comparison with previous work (Blue Bird et al., 2020; Tudorache et al., 2022). I test the persistence of the filament by trialling several significance levels: from 1.5σ to 4.0σ, in increments of 0.5. As can be seen in Figure 6.4, a spine is maintained in that region across all persistences, with some variations in the bifurcation points. The choice of the significance level ensures then that the optical filament is robust and that the large structures are picked up without washing out some of the relevant finer structures. Another point to highlight is that the filaments are identified only using the massive, optical SDSS galaxies, without including the low-mass galaxies (see Chapter 5 for a more in-depth discussion about how filament-tracing is affected by different mass thresholds in galaxy catalogues).

In order to calculate distances between the filament obtained with DISPERSE

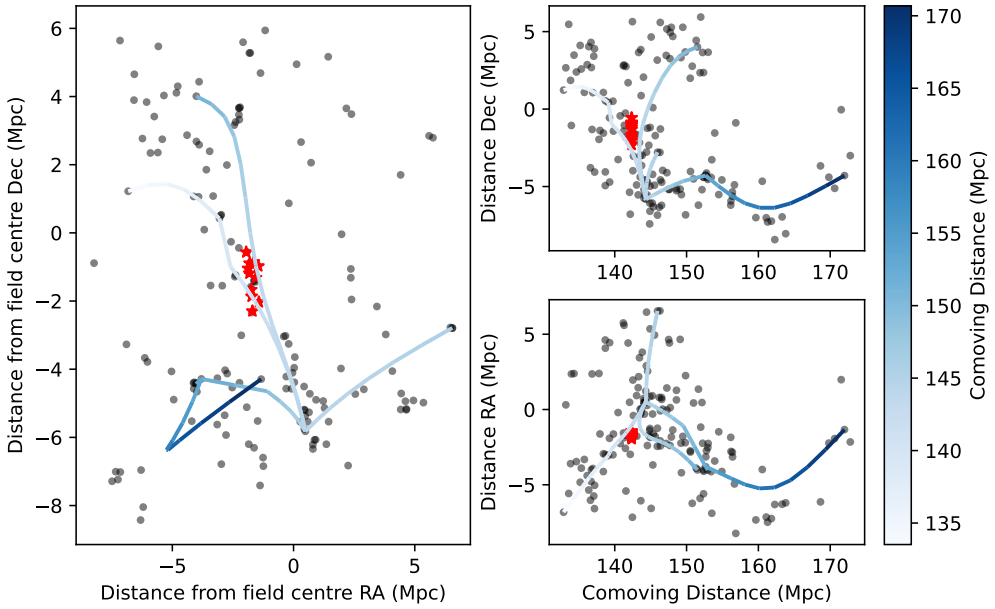

Figure 6.5: The filament distribution projected in 2D obtained by running DISPERSE with mirror boundary conditions and $\sigma = 3.5$ for the SDSS catalogue centred around the COSMOS field in a redshift interval $0.03 < z < 0.04$. Left: Angular distance in right ascension versus angular distance in declination. Top right: Radial comoving distance versus angular distance in declination. Bottom right: Radial comoving distance versus angular distance in right ascension of the filament distribution overlaid on top of the galaxies in the optical sample. The red stars represent the HI galaxies detected by MIGHTEE. The colour bar represents the radial comoving distance in Mpc.

and the HI galaxies, I crossmatch the galaxies with the mid-point of each segment generated by DISPERSE, as described in Chapter 2.2.3. As the average segment length is small, the error introduced by not calculating the line perpendicular to the segment as the distance is negligible.

6.3 Results

6.3.1 Spin-filament alignment

I calculate the distance from the HI galaxies to the cosmic web filament and I find that the closest galaxy resides within 0.56 Mpc of it, whilst the most distant one resides 2.5 Mpc away. Whilst defining a 'thickness' to a cosmic filament in observations is not straightforward, most studies agree that filaments should have radii between 1

to 2 Mpc (Bond et al., 2010; Galárraga-Espinosa et al., 2024; Wang et al., 2024).

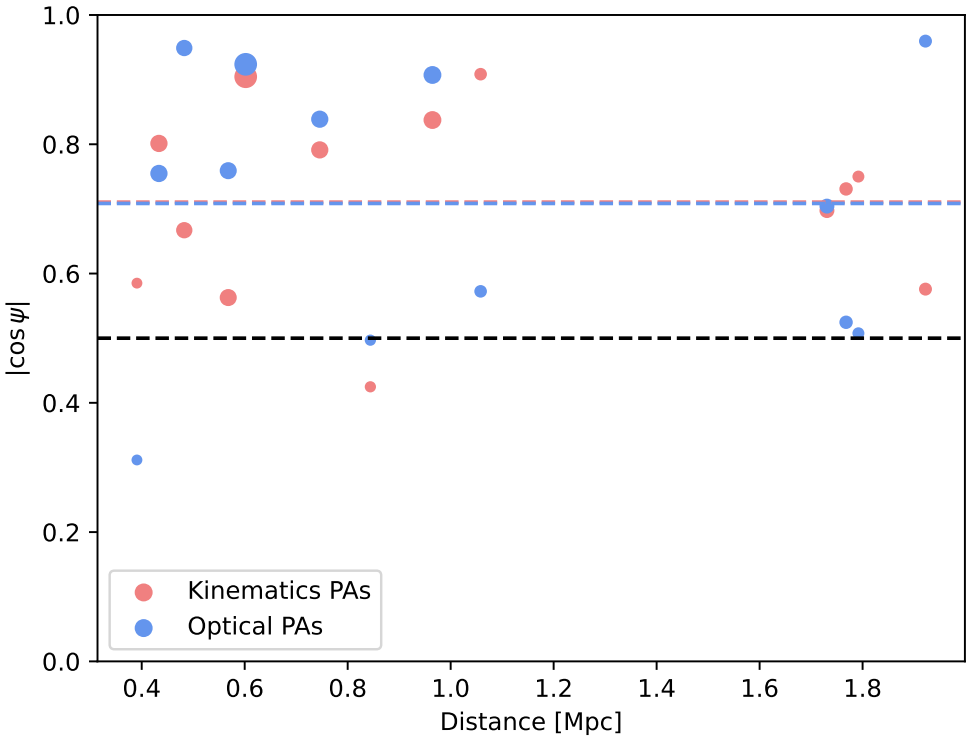

Figure 6.6: $|\cos\psi|$ for the galaxy sample as a function of distance to the closest filament computed with mirror boundary conditions for both the kinematically computed $|\cos\psi|$ (pink) and optically computed $|\cos\psi|$ (blue). The black horizontal dotted line represents the spin value 0.5, whilst the pink (blue) dotted lines mark the mean value of the kinematically (optically) computed $|\cos\psi|$. The different sizes of for the dots represent scaling with number of beams needed to observe the HI galaxies.

I then compute the spin-filament alignment $|\cos\psi|$ between the spin of each of the galaxies and their closest filaments, using the same method as in Chapter 3.3.2. Following convention (Kraljic et al., 2021; Tudorache et al., 2022), I define anything with $|\cos\psi| > 0.5$ as being aligned and $|\cos\psi| < 0.5$ as being misaligned. I find that, out of the 14 galaxies, only one galaxy has $|\cos\psi| < 0.5$ and the mean (median) value of the whole sample is $|\cos\psi| = 0.71 \pm 0.04$ (0.74 ± 0.04), indicating a strong preference for alignment, when using kinematic position angles (PA) and inclinations (i). Also of note, the galaxy which shows the preference towards misalignment is the least resolved one in the data, and as such, the position angle PA and the inclination i might not be as accurate as for the other galaxies. Furthermore, to verify this

result, I also compute the spin-filament angle for the HI galaxies using optical PAs and i's provided in SDSS, where I obtain $|\cos\psi| = 0.70 \pm 0.06$ (0.75 ± 0.06).

6.3.2 Rotation of filament

Wang et al. (2021) have found tentative evidence which predicts that cosmic filaments might also rotate around their spine. I test this theory by both only looking at the HI galaxies and their rotation, as well as the optical galaxies from SDSS used define the filament, as it would be an excellent test case for this phenomenon. I calculate the galaxies' velocities as $v \approx c \cdot z$, and then subtract the $z_{\rm med}$ of the filament spine.

As can be seen in Figure 6.7, I do not find any significant trend in the rotation of the galaxies, nor for the HI galaxies only (left side figure), nor when I include the SDSS optical galaxies which trace the filament at that position (right side figure). This could be due to the low number statistics, as there are not many galaxies (both HI and optical) in this sample, compared to Wang et al. (2021). As well, including the optical galaxies increases the velocity dispersion of the group - this is expected, as I use a proxy (redshift) to infer the velocity of the galaxies.

6.3.3 Discussion

The detection of these HI dwarf galaxies within the elongated structure of cosmic filaments at such a low redshift can prove to be an interesting environment to test models of dwarf galaxies and their behaviour within haloes/large-scale cosmic filaments - especially since such an arrangement is not necessarily predicted within the ΛCDM framework. Within the ΛCDM model, the process of structure formation, along with the assembly of increasingly massive halos through accretion and merger events, leads to the emergence of highly disordered distributions of satellite sub-haloes, within a certain virial distance of the central galaxy of the halo (Moore et al., 1998a; Gao et al., 2004; Kravtsov et al., 2004). On the other hand, observations have shown that some satellite galaxies around the Milky Way (Pawlowski et al., 2012) and Andromeda (Ibata et al., 2013) are co-rotating and aligned in thin,

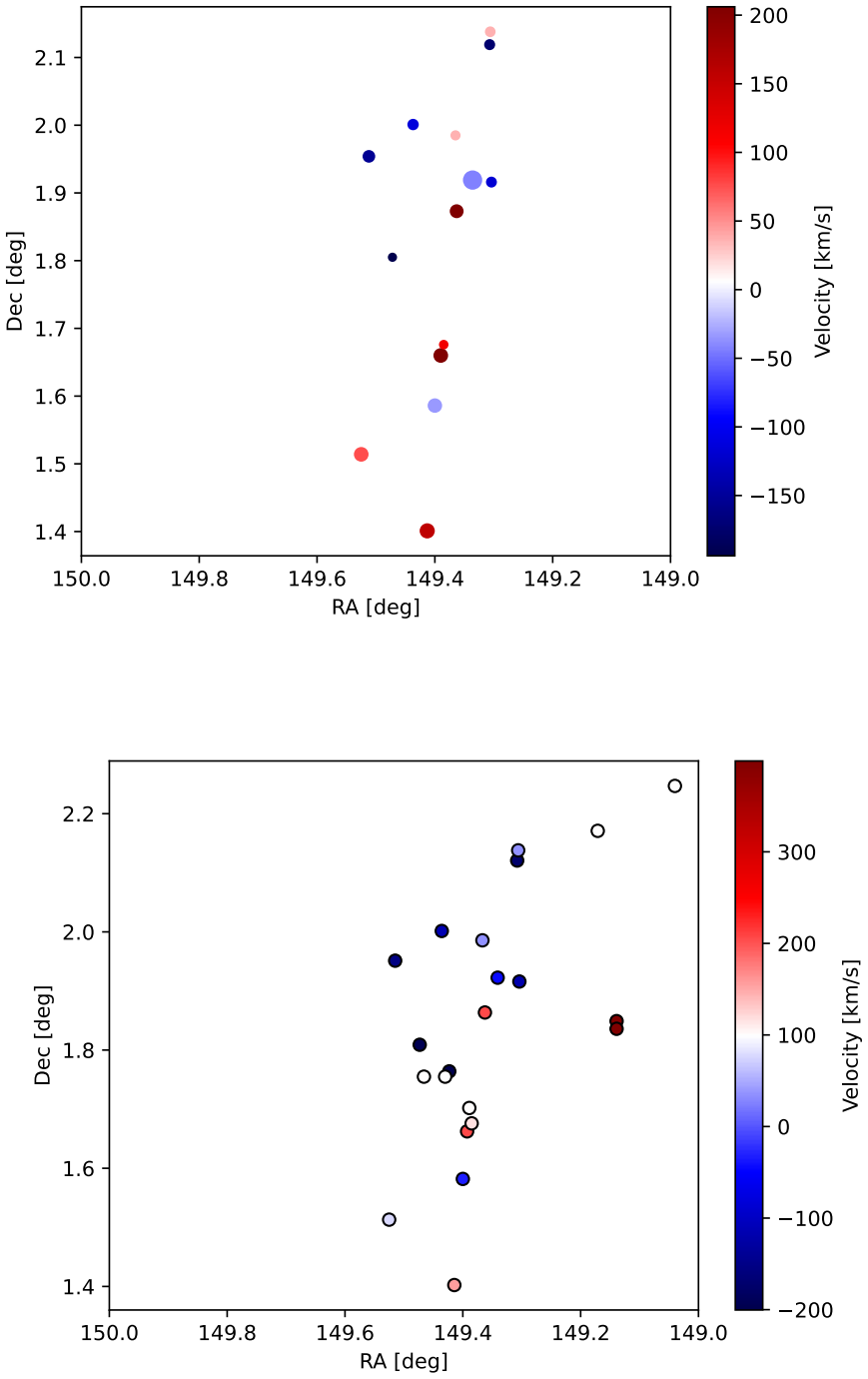

Figure 6.7: The velocity recession centred on the median redshift of the HI galaxies only (top) and both the HI galaxies and the SDSS optical galaxies (bottom). On the top figure, the different sizes of for the dots represent scaling with the beam size used for the HI galaxies.

flattened planes. This is known as the “plane of satellite" problem (Kroupa et al., 2005; Pawlowski, 2018).

However, some non-random arrangement of these sub-haloes can be possible due to different factors. One of the factors includes the preferential accretion of sub-haloes along the filamentary structures of the cosmic web (Libeskind et al., 2015), which could be further investigated with the HI structure found in this work. Other factors that could contribute to the "aligned" distribution of the dwarf galaxies include the tendency for sub-haloes to accrete in small clusters rather than individually (Lovell et al., 2011), and the overall non-spherical nature of the dark matter host haloes (Allgood et al., 2006). Consequently, some level of anisotropy in the distribution of satellite galaxies is anticipated within the framework of the ΛCDM (Knebe et al., 2004). Therefore, it remains uncertain whether configurations akin to the observed planes of satellite galaxies occur frequently enough in cosmological simulations to be considered typical or are sufficiently rare to challenge the validity of the model (Sales and Navarro, 2023).

This discovery could then also prove to be a good laboratory to test other models of dark matter (Ferreira, 2021), such as fuzzy dark matter (FDM). Fuzzy dark matter is a hypothetical form of dark matter that possesses wave-like properties on small scales, leading to a later formation of star-forming structures. The first filaments formed in such a model present an interference pattern, caused by the wave-like properties of the dark matter (Mocz et al., 2019). As such, along the filamentary structure, strings of stars would form due to constructive interference, resulting in the formation of the first galaxies (Mocz et al., 2020). On the small scales, it leads to a suppression of low-mass halos, which will have an effect on the formation and evolution of dwarf galaxies (Kulkarni and Ostriker, 2022). The "peas-in-a-pod" model predicted by FDM could explain the alignment of HI dwarf galaxies within this cosmic filament, as the interference pattern and wave-like properties of FDM may result in the concentration of matter in certain regions of space as well as the alignment and coherent motion of these galaxies within the filamentary structure (Hui et al., 2017).

In terms of the spin-filament alignment, this is consistent with other observational studies using HI selected samples (Blue Bird et al., 2020; Tudorache et al., 2022). These studies predict that HI galaxies close to a filament will be preferentially aligned with it. As gas supplied by cosmic filaments leaves an imprint on galaxy kinematics via the cold-mode accretion (Kereš et al., 2005; Dekel and Birnboim, 2006; Ocvirk et al., 2008; Brooks et al., 2009), it is expected that the spin axis of the galaxy will align with its closest filament at higher redshifts (Cadiou et al., 2022), especially at such close distances. In this scenario, it is then expected that the gas will fall in galaxies via cold flows, feeding discs with angular-momentum rich gas which will be tidally aligned with the cosmic web (Codis et al., 2015). However, this has not been directly observed at lower redshifts in simulations, and it is even debatable if the the cold mode accretion has any effects at low-z (Pichon et al., 2011).

6.4 Conclusions

I report the detection of 14 HI dwarf galaxies in the MIGHTEE-HI survey at $z = 0.03$ in the COSMOS field which form an elongated structure of 1.7 Mpc and have a velocity dispersion of 140 km/s. I find that all the HI galaxies are within 2.5 Mpc of a cosmic web filament computed from SDSS galaxies, implying that they are tracing it as well. This is the first time such a structure has been detected in HI. I also calculate the spin-filament alignment $|\cos\psi|$ for each for the galaxies, and I find that there is a strong preference for the galaxies to be aligned with the cosmic web filament, as the mean (median) value of the whole sample is $|\cos\psi| = 0.71 \pm 0.04$ (0.74 ± 0.04) when using kinematic measurements of angles and $|\cos\psi| = 0.70 \pm 0.06$ (0.75 ± 0.06) using optical measurement of angles. This structure thus shows that within a cosmic filament, the HI gas is relatively undisturbed in its angular momentum. As cosmological simulations predict the HI gas will be feasible to detect with the rise of next-generation radio telescopes (Kooistra et al., 2017; Kooistra et al., 2019), this structure can prove to be the ideal environment to attempt such a detection. Moreover, it can prove to be a good laboratory for testing other models of dark matter, as well as trying to pin down how

does filamentary accretion affect the orientation and rotation of satellite galaxies. By understanding the relationship between this HI structure and the cosmic filament it traces, it has the potential to pin down the relationship between the low density gas in the cosmic web and how the galaxies that lie within it grow using its material.

You know how Neo sees the code in the Matrix, that's how I see the Riemann tensor everywhere.

Casey Cragg

7 Conclusions

Contents

7.1 Summary and conclusions

The cosmic web is a vast, interconnected network of threads in space. These threads, made of galaxies, gas and dust, are known as filaments. Understanding its elusive nature and the way it affects galaxies in and around it is a new area, since researching it has not been possible without the technological advances made in building new, bigger and better telescopes. The field is now rapidly evolving, as more and more researchers join the effort of tracing the cosmic web and its impact. However, this means that so far we do not have a comprehensive understanding of what the main processes and what the main methods to perform analyses are. In the past, tentative links have been found between the masses of the galaxies and their positions in the cosmic web, as well as the rate at which they produce

stars and their angular momentum (e.g. Crone Odekon et al., 2018; Kraljic et al., 2017; Blue Bird et al., 2020).

In this thesis, I aimed to investigate these links in order to gain a deeper understanding of the effect of the cosmic web on galaxy evolution. In Chapter 3, I investigated how the galaxies' spin is related to the direction of the filaments in the local universe, known as the spin-filament alignment. The overall picture of the relationship between the spin vector of a galaxy and the direction of the filaments of the cosmic web in which it may reside is complicated. There are many results from both simulations and observations disagreeing to different degrees. I focused on how we can use neutral hydrogen to investigate this problem - more specifically, I used 77 HI galaxies from the MIGHTEE-HI Early Science observations. I found that the HI-to-stellar mass ratio of a galaxy ($\frac{M_{\rm HI}}{M_*}$) is related to the alignment of the galaxy spin vector and the nearest filament, such that *galaxies which are misaligned have higher HI-to-stellar mass ratios.* As gas-rich mergers are expected to increase the amount of neutral gas in galaxies, this could suggest that galaxies which have recently undergone such a gas-rich merger may have their spin-orientation disrupted with respect to the filament, whereas those galaxies which have not undergone a recent merger will tend to retain their alignment and their evolution is dictated by secular processes. This is an empirical result which is yet to be observed by other studies - mostly due to the fact that this is the biggest, deepest sample of neutral hydrogen galaxies to date. The only other observational study done with HI which tries to investigate between the spin-filament alignment (only using 10 HI-selected galaxies) also finds that galaxies closer to the filament spine are more likely to be aligned. Given that the number statistics in this study are limited, it would benefit from additional data. However, it underlines the potential of the MIGHTEE Large Survey Program, as well as the MeerKAT telescope. With more data expected in the coming years, the sample size of HI galaxies will increase significantly and enable a big step forward in understanding how galaxies are powered by fuel drawn from the cosmic web. Whilst a study with respect to redshift will be difficult with MIGHTEE alone, combining information from MIGHTEE with the deeper and

narrower Looking At the Distant Universe with the MeerKAT Array (LADUMA, Blyth et al., 2016) may provide the necessary redshift baseline. However, the need to at least marginally resolve galaxies for the kinematic modelling would limit the sample to the largest or most HI-rich galaxies, given MeerKAT's synthesised beam.

In Chapter 4, I delved further into understanding the (mis)alignment of HI galaxies with the cosmic web. One possible explanation for the disruption in the spin-filament alignment could be past mergers, which have the capacity to disrupt the spin axis of the galaxies. Such a merger history can be investigated by measuring the star formation histories (SFHs) of the galaxies (as well as ongoing enhanced star formation or morphological evidence of a merger event happening) as a function of their spin alignment with the filaments. I computed the SFHs of the 237 galaxies from the MIGHTEE-HI Survey Early Release data using photometry. I then used a sub-sample of these SFHs to analyse the link between the spin-filament alignment and the HI content of the galaxies. I did not find any episodes of recent star formation by visually inspecting the SFHs. As well, I found no correlation between the peak time of star formation of the galaxies and the spin-filament angle, nor did I find any correlation between gas depletion time and spin-filament alignment. This could be explained in two ways: either the photometric data is not good enough to constrain SFHs such that a merger history would be observed; or mergers are not the cause for the split in the spin-filament alignment. Furthermore, I explored other links between the properties of the full HI selected galaxy sample and the star formation. I do not find any strong correlations between $M_{\rm HI}$ and the peak time of star formation of the galaxies. However, I found a strong correlation between the HI-to-stellar mass ratio of a galaxy and its peak star formation time, as well as a strong anti-correlation between the stellar mass of a galaxy and its peak star formation time, independent of the SFH inferred. In terms of the gas depletion time, I also found correlations between it and the HI-to-stellar mass ratio, as well as the stellar mass. The correlations were consistent with the picture that smaller, gas-rich galaxies have a higher depletion time due to a shallower potential

well and less efficient star formation, whilst more massive galaxies have already depleted their gas and formed stars efficiently.

In Chapter 5, I explored how galaxies' positions correlate with the cosmic filaments by using a catalogue of photometric redshifts, which will introduce uncertainties in the galaxy positions. As we need the galaxy positions to infer the cosmic web, these increased uncertainties will give us different possible configurations of the network. Hence, I developed a method that uses the probability of a galaxy being at a specific redshift and repeats different iterations of possible cosmic web configurations based on the uncertainty in the redshift of each galaxy. Doing that 1000s of times gives you the most likely configuration of the cosmic web in that specific patch of sky. This allows a reconstruction of the cosmic environment which maintains all the major structures, even when accounting for all the uncertainties. Additionally, I used these networks to investigate the relationship between galaxy properties (stellar mass, specific star formation rate) and the distance to their closest filament/node. I did not find any strong evidence for a link between stellar mass and proximity to nearest filament, which could be caused by the fact that I used a mass-selected sample to perform the study. This was confirmed by obtaining different trends when I repeated the analysis with different mass cuts on the filament-finding algorithm. By removing lower mass galaxies from the filament-finding algorithm, I found that more massive galaxies are more likely to be closer to the spine of the filaments for $z > 0.4$. I also found tentative evidence of the sample being deficient in highest mass galaxies close to filaments. However, by disentangling the effects of the stellar mass as a filament-tracer, massive galaxies that lie on/above the star-formation main sequence will tend to be closer to the spine of the filaments, especially at the lower end of the redshift distribution, in comparison to their lower mass counterparts for $z < 0.4$. This enhancement of star formation in the higher mass galaxies at low redshift is likely to be caused by the flow of the cold gas in the filaments into these galaxies and is in agreement with recent results from hydrodynamic simulations.

In Chapter 6, I described the discovery of 14 HI dwarf galaxies which form an elongated structure of 1.7 Mpc with very low velocity dispersion, using the new MIGHTEE-HI 32k data. I found that all the dwarf HI galaxies are within 2.5 Mpc of a cosmic web filament computed from SDSS galaxies, which they are tracing. This is the first time such a structure has been detected. I also calculated the spin-filament alignment $|\cos\psi|$ for each for the galaxies, and I found that there is a strong preference for the galaxies to be aligned with the cosmic web filament, as the mean (median) value of the whole sample is $|\cos\psi| = 0.71 \pm 0.04$ (0.74 ± 0.04) using kinematic measurements of angles and $|\cos\psi| = 0.70 \pm 0.06$ (0.75 ± 0.06) using optical measurement of angles. This structure thus shows that within a cosmic filament, the HI gas is relatively undisturbed in its angular momentum. As well, since such an arrangement is not necessarily predicted within the ΛCDM framework, it could prove to be a good laboratory to test other models of dark matter.

7.2 Future work

In this final section, I discuss very briefly future work that can be built from this thesis, in particular the exciting new telescopes, surveys and the data sets that will become available from them in the following years.

7.2.1 HI galaxies and filaments projects

As discussed in Chapter 4, in order to do analysis on SFHs, spectroscopy is needed. Hence, for the SFHs work, instead of using photometric data, spectroscopic data would provide a better avenue into better constrained SFHs. In the future, I plan to use the MIGHTEE-MUSE program, which has been accepted as part of Cycle P112 for MUSE on the VLT. As such, I will examine the SFHs of galaxies and look for signs of ongoing star formation or merger events by using stellar populations in a smaller sample of 20 misaligned galaxies selected based on their brightness and closeness to their closest filament. By combining data from different sources and using MUSE, I will be able track the SFHs in these galaxies and confirm if past mergers are indeed responsible for the misalignment between their hydrogen

gas disks and the cosmic filaments. This will enable us to determine whether there is any evidence for mergers on a galaxy-by-galaxy basis due to the significant improvement in the quality of the spectral data.

I will explore detecting and understand the formation and distribution of the cosmic filaments themselves using multi-wavelength data. Currently, most studies on filaments use only visible light, with the assumption that the distribution of galaxies follows the distribution of filaments. However, there is a plethora of information hidden in the other wavelengths - especially in radio, as demonstrated in Tudorache et al. (2022). What I intend to do, by using radio data from galaxies which have been used as tracers for the filaments, is to try to extract the filaments themselves. This can be achieved by using the previously traced cosmic web as a proxy, then, by using the HI galaxies within their proximity, their optical disks could be removed, leaving only the residual gas. By doing so, the filaments should be observed directly using gas. Whilst there have been some attempts in literature at doing this (Tramonte et al., 2019; Kooistra et al., 2017), no other study had access to the data I do - both in terms of the photometric filaments traced and the positions/numbers of the neutral hydrogen galaxies. As a follow-up from Chapter 6, I am part of a MeerKAT proposal which aims to observe HI galaxies along the full SDSS filament spine all the way down to where the central halo should be. This would be a great laboratory for testing stacking along the filament in order to check for excess in the HI signal in between the galaxies. As well, this would provide a way to not only observe how the HI galaxies follow the spine, but how their alignment and properties change as they hit a different environment - a high density cluster.

7.2.2 Other radio data and filaments projects

Radio data can also be used to explore the supermassive black holes at the centres of galaxies. Inferring if the cosmic web has an effect all the way to the core of a galaxy is crucial for our understanding of galaxy evolution, as it has been shown (e.g. Silk and Mamon, 2012; Zinger et al., 2020; Piotrowska et al., 2022) that properties such as black hole mass or black hole activity correlate with star formation rates

and quenching. A way to investigate this problem is by looking at the bright jet emissions (AGN) from these supermassive black holes. Most studies into the nature of AGN have been done without taking into account their environment, or at the very least, only taking into account their most local environment (e.g. Gilmour et al., 2007; Malavasi et al., 2015; Bornancini and García Lambas, 2020; Santos et al., 2021). My idea is that we should not be limited by looking into the most dense regions of the Universe, and that exploring how other parts of the cosmic web contribute to the observed properties of AGN will help us shed light into how one of the most extreme processes in the Universe is fuelled. As part of my plan, I will investigate the positions of the AGN with respect to the elements of the web and how it correlates with their characteristics, such as the direction of the jets emanating from around the black holes.

7.2.3 Closing remarks

As part of my research, I have been drawing upon data from various origins, encompassing diverse forms of multi-wavelength data, to comprehend these galaxies' properties. This approach assists us in piecing together a more cohesive narrative of all the processes that contribute to the life cycle of a galaxy. This is a novel way to tackle this problem, since most studies involving galaxy evolution within the cosmic web mostly focus on the optical part of the electromagnetic spectrum. With the upcoming surveys such as Rubin/LSST, Euclid and the SKA, we need to be able to understand the large scale of the Universe and how it affects the galaxies it is formed of. Specifically, I can use the methods I have developed at higher redshift, as currently the work presented in Chapter 5 only extends up to $z = 1$, but could be used further and on larger area.

My work will come as a bridge between cosmology and galaxy evolution and will help us make the best out of new facilities and telescopes.

Appendices

A

Chapter 4: Tables for correlation tests for SFHs

Table A.1: The coefficients and p-values for the two correlation tests, Kendall's Tau and Spearman Rank, for each parameter against the $t(z_{\rm form})$ for the exponential SFH.

Parameter	**Kendall's Tau**		**Spearman Rank**	
	τ	**p-value**	**coefficient**	**p-value**
Distance	-0.082	0.079	-0.117	0.092
$\lvert\cos\psi\rvert$	0.031	0.72	0.053	0.683
$M_{\rm HI}$	-0.024	0.607	-0.038	0.589
M_*	-0.379	0.0	-0.546	0.0
$M_{\rm HI}/M_*$	0.319	0.0	0.475	0.0

Table A.2: The coefficients and p-values for the two correlation tests, Kendall's Tau and Spearman Rank, for each parameter against the $t(z_{\rm form})$ for the constant SFH.

Parameter	**Kendall's Tau**		**Spearman Rank**	
	τ	**p-value**	**coefficient**	**p-value**
Distance	-0.037	0.425	-0.053	0.445
$\lvert\cos\psi\rvert$	-0.072	0.405	-0.093	0.473
$M_{\rm HI}$	-0.025	0.595	-0.034	0.62
M_*	-0.266	0.0	-0.39	0.0
$M_{\rm HI}/M_*$	0.219	0.0	0.328	0.0

Table A.3: The coefficients and p-values for the two correlation tests, Kendall's Tau and Spearman Rank, for each parameter against the $t(z_{\rm form})$ for the lognormal SFH.

Parameter	**Kendall's Tau**		**Spearman Rank**	
	τ	**p-value**	**coefficient**	**p-value**
Distance	-0.081	0.082	-0.12	0.082
$\lvert\cos\psi\rvert$	0.038	0.666	0.072	0.578
$M_{\rm HI}$	-0.015	0.748	-0.022	0.751
M_*	-0.347	0.0	-0.497	0.0
$M_{\rm HI}/M_*$	0.291	0.0	0.435	0.0

Table A.4: The coefficients and p-values for the two correlation tests, Kendall's Tau and Spearman Rank, for each parameter against the $t(z_{\rm form})$ for the double power law SFH.

Parameter	**Kendall's Tau**		**Spearman Rank**	
	τ	**p-value**	**coefficient**	**p-value**
Distance	-0.055	0.236	-0.081	0.244
$\lvert\cos\psi\rvert$	0.031	0.72	0.031	0.812
$M_{\rm HI}$	0.042	0.361	0.068	0.329
M_*	-0.033	0.481	-0.075	0.28
$M_{\rm HI}/M_*$	0.049	0.287	0.094	0.177

Table A.5: The coefficients and p-values for the two correlation tests, Kendall's Tau and Spearman Rank, for each parameter against the $t(z_{\rm form})$ for the burst SFH.

Parameter	**Kendall's Tau**		**Spearman Rank**	
	τ	**p-value**	**coefficient**	**p-value**
Distance	-0.059	0.2	-0.085	0.222
$\lvert\cos\psi\rvert$	-0.013	0.879	-0.021	0.873
$M_{\rm HI}$	0.01	0.831	0.011	0.87
M_*	-0.427	0.0	-0.596	0.0
$M_{\rm HI}/M_*$	0.383	0.0	0.545	0.0

References

Acero, F. et al. (2009). *Science* 326.5956, p. 1080.

Adams, N. J. et al. (2021). *Monthly Notices of the Royal Astronomical Society* 506.4, pp. 4933–4951.

Aihara, H. et al. (2018). *Publications of the Astronomical Society of Japan* 70, S8, S8.

Aihara, H. et al. (2022). *Publications of the Astronomical Society of Japan* 74.2, pp. 247–272.

Alam, S. et al. (2015). *The Astrophysical Journal, Supplement* 219.1, 12, p. 12.

Alberts, S. and Noble, A. (2022). *Universe* 8.11, 554, p. 554.

Allgood, B. et al. (2006). *Monthly Notices of the Royal Astronomical Society* 367.4, pp. 1781–1796.

Almosallam, I. A., Jarvis, M. J., and Roberts, S. J. (2016a). *Monthly Notices of the Royal Astronomical Society* 462.1, pp. 726–739.

Almosallam, I. A. et al. (2016b). *Monthly Notices of the Royal Astronomical Society* 455.3, pp. 2387–2401.

Alpaslan, M. et al. (2014). *Monthly Notices of the Royal Astronomical Society* 438.1, pp. 177–194.

Alpaslan, M. et al. (2015). *Monthly Notices of the Royal Astronomical Society* 451.3, pp. 3249–3268.

Ann, H. B., Park, C., and Choi, Y.-Y. (2008). *Monthly Notices of the Royal Astronomical Society* 389.1, pp. 86–92.

Aragón-Calvo, M. A. and Szalay, A. S. (2013). *Monthly Notices of the Royal Astronomical Society* 428.4, pp. 3409–3424.

Aragón-Calvo, M. A. and Yang, L. F. (2014). *Monthly Notices of the Royal Astronomical Society* 440, pp. L46–L50.

Aragón-Calvo, M. A. et al. (2007). *Astronomy and Astrophysics* 474.1, pp. 315–338.

Aragón-Calvo, M. A., Neyrinck, M. C., and Silk, J. (2019). *The Open Journal of Astrophysics* 2.1, 7, p. 7.

Aragón-Calvo, M. A. et al. (2010). *The Astrophysical Journal* 723.1, pp. 364–382.

Arbey, A. and Mahmoudi, F. (2021). *Progress in Particle and Nuclear Physics* 119, 103865, p. 103865.

Arnett, D. (1999). *Astrophysics and Space Science* 265, pp. 29–35.

Arnouts, S. et al. (1999). *Monthly Notices of the Royal Astronomical Society* 310.2, pp. 540–556.

Babul, A. and Starkman, G. D. (1992). *The Astrophysical Journal* 401, p. 28.

Bacchi, M. et al. (2003). *Astronomy & Astrophysics* 400, pp. 465–476.

Baldry, I. K. et al. (2010). *Monthly Notices of the Royal Astronomical Society* 404.1, pp. 86–100.

Baldwin, J. A., Phillips, M. M., and Terlevich, R. (1981). *Publications of the Astronomical Society of the Pacific* 93, pp. 5–19.

Balogh, M. L. et al. (2004). *The Astrophysical Journall* 615.2, pp. L101–L104.

Barcons, X. et al. (2001). In: *X-ray Astronomy: Stellar Endpoints, AGN, and the Diffuse X-ray Background*. Ed. by N. E. White, G. Malaguti, and G. G. C. Palumbo. Vol. 599. American Institute of Physics Conference Series, pp. 3–12.

Barnes, J. and Efstathiou, G. (1987). *The Astrophysical Journal* 319, p. 575.

Barnes, J. E. and Hernquist, L. E. (1991). *The Astrophysical Journal, Letters* 370, p. L65.

Bartelmann, M. and Schneider, P. (2001). *Physics Reports* 340.4-5, pp. 291–472.

Barth, A. J., Filippenko, A. V., and Moran, E. C. (1999). *The Astrophysical Journal* 525.2, pp. 673–684.

Barton, E. J., Geller, M. J., and Kenyon, S. J. (2000). *The Astrophysical Journal* 530.2, pp. 660–679.

Bastian, N., Covey, K. R., and Meyer, M. R. (2010). *Annual Review of Astronomy and Astrophysics* 48, pp. 339–389.

Begelman, M. C. (2004). In: *Coevolution of Black Holes and Galaxies*. Ed. by L. C. Ho, p. 374.

Bell, E. F. et al. (2006). *The Astrophysical Journal* 640.1, pp. 241–251.

Benson, A. J. et al. (2003). *The Astrophysical Journal* 599.1, pp. 38–49.

Berger, E. (2014). *Annual Review of Astronomy and Astrophysics* 52, pp. 43–105.

Bergvall, N., Laurikainen, E., and Aalto, S. (2003). *Astronomy & Astrophysics* 405, pp. 31–52.

Bermejo, R. et al. (2024). *Monthly Notices of the Royal Astronomical Society* 529.4, pp. 4325–4353.

Bernardi, M. et al. (2006). *The Astronomical Journal* 131.3, pp. 1288–1317.

Bertone, G. and Hooper, D. (2018). *Reviews of Modern Physics* 90.4, 045002, p. 045002.

Bertone, S., De Lucia, G., and Thomas, P. A. (2007). *Monthly Notices of the Royal Astronomical Society* 379.3, pp. 1143–1154.

Bilicki, M. et al. (2016). *The Astrophysical Journals* 225.1, 5, p. 5.

Binggeli, B., Sandage, A., and Tammann, G. A. (1988). *Annual Review of Astronomy and Astrophysics* 26, pp. 509–560.

Binney, J. (2004). *Monthly Notices of the Royal Astronomical Society* 347.4, pp. 1093–1096.

Birkinshaw, M. (1999). *Physics Reports* 310.2-3, pp. 97–195.

Blandford, R., Meier, D., and Readhead, A. (2019). *Annual Review of Astronomy and Astrophysics* 57, pp. 467–509.

Blue Bird, J. et al. (2020). *Monthly Notices of the Royal Astronomical Society* 492.1, pp. 153–176.

Blumenthal, G. R. et al. (1984). *Nature* 311, pp. 517–525.

Blyth, S. et al. (2016). In: *MeerKAT Science: On the Pathway to the SKA*, 4, p. 4.

Bolzonella, M., Miralles, J. M., and Pelló, R. (2000). *Astronomy and Astrophysics* 363, pp. 476–492.

Bond, J. R. and Efstathiou, G. (1987). *Monthly Notices of the Royal Astronomical Society* 226, pp. 655–687.

Bond, J. R., Kofman, L., and Pogosyan, D. (1996). *Nature Astrophysics* 380.6575, pp. 603–606.

Bond, N. A., Strauss, M. A., and Cen, R. (2010). *Monthly Notices of the Royal Astronomical Society* 409.1, pp. 156–168.

Bonjean, V. et al. (2018). *Astronomy & Astrophysics* 609, A49, A49.

Bonjean, V. et al. (2020). *Astronomy and Astrophysics* 638, A75, A75.

Bornancini, C. and García Lambas, D. (2020). *Monthly Notices of the Royal Astronomical Society* 494.1, pp. 1189–1202.

Boselli, A. et al. (2005). *The Astrophysical Journal, Letters* 629.1, pp. L29–L32.

Boselli, A., Fossati, M., and Sun, M. (2022). *The Astronomy and Astrophysics Review* 30.1, 3, p. 3.

Boucaud, A. et al. (2016). *Astronomy & Astrophysics* 596, A63, A63.

Bouché, N. et al. (2016). *The Astrophysical Journal* 820.2, 121, p. 121.

Bournaud, F., Jog, C. J., and Combes, F. (2005). *Astronomy & Astrophysics* 437.1, pp. 69–85.

Bower, R. G. et al. (2006). *Monthly Notices of the Royal Astronomical Society* 370.2, pp. 645–655.

Braine, J. and Combes, F. (1992). *Astronomy & Astrophysics* 264, pp. 433–443.

Briggs, D. S. (1995). In: *American Astronomical Society Meeting Abstracts*. Vol. 187. American Astronomical Society Meeting Abstracts, 112.02, p. 112.02.

Brinkmann, W. (1989). In: *Frontier Objects in Astrophysics and Particle Physics*. Ed. by F. Giovannelli and G. Mannocchi, pp. 161–166.

Brooks, A. M. et al. (2009). *The Astrophysical Journal* 694.1, pp. 396–410.

Bruzual, G. and Charlot, S. (2003). *Monthly Notices of the Royal Astronomical Society* 344.4, pp. 1000–1028.

Bulichi, T.-E., Dave, R., and Kraljic, K. (2023). *arXiv e-prints*, arXiv:2309.03282, arXiv:2309.03282.

Bullock, J. S. and Boylan-Kolchin, M. (2017). *Annual Review of Astronomy and Astrophysics* 55.1, pp. 343–387.

Bundy, K. et al. (2015). *The Astrophysical Journal* 798.1, 7, p. 7.

Burkert, A. (1995). *The Astrophysical Journal, Letters* 447, pp. L25–L28.

Butcher, H. and Oemler A., J. (1978). *The Astrophysical Journal* 219, pp. 18–30.

Butcher, H. and Oemler A., J. (1984). *The Astrophysical Journal* 285, pp. 426–438.

Cadiou, C., Dubois, Y., and Pichon, C. (2022). *Monthly Notices of the Royal Astronomical Society* 514.4, pp. 5429–5442.

Calzetti, D. et al. (2000). *The Astrophysical Journal* 533.2, pp. 682–695.

Cantalupo, S. et al. (2014). *Nature* 506.7486, pp. 63–66.

Cappellari, M. (2023). *Monthly Notices of the Royal Astronomical Society* 526.3, pp. 3273–3300.

Carnall, A. C. et al. (2018). *Monthly Notices of the Royal Astronomical Society* 480.4, pp. 4379–4401.

Carrasco Kind, M. and Brunner, R. J. (2014). *Monthly Notices of the Royal Astronomical Society* 442.4, pp. 3380–3399.

Catelan, P. and Theuns, T. (1996a). *Monthly Notices of the Royal Astronomical Society* 282.2, pp. 436–454.

Catelan, P. and Theuns, T. (1996b). *Monthly Notices of the Royal Astronomical Society* 282.2, pp. 455–469.

Cautun, M., van de Weygaert, R., and Jones, B. J. T. (2013a). *Monthly Notices of the Royal Astronomical Society* 429.2, pp. 1286–1308.

Cautun, M., van de Weygaert, R., and Jones, B. J. T. (2013b). *Monthly Notices of the Royal Astronomical Society* 429.2, pp. 1286–1308.

Cautun, M. et al. (2014). *Monthly Notices of the Royal Astronomical Society* 441.4, pp. 2923–2973.

Cavagnolo, K. W. et al. (2008). *The Astrophysical Journal* 682.2, pp. 821–834.

Cen, R. and Zheng, Z. (2013). *The Astrophysical Journal* 775.2, 112, p. 112.

Cenci, E. et al. (2024). *Monthly Notices of the Royal Astronomical Society* 527.3, pp. 7871–7890.

Centrella, J. and Melott, A. L. (1983). *Nature* 305, pp. 196–198.

Chabrier, G. (2003). *Publications of the Astronomical Society of the Pacific* 115.809, pp. 763–795.

Chen, Y.-C. et al. (2017). *Monthly Notices of the Royal Astronomical Society* 466.2, pp. 1880–1893.

Chou, R. C. Y., Bridge, C. R., and Abraham, R. G. (2013). In: *Galaxy Mergers in an Evolving Universe*. Ed. by W. .-. Sun et al. Vol. 477. Astronomical Society of the Pacific Conference Series, p. 145.

Cignoni, M. et al. (2009). *The Astronomical Journal* 137.3, pp. 3668–3684.

Clowe, D. et al. (2006). *The Astrophysical Journal, Letters* 648.2, pp. L109–L113.

Codis, S., Pichon, C., and Pogosyan, D. (2015). *Monthly Notices of the Royal Astronomical Society* 452.4, pp. 3369–3393.

Coil, A. L. et al. (2011). *The Astrophysical Journal* 741.1, 8, p. 8.

Colberg, J. M. et al. (2005). *Monthly Notices of the Royal Astronomical Society* 360.1, pp. 216–226.

Colberg, J. M. et al. (2008). *Monthly Notices of the Royal Astronomical Society* 387.2, pp. 933–944.

Colless, M. et al. (2001). *Monthly Notices of the Royal Astronomical Society* 328.4, pp. 1039–1063.

Combes, F., Young, L. M., and Bureau, M. (2007). *Monthly Notices of the Royal Astronomical Society* 377.4, pp. 1795–1807.

Condon, J. J. (1992). *Annual Review of Astronomy and Astrophysics* 30, pp. 575–611.

Conroy, C. (2013). *Annual Review of Astronomy and Astrophysics* 51.1, pp. 393–455.

Conroy, C., Gunn, J. E., and White, M. (2009). *The Astrophysical Journal* 699.1, pp. 486–506.

Conselice, C. J. (2003). *The Astrophysical Journal, Supplement* 147.1, pp. 1–28.

Conselice, C. J. (2014). *Annual Review of Astronomy and Astrophysics* 52, pp. 291–337.

Conselice, C. J. et al. (2003). *The Astronomical Journal* 126.3, pp. 1183–1207.

Constantin, A. et al. (2015). *The Astrophysical Journal* 814.2, 149, p. 149.

Cooke, K. C. et al. (2023). *The Astrophysical Journal* 942.1, 49, p. 49.

Cool, R. J. et al. (2013). *The Astrophysical Journal* 767.2, 118, p. 118.

Cornwell, D. J. et al. (2024). *Monthly Notices of the Royal Astronomical Society* 527.1, pp. 23–34.

Cortese, L. et al. (2012). *Astronomy & Astrophysics* 540, A52, A52.

Cortijo-Ferrero, C. et al. (2017). *Astronomy & Astrophysics* 607, A70, A70.

Cox, T. J. et al. (2006). *The Astrophysical Journal* 650.2, pp. 791–811.

Crone Odekon, M. et al. (2018). *The Astrophysical Journal* 852.2, 142, p. 142.

Croom, S. M. et al. (2012). *Monthly Notices of the Royal Astronomical Society*.

Croton, D. J. et al. (2006). *Monthly Notices of the Royal Astronomical Society* 365.1, pp. 11–28.

Cui, W. et al. (2018). *Monthly Notices of the Royal Astronomical Society* 480.3, pp. 2898–2915.

da Cunha, E., Charlot, S., and Elbaz, D. (2008). *Monthly Notices of the Royal Astronomical Society* 388.4, pp. 1595–1617.

Daddi, E. et al. (2021). *Astronomy & Astrophysics* 649, A78, A78.

Danovich, M. et al. (2012). *Monthly Notices of the Royal Astronomical Society* 422.2, pp. 1732–1749.

Darvish, B. et al. (2014). *The Astrophysical Journal* 796.1, 51, p. 51.

Davé, R. et al. (2019). *Monthly Notices of the Royal Astronomical Society* 486.2, pp. 2827–2849.

Davies, L. J. M. et al. (2019). *Monthly Notices of the Royal Astronomical Society* 483.4, pp. 5444–5458.

Davis, M. et al. (1982). *The Astrophysical Journal* 253, pp. 423–445.

Davis, M. and Geller, M. J. (1976). *The Astrophysical Journal* 208, pp. 13–19.

de Bernardis, P. et al. (2000). *Nature* 404.6781, pp. 955–959.

de Lapparent, V., Geller, M. J., and Huchra, J. P. (1986). *Astrophysical Journal, Letters* 302, p. L1.

Dekel, A. and Silk, J. (1986). *The Astrophysical Journal* 303, p. 39.

Dekel, A. and Birnboim, Y. (2006). *Monthly Notices of the Royal Astronomical Society* 368.1, pp. 2–20.

Del Popolo, A. (2014). *International Journal of Modern Physics D* 23.3, 1430005, p. 1430005.

Di Matteo, P. et al. (2007). *Astronomy & Astrophysics* 468.1, pp. 61–81.

Di Matteo, P. et al. (2008). *Astronomy & Astrophysics* 492.1, pp. 31–49.

Di Matteo, T., Springel, V., and Hernquist, L. (2005). *Nature* 433.7026, pp. 604–607.

Di Teodoro, E. M. and Fraternali, F. (2015). *Monthly Notices of the Royal Astronomical Society* 451.3, pp. 3021–3033.

Díaz-García, S. and Knapen, J. H. (2020). *Astronomy & Astrophysics* 635, A197, A197.

Dolag, K. et al. (2006). *Monthly Notices of the Royal Astronomical Society* 370.2, pp. 656–672.

Draine, B. T. (2003). *Annual Review of Astronomy and Astrophysics* 41, pp. 241–289.

Draine, B. T. and Li, A. (2007). *The Astrophysical Journal* 657.2, pp. 810–837.

Dressler, A. (1980). *The Astrophysical Journal* 236, pp. 351–365.

Driver, S. P. et al. (2009). *Astronomy and Geophysics* 50.5, pp. 5.12–5.19.

Dubois, Y. et al. (2014). *Monthly Notices of the Royal Astronomical Society* 444.2, pp. 1453–1468.

Duncan, K. J. et al. (2018a). *Monthly Notices of the Royal Astronomical Society* 473.2, pp. 2655–2672.

Duncan, K. J. et al. (2018b). *Monthly Notices of the Royal Astronomical Society* 477.4, pp. 5177–5190.

Dye, S. (2008). *Monthly Notices of the Royal Astronomical Society* 389.3, pp. 1293–1305.

Ebeling, H., Stephenson, L. N., and Edge, A. C. (2014). *The Astrophysical Journal, Letters* 781.2, L40, p. L40.

Efstathiou, G. and Silk, J. (1983). *Fundamentals of Cosmic Physics* 9, pp. 1–138.

Einasto, J. (1965). *Trudy Astrofizicheskogo Instituta Alma-Ata* 5, pp. 87–100.

Einstein, A. (1915). *Sitzungsberichte der Königlich Preussischen Akademie der Wissenschaften*, pp. 844–847.

Einstein, A. (1917). *Sitzungsber. Preuss. Akad. Wiss. Berlin (Math. Phys.)* 1917, pp. 142–152.

Elias, L. M. et al. (2020). *Monthly Notices of the Royal Astronomical Society* 494.4, pp. 5439–5448.

Ellison, S. L., Catinella, B., and Cortese, L. (2018). *Monthly Notices of the Royal Astronomical Society* 478.3, pp. 3447–3466.

Elmegreen, D. M. and Elmegreen, B. G. (1987). *The Astrophysical Journal* 314, p. 3.

Emonts, B. H. C. et al. (2006). *Astronomy & Astrophysics* 454.1, pp. 125–135.

Emsellem, E. et al. (2004). *Monthly Notices of the Royal Astronomical Society* 352.3, pp. 721–743.

Fabian, A. C. (1999). *Monthly Notices of the Royal Astronomical Society* 308.4, pp. L39–L43.

Fabian, A. C. (2012). *Annual Review of Astronomy and Astrophysics* 50, pp. 455–489.

Falck, B. L. and Neyrinck, M. C. (2015). *Monthly Notices of the Royal Astronomical Society* 450.3, pp. 3239–3253.

Falck, B. L., Neyrinck, M. C., and Szalay, A. S. (2012). *The Astronomical Journal* 754.2, 126, p. 126.

Fall, S. M. and Efstathiou, G. (1980). *Monthly Notices of the Royal Astronomical Society* 193, pp. 189–206.

Faucher-Giguère, C.-A. et al. (2010). *The Astrophysical Journal* 725.1, pp. 633–657.

Feldmann, R. and Mayer, L. (2015). *Monthly Notices of the Royal Astronomical Society* 446.2, pp. 1939–1956.

Fernández, X. et al. (2016). *The Astrophysical Journal* 824.1, p. L1.

Fernández-Soto, A. et al. (2001). *The Astrophysical Journals* 135.1, pp. 41–61.

Feroz, F. and Hobson, M. P. (2008). *Monthly Notices of the Royal Astronomical Society* 384.2, pp. 449–463.

Feroz, F., Hobson, M. P., and Bridges, M. (2009). *Monthly Notices of the Royal Astronomical Society* 398.4, pp. 1601–1614.

Ferrari, C. et al. (2008). *School Science Review* 134.1-4, pp. 93–118.

Ferreira, E. G. M. (2021). *The Astronomy and Astrophysics Review* 29.1, 7, p. 7.

Forero-Romero, J. E. et al. (2009). *Monthly Notices of the Royal Astronomical Society* 396.3, pp. 1815–1824.

Forero-Romero, J. E., Contreras, S., and Padilla, N. (2014). *Monthly Notices of the Royal Astronomical Society* 443.2, pp. 1090–1102.

Fraser-McKelvie, A. et al. (2021). *Monthly Notices of the Royal Astronomical Society* 503.4, pp. 4992–5005.

Frenk, C. S. and White, S. D. M. (2012). *Annalen der Physik* 524.9-10, pp. 507–534.

Fumagalli, M. et al. (2017). *Monthly Notices of the Royal Astronomical Society* 471.3, pp. 3686–3698.

Galárraga-Espinosa, D. et al. (2020). *Astronomy & Astrophysics* 641, A173.

Galárraga-Espinosa, D. et al. (2021). *Astronomy & Astrophysics* 649, A117, A117.

Galárraga-Espinosa, D. et al. (2024). *Astronomy & Astrophysics* 684, A63, A63.

Gallart, C., Zoccali, M., and Aparicio, A. (2005). *Annual Review of Astronomy and Astrophysics* 43.1, pp. 387–434.

Gallazzi, A. and Bell, E. F. (2009). *The Astrophysical Journal, Supplement* 185.2, pp. 253–272.

Ganeshaiah Veena, P. et al. (2018). *Monthly Notices of the Royal Astronomical Society* 481.1, pp. 414–438.

Gao, L. et al. (2004). *Monthly Notices of the Royal Astronomical Society* 355.3, pp. 819–834.

Gheller, C. and Vazza, F. (2019). *Monthly Notices of the Royal Astronomical Society* 486.1, pp. 981–1002.

Gilmour, R. et al. (2007). *Monthly Notices of the Royal Astronomical Society* 380.4, pp. 1467–1487.

Giovannini, G., Tordi, M., and Feretti, L. (1999). *Nature Astronomy* 4.2, pp. 141–155.

Glasser, G. J. and Winter, R. F. (1961). *Biometrika* 48.3/4, pp. 444–448.

González, R. E. and Padilla, N. D. (2010). *Monthly Notices of the Royal Astronomical Society* 407.3, pp. 1449–1463.

Gould, A. and Weinberg, D. H. (1996). *The Astrophysical Journal* 468, p. 462.

Grootes, M. W. et al. (2017). *The Astronomical Journal* 153.3, 111, p. 111.

Gunn, J. E. and Gott J. Richard, I. (1972). *The Astrophysical Journal* 176, p. 1.

Gunn, J. E. and Peterson, B. A. (1965). *The Astrophysical Journal* 142, pp. 1633–1636.

Hahn, O., Teyssier, R., and Carollo, C. M. (2010). *Monthly Notices of the Royal Astronomical Society* 405.1, pp. 274–290.

Hanish, D. J. et al. (2006). *The Astrophysical Journal* 649.1, pp. 150–162.

Hannestad, S. et al. (2010). *Journal of Cosmology and Astroparticle Physics* 2010.8, 001, p. 001.

Hardcastle, M. J. and Croston, J. H. (2020). *New Astronomy Reviews* 88, 101539, p. 101539.

Hasan, F. et al. (2023a). *arXiv e-prints*, arXiv:2311.01443, arXiv:2311.01443.

Hasan, F. et al. (2023b). *arXiv e-prints*, arXiv:2303.08088, arXiv:2303.08088.

Hatfield, P. W. et al. (2022). *Monthly Notices of the Royal Astronomical Society* 513.3, pp. 3719–3733.

Haynes, M. P., Giovanelli, R., and Chincarini, G. L. (1984). *Annual Review of Astronomy and Astrophysics* 22, pp. 445–470.

He, S. et al. (2019). *Proceedings of the National Academy of Science* 116.28, pp. 13825–13832.

Heckman, T. M. and Best, P. N. (2014). *Annual Review of Astronomy and Astrophysics* 52, pp. 589–660.

Heß, S., Kitaura, F.-S., and Gottlöber, S. (2013). *Monthly Notices of the Royal Astronomical Society* 435.3, pp. 2065–2076.

Heywood, I. et al. (2021). *Monthly Notices of the Royal Astronomical Society* 509.2, pp. 2150–2168.

Heywood, I. et al. (2022). *Monthly Notices of the Royal Astronomical Society* 509.2, pp. 2150–2168.

Hirv, A. et al. (2017). *Astronomy & Astrophysics* 599, A31.

Ho, S. H. and Martin, C. L. (2020). *The Astrophysical Journal* 888.1, 14, p. 14.

Hoekstra, H. (2003). *Monthly Notices of the Royal Astronomical Society* 339.4, pp. 1155–1162.

Hoekstra, H. (2007). *Monthly Notices of the Royal Astromical Society* 379.1, pp. 317–330.

Hoekstra, H., Yee, H. K. C., and Gladders, M. D. (2002). *New Astronomy Reviews* 46.12, pp. 767–781.

Hoffman, Y. et al. (2012). *Monthly Notices of the Royal Astronomical Society* 425.3, pp. 2049–2057.

Hogan, C. J. and Weymann, R. J. (1987). *Monthly Notices of the Royal Astronomical Society* 225, 1P–5P.

Hoosain, M. et al. (2024). *Monthly Notices of the Royal Astronomical Society*.

Hopkins, P. F., Quataert, E., and Murray, N. (2012). *Monthly Notices of the Royal Astronomical Society* 421.4, pp. 3522–3537.

Hopkins, P. F. et al. (2014). *Monthly Notices of the Royal Astronomical Society* 445.1, pp. 581–603.

Hoyle, F. and Vogeley, M. S. (2004). *The Astrophysical Journal* 607.2, pp. 751–764.

Hoyle, F. et al. (2005). *The Astrophysical Journal* 620.2, pp. 618–628.

Hu, W., Barkana, R., and Gruzinov, A. (2000). *Physical Review Letters* 85.6, pp. 1158–1161.

Hubble, E. (1926). *The Astrophysical Journal* 64, pp. 321–369.

Hubble, E. (1929). *Proceedings of the National Academy of Science* 15.3, pp. 168–173.

Huchra, J. P. and Geller, M. J. (1982). *The Astrophysical Journal* 257, pp. 423–437.

Huchra, J. P. et al. (2012). *The Astrophysical Journals* 199.2, 26, p. 26.

Huege, T. (2016). *Physics Reports* 620, pp. 1–52.

Hugo, B. V. et al. (2022). In: *Astronomical Society of the Pacific Conference Series*. Ed. by J. E. Ruiz, F. Pierfedereci, and P. Teuben. Vol. 532. Astronomical Society of the Pacific Conference Series, p. 541.

Hui, L. et al. (2017). *Physical Review D* 95.4, 043541, p. 043541.

Hutchens, Z. L. et al. (2023). *The Astrophysical Journal* 956.1, p. 51.

Ibata, R. A. et al. (2013). *Nature* 493.7430, pp. 62–65.

Ilbert, O. et al. (2006). *Astronomy & Astrophysics* 457.3, pp. 841–856.

Ilbert, O. et al. (2009). *The Astrophysical Journal* 690.2, pp. 1236–1249.

Ilbert, O. et al. (2013). *Astronomy and Astrophysics* 556, A55, A55.

Ilić, S., Blanchard, A., and Douspis, M. (2015). *Astronomy & Astrophysics* 582, A79, A79.

Iyer, K. G. et al. (2019). *The Astrophysical Journal* 879.2, 116, p. 116.

Janka, H.-T. (2012). *Annual Review of Nuclear and Particle Science* 62.1, pp. 407–451.

Jarvis, M. J. et al. (2010). *Monthly Notices of the Royal Astronomical Society* 409.1, pp. 92–101.

Jarvis, M. J. et al. (2013). *Monthly Notices of the Royal Astronomical Society* 428.2, pp. 1281–1295.

Jarvis, M. J. et al. (2016). In: *MeerKAT Science: On the Pathway to the SKA*, 6, p. 6.

Jaskot, A. E. et al. (2015). *The Astrophysical Journal* 808.1, 66, p. 66.

Jeffreys, H. (1998). *The theory of probability*. OuP Oxford.

Johnston, R. et al. (2015). *Monthly Notices of the Royal Astronomical Society* 453.3, pp. 2540–2557.

Jonas, J. L. (2009). *Proceedings of the IEEE* 97.8, pp. 1522–1530.

Katz, N. (1992). *The Astrophysical Journal* 391, p. 502.

Katz, N. and Gunn, J. E. (1991). *The Astrophysical Journal* 377, p. 365.

Kauffmann, G. and Fairall, A. P. (1991). *Monthly Notices of the Royal Astronomical Society* 248, pp. 313–324.

Kauffmann, G., White, S. D. M., and Guiderdoni, B. (1993). *Monthly Notices of the Royal Astronomical Society* 264, pp. 201–218.

Kauffmann, G., Li, C., and Heckman, T. M. (2010). *Monthly Notices of the Royal Astronomical Society* 409.2, pp. 491–499.

Kauffmann, G. et al. (2003). *Monthly Notices of the Royal Astronomical Society* 341.1, pp. 54–69.

Kendall, M. G. (1938). *Biometrika* 30.1-2, pp. 81–93.

Kennicutt, R. C. (1998). *Annual Review of Astronomy and Astrophysics* 36, pp. 189–232.

Kennicutt, R. C. and Evans, N. J. (2012). *Annual Review of Astronomy and Astrophysics* 50, pp. 531–608.

Kenyon, J. S. et al. (2018). *Monthly Notices of the Royal Astronomical Society* 478.2, pp. 2399–2415.

Kereš, D. et al. (2005). *Monthly Notices of the Royal Astronomical Society* 363.1, pp. 2–28.

Kewley, L. J., Nicholls, D. C., and Sutherland, R. S. (2019). *Annual Review of Astronomy and Astrophysics* 57, pp. 511–570.

Kewley, L. J. et al. (2006). *Monthly Notices of the Royal Astronomical Society* 372.3, pp. 961–976.

Khochfar, S. and Silk, J. (2009). *Monthly Notices of the Royal Astronomical Society* 397.1, pp. 506–510.

Kikuta, S. et al. (2019). *Publications of the Astronomical Society of Japan* 71.3, L2, p. L2.

Kim, C.-G. and Ostriker, E. C. (2015). *The Astrophysical Journal* 802.2, 99, p. 99.

King, A. (2005). *The Astrophysical Journal, Letters* 635.2, pp. L121–L123.

Kitaura, F.-S. et al. (2012). *Monthly Notices of the Royal Astronomical Society* 425.4, pp. 2422–2435.

Klar, J. S. and Mücket, J. P. (2012). *Monthly Notices of the Royal Astronomical Society* 423.1, pp. 304–319.

Kleiner, D. et al. (2017). *Monthly Notices of the Royal Astronomical Society* 466.4, pp. 4692–4710.

Klypin, A. A. and Shandarin, S. F. (1983). *Monthly Notices of the Royal Astronomical Society* 204, pp. 891–907.

Knebe, A. et al. (2004). *The Astrophysical Journal* 603.1, pp. 7–11.

Kooistra, R., Silva, M. B., and Zaroubi, S. (2017). *Monthly Notices of the Royal Astronomical Society* 468.1, pp. 857–869.

Kooistra, R. et al. (2019). *Monthly Notices of the Royal Astronomical Society* 490.1, pp. 1415–1424.

Kormendy, J. and Bender, R. (2012). *The Astrophysical Journal, Letters* 198.1, 2, p. 2.

Kormendy, J. and Ho, L. C. (2013). *Annual Review of Astronomy and Astrophysics* 51.1, pp. 511–653.

Kormendy, J. and Richstone, D. (1995). *Annual Review of Astronomy and Astrophysics* 33, p. 581.

Kotecha, S. et al. (2022). *Monthly Notices of the Royal Astronomical Society* 512.1, pp. 926–944.

Kraljic, K. et al. (2017). *Monthly Notices of the Royal Astronomical Society* 474.1, pp. 547–571.

Kraljic, K., Davé, R., and Pichon, C. (2020). *Monthly Notices of the Royal Astronomical Society* 493.1, pp. 362–381.

Kraljic, K. et al. (2021). *Monthly Notices of the Royal Astronomical Society* 504.3, pp. 4626–4633.

Kravtsov, A. V. and Borgani, S. (2012). *Annual Review of Astronomy and Astrophysics* 50, pp. 353–409.

Kravtsov, A. V. et al. (1998). *The Astrophysical Journal* 502.1, pp. 48–58.

Kravtsov, A. V. et al. (2004). *The Astrophysical Journal* 609.1, pp. 35–49.

Krolewski, A. et al. (2019). *The Astrophysical Journal* 876.1, p. 52.

Kroupa, P., Theis, C., and Boily, C. M. (2005). *Astronomy & Astrophysics* 431, pp. 517–521.

Kroupa, P. (2001). *Monthly Notices of the Royal Astronomical Society* 322.2, pp. 231–246.

Krumholz, M. R., Leroy, A. K., and McKee, C. F. (2011). *The Astrophysical Journal* 731.1, 25, p. 25.

Krumholz, M. R., McKee, C. F., and Tumlinson, J. (2009). *The Astrophysical Journal* 699.1, pp. 850–856.

Kulkarni, M. and Ostriker, J. P. (2022). *Monthly Notices of the Royal Astronomical Society* 510.1, pp. 1425–1430.

Kuutma, T., Tamm, A., and Tempel, E. (2017). *Astronomy & Astrophysics* 600, p. L6.

Lacey, C. and Cole, S. (1993). *Monthly Notices of the Royal Astronomical Society* 262.3, pp. 627–649.

Laigle, C. et al. (2017). *Monthly Notices of the Royal Astronomical Society* 474.4, pp. 5437–5458.

Laigle, C. et al. (2016). *The Astrophysical Journals* 224.2, 24, p. 24.

Laigle, C. et al. (2018). *Monthly Notices of the Royal Astronomical Society* 474.4, pp. 5437–5458.

Laor, A. and Brandt, W. N. (2002). *The Astrophysical Journal* 569.2, pp. 641–654.

Larson, R. B. (1976). *Monthly Notices of the Royal Astronomical Society* 176, pp. 31–52.

Larson, R. B., Tinsley, B. M., and Caldwell, C. N. (1980). *The Astrophysical Journal* 237, pp. 692–707.

Le Fèvre, O. et al. (2013). *The Astrophysical Journal* 559, A14, A14.

Lee, J. (2004). *The Astrophysical Journal, Letters* 614.1, pp. L1–L4.

Lee, J. and Erdogdu, P. (2007). *The Astrophysical Journal* 671.2, pp. 1248–1255.

Lee, J. and Moon, J.-S. (2022). *The Astrophysical Journal* 936.2, 119, p. 119.

Lee, J. and Pen, U.-L. (2000). *The Astrophysical Journal, Letters* 532.1, pp. L5–L8.

Leitner, S. N. (2012). *The Astrophysical Journal* 745.2, 149, p. 149.

Leja, J. et al. (2017). *The Astrophysical Journal* 837.2, 170, p. 170.

Leja, J. et al. (2019). *The Astrophysical Journal* 876.1, 3, p. 3.

Leroy, A. K. et al. (2008). *The Astronomy Journal* 136.6, pp. 2782–2845.

Leslie, S. K. et al. (2020). *The Astrophysical Journal* 899.1, 58, p. 58.

Li, Y. A., Ho, L. C., and Shangguan, J. (2023). *The Astrophysics Journal* 953.1, 91, p. 91.

Liao, S. and Gao, L. (2019). *Monthly Notices of the Royal Astronomical Society* 485.1, pp. 464–473.

Libeskind, N. I. et al. (2015). *Monthly Notices of the Royal Astronomical Society* 452.1, pp. 1052–1059.

Libeskind, N. I. et al. (2017). *Monthly Notices of the Royal Astronomical Society* 473.1, pp. 1195–1217.

Lilly, S. J. et al. (1995). *The Astrophysical Journal* 455, p. 50.

Lilly, S. J. et al. (2009). *The Astrophysical Journal, Supplement* 184.2, pp. 218–229.

Lin, L. et al. (2010). *The Astrophysical Journal* 718.2, pp. 1158–1170.

Liu, F. S. et al. (2009). *Monthly Notices of the Royal Astronomical Society* 396.4, pp. 2003–2010.

Lotz, J. M. et al. (2011). *The Astrophysical Journal* 742.2, 103, p. 103.

Lovell, M. R. et al. (2011). *Monthly Notices of the Royal Astronomical Society* 413.4, pp. 3013–3021.

Lu, Y. S. et al. (2024). *Monthly Notices of the Royal Astronomical Society* 527.4, pp. 11256–11287.

Luber, N. et al. (2019). *The Astronomical Journal* 157, p. 254.

Lutz, K. A. et al. (2017). *Monthly Notices of the Royal Astronomical Society* 467.1, pp. 1083–1097.

MacArthur, L. A. et al. (2004). *The Astrophysical Journal, Supplement* 152.2, pp. 175–199.

Madau, P. and Dickinson, M. (2014). *Annual Review of Astronomy and Astrophysics* 52.1, pp. 415–486.

Maddox, N. et al. (2021). *Astronomy & Astrophysics* 646, A35.

Maddox, N. et al. (2015). *Monthly Notices of the Royal Astronomical Society* 447.2, pp. 1610–1617.

Magorrian, J. et al. (1998). *The Astronomical Journal* 115.6, pp. 2285–2305.

Malavasi, N. et al. (2015). *Astronomy & Astrophysics* 576, A101, A101.

Malavasi, N. et al. (2017). *Monthly Notices of the Royal Astronomical Society* 465.4, pp. 3817–3822.

Malavasi, N. et al. (2020). *Astronomy & Astrophysics* 642, A19, A19.

Malavasi, N. et al. (2022). *Astronomy and Astrophysics* 658, A113, A113.

Mandelker, N. et al. (2021). *The Astrophysical Journal* 923.1, 115, p. 115.

Mann, H. B. and Whitney, D. R. (1947). *The Annals of Mathematical Statistics* 18.1, pp. 50–60.

Martin, D. C. et al. (2016). *The Astrophysical Journal, Letters* 824.1, L5, p. L5.

Martínez, H. J., Muriel, H., and Coenda, V. (2016). *Monthly Notices of the Royal Astronomical Society* 455.1, pp. 127–135.

Massey, R., Kitching, T., and Richard, J. (2010). *Reports on Progress in Physics* 73.8, 086901, p. 086901.

McCarthy, I. G. et al. (2008). *Monthly Notices of the Royal Astronomical Society* 383.2, pp. 593–605.

McCracken, H. J. et al. (2012). *Astronomy & Astrophysics* 544, A156, A156.

McKee, C. F. and Ostriker, E. C. (2007). *Annual Review of Astronomy and Astrophysics* 45.1, pp. 565–687.

McMullin, J. P. et al. (2007). In: *Astronomical Data Analysis Software and Systems XVI*. Ed. by R. A. Shaw, F. Hill, and D. J. Bell. Vol. 376. Astronomical Society of the Pacific Conference Series, p. 127.

McNamara, B. R. and Nulsen, P. E. J. (2007). *Annual Review of Astronomy and Astrophysics* 45.1, pp. 117–175.

Meurer, G. R. et al. (2006). *The Astrophysical Journal, Supplement* 165.1, pp. 307–337.

Milnor, J. (1963). *Stud* 51.

Miralda-Escudé, J. (2003). *Science* 300.5627, pp. 1904–1909.

Mocz, P. et al. (2019). *Physical Review Letters* 123.14, 141301, p. 141301.

Mocz, P. et al. (2020). *Monthly Notices of the Royal Astronomical Society* 494.2, pp. 2027–2044.

Momcheva, I. G. et al. (2016). *The Astrophysical Journal, Supplement* 225.2, 27, p. 27.

Montes, M. (2019). *arXiv e-prints*, arXiv:1912.01616, arXiv:1912.01616.

Moon, J.-S. and Lee, J. (2024). *arXiv e-prints*, arXiv:2401.11707, arXiv:2401.11707.

Moore, B. et al. (1998a). *The Astrophysical Journal, Letters* 499.1, pp. L5–L8.

Moore, B., Lake, G., and Katz, N. (1998b). *The Astrophysical Journal* 495.1, pp. 139–151.

Moore, B. et al. (1996). *Nature* 379.6566, pp. 613–616.

Moreno, J. et al. (2019). *Monthly Notices of the Royal Astronomical Society* 485.1, pp. 1320–1338.

Morganti, R. (2017). *Frontiers in Astronomy and Space Sciences* 4, 42, p. 42.

Moutard, T. et al. (2016). *Astronomy and Astrophysics* 590, A102, A102.

Murray, N. and Chiang, J. (1995). *The Astrophysical Journal, Letters* 454, p. L105.

Navarro, J. F. and Benz, W. (1991). *The Astrophysical Journal* 380, p. 320.

Navarro, J. F., Eke, V. R., and Frenk, C. S. (1996a). *Monthly Notices of the Royal Astronomical Society* 283.3, pp. L72–L78.

Navarro, J. F., Frenk, C. S., and White, S. D. M. (1996b). *The Astrophysical Journal* 462, p. 563.

Navarro, J. F. and White, S. D. M. (1994). *Monthly Notices of the Royal Astronomical Society* 267.2, pp. 401–412.

Negroponte, J. and White, S. D. M. (1983). *Monthly Notices of the Royal Astronomical Society* 205, pp. 1009–1029.

Nelson, D. et al. (2019). *Monthly Notices of the Royal Astronomical Society* 490.3, pp. 3234–3261.

Nersesian, A. et al. (2024). *Astronomy & Astrophysics* 681, A94, A94.

Noeske, K. G. et al. (2007). *The Astrophysical Journal, Letters* 660.1, pp. L43–L46.

Noether, G. (1978). *Studies in statistics*, pp. 39–65.

Novikov, D., Colombi, S., and Doré, O. (2006). *Monthly Notices of the Royal Astronomical Society* 366.4, pp. 1201–1216.

Ocvirk, P., Pichon, C., and Teyssier, R. (2008). *Monthly Notices of the Royal Astronomical Society* 390.4, pp. 1326–1338.

Ocvirk, P. et al. (2006). *Monthly Notices of the Royal Astronomical Society* 365.1, pp. 46–73.

Offringa, A. R. et al. (2014). *Monthly Notices of the Royal Astronomical Society* 444.1, pp. 606–619.

Pahwa, I. et al. (2016). *Monthly Notices of the Royal Astronomical Society* 457.1, pp. 695–703.

Pan, H. et al. (2023). *Monthly Notices of the Royal Astronomical Society* 525.1, pp. 256–269.

Parkash, V. et al. (2018). *The Astrophysical Journal* 864.1, 40, p. 40.

Pawlowski, M. S., Pflamm-Altenburg, J., and Kroupa, P. (2012). *Monthly Notices of the Royal Astronomical Society* 423.2, pp. 1109–1126.

Pawlowski, M. S. (2018). *Modern Physics Letters A* 33.6, 1830004, p. 1830004.

Pearson, W. J. et al. (2019). *Astronomy & Astrophysics* 631, A51, A51.

Peebles, P. (1969). *apj* 155, pp. 393–+.

Peng, Y., Maiolino, R., and Cochrane, R. (2015). *Nature* 521.7551, pp. 192–195.

Peng, Y.-J. et al. (2012). *The Astrophysical Journal* 757.1, 4, p. 4.

Penzias, A. A. and Wilson, R. W. (1965). *The Astrophysical Journal* 142, pp. 419–421.

Perret, V. et al. (2014). *Astronomy & Astrophysics* 562, A1, A1.

Pessa, I. et al. (2023). *Astronomy & Astrophysics* 673, A147, A147.

Pichon, C. et al. (2011). *Monthly Notices of the Royal Astronomical Society* 418.4, pp. 2493–2507.

Pillepich, A. et al. (2018). *Monthly Notices of the Royal Astronomical Society* 475.1, pp. 648–675.

Piotrowska, J. M. et al. (2022). *Monthly Notices of the Royal Astronomical Society* 512.1, pp. 1052–1090.

Planck Collaboration et al. (2020). *Astronomy & Astrophysics* 641, A6, A6.

Poggianti, B. M. et al. (2017). *The Astrophysical Journal* 844.1, 48, p. 48.

Ponomareva, A. A. et al. (2021). *Monthly Notices of the Royal Astronomical Society* 508.1, pp. 1195–1205.

Popescu, C. C. et al. (2011). *Astronomy & Astrophysics* 527, A109, A109.

Popesso, P. et al. (2019a). *Monthly Notices of the Royal Astronomical Society* 483.3, pp. 3213–3226.

Popesso, P. et al. (2019b). *Monthly Notices of the Royal Astronomical Society* 490.4, pp. 5285–5299.

Popping, G., Somerville, R. S., and Trager, S. C. (2014). *Monthly Notices of the Royal Astronomical Society* 442.3, pp. 2398–2418.

Porciani, C., Dekel, A., and Hoffman, Y. (2002). *Monthly Notices of the Royal Astronomical Society* 332.2, pp. 325–338.

Pozzetti, L. et al. (2010). *Astronomy and Astrophysics* 523, A13, A13.

Pratt, G. W. et al. (2010). *Astronomy & Astrophysics* 511, A85, A85.

Prochaska, J. X., Lau, M. W., and Hennawi, J. F. (2014). *The Astrophysical Journal* 796.2, 140, p. 140.

Qu, Y. et al. (2011). *Astronomy & Astrophysics* 530, A10, A10.

Quinn, P. J., Hernquist, L., and Fullagar, D. P. (1993). *The Astrophysical Journal* 403, p. 74.

Ramachandra, N. and Shandarin, S. F. (2017). In: *APS April Meeting Abstracts*. Vol. 2017. APS Meeting Abstracts, M5.003, p. M5.003.

Ramakrishnan, V. et al. (2024). *arXiv e-prints*, arXiv:2406.08645, arXiv:2406.08645.

Rees, M. J. (1984). *Annual Review of Astronomy and Astrophysics* 22, pp. 471–506.

Renaud, F. et al. (2014). *Monthly Notices of the Royal Astronomical Society* 442, pp. L33–L37.

Rhoads, J. E. and Malhotra, S. (2001). *The Astrophysical Journal, Letters* 563.1, pp. L5–L9.

Riess, A. G. et al. (1998). *The Astronomical Journal* 116.3, pp. 1009–1038.

Riess, A. G. et al. (2016). *The Astrophysical Journal* 826.1, 56, p. 56.

Riess, A. G. et al. (2022). *The Astrophysical Journal, Letters* 934.1, L7, p. L7.

Robertson, H. P. (1935). *The Astrophysical Journal* 82, p. 284.

Robotham, A. S. G. et al. (2013). *Monthly Notices of the Royal Astronomical Society* 431.1, pp. 167–193.

Robotham, A. S. G. et al. (2014). *Monthly Notices of the Royal Astronomical Society* 444.4, pp. 3986–4008.

Rodríguez Montero, F. et al. (2019). *Monthly Notices of the Royal Astronomical Society* 490.2, pp. 2139–2154.

Rodríguez-Baras, M. et al. (2014). *Monthly Notices of the Royal Astronomical Society* 442.1, pp. 495–508.

Rosati, P., Borgani, S., and Norman, C. (2002). *Annual Review of Astronomy and Astrophysics* 40, pp. 539–577.

Rosdahl, J. and Blaizot, J. (2012). *Monthly Notices of the Royal Astronomical Society* 423.1, pp. 344–366.

Rubin, V. C. and Ford W. Kent, J. (1970). *The Astrophysical Journal* 159, p. 379.

Saintonge, A. and Catinella, B. (2022). *Annual Review of Astronomy and Astrophysics* 60, pp. 319–361.

Saintonge, A. et al. (2012). *The Astrophysical Journal* 758.2, 73, p. 73.

Sajina, A., Lacy, M., and Pope, A. (2022). *Universe* 8.7, 356, p. 356.

Sales, L. V. and Navarro, J. F. (2023). *Nature Astronomy* 7, pp. 376–377.

Salpeter, E. E. (1955). *The Astrophysical Journal* 121, p. 161.

Sandage, A. (1986). *Astronomy & Astrophysics* 161, pp. 89–101.

Santos, D. J. D. et al. (2021). *Monthly Notices of the Royal Astronomical Society* 507.2, pp. 3070–3088.

Schaap, W. E. and van de Weygaert, R. (2000). *Astronomy and Astrophysics* 363, pp. L29–L32.

Schaye, J. et al. (2015). *Monthly Notices of the Royal Astronomical Society* 446.1, pp. 521–554.

Schreiber, C. et al. (2018). *Astronomy and Astrophysics* 618, A85, A85.

Scoville, N. Z. et al. (1989). *The Astrophysical Journal, Letters* 345, p. L25.

Scoville, N. Z. et al. (2007). *Astrophysical Journal, Supplement* 172.1, pp. 1–8.

Shapley, A. E. (2011). *Annual Review of Astronomy and Astrophysics* 49.1, pp. 525–580.

Shirley, R. et al. (2019). *Monthly Notices of the Royal Astronomical Society* 490.1, pp. 634–656.

Silk, J. and Mamon, G. A. (2012). *Research in Astronomy and Astrophysics* 12.8, pp. 917–946.

Silverman, J. D. et al. (2015). *The Astrophysical Journal, Supplement* 220.1, 12, p. 12.

Simha, V. et al. (2014). *arXiv e-prints*, arXiv:1404.0402, arXiv:1404.0402.

Skelton, R. E. et al. (2014). *The Astrophysical Journal, Supplement* 214.2, 24, p. 24.

Smith, M. W. L. et al. (2012a). *The Astrophysical Journal* 748.2, 123, p. 123.

Smith, R. J. et al. (2012b). *Monthly Notices of the Royal Astronomical Society* 419.4, pp. 3167–3180.

Soifer, B. T. et al. (2000). *The Astronomical Journal* 119.2, pp. 509–523.

Soifer, B. T. et al. (2001). *The Astronomical Journal* 122.3, pp. 1213–1237.

Somerville, R. S., Popping, G., and Trager, S. C. (2015). *Monthly Notices of the Royal Astronomical Society* 453.4, pp. 4337–4367.

Somerville, R. S., Primack, J. R., and Faber, S. M. (2001). *Monthly Notices of the Royal Astronomical Society* 320.4, pp. 504–528.

Somerville, R. S. et al. (2008). *Monthly Notices of the Royal Astronomical Society* 391.2, pp. 481–506.

Sorba, R. and Sawicki, M. (2018). *Monthly Notices of the Royal Astronomical Society* 476.2, pp. 1532–1547.

Sorce, J. G. et al. (2016). *Monthly Notices of the Royal Astronomical Society* 455.2, pp. 2078–2090.

Sousbie, T. (2011). *Monthly Notices of the Royal Astronomical Society* 414.1, pp. 350–383.

Sousbie, T., Pichon, C., and Kawahara, H. (2011). *Monthly Notices of the Royal Astronomical Society* 414.1, pp. 384–403.

Sousbie, T. et al. (2008). *Monthly Notices of the Royal Astronomical Society* 383.4, pp. 1655–1670.

Sparre, M. and Springel, V. (2016). *Monthly Notices of the Royal Astronomical Society* 462.3, pp. 2418–2430.

Spergel, D. N. et al. (2003). *The Astrophysical Journal, Supplement* 148.1, pp. 175–194.

Spergel, D. N. and Steinhardt, P. J. (2000). *Physical Review Letters* 84.17, pp. 3760–3763.

Spilker, J. et al. (2018). *The Astrophysical Journal* 860.2, 103, p. 103.

Springel, V. et al. (2005). *Nature Astrophysics* 435.7042, pp. 629–636.

Steidel, C. C. et al. (2000). *The Astrophysical Journal* 532.1, pp. 170–182.

Stewart, K. R. et al. (2011). *The Astrophysical Journal* 738.1, 39, p. 39.

Stoica, R. S., Martínez, V. J., and Saar, E. (2007). *Journal of the Royal Statistical Society: Series C (Applied Statistics) 56 (4* 56, p. 1.

Stoica, R. S. et al. (2005). *Astronomy & Astrophysics* 434.2, pp. 423–432.

Sunyaev, R. A. and Zeldovich, Y. B. (1972). *Comments on Astrophysics and Space Physics* 4, p. 173.

Tacchella, S. et al. (2022). *The Astrophysical Journal* 926.2, 134, p. 134.

Tal, T. et al. (2009). *The Astronomical Journal* 138.5, pp. 1417–1427.

Tanaka, T. S. et al. (2023). *arXiv e-prints*, arXiv:2307.14235, arXiv:2307.14235.

Taylor, A. R. et al. (2024). *Monthly Notices of the Royal Astronomical Society* 528.2, pp. 2511–2522.

Tempel, E., Stoica, R. S., and Saar, E. (2013). *Monthly Notices of the Royal Astronomical Society* 428.2, pp. 1827–1836.

Tempel, E. et al. (2014). *Monthly Notices of the Royal Astronomical Society* 438.4, pp. 3465–3482.

Tempel, E. et al. (2016). *Astronomy and Computing* 16, pp. 17–25.

Tempel, E. and Libeskind, N. I. (2013). *The Astrophysical Journal, Letters* 775.2, L42, p. L42.

Teyssier, R., Chapon, D., and Bournaud, F. (2010). *The Astrophysical Journal, Letters* 720.2, pp. L149–L154.

Toomre, A. (1977). In: *Evolution of Galaxies and Stellar Populations*. Ed. by B. M. Tinsley and D. C. Larson Richard B. Gehret, p. 401.

Toomre, A. and Toomre, J. (1972). *The Astrophysical Journal* 178, pp. 623–666.

Tosi, M. (2009). In: *The Ages of Stars*. Ed. by E. E. Mamajek, D. R. Soderblom, and R. F. G. Wyse. Vol. 258, pp. 61–72.

Tramonte, D. et al. (2019). *Monthly Notices of the Royal Astronomical Society* 489.1, pp. 385–400.

Tremaine, S. (1981). In: *Structure and Evolution of Normal Galaxies*. Ed. by S. M. Fall and D. Lynden-Bell, pp. 67–84.

Treu, T. and Koopmans, L. V. E. (2004). *The Astrophysical Journal* 611.2, pp. 739–760.

Treyer, M. et al. (2018). *Monthly Notices of the Royal Astronomical Society* 477.2, pp. 2684–2704.

Trujillo, I., Carretero, C., and Patiri, S. G. (2006). *The Astrophysical Journal* 640.2, pp. L111–L114.

Tudorache, M. N. et al. (2022). *Monthly Notices of the Royal Astronomical Society* 513.2, pp. 2168–2177.

Tulin, S. and Yu, H.-B. (2018). *Physics Reports* 730, pp. 1–57.

Tumlinson, J., Peeples, M. S., and Werk, J. K. (2017). *Annual Review of Astronomy and Astrophysics* 55.1, pp. 389–432.

Umehata, H. et al. (2019). *Science* 366.6461, pp. 97–100.

van de Weygaert, R. and Schaap, W. E. (2009). "The Cosmic Web: Geometric Analysis". In: *Data Analysis in Cosmology*. Ed. by V. J. Martínez et al. Vol. 665, pp. 291–413.

Varadaraj, R. G. et al. (2023). *Monthly Notices of the Royal Astronomical Society* 524.3, pp. 4586–4613.

Veilleux, S., Kim, D. .-., and Sanders, D. B. (2002). *The Astrophysical Journal, Supplement* 143.2, pp. 315–376.

Veilleux, S., Cecil, G., and Bland-Hawthorn, J. (2005). *Annual Review of Astronomy and Astrophysics* 43.1, pp. 769–826.

Viel, M. et al. (2005). *Physical Review D* 71.6, 063534, p. 063534.

Vink, J. (2020). *Physics and Evolution of Supernova Remnants*.

Vulcani, B. et al. (2011). *Monthly Notices of the Royal Astronomical Society* 412.1, pp. 246–268.

Vulcani, B. et al. (2019). *Monthly Notices of the Royal Astronomical Society* 487.2, pp. 2278–2295.

Walcher, J. et al. (2011). *Astrophysics and Space Science* 331, pp. 1–52.

Walker, I. R., Mihos, J. C., and Hernquist, L. (1996). *The Astrophysical Journal* 460, p. 121.

Wang, J. et al. (2012). *Astronomy & Astrophysics* 538, A121, A121.

Wang, P. et al. (2021). *Nature Astronomy* 5, pp. 839–845.

Wang, W. et al. (2024). *arXiv e-prints*, arXiv:2402.11678, arXiv:2402.11678.

Welker, C. et al. (2014). *Monthly Notices of the Royal Astronomical Society* 445, pp. L46–L50.

Welker, C. et al. (2020). *Monthly Notices of the Royal Astronomical Society* 491.2, pp. 2864–2884.

Whitaker, K. E. et al. (2012). *The Astrophysical Journal Letters* 754.2, p. L29.

White, S. D. M. (1984). *The Astrophysical Journal* 286, pp. 38–41.

White, S. D. M. and Rees, M. J. (1978). *Monthly Notices of the Royal Astronomical Society* 183, pp. 341–358.

White, S. D. M. and Frenk, C. S. (1991). *The Astrophysical Journal* 379, p. 52.

Wilson, C. D. et al. (2008). *The Astrophysical Journal, Supplement* 178.2, pp. 189–224.

Winkel, N. et al. (2021). *Monthly Notices of the Royal Astronomical Society* 505.4, pp. 4920–4934.

Wong, T. and Blitz, L. (2002). *The Astrophysical Journal* 569.1, pp. 157–183.

Xu, W. et al. (2020). *Monthly Notices of the Royal Astronomical Society* 498.2, pp. 1839–1851.

Yamada, T. et al. (2012). *The Astronomical Journal* 143.4, 79, p. 79.

York, D. G. et al. (2000). *The Astronomical Journal* 120.3, pp. 1579–1587.

Yun, M. S., Ho, P. T. P., and Lo, K. Y. (1994). *Nature Astronomy* 372.6506, pp. 530–532.

Zakharova, D. et al. (2023). *arXiv e-prints*, arXiv:2307.05240, arXiv:2307.05240.

Zel'dovich, Y. B. (1970). *Astronomy and Astrophysics* 500, pp. 13–18.

Zel'dovich, Y. B., Einasto, J., and Shandarin, S. F. (1982). *Nature* 300.5891, pp. 407–413.

Zhang, J., Liu, H., and Chu, M.-C. (2018). *Frontiers in Astronomy and Space Sciences* 5, 48, p. 48.

Zinger, E. et al. (2020). *Monthly Notices of the Royal Astronomical Society* 499.1, pp. 768–792.

Zwicky, F. (1937). *The Astrophysical Journal* 86, p. 217.